OAK RIDGE NATIONAL LABORATORY LIBRARIES
3 4456 0548375 9

CENTRAL RESEARCH LIBRARY
DOCUMENT COLLECTION

ORNL-3760
UC-20 - Controlled Thermonuclear Processes
TID-4500 (37th ed.)

THERMONUCLEAR DIVISION

SEMIANNUAL PROGRESS REPORT

FOR PERIOD ENDING OCTOBER 31, 1964

OAK RIDGE NATIONAL LABORATORY
operated by
UNION CARBIDE CORPORATION
for the
U.S. ATOMIC ENERGY COMMISSION

CENTRAL RESEARCH LIBRARY
DOCUMENT COLLECTION
LIBRARY LOAN COPY
DO NOT TRANSFER TO ANOTHER PERSON
If you wish someone else to see this
document, send in name with document

Printed in USA. Price $4.00. Available from the Clearinghouse for Federal Scientific and Technical Information, National Bureau of Standards, U.S. Department of Commerce, Springfield, Virginia

LEGAL NOTICE

This report was prepared as an account of Government sponsored work. Neither the United States, nor the Commission, nor any person acting on behalf of the Commission:

A. Makes any warranty or representation, expressed or implied, with respect to the accuracy, completeness, or usefulness of the information contained in this report, or that the use of any information, apparatus, method, or process disclosed in this report may not infringe privately owned rights; or

B. Assumes any liabilities with respect to the use of, or for damages resulting from the use of any information, apparatus, method, or process disclosed in this report.

As used in the above, "person acting on behalf of the Commission" includes any employee or contractor of the Commission, or employee of such contractor, to the extent that such employee or contractor of the Commission, or employee of such contractor prepares, disseminates, or provides access to, any information pursuant to his employment or contract with the Commission, or his employment with such contractor.

ORNL-3760

Contract No. W-7405-eng-26

THERMONUCLEAR DIVISION

SEMIANNUAL PROGRESS REPORT

For Period Ending October 31, 1964

FEBRUARY 1965

OAK RIDGE NATIONAL LABORATORY
Oak Ridge, Tennessee
operated by
UNION CARBIDE CORPORATION
for the
U. S. ATOMIC ENERGY COMMISSION

OAK RIDGE NATIONAL LABORATORY LIBRARIES

3 4456 0548375 9

Contents

INTRODUCTION vii

ABSTRACTING SUMMARY ix

1. INJECTION AND ACCUMULATION: SINGLE-PASS EXPERIMENTS (DCX-1) 1
   - 1.1 Introduction 1
   - 1.2 Studies of Radio-Frequency Signals 1
   - 1.3 Investigations of Proton Losses from Plasmas Formed by Lorentz-Force Trapping 5
     - 1.3.1 Introduction 5
     - 1.3.2 Checks on the Trapping Fraction 5
     - 1.3.3 Search for Mirror Losses 6
     - 1.3.4 Measurements of Fast-Proton Radial Losses 6
   - 1.4 Plasma Potential Probe 9

2. INJECTION AND ACCUMULATION: MULTIPLE-PASS EXPERIMENTS (DCX-2) 10
   - 2.1 Introduction 10
   - 2.2 Foil Detector Signals 13
   - 2.3 Radio-Frequency Measurements 15
   - 2.4 Angular and Energy Analysis of Emitted Neutrals 17

3. ELECTRON-CYCLOTRON HEATING 23
   - 3.1 Electron-Cyclotron Heating Experiments in the EPA Facility 23
     - 3.1.1 Introduction 23
     - 3.1.2 Bremsstrahlung Spectrum 23
     - 3.1.3 Neutral-Beam Injection Studies 25
     - 3.1.4 Detector and Amplifier for Charge-Exchange Neutrals 26
   - 3.2 The Redesigned ELMO Facility 27
     - 3.2.1 Construction of the ELMO Facility 27
     - 3.2.2 Expected Plasma Volume and Density in the ELMO Facility 28

4. PLASMA PHYSICS 30
   - 4.1 Application of the Burnout Phenomena to Ion and Electron Heating (Experimental) 30
     - 4.1.1 Introduction 30
     - 4.1.2 Indications of Complete Ionization 32
     - 4.1.3 Indications of Ion Heating 32
     - 4.1.4 Indications of Electron Heating 34
     - 4.1.5 Plasma Density Measurements 34
     - 4.1.6 Plasma Potential Measurements 35
     - 4.1.7 Neutron Emission 35

4.2 A Simple Momentum Probe for Plasma Studies 36
4.3 A Sampling Oscilloscope as a Coherent Detector 39
4.4 Ionic-Sound-Wave Time-of-Flight Measurements in Quiescent Plasmas 41
4.5 Beam Stabilization in the Calutron 45
4.6 The Beam Plasma Facility 47
4.7 Stabilization of the Deuterium Arc 49
4.8 The Hydrogen Arc in the Long Solenoid: Baffle Studies 52
4.8.1 Introduction 52
4.8.2 Baffle Saturation Current 52
4.8.3 Water-Cooled Probe 53
4.8.4 Langmuir Probe 54
4.8.5 Gridded Probe Measurements 54
4.9 Spectroscopic Studies of the Hydrogen Arc in the Long Solenoid 55

5. CROSS-SECTION MEASUREMENTS 57
5.1 Formation of Excited H^0 by Arc Dissociation of H_2^+ 57
5.2 Production of Highly Excited Neutral Atoms by Passing Protons Through Atomic Hydrogen 60
5.3 Electric Field Ionization of H_2 62
5.4 Particle Detectors 63

6. PRODUCTION, ACCELERATION, AND INJECTION OF IONIC AND ATOMIC BEAMS 64
6.1 High-Current Ion-Beam Production and Injection 64

7. PLASMA THEORY AND COMPUTATION 69
7.1 Velocity Diffusion by Microinstabilities 69
7.2 Effect of a Loss Cone on the Electrostatic Stability of a Uniformly Magnetized Plasma 70
7.3 Electrostatic Instabilities in a Plasma 72
7.4 DCX-2 Decay Curves 72
7.5 Collisional and Anomalous Diffusion 74
7.6 Effect of Plasma Potential on Minimum-*B* Stability 76

8. MAGNETICS AND SUPERCONDUCTIVITY 77
8.1 DCX-2 Beam Injection Duct 77
8.2 Design of a High-Homogeneity, Power-Optimized Solenoid 80
8.3 Two Computer Programs for Fields of Idealized Magnetic Rings and Cylinders 87
8.3.1 Introduction 87
8.3.2 The Zonal Harmonic Method 88
8.3.3 The Elliptic Integral Method 88
8.4 Magnetic Field Codes Developed in ORNL Thermonuclear Division 89
8.4.1 Program STORE 89
8.4.2 Program MADCAP 89
8.4.3 Programs IOFFIN and TERPJO 90
8.4.4 Programs FINDRZ and FINDRT 90
8.4.5 Zonal Harmonics Package 90
8.4.6 Elliptic Integral—Gaussian Quadrature Package 90

8.4.7 Double Gaussian Integration Code 90
8.4.8 Infinitely Long Nonzero-Cross-Section Ioffe Bars 90
8.4.9 Power and Homogeneity Optimization 91
8.4.10 Semi-Infinite Current Sheets 91
8.5 A New Vibrating-Coil Magnetometer 91
8.5.1 Introduction 91
8.5.2 Principle of a New Vibrating-Coil Magnetometer 91
8.5.3 Block Diagram of the Electric Circuits 92
8.5.4 Present State of Development 93

9. VACUUM SYSTEMS, TECHNIQUES, AND MATERIALS STUDIES 94
9.1 Introduction 94
9.2 Gas Evolution from Sputter-Ion Pumps 95
9.3 Mass Transport of Oil in Vacuum Systems 96
9.4 Hydrogen Production by Nude Ion Gages in the Presence of Oil 97

10. FUSION CHAIN REACTIONS 98

11. DESIGN AND ENGINEERING: SERVICE REPORT 100

PUBLICATIONS, ORNL REPORTS, AND PAPERS 101

Introduction

A. H. Snell

In Sect. 1.3, the puzzling loss of fast protons from the DCX-1 apparatus at densities above about 2×10^8 cm^{-3} is resolved. The loss process is one of radial escape across the magnetic field (there may be axial losses too), and the powerful trapping method of Lorentz-force dissociation has thus shown that we are squarely up against a density limit that arises from microinstabilities. The experimental picture is sufficiently detailed to be satisfying, so the question arises: what next?

Before attempting to answer, it may be well to consider the performance of DCX-1 in relation to the world's other injection-accumulation experiments as summarized in Fig. 2.1. There is a lesson to be gained in comparing the performance of DCX-1, for example, with ALICE. The DCX-1 plasma is generated by trapping 300-kev protons, and the plasma is about 2 Larmor diameters across. The ALICE plasma is generated by trapping 20-kev protons, and the Larmor size is about 5. At a density of 4×10^7 fast protons/cm^3, ALICE exhibited flutes; at 2×10^8, DCX-1 does not. The flutes in ALICE were controlled by Ioffe bars, and the density rose until it equaled that of DCX-1; now in both experiments the density is apparently limited at about 2×10^8 fast protons cm^{-3} through losses caused by microinstabilities. According to our understanding of late reports from Livermore, the performances of ALICE and DCX-1 are now strikingly similar, with ion cyclotron radiofrequency activity, plasma potential jumps, and the spitting of electrons along the magnetic field.

The immediate plans for DCX-1 must be aimed at introducing disorder so as to reduce the onset of the microinstabilities. Several schemes have been proposed. If this can be done, it would be interesting indeed to see to what level the ion density in DCX-1 can be raised before flutes appear. Meanwhile, the point in Fig. 2.1 illustrating the performance of DCX-1 with the carbon arc still arrests attention. With the vastly improved beam, arc, and diagnostic techniques that we have developed since 1960, it would seem very attractive to return sometime to the high-density regime in DCX-1, and to study it with renewed thoroughness. However, it would be even better if control of microinstabilities permits us to approach the same density without the use of an arc.

The operation of DCX-2 has been beset with severe mechanical and electrical difficulties, and we have not obtained much operating time during the past few months. The fast-ion densities have been lower by nearly a factor of 10 than had previously been the rule, and although the last run showed improvement, the exact reason for the large variation has not yet been found. In spite of difficulties and uncertainties, two new features of DCX-2 performance have emerged; they are (1) a double-structural feature of the DCX-2 plasma whereby the central plasma that carries the longitudinal energy of injection can act somewhat independently of the peripheral plasma, which has no longitudinal motion but contains the most energetic ions (in $v_\perp$), and (2) a strong correlation between neutral-particle ejection at points on the same field lines but widely separated lengthwise. These and other features are set forth in Sect. 2 in the following pages, and if the reader can suffer another reference to Fig. 2.1, he can see not only the great potential of DCX-2, but also that there are severe losses which have to be better understood, some at least of which would seem to have their origin in microinstabilities.

While on the subject of microinstabilities, one might point to the continuing theoretical contributions summarized in Sect. 7. In particular, the energy spreads in DCX-1 and DCX-2 are interpreted

as indicating that the electric-field energy that drives the microinstabilities of these experiments is only 10^{-4} to 10^{-5} of the transverse kinetic ion energy. In the closely allied subject of instability due to velocity anisotropy in open-ended devices, Sect. 7.2 maps regions of stability and instability for a plausible ion velocity distribution function, with T_e as a parameter.

The experiments on electron cyclotron heating have been largely in a construction phase, but now ELMO is about ready to start the first plasma heating with 8-mm microwave power (Sect. 3.2). In EPA (Sect. 3.13), injection of 20-kev hydrogen neutrals into the 50-liter plasma volume has started; the first indications are that the charge-exchange time for the trapped ions is increased by a factor of 15 by the presence of the hot-electron plasma. This factor is thought to be related to the penetration of Franck-Condon neutrals, and its precise meaning must await fuller information about the size and distribution of the trapped 20-kev proton population.

The "Burnout" series of steady-state beam-plasma interaction experiments ("Mode II") is historically summarized in Sect. 4.1. These experiments afford a contrast to our discussion of microinstabilities above, because here we are trying to see to what extent one can drive electrostatic instabilities for the sake of ion heating. The answer from Burnout IV (Sect. 4.1.3) is that you can do pretty well: a group of deuterons is accelerated (in $v_\perp$) to 20–25 kev in orbits that appear approximately to intersect the axis, with 7 kw in the input electron beam. Another, more intense group is found at 65–75 ev, which corresponds for deuterons to the energy pocket that is expected to be filled because of the balancing energy dependence of the cross sections for charge exchange and scattering.

Other items in the realm of plasma physics that appear in the following pages relate to refined ionic-sound-wave velocity measurements that reveal sheath effects and set the effective value of the adiabatic compression coefficient γ at 1 (Sect. 4.4), further studies of the stabilization of the ion beam in the calutron by boundary-wall treatment (Sect. 4.5), and the use of a soldering gun to measure Debye lengths (Sect. 4.2).

The small flutes of the deuterium arc have previously been characterized rather completely as to size, velocity, etc., and they probably account for escape of deuterium from the arc column. It is now found (Sect. 4.7) that use of a magnetic field of favorable curvature suppresses the flutes dramatically. Meanwhile the practical goal of reducing the ambient pressure around a hydrogen arc is being pursued in the long solenoid (Sect. 4.8), with an observation that electrode configuration is a sensitive factor.

In the field of atomic cross-section measurements, concentration during the past few months has been upon the yield of excited ($n > 8$) and nonexcited H^0 from dissociation of H_2^+ in a carbon arc. The results show no essential advantage in yield of an arc over an argon gas cell (Sect. 5.1), and the similarity of angular divergence of the dissociation products suggests that the dissociation mechanism is similar in the two cases.

Turning to matters closer to technology, we have the difficult challenge of the injection snout to DCX-2 (Sect. 8.1), and we have the design of a power-optimized solenoid with a field homogeneous to the 8th order (Sect. 8.2), the establishment of codes for calculation of the effect of introducing iron into axially symmetric magnetic systems (Sect. 8.3), and the development of a vibrating-coil magnetometer (Sect. 8.5). The adaptation of the duoplasmatron ion source toward the production of large, well-collimated beams in combination with accel-decel systems has led to an essentially divergenceless 50-ma beam as is illustrated with some impact in Fig. 6.4. In vacuum studies (Sect. 9), attention has been given to gas evolution in sputter-ion pumps (water is a basic culprit), and the spread of oil from a diffusion pump has been shown to take place by surface creepage rather than vapor flow.

Finally (Sect. 10) the observation is made that the burning of ^6Li within an idealized containment system can lead to multiplicative chains and a complex of nuclear reactions in the Mev energy regime, most of which degrade the ^6Li to ^4He in exothermic reactions that produce charged reaction products. However, the implied plasma control problems would seem to be even more severe than those that oppose us in the DD and DT systems.

Abstracting Summary

1. INJECTION AND ACCUMULATION: SINGLE-PASS EXPERIMENTS (DCX-1)

Experiments with plasmas established by Lorentz-force trapping at low pressures were emphasized during this report period. Two essentially parallel investigations were carried out: (1) additional studies of the radio-frequency (rf) signals generated by plasma instabilities and (2) experiments designed to pinpoint the anomalous proton losses suggested by earlier data. The use of panoramic receivers and intensity-modulated oscilloscope displays provided simultaneous time-resolved spectra of both polarizations of magnetic signals and led to the recognition of several modes of rf signal behavior. The experiments on anomalous proton losses included: (1) verification that the trapping fraction does not decrease as the product of injected beam current and charge-exchange decay time is increased; (2) studies with radial probes that have shown radial losses of fast protons; and (3) an inconclusive search for mirror loss of fast protons. The radial losses were found to be time-correlated with rf signals which can be interpreted as the result of unstable "clusters" in that portion of the trapped proton population which precesses so as to contribute to density near the outer radius of the plasma.

2. INJECTION AND ACCUMULATION: MULTIPLE-PASS EXPERIMENTS (DCX-2)

Studies of the plasma in DCX-2 were continued, as previously, with the 600-kev H_2^+ beam dissociated in a lithium arc. The density, as estimated from the integrated charge-exchange neutral flux following beam turnoff, was only $\sim 2 \times 10^9$ ions/cm^3, and the energy spread was also smaller than had been found during the previous report period. This variation in plasma behavior has not been explained. From the evidence of the scanning energy analyzer, the plasma appears to consist of two parts: a group of ions which maintain their injected longitudinal energy (with, however, a rather wide spread in total energy), and a group with very low longitudinal energy. This latter group is trapped in a very weak mirror (mirror ratio $1 + 10^{-3}$) produced by the careful adjustment of the magnetic field. The energy distribution of this group shows a mean energy considerably higher ($\sim$500–800 kev) than the injected energy.

The loss rate of plasma from the machine has not been completely established, but experiments have ruled out losses to the walls. Fluctuations seen in the foil detector signals have been established as fluctuations in the neutral flux. Surprisingly strong correlations in these signals along the field, with poorer correlations in azimuthally distributed detectors, suggest radially limited perturbations in the charge-exchange rate which extended from one end of the volume to the other.

Correlation studies of the radio-frequency emission at the cyclotron frequency and its harmonics have been undertaken, but the variation of frequency content for large probe separations makes analysis difficult. An attempt to establish a correlation distance has so far been unsuccessful, although when the probes are very close (less than 5 cm), fairly good correlation is seen.

An experimental estimate of the charge-exchange cross section of the lithium arc was made. Assuming a density of 5×10^{13} ions/cm^3 and a reasonable arc diameter, the cross section was not very different from that for protons in hydrogen and agreed with a similar estimate made by the OGRA workers.

3. ELECTRON-CYCLOTRON HEATING

Bremsstrahlung measurements have continued on the electron-cyclotron plasma in the EPA Facility. The present measurements show that the electron temperature is remarkably constant under a wide variety of conditions. The electron density shows some increase with microwave heating power and a strong dependence on gas pressure.

The neutral beam experiment has finally begun. A 20-ma beam of neutral hydrogen has been injected into the EPA plasma. Preliminary measurements have shown a factor of 15 increase in trapped proton lifetime due to neutral density reduction in the hot-electron plasma.

The first experiments to be performed on the redesigned ELMO Facility will be electron-cyclotron heating at 8 and 5.5 mm, with ELMO operated with a mirror field. The facility will also be operated as a double-folded cusp with 3-cm microwave power.

4. EXPERIMENTAL PLASMA PHYSICS AND VACUUM ARC RESEARCH

The method of fully ionizing plasma has been further examined in successively larger devices called "Burnout I" through "Burnout V." A reflex electron beam interacts with the self-generated plasma within the anode region of the pressure gradient discharge. After initial ionization and stripping of light ions, the beam appears to continue to lose energy to the plasma. Preliminary Burnout IV data are presented and indicate ion and electron temperatures above thermal at densities of above 10^{12} cm^{-3}.

A simple momentum probe – a wire carrying a high current – has been used to study plasma properties. One interesting aspect of the device is that it apparently can measure directly the Debye distance in a plasma.

Following the suggestions of A. Garscadden and P. Bletzinger of the Wright-Patterson Air Force Base, we have replaced the gated amplifier of our old coherent detector, made with a Tektronix CA preamplifier, with a Tektronix 561A sampling oscilloscope. The improved coherent detector is much more free of slow drift than was the earlier device, and our ionic sound wave studies are correspondingly easier.

Very accurate and clear-cut measurements of ionic sound wave properties are now possible, both due to a new technique of producing a quiescent plasma and to a coherent detector. We have now measured: (1) the velocity of the waves as a function of ionic mass and electron temperature; (2) the value of γ, the adiabatic compression coefficient of the electron gas; (3) the thickness of sheaths on the emitting and detecting ion-wave probes; and (4) the radial drift velocity of the plasma to the walls of the container.

Studies of the effect of boundary condition on beam focus have been continued. A comparison between the flat plate wall and the boundary impedance network has been made. Either boundary wall treatment extends the pressure range where the beam imperfection value remains in the operable range of ~ 1.2. This extension of the operable pressure holds for a variety of positions of the boundary surface walls with respect to the beam.

A reflexive discharge has been operated in BPF at input powers from 10 to 25 kw. The neutrons observed when operating with a deuterium discharge appear to originate predominantly at the anticathode. There is evidence for resonances in the neutron intensity at certain ratios of the electron oscillation frequency to the ion cyclotron frequency.

The flutes emitted from the deuterium arc core which were described in earlier progress reports have been stabilized by moving the arc anode toward the cathode. This new electrode geometry results in the arc running through a field whose average radial gradient is apparently positive. Stabilization is determined by a rather discontinuous change in the average saturation ion current to a probe, 1 cm radially from the arc core, and a simultaneous reduction in the frequency and amplitude of current spikes in the time-resolved signals.

Studies of the hydrogen arc in the long solenoid have been continued. A density of 1.5×10^{13} ions cm^{-3} is obtained from water-cooled copper probe measurements. The ion saturation currents to baffles placed around the arc are found to vary with the type of cathode used and to decrease with increasing magnetic field. Langmuir probe measurements of the ion density as a function of radius show a decrease in the radial e-folding distance from about 0.8 to 0.6 cm with an increase in field from 5500 to 9625 gauss.

Transverse observations of a high-current-density hydrogen arc in the long solenoid have given spectral line broadening and slant (Doppler effect due to ordered rotation about arc axis) on the hydrogen 4340-A line. In a relatively diffuse hydrogen arc the slant effect on the hydrogen line was absent or undetected, and there was only a very slight slant of the ionic impurity spectrum lines in the main body of the arc. However, in the peripheral region of the arc the ionic impurities did have a typically large slant.

5. CROSS-SECTION MEASUREMENTS

Measurements have been completed for the production of excited hydrogen atoms resulting from the dissociation of 500-kev H_2^+ by a carbon arc. The optimum ratio of H^0/H_2^+ for arc production was 0.20 compared to argon gas production of 0.14. The fraction of H^0 in principal quantum numbers $n > 8$ compared to the total neutral yield was 0.0046, which may be compared to a fraction of 0.0127 produced by argon gas collisions.

Attempts to measure resonances in the cross section for electron capture into excited states by passing of protons through atomic hydrogen have been temporarily unsuccessful due to mechanical failure of the tungsten oven used to produce atomic hydrogen. By passing protons through molecular hydrogen and helium, the fraction of H^0 with principal quantum number $n = 12$ or greater has been determined in the energy range 16–34 kev. The fraction increases monotonically with energy, with values at 34 kev of 0.002 and 0.0014 for hydrogen and helium respectively.

Evaluation of the Bendix magnetic electron multiplier indicates variations in gains of 10^5 over the surface of the $\frac{3}{4}$- by $\frac{3}{4}$-in. tungsten cathode. Orders of magnitude in the change of gain render the multiplier useless as an absolute particle detector, and it can be used for relative measurements only if the spatial distribution of the particles remains constant during the measurements.

6. PRODUCTION, ACCELERATION, AND INJECTION OF IONIC AND ATOMIC BEAMS

After the elimination of a large energy modulation of the beam, 100 ma of H_2^+ can be injected through an exact geometrical duplicate of the DCX-2 injector duct on the 600-kv test stand. Total hydrogen ion currents of 350 ma at 600 kv have been obtained by using a modified duoplasmatron ion source with an expanded plasma extraction region. The beam emittance from these sources is inferior to the "small cup" duoplasmatron, which makes a study to improve the H_2^+ production difficult with the present 600-kev analyzing geometry. A series of studies is being made with the 100-kv test stand to evaluate the extraction of large currents with these large plasma surface ion sources. Based on studies with the 100-kv test stand, an increase of a factor of 3–5 in the beam available for Lorentz-force dissociation in DCX-1 seems possible. This "large cup" extraction geometry also has yielded beams of 100 ma of H^+ or H_2^+ at 40 kev which were, by visual observations, approximately parallel and $\frac{3}{4}$ in. in diameter. A total current of 200 ma has been extracted at 20 kev but with large divergence.

7. PLASMA THEORY AND COMPUTATION

Energy spread in injection machines, a manifestation of microinstabilities, is analyzed from the thermodynamic point of view applied previously to diffusion in a torus. In this light, the observed energy spread is seen to be relatively small. In particular, the potentially large energy reservoir in plasma anisotropy makes a small contribution to the ultimate growth of electric fields.

The dispersion relation derived by Harris has been analyzed for distributions which simulate the loss-cone effect of mirror confinement. Amplification of electrostatic waves at frequencies near harmonics of the ion gyrofrequency can occur for waves propagating almost perpendicular to the magnetic field. Stability zone diagrams are presented, and their interpretation is discussed.

It has been shown that a system described by a bi-Maxwellian distribution function, situated in a constant magnetic field, is stable against electrostatic instabilities if $T_{\parallel}/T_{\perp} > \frac{1}{2}$.

Numerical computation of the decay of neutral particle current from DCX-2 has been attempted. Effects included are charge exchange, ion cooling by arc electrons, ion-ion diffusion (Coulomb), and ion scattering out mirrors.

Diffusion across a magnetic field is calculated for a given fluctuating electric field. The field

may arise from microinstabilities, or, as in the example treated, it may represent two-body collisions.

It is shown that the plasma potential to be expected with mirror confinement should not destroy flute stabilization by magnetic wells. The stabilization of flutes in arcs by very shallow average wells may provide experimental confirmation (see Sect. 4.7).

8. MAGNETICS AND SUPERCONDUCTIVITY

The injection duct (snout) of DCX-2 in its original form must be operated with additional helical coils in order to compensate the influence of the radial change of the main magnetic field. In close cooperation with the DCX-2 group, a new snout was built using an improved design with a helical coil of variable pitch which is arranged inside the can of the injection duct. This compact design simplifies the shielding of the snout against impinging ions. The current densities in the snout windings are very high, and extended tests were necessary to find reliable technological solutions. The new injection duct design is an appreciable technical improvement; furthermore, having a new snout leaves the old one as a spare for the operation of DCX-2.

In the previous semiannual report a new analytical method was presented for optimizing the power of solenoid systems which produce very homogeneous fields. Recently this method has been applied to the design of a 7-Mw, 60-kilogauss magnet coil with 13 in. inner diameter. Several technological problems had to be solved. For instance, it was necessary to devise new winding schemes in order to approximate closely the analytical solutions of the current density distribution in the solenoid. This task is aggravated by the need to use only a finite number of turns of rather large conductors and by the desirability of an economically small number of conductor cross sections. In this connection a new type of "triple pancake coils" is described. Finally, conductor dislocation calculations were made to investigate the influence of mechanical inaccuracies on the field homogeneity.

These considerations showed that an optimized eighth-order solenoid is not more difficult to build than one of sixth order. Therefore, it was decided to take advantage of the higher field homogeneity of the eighth-order type. It must be emphasized that great engineering skill and an appreciable amount of additional computer work were necessary to find a practical coil design using the relatively simple original idea of power optimization of solenoids of higher order.

Most vacuum fields for plasma experiments can be produced by appropriate coil systems without employing ferromagnetic materials. In some cases, however, the use of these materials is advantageous. Examples are the design of the injection duct for DCX-2 or the iron quadrupole systems for minimum-B field configurations, as described in previous reports.

In general, calculations of magnetic fields containing ferromagnetic materials are very involved. There are, however, significant cases in which the mathematical difficulties are not too formidable. If the distribution of magnetization is known in an axially symmetric system, the resulting magnetic fields can be calculated quite simply by superposing the fields of elementary magnetized rings. In special cases, sets of adjacent ring elements can be combined into a smaller number of annular or cylindrical magnetized sheets. Two previously reported general utility codes for computing magnetic properties of current systems have now been extended to permit the inclusion of such magnetostatic elements.

Finally, a list has been prepared containing brief descriptions of magnetic field computer codes used at this laboratory. The purpose of this list is obvious: Thermonuclear research requires increasingly precise calculations of complicated magnetic fields and of particle orbits. A general interchange of information about available codes among participating laboratories should help to minimize duplication of effort.

In superconductivity research the measurement of magnetic moments is of great importance. Ballistic methods are widely used. Recently, vibrating-coil magnetometers have been built which allow continuous measurements with relatively high signal-to-noise ratios. A design of a vibrating-coil magnetometer has been conceived here which differs from the known types in that the flux is measured in the homogeneous middle zones of samples with demagnetization factors $n \sim 1$. Such an instrument has been built, and tests in fields, produced by a superconducting 50-kilogauss magnet, showed encouraging results.

It is hoped that it will be possible to develop the new vibrating-coil magnetometer into a tool of superior accuracy.

9. VACUUM SYSTEMS, TECHNIQUES, AND MATERIALS STUDIES

The composition of gas which evolves from a sputter-ion pump after the pump is turned off was found to be strongly dependent on the water partial pressure in the vacuum system. Although methane and ethane were observed to be evolved at constant rates, hydrogen and carbon monoxide constituted 60% of the gas at a water pressure of 3×10^{-7} torr but less than 1% at a water pressure of about 3×10^{-9} torr. A study was made to distinguish between surface diffusion and vaporization transport processes for diffusion pump oil in specially designed apparatus. Surface diffusion was found to be the dominant process. An attempt to measure the heat of activation for the process yielded a value of 14 kcal/mole, which agrees with the value estimated for surface diffusion. The response of ionization gages to the local presence of oil was studied by measuring the hydrogen partial pressure at various gage emission currents. The hydrogen pressure was found to be a linear function of emission with some hydrogen being produced even at very low emissions, presumably by pyrolysis at the hot filament.

10. FUSION CHAIN REACTIONS

A qualitative discussion is presented on the concept of fusion chain reactions in which protons (deuterons, tritons, ^{3}He, or energetic alphas) may catalyze the burning of ^{6}Li or other nuclear fuels, quite analogous to chemical chain reactions except for the energy scale of the events.

1. Injection and Accumulation: Single-Pass Experiments (DCX-1)

J. L. Dunlap
R. S. Edwards
G. R. Haste
L. A. Massengill
C. E. Nielsen[1]
H. Postma
L. H. Reber
R. G. Reinhardt
W. J. Schill
E. R. Wells

1.1 INTRODUCTION

The mechanical configuration of the facility was not modified to any appreciable extent during this report period. Most of the experiments were performed with Lorentz-force trapping, large H_2^{+*} beam currents, and low operating pressures. (H_2^{+*} is defined as the H_2^+ which results from dissociation of H_3^+ in a water vapor cell in the ion source, and thus has its full complement of vibrational levels filled.) There were essentially two parallel investigations: (1) additional studies of the rf signals generated by plasma instabilities and (2) experiments designed to pinpoint the anomalous proton losses suggested by earlier data.

The details of these investigations are given in the following sections.

1.2 STUDIES OF RADIO-FREQUENCY SIGNALS

Studies of radio-frequency (rf) signals generated by plasma instabilities were continued. Two median-plane magnetic probes were used, one oriented for maximum sensitivity to azimuthal current fluctuations (θ rf) and one for sensitivity to longitudinal current fluctuations (Z rf). The construction of these probes and the associated electronic equipment were described in a previous report.[2]

During the present report period, we have concentrated on the frequency composition of the magnetic probe signals. Under all operating conditions the θ signals consist principally of proton cyclotron harmonics. At high pressures the same is true of the Z signals. However, at low pressures the Z rf signals are characterized by additional nonharmonic components, as previously described,[3] and much more complex behavior. The complexity of the Z spectrum increases with beam current and plasma lifetime, and for this reason most of the measurements were made near base pressure with Lorentz-force trapping of large H_2^{+*} beams.

Frequency spectra were obtained using a Panoramic model RE-5 receiver (10–100 Mc), a Panoramic Spectrum Analyzer model SPA-3/25 (for high resolution near ω_{ci}), and a Pentrix Spectro-Pulse Analyzer model L-20 (usually adjusted for a 5- to 50-Mc display). Intensity modulation techniques were used in addition to the usual panoramic displays to provide time-resolved spectra. In a number of runs several oscilloscopes and fairly elaborate interconnections were arranged to give simultaneous recordings of (1) the frequency compositions of θ and Z signals by the usual

[1]Consultant from Ohio State University.

[2]*Thermonuclear Div. Semiann. Progr. Rept. Oct. 31, 1963*, ORNL-3564, sect. 1.2, pp. 1 and 2.

[3]*Thermonuclear Div. Semiann. Progr. Rept. Apr. 30, 1964*, ORNL-3652, sect. 1.3, pp. 8–14.

panoramic displays, (2) the time-resolved frequency compositions by intensity modulation displays, (3) direct oscilloscope displays of signal envelopes, and (4) rf correlated phenomena.

Figures 1.1 to 1.3 are examples of these rf displays. (In Fig. 1.1, the oscilloscope which gave the Z panoramic display was sweeping somewhat more slowly than the others; as a reference point to assist in detailed comparisons, 7.2 cm in the uppermost display corresponds to 7.7 cm in the other two.) From these and similar data, five modes of characteristic behavior have been recognized:

1. Nonharmonics in Z, particularly about 25 Mc, which can drift up and down in frequency over a range of approximately 3 Mc. Examples are shown in the first 5 cm of Fig. 1.1, at 3 cm in Fig. 1.2, and at several places in Fig. 1.4.
2. Z signals with fast frequency sweeps up and down over a very wide frequency range. Examples are at 3 cm in Fig. 1.2.

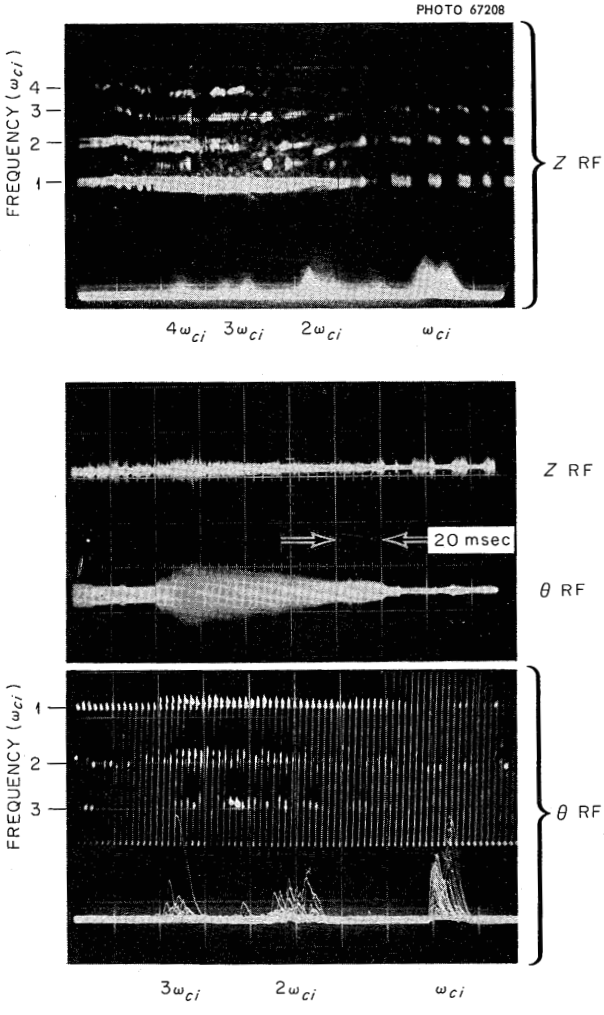

Fig. 1.1. Simultaneous Envelope and Panoramic Displays of the Signals from Two Median-Plane Magnetic Probes. 220 μa H_2^{+*}, 2×10^{-9} torr.

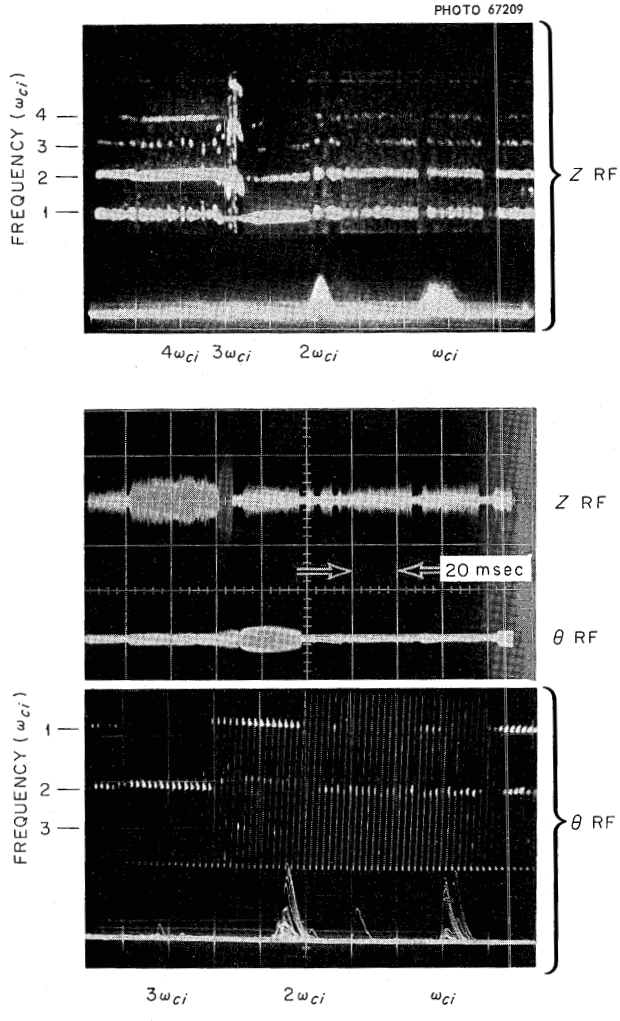

Fig. 1.2. Simultaneous Envelope and Panoramic Displays of the Signals from Two Median-Plane Magnetic Probes. 220 μa H_2^{+*}, 2×10^{-9} torr.

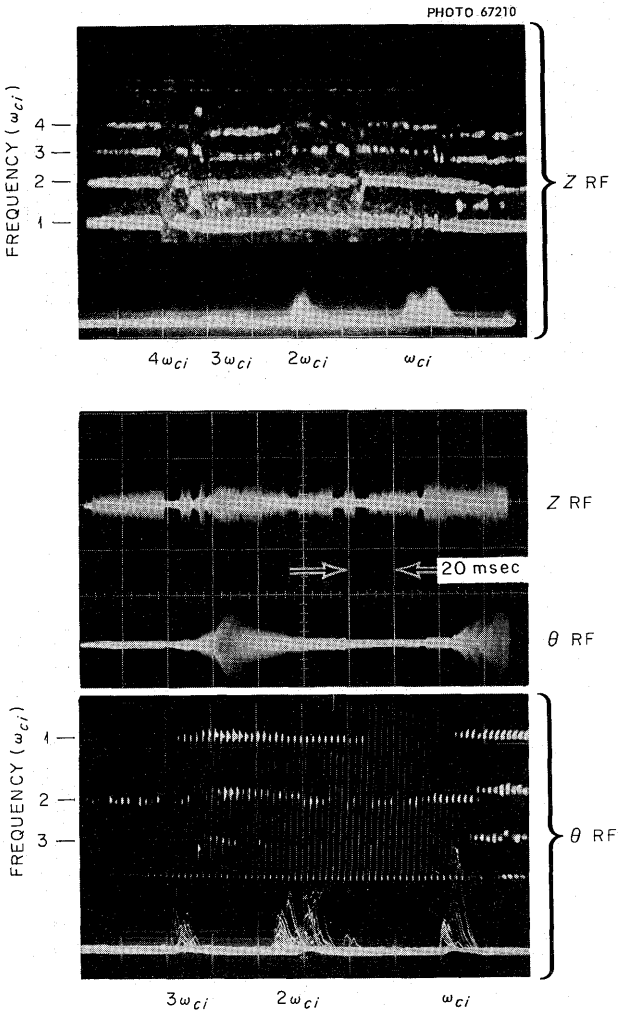

Fig. 1.3. Simultaneous Envelope and Panoramic Displays of the Signals from Two Median-Plane Magnetic Probes. 220 μa H_2^{+*}, 2×10^{-9} torr.

3. Continuous $2\omega_{ci}$ and $4\omega_{ci}$ in Z with no continuous ω_{ci} in θ or Z. An example is the first 3 cm of Fig. 1.2.
4. Intermittent ω_{ci} and $3\omega_{ci}$ in Z, with $2\omega_{ci}$ but no ω_{ci} in θ. An example is again the first 3 cm of Fig. 1.2.
5. Frequencies visible in Z but concentrated in the θ signal some 2 Mc below the usual ω_{ci}. Figures 1.1 and 1.3 show this.

There are logical interpretations of some of these modes and additional observations concerning all of them. These points are covered in the following comments:

1. An explanation for nonharmonics in Z has been given previously in terms of unstable electrostatic coupling of proton axial oscillation waves with electrons oscillating axially at a frequency determined primarily by the plasma potential.[3] It was shown that such coupling could produce unstable oscillations at frequencies $n\omega_\Phi - \omega_z$, where $n = 1, 2, \ldots$, ω_Φ is the proton cyclotron frequency, and ω_z is the proton axial oscillation frequency. Computer orbit studies of protons with Z oscillation amplitudes up to a few inches and orbit centers on axis show that ω_z is nearly constant, while ω_Φ changes by several megacycles. For the $2\omega_\Phi - \omega_z$ mode, ω_Φ need only be shifted by 1.5 Mc to account for a 3-Mc total shift in mode frequency. The observation of nonharmonic frequency drifts (mode 1) may involve changes in the axial oscillation amplitude of the protons associated with this unstable mode. Often there is evidence of fairly steady electron ejection during this mode (Fig. 1.4).

2. We observe that the fast frequency sweeps (mode 2) are associated with fast ejections of electrons through the mirrors (Fig. 1.4). Also on

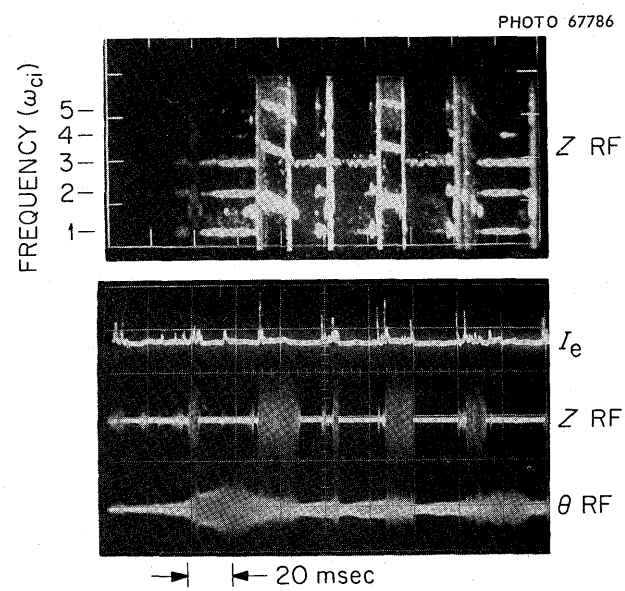

Fig. 1.4. Simultaneous Displays of Z RF, θ RF, and Slow Plasma Current to a Collector at +9 v Bias. 220 μa H_2^{+*}, 1.7×10^{-9} torr.

sweeps of the intensity modulation panoramic display that are fast enough to resolve individual elements of the raster we note that all frequency components are not present (Fig. 1.5).

3. Modes 3 and 4 can occur simultaneously or independently. They are both associated with electron ejection. In many cases, but apparently not in all, the ejections tend to be more continuous than those correlated with mode 2.

4. Intensity modulation displays of the θ rf signals have been made with high resolution in the vicinity of ω_{ci} to investigate mode 5. Figure 1.6 shows signals at the two frequency bands indicated in the earlier discussion of this mode, one which ranges from about 14.4 to 15 Mc and one from 12.5 to 14 Mc. Figure 1.7 shows the upper range with higher resolution. These frequencies are attributed to clusters near the stable orbit. More than one of these can be present at any given time, a point in agreement with the proposed explanation given earlier for oscilloscope observations of θ rf beat frequencies in the order of 100 kc.[4] The signals in the 14.4- to 15-Mc range begin near the lower limit and sweep upward in frequency toward the higher limit. The lower frequency limit is about the ω_{ci} for stable-orbit protons. It is reasonable to expect clusters

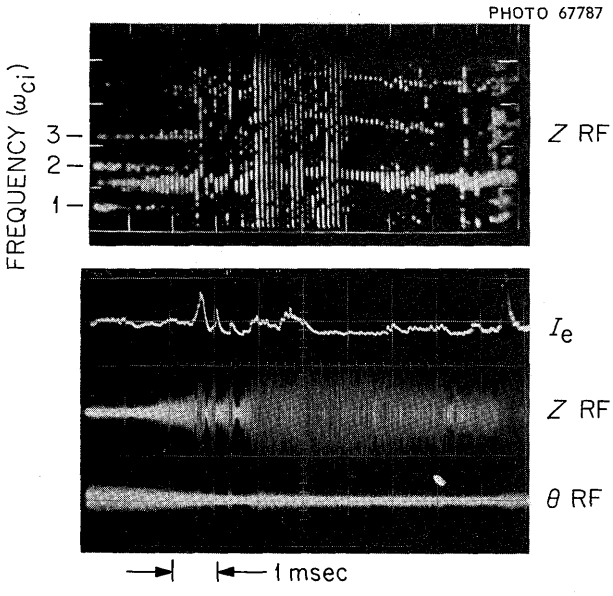

Fig. 1.5. Simultaneous Displays of Z RF, θ RF, and Slow Plasma Current to a Collector at +9 v Bias. 220 μa H_2^{+*}, 2.2×10^{-9} torr.

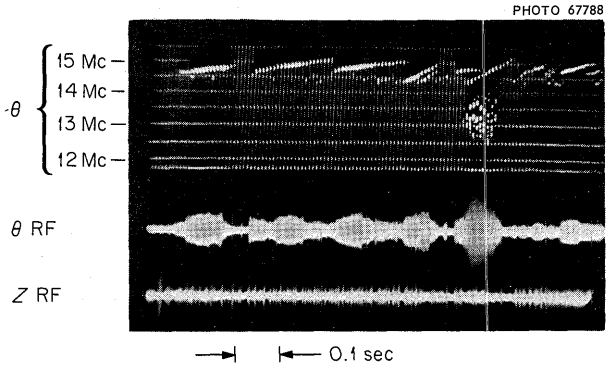

Fig. 1.6. Frequency Composition of θ RF in the 12- to 15-Mc Range. 190 μa H_2^{+*}, τ_{DK} = 8 sec.

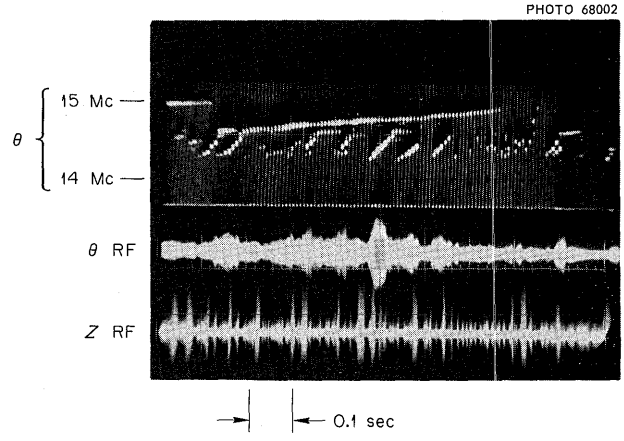

Fig. 1.7. Frequency Composition of θ RF in the 14- to 15-Mc Range. 190 μa H_2^{+*}, τ_{DK} = 8 sec.

to form here since this is the locus of the most ordered proton orbits. The upward sweeps in frequency may be the result of increasing average Z amplitude, as proposed in 1 above. The upper frequency limit could then be a measure of the Z oscillation amplitude required to disperse the cluster. Frequencies in the range 12.5 to 14 Mc are observed only at the lowest pressures. These have been found to be correlated with the radial loss of protons and are described in more detail in Sect. 1.3.4.

[4] *Thermonuclear Div. Semiann. Progr. Rept. Oct. 31, 1963*, ORNL-3564, sect. 1.2, p. 3.

1.3 INVESTIGATIONS OF PROTON LOSSES FROM PLASMAS FORMED BY LORENTZ-FORCE TRAPPING

1.3.1 Introduction

The two previous semiannual reports[5,6] described a number of experiments with Lorentz-force trapping in which the charge-exchange loss current was measured as a function of charge-exchange decay time (pressure) in the τ_{DK} range (>0.1 sec), in which Lorentz-force trapping dominated and the proton input current to the plasma was believed to be constant for a fixed injected H_2^{+*} beam current. These experiments showed that the charge-exchange loss current began to decrease with increasing τ_{DK} once a central fast-proton density of $\sim 10^8$ cm^{-3} was obtained, at a product of injected H_2^{+*} current and τ_{DK} of approximately 1000 μa-sec. They also showed that (1) any additional proton losses were not materially affected by a reduction in the radius of the energetic plasma from $8\frac{5}{8}$ to $6\frac{5}{8}$ in.; (2) if axial, they were not the result of a slow diffusion out of the mirrors; and (3) additional losses were enhanced by electron cyclotron heating.

Further investigations of these proton losses have been the principal activity of this group during the present report period. In effect, three separate investigations were made: (1) verification that the trapping fraction did not decrease at longer τ_{DK} values; (2) direct measurement to show whether or not there was a very rapid transport of fast protons out of the mirrors; and (3) direct measurements of radial fast-proton losses. The details of these experiments are given in the following three sections.

1.3.2 Checks on the Trapping Fraction

It was accepted as an unlikely possibility that the trail-off of charge-exchange loss current was the result of a decrease in the Lorentz-force trapping fraction due to the influence of trapped plasma on the excited states of the incoming H_2^{+*}. For a constant H_2^{+*} beam, variation of this trapping fraction would produce proportional changes in the 300-kev proton current and the 300-kev atomic hydrogen current produced by dissociation of H_2^{+*} within the plasma volume. A comparison of the step-function variations of either of these currents at beam turn-on (no accumulated plasma, and hence no possibility of a plasma-induced effect) and a later beam turn-off (after the plasma had reached a steady-state density apparently limited by losses other than charge exchange) would reveal whether or not the plasma reduced the trapping fraction.

A gridded radial detector (described in detail in Sect. 1.3.4) was positioned as a radial limiter in the median plane, as shown in Fig. 1.8. It was operated so as to repel plasma electrons and also ions of energies less than 1 kev. Step-function signals to this detector would be composed of fast dissociation neutrals (by secondary emission from the collector) and energetic precessing protons produced by dissociation of H_2^{+*} just within the outer radius of the trapped plasma. Comparison of the step functions on turn-on and turn-off showed no reduction in the trapping fraction along this portion of the beam trajectory.

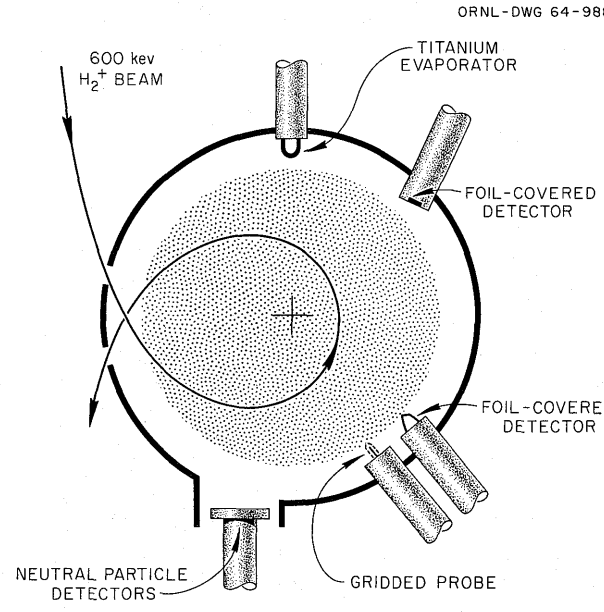

Fig. 1.8. Midplane Section, Showing Radial Detectors.

[5] *Thermonuclear Div. Semiann. Progr. Rept. Oct. 31, 1963*, ORNL-3564, sect. 1.5, pp. 10–12.

[6] *Thermonuclear Div. Semiann. Progr. Rept. Apr. 30, 1964*, ORNL-3652, sect. 1.2, pp. 1–8.

A second check was made using a foil-covered Faraday cup (upper right, Fig. 1.8) as a detector of dissociation neutrals from a portion of the beam trajectory near the H^+ stable-orbit radius. Again there was no indication of a reduction in trapping fraction.

From these experiments we conclude that the trapping fraction is not reduced at long τ_{DK} values and that, therefore, some proton losses other than charge exchange are indeed involved in this operating regime.

1.3.3 Search for Mirror Losses

Experiments reported earlier had shown that significant mirror losses of fast protons would probably be the result of a very rapid transport of these protons out of the mirrors.[6] A foil-covered Faraday cup was mounted near the magnetic axis just outside one of the mirrors, inclined at an angle of about 15° with respect to the median plane so as to be sensitive to such proton losses. Current to this collector was monitored as the operating pressure was varied to provide measurements under conditions of complete charge-exchange accountability and of deficient charge-exchange current. Currents were observed, but since these could be reduced to zero or changed in sign by the application of modest bias voltages to the cup, it is believed that they were at least partially due to slow plasma leaking through small pinholes in the foil (10-μin. nickel). As a measure of end losses, these experiments were inconclusive and must be repeated.

1.3.4 Measurements of Fast-Proton Radial Losses

Current detectors which act as plasma radial limiters in the median plane have been used in measurements of fast-proton radial losses.

One of the probes employed was a gridded radial probe located as shown in Fig. 1.8 and constructed as shown in Fig. 1.9. This gridded probe utilized the elements of a 4-65A tetrode vacuum tube and was similar to one already described.[7] The current to the collector post was measured while the outer grid was biased

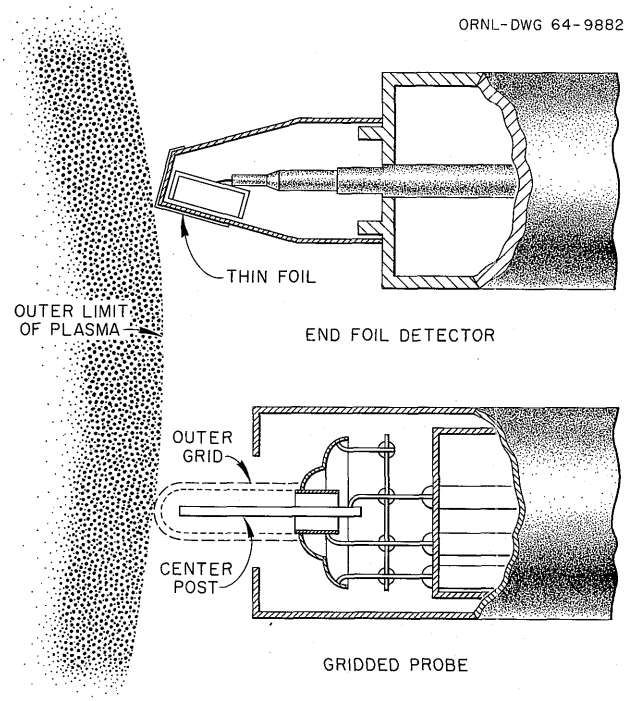

Fig. 1.9. Probes Used in Investigations of Proton Radial Losses.

negative with respect to the collector and the inner grid was biased at about 1 kv positive. An indication of positive current to the post might therefore be due to a release of secondary electrons by charge-exchange neutrals arriving at the post or to a collection of ions with energies greater than 1 kev.

One component of signal to the gridded probe is due to the dissociation of incoming 600-kev molecular ions. This component is a step function which comes and goes with the H_2^{+*} beam. It has no relationship to the radial loss process, but, as indicated in Sect. 1.3.2, is a useful check on the trapping rate for protons.

When other probes are retracted so that the gridded probe acts as the plasma radial limiter and operation is in the regime characterized by deficient charge-exchange loss, a second signal component is observed. As shown in Fig. 1.10, there are pulses of current that are time-correlated with the appearance of strong θ rf

[7] *Thermonuclear Div. Semiann. Progr. Rept. Apr. 30, 1963,* ORNL-3472, sect. 2.3, pp. 15 and 16.

(the signals to magnetic probes oriented for maximum sensitivity to azimuthal currents). These pulses are present only under operating conditions in which the charge-exchange measurements indicate an additional proton loss mechanism. Once in this regime, the time-averaged pulse current increases as the charge-exchange accountability decreases (Fig. 1.11). The time-averaged pulse current was also increased slightly by electron cyclotron heating, as were the θ rf signals. It is interesting that these increases in time-averaged pulse current occur primarily as the result of increases in the pulse repetition rate (as low as 1 pulse about every 5 sec for 5 to 10% anomalous losses), not as the result of any significant increase in the amount of current involved in single pulses.

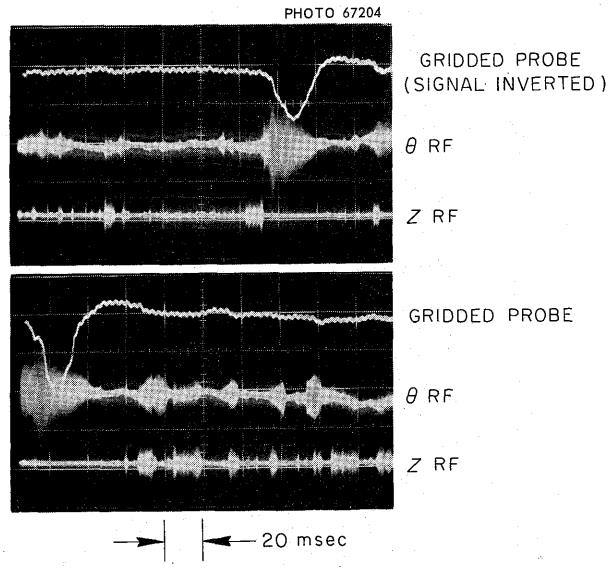

Fig. 1.10. Two Examples of Simultaneously Recorded Signals from Median-Plane Magnetic Probes and a Gridded Probe. 380 μa H_2^{+*}; τ_{DK} = 9 sec; probe bias at +900 v.

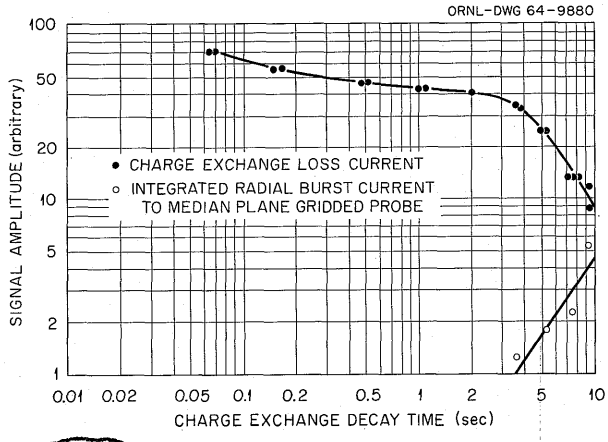

Fig. 1.11. Charge-Exchange Loss Current and Time-Integrated Radial Proton Loss Current to a Median-Plane Gridded Probe as Functions of τ_{DK}. 400 μa H_2^{+*}.

The second detector used in these investigations was a foil-covered Faraday cup. Figure 1.8 shows its position (adjacent to the gridded probe), and Fig. 1.9 indicates details of construction. The dead area at the tip of the probe (the foil area which an energetic particle might penetrate without registering at the Faraday cup) is only about 0.01 in. long in radius. This probe was used as the median-plane radial limiter in the same fashion as the gridded probe. When so employed, the behavior of the signals to the Faraday cup was identical to those of the gridded probe. From these observations we conclude that the particles being measured have energies greater than 150 kev, the cutoff of the 25-μin. nickel foil that was used. Care was taken to employ hole-free foils, so slow plasma effects did not confuse these experiments.

In some runs both probes were employed, and the radial position of the foil-covered detector was varied in order to determine over what distance it would have to be advanced in order to significantly affect the amplitude of the pulse signals to the gridded probe. Initially the two probes were at the same radius, and then the gridded probe was gradually retracted. The ratio of the gridded probe signal to the end-foil detector signal decreased with an e-folding distance of about $^1/_{10}$ in. The sharpness of the shadowing effect shows that the pulses represent a current of ions, not of fast neutrals, and that the outward radial velocity of these ions is much less than the precessional velocity.

Very recent studies of the frequency distribution of the θ rf signals that are correlated with the radial proton losses have been informative. As shown in Fig. 1.12, these particular signals are characterized by significant amplitudes of frequency components in the range 12.5 to 14 Mc. In the numerous cases examined, the appearance of θ rf components in this frequency range has always involved simultaneous radial proton losses. There do appear to be some much smaller

fluctuations of radial probe signals that are not correlated with these θ rf components. It is not yet clear that these particular fluctuations represent real proton losses or to what extent problems of rf sensitivity are involved.

As described in Sect. 1.2, the θ rf fundamental frequency band associated with clustering near the stable-orbit radius is 14.4 to 15 Mc. We interpret the 12.5- to 14-Mc signals as indicating cluster formation in that portion of the fast-proton population which precesses so as to contribute to plasma density near the radial limiter. This interpretation is encouraged by two observations: (1) the calculated θ frequency for protons precessing so as to barely miss the radial limiter (at R = 9 in.) is about 12.5 Mc; and (2) there are a number of spectra which show that the 12.5- to 14-Mc band is the result of oscillations which begin near the lower frequency limit and then sweep to higher frequencies as though a displacement to higher average field regions is involved, as proposed in Sect. 1.2 in connection with other rf data.

Signals from the precessing clusters are usually accompanied or preceded by signals from stable-orbit clusters. However, there have been several observations in which the 12.5- to 14-Mc signals preceded those at 14.4 to 15 Mc. Precessing clusters can therefore exist without a driving force associated with stable-orbit clusters.

As shown in Fig. 1.12, the radial losses are accompanied by an increase in the net negative current to a biased (+9 v) slow plasma collector positioned outside a magnetic mirror. This current signal has been filtered somewhat to reduce the displayed amplitude of the very fast (tens of microseconds duration) electron ejections associated with the longitudinal instability (Z rf). Sweeps without this filtering show that the displacement during radial loss is not just the result of a pileup of these very fast ejections but that there is a slowly varying component as shown in the figure. It is not yet clear to what extent the slow variation is a result of an increase of electron current or a decrease in a slow-ion current. Since the slow-ion component of the stored plasma is believed to be quite small, the signal could represent a dump of electrons in just the amount required to maintain a fairly constant gross plasma potential level during the interval of proton loss. Time-resolved plasma potential displays of the type described

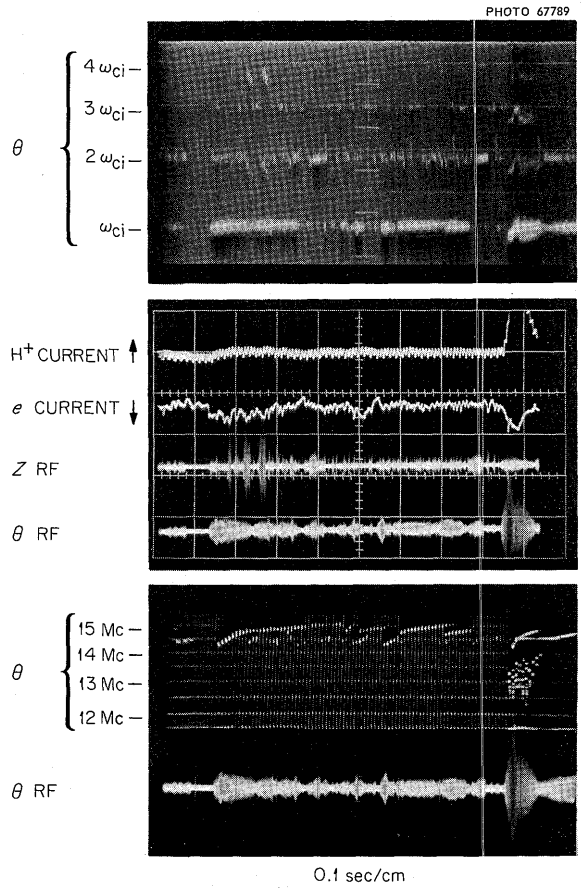

Fig. 1.12. Simultaneous Displays of Z and θ RF, Radial Proton Losses, and Slow Plasma Current to a Collector at +9 v Bias. 200 μa H_2^{+*}, 2×10^{-9} torr.

in Sect. 1.4 should be of use in resolving these questions.

Displays of the charge-exchange signals show that the radial losses are also accompanied by fluctuations of charge-exchange current like those previously described.[8] Since the charge-exchange cross section increases very rapidly toward lower proton energies, a decrease of proton energy is indicated. This decrease could be a net one, as would be involved if the plasma potential increased during radial loss, or it could be an apparent one, as would be associated with an increase in energy dispersion during the loss interval. Again time-resolved plasma potential displays would be useful.

[8] *Thermonuclear Div. Semiann. Progr. Rept. Oct. 31, 1962,* ORNL-3392, sect. 1.3, pp. 3–7.

In summary, the radial loss of energetic protons has been detected. The losses appear to be the result of an instability mode characterized by the formation of clusters near the outer radius of the plasma. The losses are time-correlated with θ rf signals that indicate the formation of these clusters, with an increase in the slow plasma current to an end collector at positive bias, and with fluctuations in charge-exchange signals that indicate proton energy degradation or dispersion. The behavior of the radial losses is in qualitative agreement with features of the anomalous losses deduced from charge-exchange current measurements: the radial losses are observed only in the region of deficient charge-exchange current; they increase at the same rate as the difference in trapping and charge-exchange loss currents increases as one probes to higher $I\tau$ products; and they increase with electron cyclotron heating.

An important question is whether or not the radial losses account for all the anomalous loss currents. In principle, an answer can be arrived at in either of two ways, by obtaining the total radial loss current or by excluding mirror losses. We have attempted to calculate the geometric factor that relates the measured radial loss current to the total radial loss current. From simple orbit considerations it is not difficult to demonstrate that the measured radial losses are possibly within an order of magnitude of the total. An accurate estimate would, however, require a much more precise knowledge of the proton distribution than is available. So in practice it appears that the question can only be resolved by a measurement of the mirror losses.

1.4 PLASMA POTENTIAL PROBE

The development and use of a lithium ion beam as a plasma potential probe for the DCX-1 plasma have been reported earlier.[9] As previously employed, this probe did not give good time resolution of a fluctuating potential.

[9] *Thermonuclear Div. Progr. Rept. Oct. 31, 1961*, ORNL-3239, p. 6.

Following work by the ALICE group at Lawrence Radiation Laboratory,[10] we now use a sawtooth voltage generator to supply the ion acceleration potential. This sawtooth is displayed on an oscilloscope and is intensified by a pulse when the transmitted ion current reaches 50% of its full value. This pulse is controlled by a Tektronix type Z preamplifier, which samples the transmitted ion current.

Figure 1.13 shows two examples of this display technique. Here the time interval between potential determinations is 5 msec. The sawtooth generator has recently been improved and now recycles at about a 1-msec rate.

Studies of the plasma potential with this new technique should prove valuable in answering questions posed in Sect. 1.3.

[10] A. F. Waugh and A. H. Futch, *A Method for Continuous Measurement of Plasma Potential over a Range of 0 to 40 KV*, UCRL-7414 (unpublished).

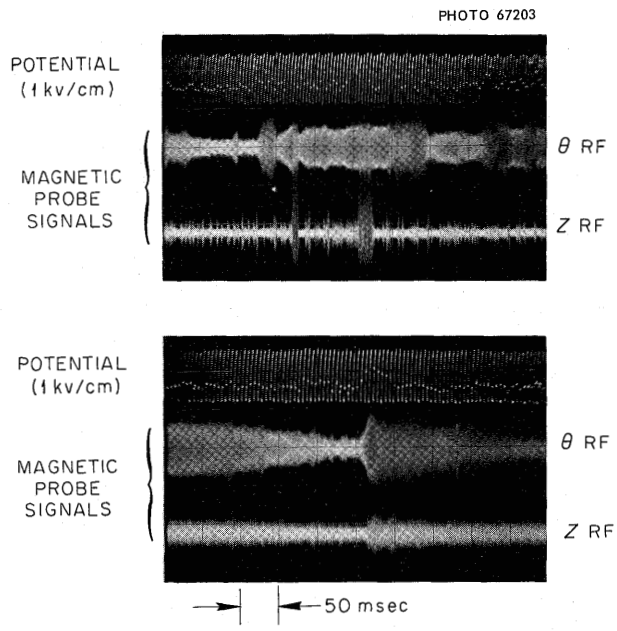

Fig. 1.13. Simultaneous Displays of Plasma Potential and RF Signals from Median-Plane Magnetic Probes. 350 μa H_2^{+*}, 4×10^{-9} torr.

2. Injection and Accumulation: Multiple-Pass Experiments (DCX-2)

P. R. Bell
J. S. Culver
R. C. Davis
S. M. DeCamp
J. C. Ezell
R. A. Gibbons
G. G. Kelley
N. H. Lazar
J. F. Lyon
O. B. Morgan
T. F. Rayburn
R. F. Stratton
C. W. Wright
A. J. Wyrick

2.1 INTRODUCTION

During this report period, studies of the plasma produced by lithium arc dissociation of 600-kev H_2^+ continued. Operation was hampered by technical difficulties of several kinds. During the last part of the previous report period, the 600-kv accelerator supply had to have extensive rectifier replacement (see Sect. 6), and it was clear that there had been gradually increasing energy modulation of the injected beam before the repair. Several small sections of the east mirror coil had shorts present in them for a long time, and these had been balanced by intentional shorts in the west mirror to secure the extremely exact field shape required for maximum plasma density. Shortly after power supply repair, one of the shorts in the east mirror vanished, requiring a change in the west mirror condition, and one of the remaining shorts appeared and disappeared several times, each time requiring remeasurement of the field shape. We have found that at no time after the power supply repair have we obtained as high a plasma density as before (density by neutral particle integral methods 2×10^9 ions/cm^3 now vs 10^{10} ions/cm^3 before). The lesser density is indicated by various different characteristics of the plasma which reflect density changes (see below), but it is not clear whether minor changes in the field shape to which the plasma density is quite sensitive or the lack of energy modulation of the injected ions is responsible for the lower maximum density.

To display clearly the plasma density region studied, compared to that studied in other high-energy injection machines, the expected and obtained plasma density is plotted against the ion input to the various machines. So that all experiments could be plotted on a single plot, the ion input is normalized so as to represent the pressure-independent ion input during one average ion charge-exchange lifetime to each cubic centimeter of plasma volume, which is assumed to be constant. By this means, any additional beam input produced, for example, by gas dissociation, becomes evident, and any plasma spreading and ion loss processes are easily noted. Figure 2.1 shows such a plot for DCX-1 and DCX-2. Results for ALICE, PHOENIX, and OGRA are also shown for comparison. In the higher-density operation of DCX-2, the density was a factor of 2 to 40 below the maximum density expected under these conditions, while at present the density is a factor ~75 below that expected.

Enough experience has now been accumulated with the DCX-2 plasma that a description of the plasma condition from an experimenter's point of view is worth while.

It is clear that the plasma exhibits no macro-instabilities or at most very weak ones. No flutes are seen and no evidence of plasma rotation can be observed. Weak radial bursts of fast ions have been seen over the whole range of density from 10^7 to 10^{10} fast ions/cm^3 with no important change in their intensity. These irregular bursts, which

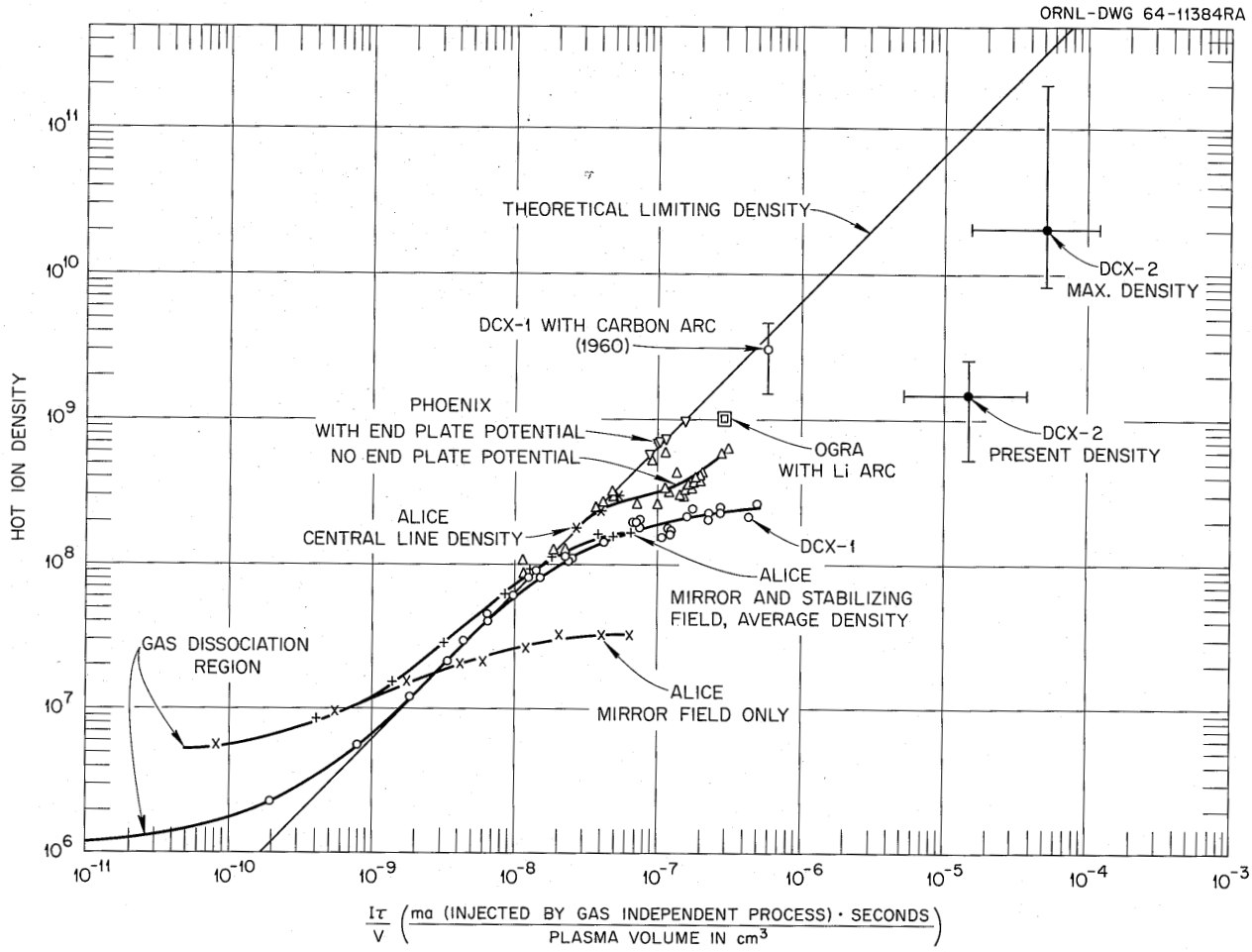

Fig. 2.1. Plasma Density Regions Studied in Various High-Energy-Injection Plasma Experiments. Different definitions of plasma volume, input current, and charge-exchange lifetime cause slight disturbances of the position of the various experiments.

do not resemble flutes, do not seem to constitute any significant plasma loss.

There is strong evidence of microinstabilities of several kinds. Strong radio-frequency (rf) emission at the ion cyclotron frequency and its harmonics is noted in DCX-2 as indeed it is in *all* hot-ion injection experiments whether fed by ions or by neutrals, whether trapping is accomplished by Lorentz ionization, Lorentz dissociation, residual gas ionization or dissociation, or by arc dissociation. In DCX-2 this rf is associated with a spreading of the plasma ion energy both above and below the injected energy. The energy spread increases with plasma density, and when it becomes large the average energy of the trapped plasma is considerably increased. At the higher densities the rf is stronger in the higher harmonics of the ion cyclotron frequencies. Although the rf from the short mirror machine DCX-1 shows in addition some frequencies corresponding to longitudinal oscillations of the hot ions, none of these are seen in DCX-2.

Although the energy of the plasma ions is spread from below 100 kev to above 2 Mev in the direction perpendicular to the magnetic field, it is clear that the energy spread along the field is quite low. Except for the appearance of a distinct low *z*-energy group, the energy in the *z* direction remains at the 1.5–2 kev value at which it was injected with a spread of 1–2 kev at most.

The angular distribution in the direction perpendicular to the field axis of the charge-exchange neutrals (and hence the fast ions that produced them) shows the existence of these several distinct groups of ions. At low injection current the two expected groups of ions traveling from each mirror toward the opposite one are found. These groups have rather exactly the pitch angle at which they are injected. At high injected currents these two groups are rather wider in angular distribution but have a variation of angular positions with the total energy of the ions such that the longitudinal energy of the ions is approximately unchanged. In addition to these two groups the third distinct group mentioned above appears with very small pitch angles and small angular spread. This group can be found even with gas breakup, although quite weakly, and only with careful adjustment of the magnetic field shape. This proves that the effect is not produced in some way by the dissociation arc. With arc dissociation and the much denser plasma that results, this group becomes dominant, accounting for most of the plasma. In the highest-density case this part of the plasma accounted for a fourth or a fifth of all of the injected ions (based on current accountability) and three quarters of all those that decayed by charge exchange. The magnetic field adjustment required to produce this effect strongly, with a considerable increase of plasma density over unoptimized conditions, is such as to make it clear that these particles are trapped. This low z-energy group consists of particles having pitch angles of less than $\pm 2°$. A mirror ratio of $R \approx 1 \times 10^{-3}$ is sufficient to reflect them. Such a mirror is produced by the optimum field adjustment in the region between the injection dips. As a result, very large energy spreads may be accommodated since the injection snout, normally only one Larmor diameter from the plasma, is not visited by these trapped protons. Rather, the tank wall becomes the closest immovable obstacle. It seems possible that field optimization influences both the mechanism for retaining and the mechanism for producing this group. A possible driving force for the production of this group lies in the two well-defined velocity groups of ions streaming through each other from mirror to mirror.

Another and perhaps also separate disturbance is indicated by the quasiperiodic fluctuation in amplitude of the neutral particle detector signals. The excellent correlation of these signals along the whole length of the plasma and the considerably poorer correlation around the plasma, despite the nondirectional response of the foil detectors, show that: (1) the underlying disturbances among the plasma ions must be extremely asymmetric and (2) there must be nonuniformities in the charge-exchanging medium over distances comparable to the Larmor orbit size of the hot ions.

To clarify these facts, certain experiments appear desirable. To what extent the field adjustment is critical is not well defined. Certainly, variations of about a factor of 10 in density of the plasma trapped in the weak mirror can be seen for field variations on axis of 20–30 gauss from optimum. The shape of the fields off axis may play an important role. This off-axis field shape is especially sensitive to the balance between the dip coil current and the mirror coil current, particularly at the ends of the weak trapping region. Further experiments to establish at least semiquantitative relations between the desired field shape and trapped plasma density are needed.

Further, the amount of plasma trapped in this weak mirror is evidently related to the total dissociated current. Therefore, a detailed study of the relation between injected beam current and trapped density seems to be in order. At present we find that the integrated neutral flux after beam turnoff seems to saturate (under certain conditions) for injected beams greater than ~ 20 ma. We have not yet established if the limit to the density is determined by a limit of the injection rate into these weak mirrors or if the loss rate out of the region is enhanced as the density is increased.

The problem of establishing the lifetime of the particles in the plasma has not yet been satisfactorily solved. As we have reported previously, the observed current "decay time" is not a satisfactory measure of the mean life of the particles since the large energy spread results in a nonexponential decay. We have defined a mean life $\overline{\tau}_{cx}$ such that

$$I_{cx}\,\overline{\tau}_{cx} = nV\ ,$$

where I_{cx} is the total charge-exchange flux to the walls and n and V are the properly averaged density and volume of the plasma.

$$\overline{\tau}_{cx} = \frac{1}{n_0}\,\frac{\int I_{cx}\,dE/\sigma_{cx}v}{\int I_{cx}\,dE}\ ,$$

where n_0 is the averaged charge-exchanging density and the integrals may be evaluated from the observed energy distribution of charge-exchange neutrals. The difficulties at present are that we have no good measure of n_0 since we infer from the observed angular distribution of charge-exchange neutrals that the unstripped cold plasma ions must increase substantially the charge-exchanging density. A second difficulty arises in trying to correlate the known energy spectrum with the observed current decay. Calculations in progress do not seem to offer much hope of being able to predict the observed decay trace from the initial energy distribution, even including energy degradation in the arc, without including additional energy mixing after the beam is off. Therefore, we have no additional experimental check on $\overline{\tau}_{cx}$. The significance of an accurate value of $\overline{\tau}_{cx}$ lies in being able to establish whether losses other than charge exchange are important.

Certain particular loss mechanisms other than charge exchange may be eliminated. First, there are no significant charged particle losses to the walls. Second, although in our highest densities we observe considerable trapping in an extremely weak mirror ($R \sim 1 \times 10^{-3}$), we probably do not have significant scattering out of this mirror by "classical" Coulomb scattering either in the arc or in the cold plasma.

Spitzer[1] gives the classical scattering time for a particle in a plasma of cold particles as

$$t_D = \frac{v^3 m^2}{8\pi e^4 n_0 Z^2 \ln \Lambda(\phi - G)} ,$$

where t_D is the classical scattering time. From our present data, reasonable assumptions for the cold plasma are $n_0 = 10^{11}$, $\phi - G = 1$, $Z = 2$. For $v = 5 \times 10^9$, $t_D = 500$ sec. Classical rates are clearly too slow to lose a significant fraction of the plasma in 50 msec. The scattering rate in the arc may have been expected to be larger, since the density of lithium ions seems to be $\sim 5 \times 10^{13}$ ions/cm^3. However, most particles spend only a small fraction of their lifetime in the arc. One can reasonably expect $t_{arc} \gtrsim 10^2$ sec. This seems to be sufficiently long to expect that arc scattering also does not dominate the loss rate. Better experimental information on the variation of density with beam current should settle this question, since the scattering rate is independent of hot-ion density.

[1] L. Spitzer, Jr., *Physics of Fully Ionized Gases*, 2d ed., Interscience, New York, 1962.

2.2 FOIL DETECTOR SIGNALS

The current received by the foil neutral detectors during steady-state operation shows quasiperiodic fluctuations. A typical picture may be seen in Fig. 2.2. The two traces were made simultaneously using a dual-beam oscilloscope. The upper and lower traces were from detectors in port positions 1-8 and 7-8 respectively. Figure 2.1 in ORNL-3472 is a key to port locations; position 1-8 means ring 1, position 8, etc. The resulting excellent correlation between the two fluctuations is typical of the response of detectors at the same azimuthal position in the machine. Figure 2.3 shows the poor but obviously nonzero correlation between signals from detectors with azimuthal separation. A careful study of these pictures shows that there is a tendency for fluctuation peaks to be delayed from one azimuthal position to another around the machine in the direction of ion motion and in the direction of precession in the magnetic field. This delay corresponds to a period of roughly 80–100 μsec for 360°. The period is within the range of times expected for precession of ions during reflection from the mirrors. The gross

PHOTO 68003

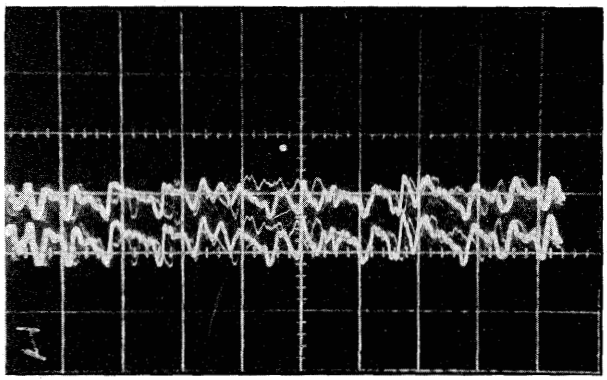

Fig. 2.2. Simultaneous Response of Neutral-Particle Detectors at Same Azimuthal Position but Separated Axially by 92 in. Port location 1-8 and 7-8 (see text). Sweep speed was 0.5 msec/cm. The trace started 5 msec after the beginning of injection.

PHOTO 68004

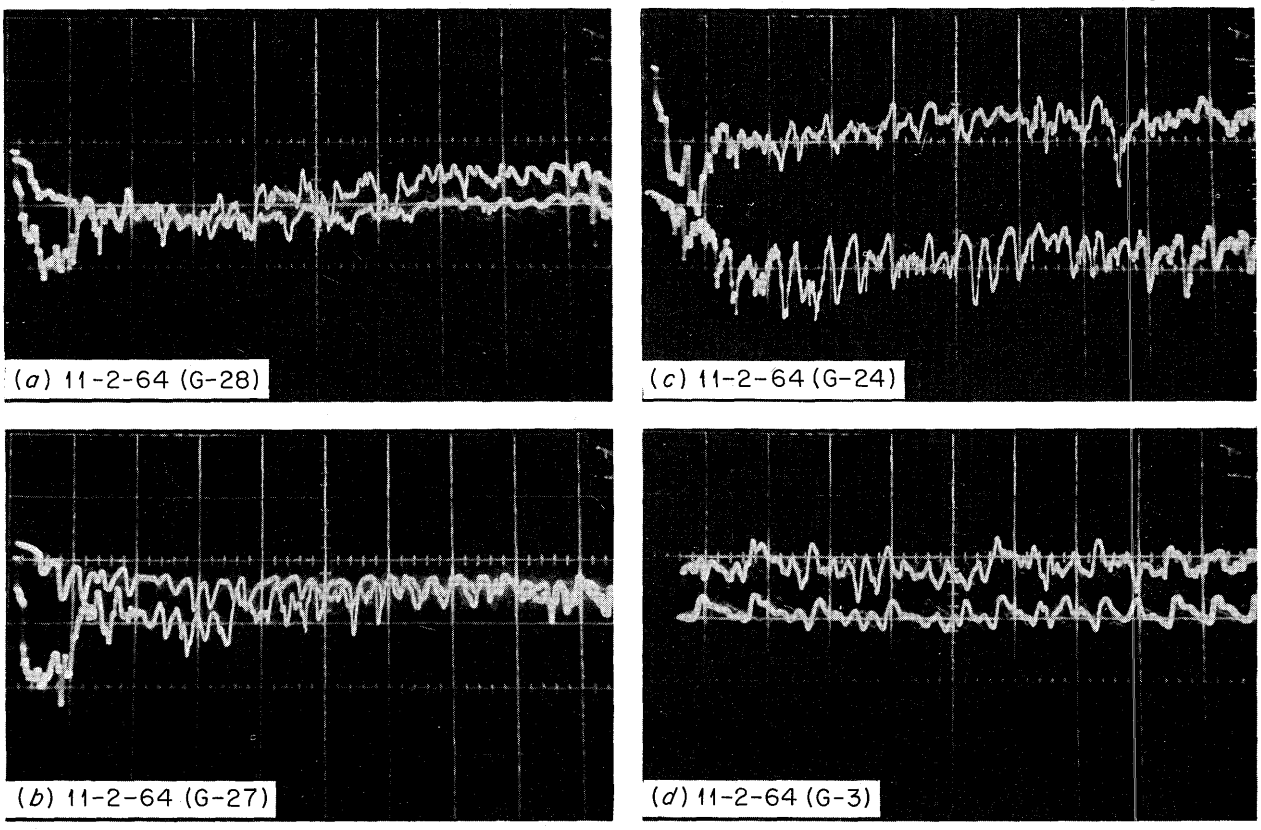

Fig. 2.3. Simultaneous Response of Neutral-Particle Detectors at Different Azimuths. The pairs of traces are at (*a*) 0 and 315°, (*b*) 90 and 315°, (c) 315 and 180°, and (*d*) 225 and 315°. The responses were measured in the direction of ion motion from the point of injection. The sweep speed was 0.5 msec/cm.

variations appear to be approximately evenly spaced. When this signal was viewed on a spectrum analyzer, however, the pattern of Fig. 2.4 resulted. The broad indistinct peaks show two poorly defined frequencies at about 3 and 6 kc. A measurement at another time showed a single poorly defined peak at about 5 kc.

These fluctuations were shown to be due to variations in the flux of neutral particles from charge exchange. The possibility that they were due to charged particles scattered outward from the plasma was eliminated by an experiment which prevented orbiting ions from passing into the detector. A perpendicular plane barrier was placed beside the detectors extending inward 1 in. radially and in such a position that the orbiting ions would strike the barrier unless they were moving almost exactly radially (see Fig. 2.5).

PHOTO 68005

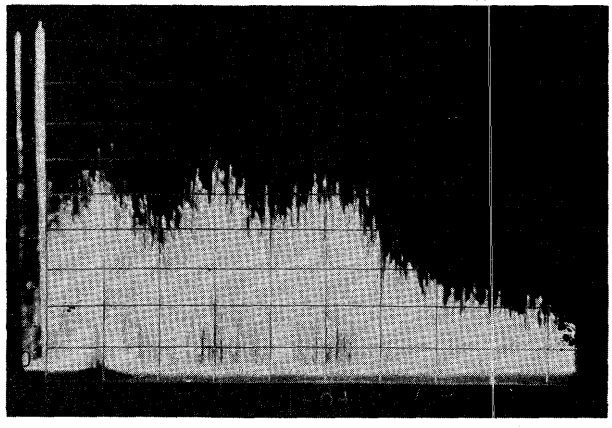

Fig. 2.4. Frequency Spectrum of the Fluctuation of the Foil Neutral Detector Current. Data of 11/2/64 (A-7).

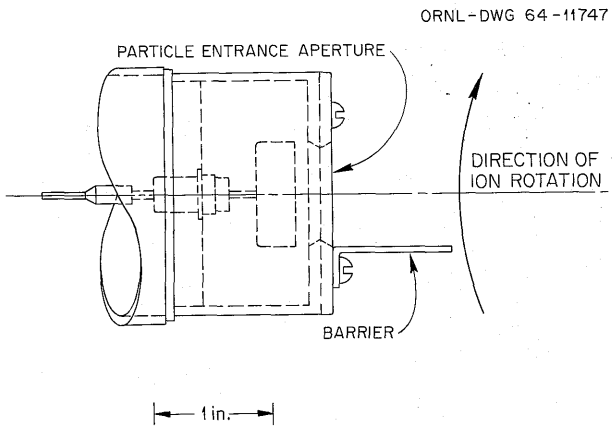

Fig. 2.5. Fast-Ion Barrier for Foil Neutral Detector.

There was no change in the received signal when the detector and barrier were rotated.

Since the signal to the detectors must be energetic neutral particles from the charge exchange of energetic ions in the plasma, it is perhaps surprising that the correlation around the axis is not any better than it is. Apparently, the processes producing energy spread or causing particle loss occur in small regions in the plasma, and the difference in signals to the various detectors is due to the occurrence of these disturbances at specific places in the plasma. Also, since there is some correlation around the machine but with a time delay, the particles of a disturbance must remain together for times long enough to see the effect of precession. The shape of the signals changes from time to time and from one detector to another. Sometimes sudden increases in current can be seen. These most likely are due to energy spreading in the plasma. Only a small spread in the spectrum is required to produce a large momentary increase in the charge-exchange current. At other times, however, there are sudden decreases in the current to the detectors. This effect may indicate a loss of either hot or cold plasma in the region viewed by the detector.

A study of these pictures in more detail, particularly with collimated detectors, is expected to give information on the extent and nature of the disturbances producing the fluctuations, which also most likely are connected with the loss of fast ions from the plasma. Correlations of these signals with the signals to gridded probes, looking at both electrons and fast ions, with the current to the snout target, and with the cyclotron harmonic rf spectrum have been looked for but none have been found. It would be very surprising if there is really no effect upon the cold plasma along flux lines through a disturbance, but since the signals seen by the detectors are the sum of the effects of disturbances from a large region of the plasma, while the gridded probes see only the exact flux lines which pass through them, the interrelationship may be hard to find. Blinders are being added to the detectors to limit the view of the plasma. This arrangement should localize the response enough to find a correlation if it exists.

2.3 RADIO-FREQUENCY MEASUREMENTS

The radio-frequency emission spectrum of the DCX-2 plasma at the highest density contained the second, third, and fourth harmonics of the proton cyclotron frequency and a considerable amount of white noise (see ORNL-3652, Fig. 2.12). The fundamental of the proton cyclotron emission was extremely weak, as was the fifth harmonic. At the somewhat lower densities now obtained, much less white noise and a much greater amount of fundamental and fifth harmonic are seen (Fig. 2.6). The fundamental line is not present as a

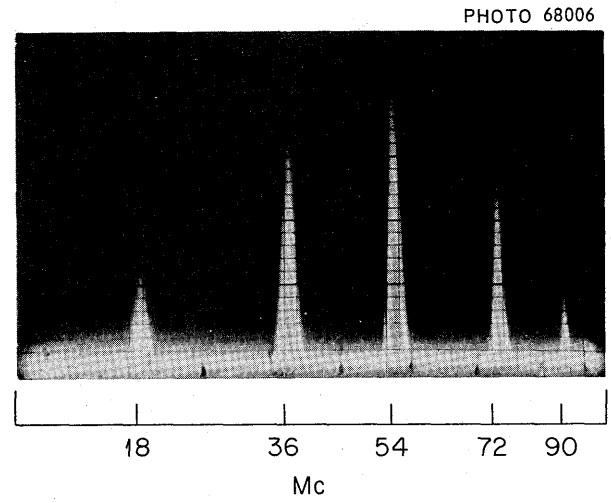

Fig. 2.6. Radio-Frequency Signals on a Radial Electric Probe at the Liner Wall. The white noise is much weaker and the fundamental stronger than what was found at higher density. The peaks are from left to right, the fundamental, and the second, third, fourth, and fifth harmonics. Data of 11/2/64, N-5.

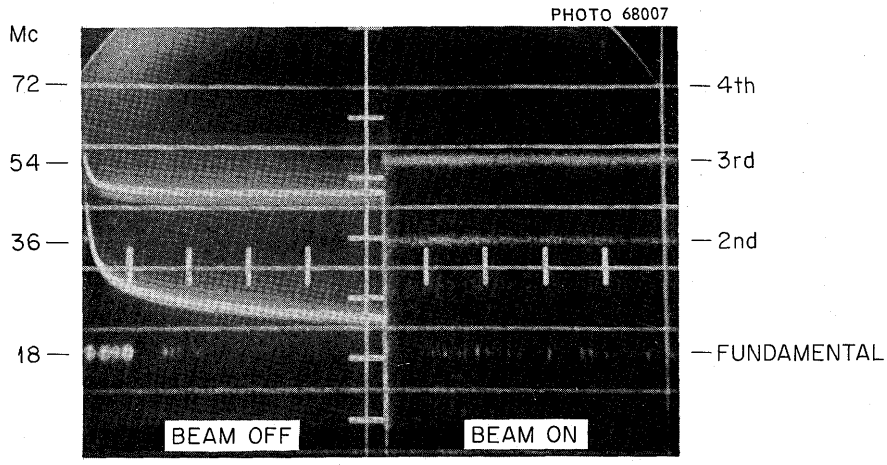

Fig. 2.7. Frequency-Time Display of Signals on a Radial Electric Probe near the Liner Wall. Note slight persistence of the second harmonic after beam turnoff at extreme left. The fundamental appears in short bursts with the beam on (right half). Sweep length 1 sec total. Data of 9/3/64 (P-3).

relatively continuous emission but rather is quite intermittent. Figure 2.7 shows an example of this effect. The sweep length is 1 sec, and the beam is turned off at the beginning of the sweep and on again at the middle. The two curved lines are integrals of foil detector signals. The vertical scale is frequency from 10 to 100 Mc with amplitude of emission used for intensification. Note that the fundamental appears strongly for ~0.1 sec after beam turnoff. In the right half of the figure while the beam is on, the fundamental appears in short irregular bursts while the second, third, and fourth harmonics appear more steadily although they are heavily amplitude modulated.

The arrangement of second, third, and fourth harmonics is suggestive of a carrier modulated by a lower frequency (i.e., third harmonic modulated at the fundamental). Several single-trace high-speed oscillograph traces (Fig. 2.8) show alternately on each trace the signal from two electric probes spaced several centimeters apart along field lines at the outer edge of the plasma near the machine center. It can be seen that the alternate sections from the two probes are accurately in phase and agree in shape and are a complex waveform of the third harmonic frequency with a

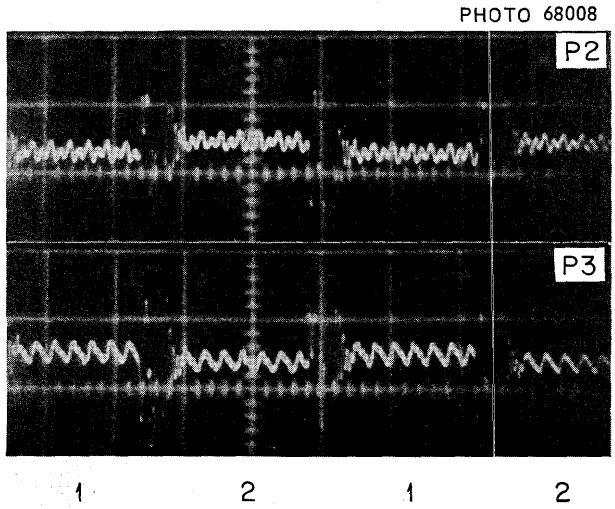

Fig. 2.8. High-Speed Sweep (0.2 μsec/cm) Showing Signals on Radial Electric Probes 2.5 cm Apart. Alternate 0.5-μsec segments are from the two probes. The upper and lower traces were made some minutes apart. Data from 10/14/64 (P-2,3).

fundamental frequency of repetition of the pattern. When the probe spacing is increased, changes in signal amplitude and apparently in harmonic phase or amplitude make difficult any determination of the spacing at which correlation becomes small. At a probe spacing of 5 cm in the circumferential direction, the waves are still similar in shape and well correlated. The patterns are quite different on the two traces, which are merely representative of different time. The patterns change whenever the machine parameters are changed but will also change with no evident reason.

2.4 ANGULAR AND ENERGY ANALYSIS OF EMITTED NEUTRALS

Measurement of the neutral flux from charge exchange within the DCX-2 plasma yields considerable information about the plasma without disturbing it. The energy analyzer which is used for these measurements was described previously (ORNL-3564, p. 16). It consists of a silicon barrier detector now collimated by means of a combination of a 20-μ pinhole in a platinum foil and a 5-μ slit. The collimation is designed to sample all the particles emitted in a fan $0.1 \times 40°$. As a result of this collimation, it is possible to make a parallel slit scan of the plasma (scanning across the plasma with the acceptance fan parallel to the axial magnetic field) and obtain an idea of the radial distribution of charge-exchange events as shown in Fig. 2.9. The 200-kev peaks seen in this figure are not normally observed and are seen here because the energy range examined is around 200 kev and more H_3^+ ions were injected than usual. The source pressure was abnormally high, favoring the production of H_3^+ ions, and a barrier which is sometimes used to intercept the H_3^+ ion beam on its first turn in the magnetic field was absent.

Alternatively, a perpendicular slit scan can be made (scanning in angle horizontally along the plasma axis with the acceptance fan perpendicular to the field), giving the distribution of pitch angles of the gyrating ions (the fast charge-exchange neutrals retain this angle with respect to the magnetic axis), as is shown in Fig. 2.13. Figure 2.10 shows the location of the energy-sensitive detectors in DCX-2.

A typical energy spectrum which was obtained while sweeping the energy analyzer so as to sample all plasma particles is shown in Fig. 2.11. Also shown in this figure is the spectrum of contained particles obtained by correcting for the charge-exchange rate as a function of energy. The most striking feature of the energy spectra obtained during this report period is the narrower

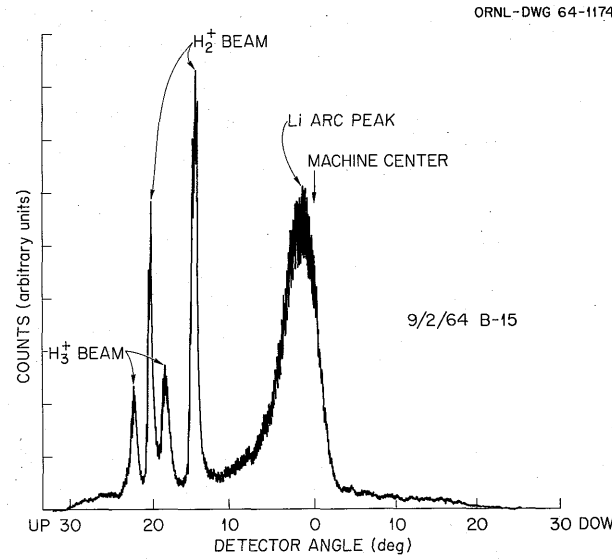

Fig. 2.9. Parallel Slit Scan of Charge-Exchange Neutrals from 225 to 275 kev as Seen from Port Position 4-3.

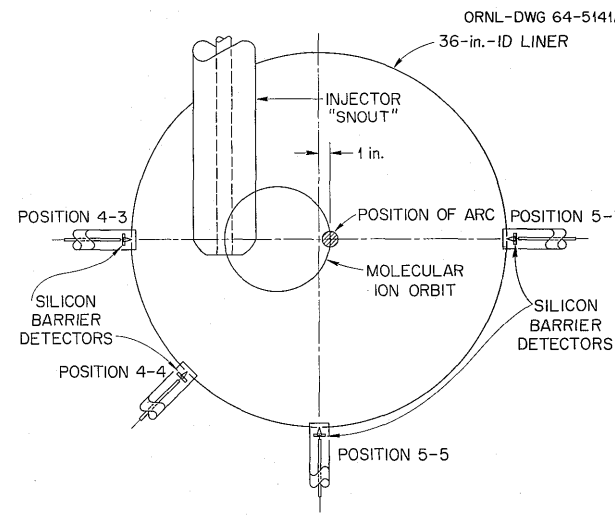

Fig. 2.10. A Transverse Section of DCX-2 Showing the Location of Energy-Sensitive Detectors.

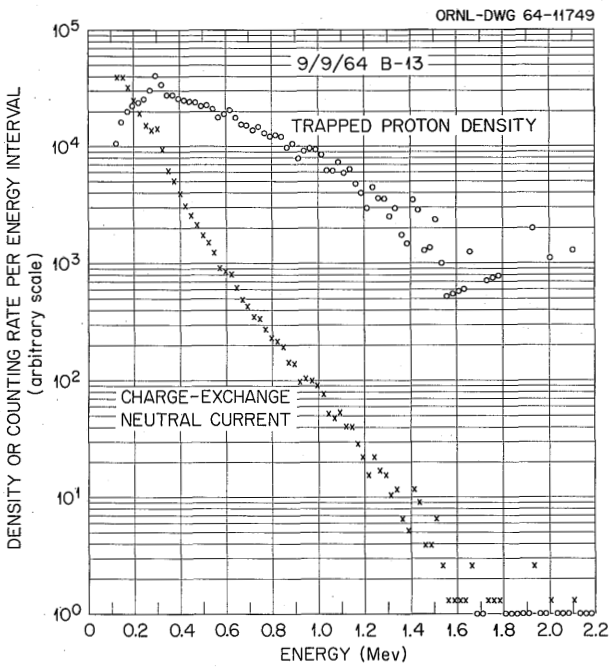

Fig. 2.11. Spectrum of Charge-Exchange Neutral Particles from the DCX-2 Plasma and the Corresponding Energy Distribution of the Trapped Plasma as Seen from Port Position 4-4. Circles printed on the bottom line are actually zero counts. Data for operating conditions of present report period.

energy spread (note the fast dropoff of the high-energy part of the spectrum). Compare this with a typical spectrum obtained during the high-density part of the last report period as shown in Fig. 2.12. Typical values for the mean energy of the contained particles for this report period were between 400 and 600 kev with a high of 690 kev in contrast with typical values of 600 to 900 kev and a high of 1.17 Mev obtained in the last report period.

Using the pressure as measured on the ion gage as a measure of the charge-exchange center density and the charge-exchange cross section for protons in N_2 extended above 1 Mev by an analytic best fit to the data at lower energies, one obtains values for the mean charge-exchange lifetime $\overline{\tau}_{cx}$ of 15 to 30 msec with a high of 47 msec. Similar calculations for the last report period gave $\overline{\tau}_{cx}$ values of 70 to 150 msec with a high of 186 msec. It is apparent that the condition of the DCX-2 plasma during this report period was quite different from the condition during the preceding six months. Possible reasons for this difference are discussed elsewhere in this report. However, on the last day of this report period, Nov. 2, 1964, the mean energies of the contained particles were found to be in the range of 700 to 800 kev with a high of 936 kev and the calculated $\overline{\tau}_{cx}$ on the order of 100 msec. The reason for this large difference in behavior is not known at this time.

A typical perpendicular slit scan is shown in Fig. 2.13. It has the high, narrow central peak and low, wide side lobes symmetric about the central peak that were also seen in the last report period with high density, although the central peak was noticeably wider then. However, the energy spectrum of the central peak is not approximately the same as that of the side lobes as reported last time and in fact differs considerably (see Fig. 2.14). The energy spectra of the two side lobes are approximately the same, and both have a large peak at 300 kev. This peak results

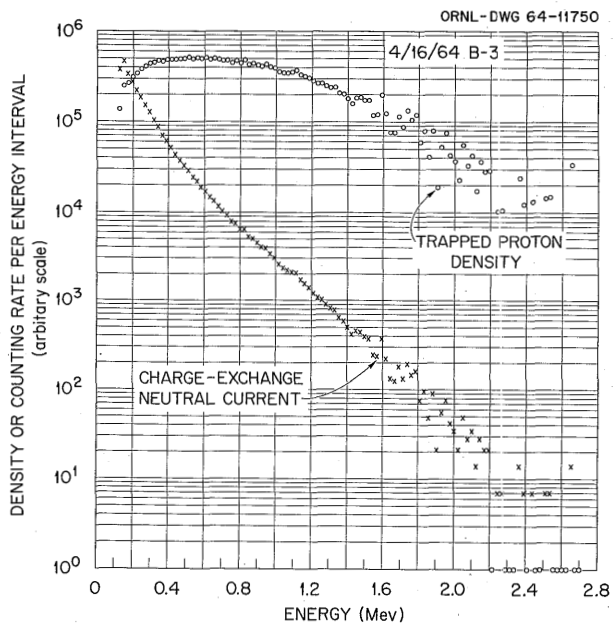

Fig. 2.12. Spectrum of Charge-Exchange Neutral Particles from the DCX-2 Plasma and the Corresponding Energy Distribution of the Trapped Plasma as Seen from Port Position 4-4. Circles printed on the bottom line are actually zero counts. Data for operating conditions of last report period.

from the 300-kev dissociation neutrals from the 600-kev H_2^+ beam in the background and plasma as it travels down and back in the machine; it is not seen when the detector is at an azimuthal position that escapes the dissociation neutrals.

The energy spectrum of the central peak (Fig. 2.15) has no 300-kev peak (since it does not contain the beam angle) and contains more high-energy particles than the side lobes. The highest-energy spectrum is obtained by looking directly at zero angle, as is shown in the same figure.

Figure 2.16 shows perpendicular slit scans seen from the midplane of DCX-2 at different energies. As the energy increases, the side lobes move in

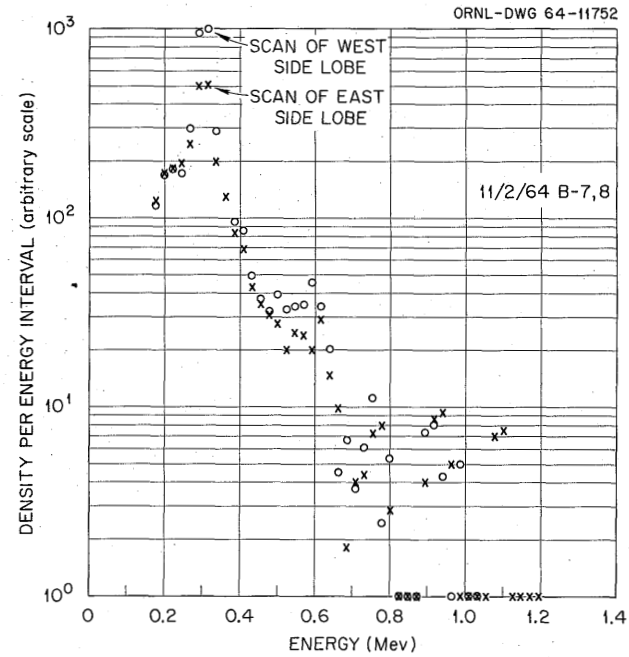

Fig. 2.14. Two Energy Distributions of the Trapped DCX-2 Plasma as Seen from Port Position 4-3. The crosses result from a scan of the east side lobe (between points *A* and *B* in Fig. 2.13) and the circles from a scan of the west side lobe (between points *D* and *E* in Fig. 2.13). Symbols printed on the bottom line represent zero counts.

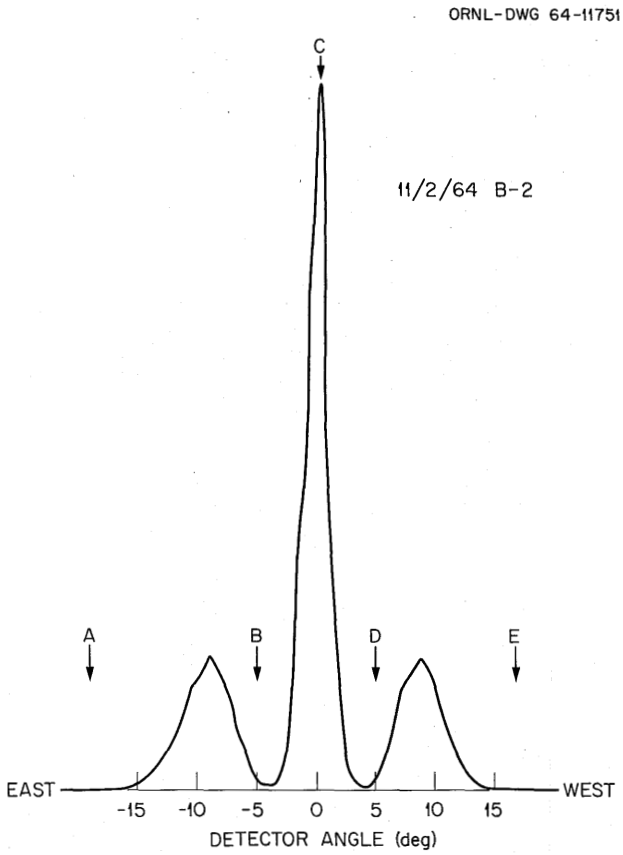

Fig. 2.13. Perpendicular Slit Scan of Charge-Exchange Current above 75 kev as Seen from Port Position 4-4. The positive pitch angles are from ions spiraling away from the injection snout and the negative pitch angles from the returning reflected ions. An *X-Y* recorder was used with vertical input from a linear count-rate meter and horizontal input from a voltage proportional to the angular position of the detector.

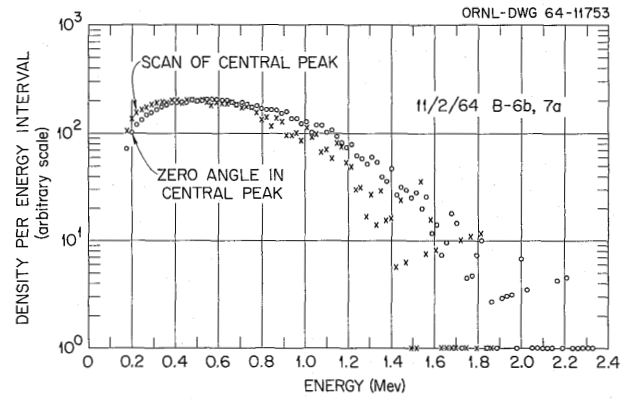

Fig. 2.15. Two Energy Distributions of the Trapped DCX-2 Plasma as Seen from Port Position 4-3. The crosses result from a scan of the central peak (between points *B* and *D* in Fig. 2.13) and the circles from looking directly at the central peak (point *C* in Fig. 2.13). The curves have been normalized to the same value at intermediate energies. Symbols printed on the bottom line represent zero counts.

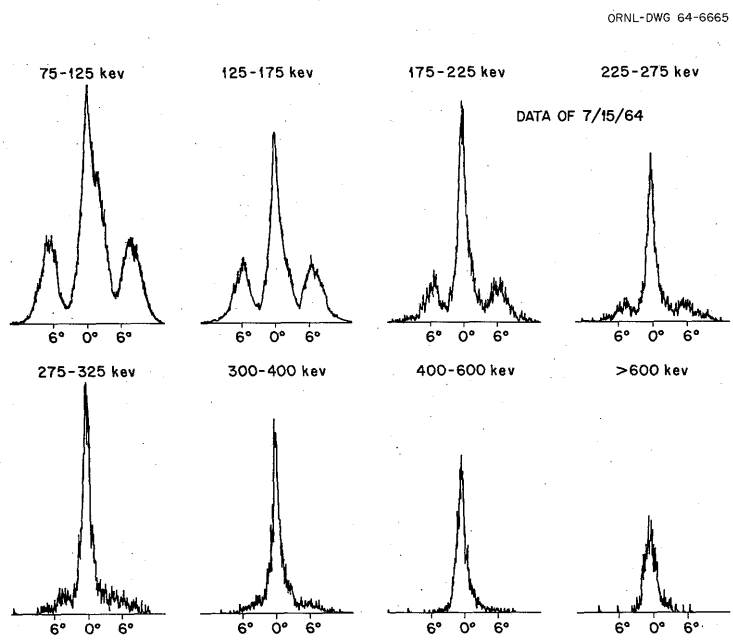

Fig. 2.16. Pitch Angle Distribution of Charge-Exchange Neutrals at Different Energies as Seen from Port Position 4-4.

toward the central peak and their height decreases relative to it. The axial energy can be calculated from the total energy and the pitch angle. Figure 2.17 shows that the axial energy is approximately constant and corresponds to the axial energy that a 300-kev proton has upon being dissociated from the 600-kev H_2^+ beam. The spread in axial energy is very much less than that in the perpendicular energy.

Energy spectra taken during eight consecutive 1-msec periods immediately following turnon of the 600-kev H_2^+ beam show some spread in the first 1-msec period and a gradual increase of the high-energy particles with respect to the low during the other periods, the energy spread being nearly complete at the end of 8 msec. It appears that the establishment of the steady-state energy spectrum (or rather the time-average spectrum, since no steady state exists) while the H_2^+ beam is on occurs in a time of the order of 10 msec. A similar experiment following beam turnoff shows a very rapid decay of the lower-energy particles and a much slower decay of the high-energy particles. However, the very lowest energy groups of particles decay slower (rather than much faster) than the groups of particles immediately above them in energy, resulting in a slight turnup of the spectrum at low energies. This turnup at low energies has been seen before in a turnoff experiment (see ORNL-3564, Fig. 2.12) and suggests that some mechanism is still occurring during the

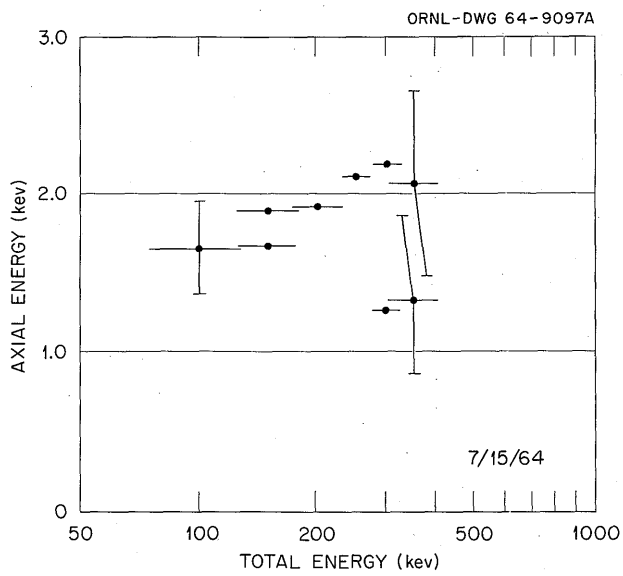

Fig. 2.17. Axial Energy Component of the Side Lobe Peaks for Different Total Ion Energies.

early stages of beam turnoff that tends to repopulate the very low-energy group of particles. These results cannot be explained just by the difference in charge-exchange rates of the high- and low-energy particles and energy loss of the hot ions to the cold electrons, and it seems necessary to include continuing nonclassical energy dispersion to explain these results. The second cyclotron harmonic persists in bursts for tens of milliseconds following beam turnoff and the fundamental up to ~1 sec, so it is not entirely unreasonable that some energy spreading is occurring after beam turnoff. Experiments of a less preliminary nature must be performed before more definite statements can be made about the time evolution of the energy spectrum following beam turnon and turnoff.

The neutral flux to the energy-sensitive detectors is due to charge exchange of the protons with the arc and the background gas and from dissociation neutrals from the H_2^+ beam. Using a set of energy-resolved parallel slit scans of the plasma as in Fig. 2.7, ORNL-3652, it is possible to approximately separate these effects and thus obtain the charge-exchange profile presented by the arc at different energies. The apparent arc diameter obtained in this manner varies with energy and is typically 5 cm (around 3 to 4 times that obtained from spectroscopic measurement of the arc). Thus the arc plasma surrounding the arc core contributes significantly to the arc charge exchange. Enough H_2 gas was bled in to raise the pressure by approximately a factor of 7 and thus ensure that the dominant charge-exchange centers in the background gas are H_2. The energy dependence of the contributions of charge exchange in the arc and in the background gas gives a rough measure of the energy dependence of the arc charge-exchange cross section relative to that for protons in H_2. The charge-exchange cross section σ_{cx} for protons in H_2 is shown in Fig. 2.18. It is extended above 1 Mev by an analytic best fit to the data at lower energies, as was done previously for protons in N_2, giving

$$\sigma_{cx}(H^+ \text{ in } H_2) = \frac{4.16 \times 10^{-4} E}{(E + 100)^5 (E^2 + 625)} ,$$

where E is in kev and σ_{cx} in cm^2. This was found necessary because of the large energy spread of the contained protons in DCX-2. The calculated σ_{cx}

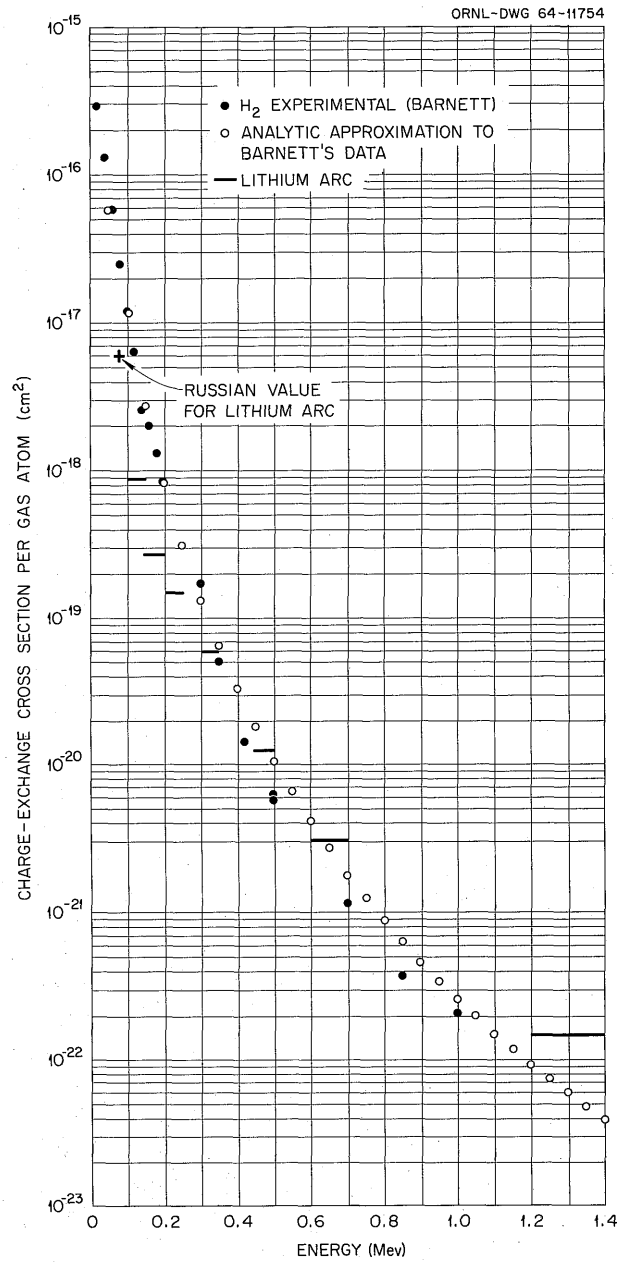

Fig. 2.18. Charge-Exchange Cross Section vs Energy for Protons in H_2 and in the Lithium Arc. The circles represent the values for H_2. The solid circles are from the experimental data of C. F. Barnett, J. A. Ray, and J. C. Thompson [*Atomic and Molecular Collision Cross Sections of Interest in Controlled Thermonuclear Research*, ORNL-3113 (revised) (August 1964)] and the open circles from an analytic fit $\sigma = 4.16 \times 10^{-4} E[(E + 100)^5 (E^2 + 625)]^{-1}$. Also shown is a rough estimate of the charge-exchange curve for protons in the lithium arc.

for protons in the arc (on the Li, Li^+, and Li^{2+} present in the arc) is shown on this same figure and varies more slowly with energy than that for protons in H_2. Establishing the absolute value of the arc σ_{cx} requires knowledge of the relative densities of arc and background gas and relative path lengths of the ions through each. Thus the energy dependence of the arc σ_{cx} is better known than its absolute value, since the energy dependence depends only on ratios at different energies and is less sensitive to these somewhat uncertain parameters. The arc density was assumed to be 5×10^{13} cm^{-3}. Also shown is a lithium-arc charge-exchange point at 80 kev obtained by Russian workers (reported by V. I. Pistunovich during USSR fusion exchange visit in June 1964).

3. Electron-Cyclotron Heating

3.1 ELECTRON-CYCLOTRON HEATING EXPERIMENTS IN THE EPA FACILITY

W. B. Ard
M. C. Becker[1]
R. A. Dandl[1]
H. O. Eason
A. C. England
G. M. Haas
H. C. Hoy
R. L. Knight
N. H. Lazar
R. L. Livesey
O. D. Matlock
M. W. McGuffin

3.1.1 Introduction

Further bremsstrahlung measurements have been made of the electron temperature and density in the electron-cyclotron plasma (ECP) in the EPA Facility. Previous measurements had shown that the plasma is a roughly spherical body with a volume of ~50 liters, an electron temperature of ~120 kev, and a density $\sim 5 \times 10^{11}$ when operated with 25 kw of microwave power. The present studies have measured the temperature and density as a function of power and pressure.

Some preliminary measurements have been made with an energetic neutral beam injected into the ECP. This beam experiment is designed to measure the neutral density in the plasma and, at high densities, to look for stabilizing effects by the ECP.

3.1.2 Bremsstrahlung Spectrum

In order to further investigate the bremsstrahlung from the ECP in the EPA, an improved collimator was built during the period of this report. Care was taken to eliminate scattering from the collimator walls and x-ray transmission through the sides of the collimator. The collimator and its position relative to the EPA Facility are shown in Fig. 3.1.

A high-intensity gamma-ray source (100 mc of ^{137}Cs) was placed in the EPA Facility to locate the volume scanned by the collimator. Figure 3.2 shows the experimentally determined aperture, as well as the aperture for a distant line source, calculated from the theory of Mather.[2] The calculated distribution contains both the geometrical aperture and the penetration aperture, but owing to the geometry of this collimator, no attempt was made to calculate the scattering aperture.

It can be seen that the experimental distribution is asymmetric. This was first thought to be due to misalignment; however, x-ray pinhole photographs of the source show it to be nonuniform in intensity and shape, and it is now believed that the asymmetry is due to the source.

The experimental width at half maximum for 662-kev photons is 0.52 in. Since the penetration aperture effect is small, and since the Compton scattering cross section in the region of 100 to 500 kev does not change drastically, the volume as determined using 662-kev photons should not change significantly over the range of photon energies of interest (100–500 kev).

The linear dimension through the plasma was obtained from an x-ray pinhole photograph[3] with 25 kw of heating power, and using the measured half-width one obtains a volume as seen by the collimator of 65.4 cm^3. The bremsstrahlung was observed by a 3- × 3-in. NaI(Tl) crystal and phototube located 276 in. from the axis of the machine. The fractional solid angle subtended by the crystal through the collimator was 5.14×10^{-8}. As in previous experiments,[4] a "black" hole was located on the opposite side of the cavity to eliminate x-ray scattering from the back wall.

---

[1] Instrumentation and Controls Division.

[2] R. L. Mather, *J. Appl. Phys.* **28**, 1200 (1957).

[3] *Thermonuclear Div. Semiann. Progr. Rept. Apr. 30, 1964*, ORNL-3652, sect. 3.1.

[4] *Thermonuclear Div. Semiann. Progr. Rept. Oct. 31, 1963*, ORNL-3564, sect. 3.1.

ORNL-DWG 64-11755

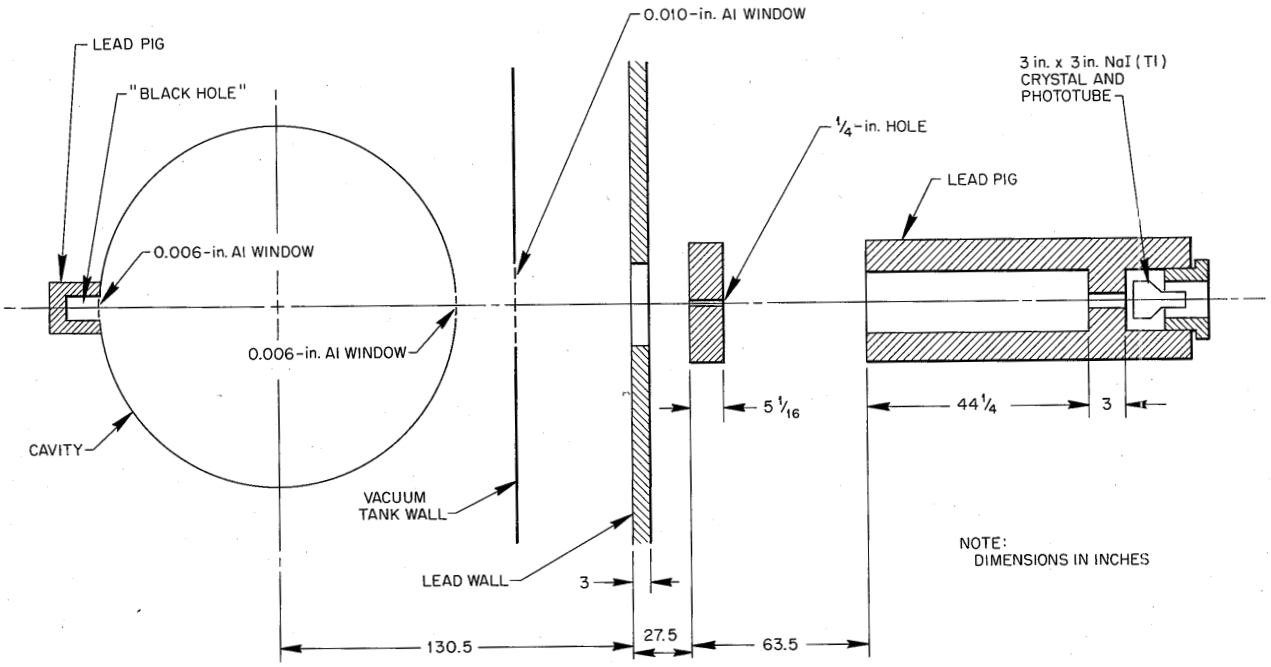

Fig. 3.1. Schematic Diagram of the New Bremsstrahlung Collimator and EPA Cavity.

ORNL-DWG 64-11756

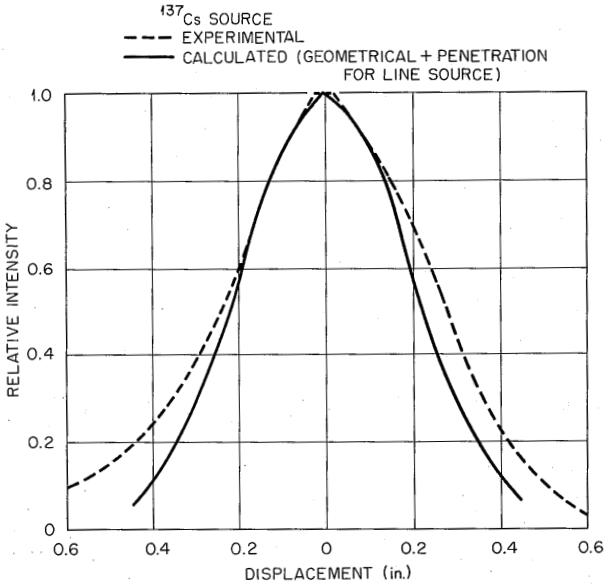

Fig. 3.2. Plot of Gamma-Ray Intensity vs Position for a ^{137}Cs Source in the EPA Cavity. The calculated distribution is also shown.

Measurements of the bremsstrahlung spectrum as a function of microwave power and pressure were made. Electron temperature and density were determined as in a previous semiannual report.[4] Figure 3.3 shows the new measurements of electron temperature and density as a function of microwave power for a fixed pressure and magnetic field. In computing the density as a function of power, it was assumed that the plasma volume was proportional to the microwave power. The x-ray pinhole photographs showed that the radius increased as the square root of the applied microwave power. The error bars are the statistical errors in counting and therefore represent only a lower limit on the errors. It is seen that the temperature shows little change with power but the density increases with power.

Figure 3.4 shows the new measurements of electron temperature and density as a function of pressure. The electron temperature shows little change with pressure, while the density of hot electrons decreases as the pressure increases. Figures 3.3 and 3.4 are not consistent and show that the ECP properties change from day to day.

It should be noted that these measurements can only be made when the plasma is stable. When the plasma is unstable, as indicated by large fluctuations in the microwave noise amplitude, anomalously high values for the electron temperature are observed. This is believed to be due to instabilities in the plasma producing bursts of x rays. Even under these conditions, however, the distribution still retains its Maxwellian character. An attempt to determine the effect of the bursts on the scintillator and phototube is being pursued in order to find out their effect on the bremsstrahlung spectrum.

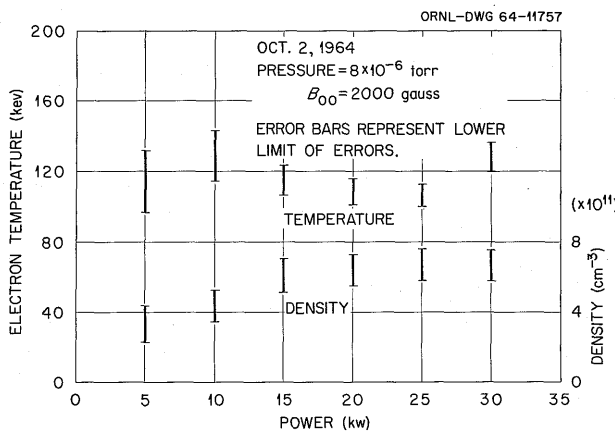

Fig. 3.3. Electron Temperature and Density as a Function of Microwave Power in the EPA. The symbol B_{00} refers to the magnetic field on the axis at the midplane ($r = 0$, $z = 0$).

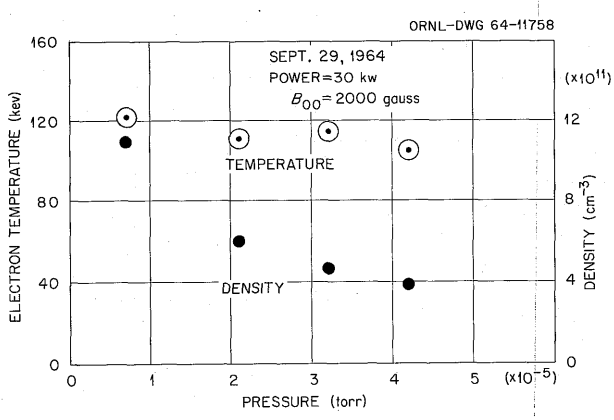

Fig. 3.4. Electron Temperature and Density as a Function of Gas Pressure in the EPA. The symbol B_{00} refers to the magnetic field on the axis at the midplane ($r = 0$, $z = 0$).

3.1.3 Neutral-Beam Injection Studies

The 20-kev energetic neutral beam, described in the last semiannual report,[5] has been used in preliminary experiments on the ECP in the EPA Facility. Although the beam has been incorporated into the machine for some time, there have been considerable delays. These have been due to difficulties in operating the beam with sufficient current, as well as difficulties caused by arcing in the microwave power waveguides.

Modifications in the acceleration region at the exit of the ion source previously described[5] have enabled us to inject over 20 ma of energetic neutral atoms into the ECP in the EPA Facility. Following the suggestions and advice of Morgan[6] an accel-decel system was installed in place of the usual simple accelerator at the source exit. In addition, the plasma from the source now expands into a large cup before acceleration. This modification apparently results in a smaller divergence of the accelerated beam, as well as space-charge neutralization of the beam by electron trapping between the magnetic mirror of the focus lens and the electrostatic field in the deceleration region. The source was then moved further from the lens without significant increase of the spot size; this resulted in almost complete absence of influence of the lens field on the source plasma. Typical operation is with +40 kv applied to the source and −25 kv to the accelerator electrode. Deceleration to tank potential takes place in the second gap.

Conversion of the 40-kev H_2^+ ions to 20-kev H^0 atoms takes place along the entire length of the 20-ft-long beam tube. Since the gas influx into the EPA Facility necessary to operate the ECP is of the order of 1 atm cm^3 sec^{-1}, the additional gas influx from the beam tube does not appreciably affect the cavity pressure. Equilibrium between the H_2^+ and H^0 beams is reached at beam tube gage pressures $\sim 5 \times 10^{-5}$ mm Hg.

[5] *Thermonuclear Div. Semiann. Progr. Rept. Apr. 30, 1964*, ORNL-3652, sect. 7.5.

[6] Section 6 of this report by O. B. Morgan; also, private communication.

Based on published cross sections,[7] this value is in reasonable agreement with expectations. Roughly, one H^0 is injected for each H_2^+ formed.

The purpose of the experiment is twofold. First, for low beam currents, the measurement of the charge-exchange decay time is used to determine the number of neutral atoms in the center of the ECP. Second, for high beam currents, a plasma of density $\sim 10^8/cm^3$ is possible, and studies will be made of its stability in the presence of the ECP.

The neutral atoms are injected into the cavity of the EPA Facility so that the beam center line is on the magnetic field midplane, but displaced 2 in. above the axis. Neutral atoms are ionized by or undergo charge exchange with the cold plasma ions in the ECP. Some ionization by electrons is expected. All these processes result in the trapping of ions near the midplane.

For low beam currents of a few milliamperes, the trapped hot-ion density is much less than the density of the ECP, and no coherent plasma effects are expected. The dominant loss process of this beam will be by charge exchange with neutral gas atoms in the plasma. Since the ECP is several mean free paths thick to thermal H_2 molecules, the primary neutral species is expected to be atomic hydrogen resulting from ionization of H_2 or charge exchange of H^+ on H_2. Atomic hydrogen from the ionization of H_2 can be produced with an energy of 5 to 7 ev when dissociated from the $^2\Sigma_u$ molecular state of H_2^+ and, due to its higher velocity, easily penetrates the ECP. These atoms, sometimes called "Franck-Condon neutrals," have mean free paths for ionization on the order of the plasma diameter, since their velocity is ~ 15 times higher than H_2 thermal velocities. Franck-Condon neutrals of ~ 3 ev energy are also formed when the H_2 molecule is excited by electron impact to the repulsive 1 $^3\Sigma_u$ molecular level. In this case, both atoms in the molecule come off as neutrals with about the same energy. These atoms will also easily penetrate the ECP, since their velocity is ~ 10 times higher than H_2 thermal molecules.

The experiment has been run with up to 20 ma of neutral beam current (a mixture of H^0 and H_2^0) into an ECP supplied with 30 kw of microwave power. From the observed increase in decay time of the beam, a 15-times reduction in the neutral density in the center of the ECP is calculated. This factor of 15 improvement is approximately that expected on the assumption that the chief neutral species is 5-ev H^0 from the dissociation of H_2^+ by electrons.

Due to questions regarding the detector sensitivity (discussed in Sect. 3.1.4) and solid angle calculations, the experimental results are not sufficiently precise to give a trapped hot-ion density. Further modifications in the detector geometry and collimation are being made to improve the signal and to scan various parts of the trapped volume.

3.1.4 Detector and Amplifier for Charge-Exchange Neutrals

A schematic diagram of the silicon barrier detector, bias batteries, and current amplifier is shown in Fig. 3.5. The silicon barrier detector is sensitive to light and x rays, and hence is shielded by a lead collimator and a thin aluminum window. The aluminum window is made by evaporating a 600-A layer of aluminum on a Zapon backing and dissolving the Zapon. The aluminum film is supported on a grid structure with $\frac{1}{8}$- × $\frac{1}{8}$-in. holes. The lead collimator is designed to shield the detector from x rays originating at the mirror throats. The detector is mounted in a metal can and views the plasma through a beyond-cutoff waveguide to prevent microwave leakage into the detector. The amplifier is a transistorized dc linear amplifier (ORNL Q-2773-2) which has a gain of 1 v out per 10^{-8} amp in. Its response time is less than 5 μsec. The 16-v bias battery control shown in Fig. 3.5 is used to bias out the leakage current resulting from x-ray irradiation of the detector.

It is estimated that the 600-A aluminum film absorbs 5 to 10 kev from an incident 20-kev proton. Measurements have shown that the 10- to 15-kev particles which reach the silicon barrier detector produce ionization less efficiently than higher-energy particles; specifically, 15–20 ev per ion pair is required. Hence, this process produces a current gain on the order of 500. There is some question as to the constancy of

[7] C. F. Barnett, J. A. Ray, and J. C. Thompson, *Atomic and Molecular Collision Cross Sections of Interest in Controlled Thermonuclear Research*, ORNL-3113 (revised), p. 17 (August 1964).

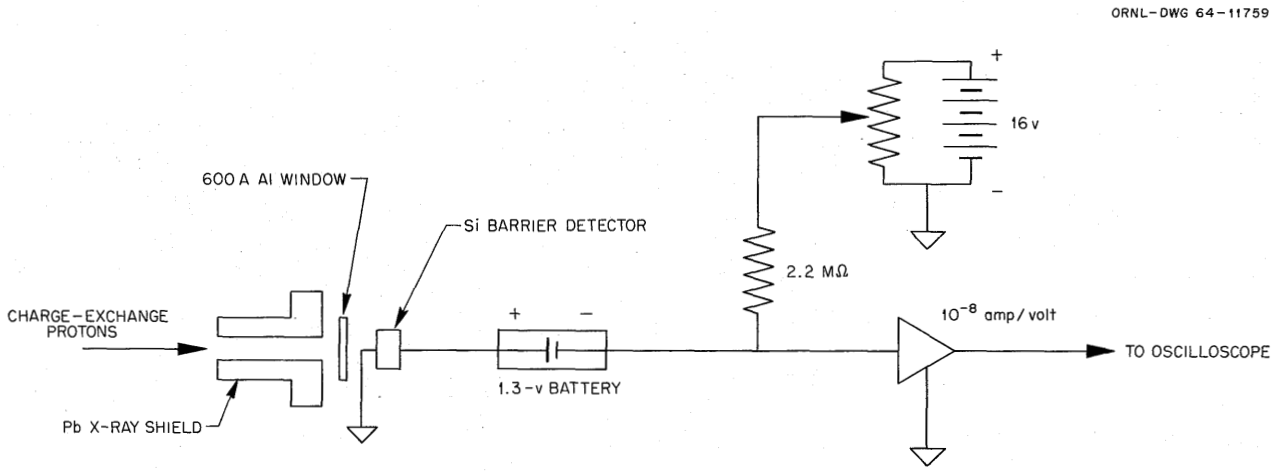

Fig. 3.5. Schematic Diagram of Silicon Barrier Detector, DC Amplifier, and Bias Circuit Used for EPA Neutral-Beam Experiment.

this gain with current, however, as the detector output drifts at high input currents. Further measurements of the current gain as a function of input energy and input current will be made.

3.2 THE REDESIGNED ELMO FACILITY

W. B. Ard
M. C. Becker[8]
R. A. Dandl[8]
H. O. Eason
A. C. England
G. M. Haas
R. L. Livesey
M. W. McGuffin

3.2.1 Construction of the ELMO Facility

The ELMO Facility, described in previous semiannual reports,[9,10] has been redesigned and rebuilt to provide a flexible research facility. In the new design, the services of the Engineering Sciences Group and the Engineering Support Group were used. It will be used with 3-cm microwave heating with a double-folded cusp magnetic field and will be used with 8- and 5.5-mm microwave heating as a variable mirror. Two tubes which each produce 1 kw of 35-Gc (8 mm) continuous-wave microwave power have been purchased from Watkins-Johnson. Figure 3.6 is a photograph of one of these traveling-wave-tube oscillators. A tube rated at 1 kw continuous wave at 55 Gc (5.5 mm) has been received from Hughes Research Laboratories. This tube is a traveling-wave-tube amplifier. The plasmas produced by millimeter microwave power sources are expected to have densities in the neighborhood of $10^{13}/cm^3$ and electron temperatures near 100 kev when sufficient power is available. However, because of the increased scattering losses at these higher densities, we expect that the plasma volumes will be quite small. The initial experiments in ELMO will use these millimeter microwave power sources.

The 10.6-Gc microwave power source, currently in use on the PTF, will be used for experiments in ELMO with the double-folded cusp configuration. Figure 3.7 is a schematic illustration of a half-section of the double-folded cusp. It shows the magnetic flux lines, the surfaces of B = constant, the vacuum tank walls, and magnetic field coils. A design criterion for the redesigned machine specified that there would be a closed surface of constant B suitable for electron-cyclotron resonance at 10.6 Gc which did not touch the machine walls. This surface is that

[8] Instrumentation and Controls Division.

[9] *Thermonuclear Div. Semiann. Progr. Rept. Oct. 31, 1961*, ORNL-3239, sect. 3.1.2.

[10] *Thermonuclear Div. Semiann. Progr. Rept. Apr. 30, 1962*, ORNL-3315, sect. 3.2.

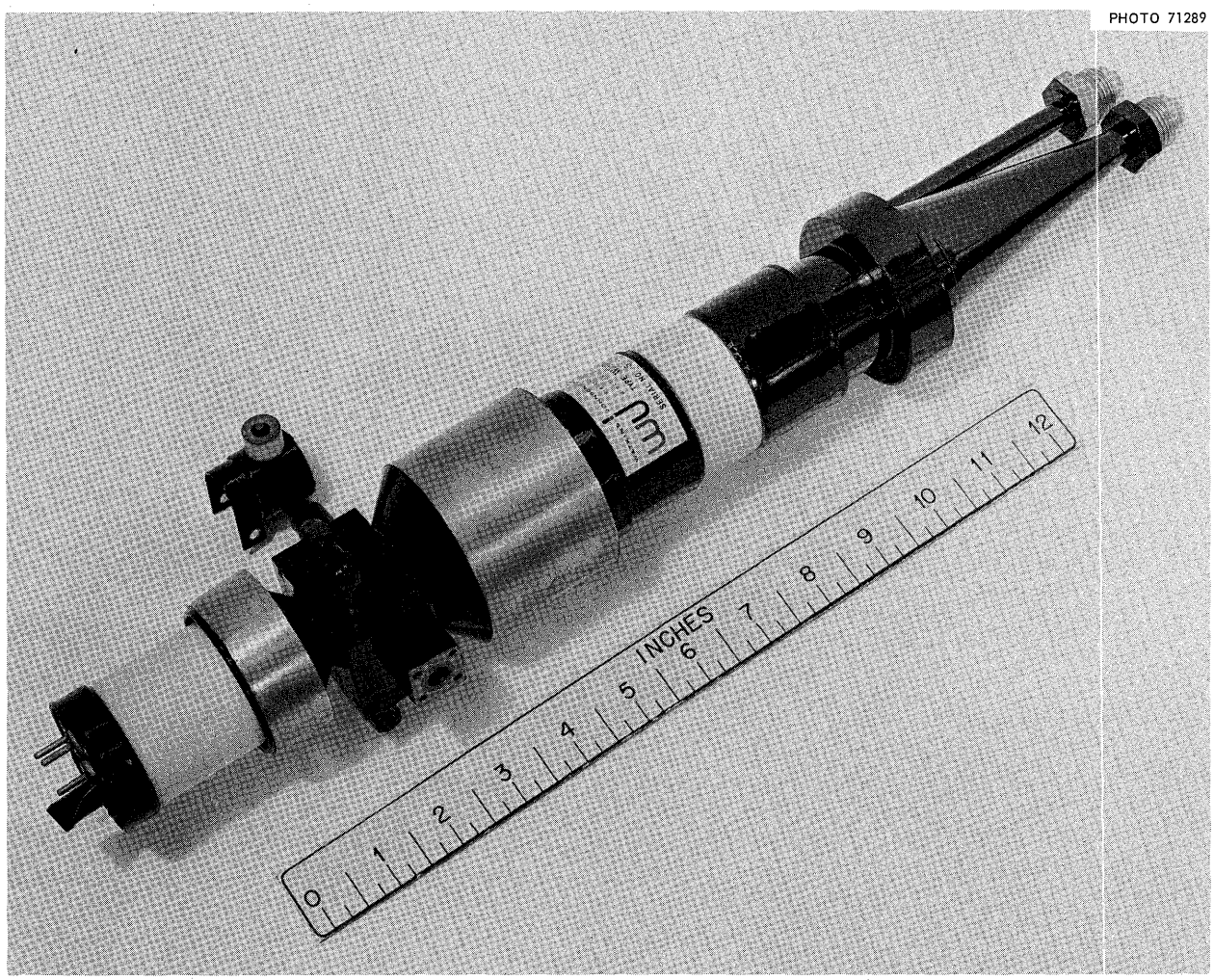

Fig. 3.6. Photograph of 1-kw Continuous-Wave 8-mm Traveling-Wave-Tube Oscillator To Be Used with the ELMO Facility.

labeled 1.00 in the figure. In addition, another criterion specified that there should be another constant-B surface that had a 50% higher field and did not touch the walls. The figure shows that there will be flux lines lying outside this second surface which leave the main volume of the machine through the point and line cusps without touching the walls anywhere else.

3.2.2 Expected Plasma Volume and Density in the ELMO Facility

There is some speculation as to the type of plasma which will be formed in the ELMO Facility when operated as a mirror machine with 8-mm power.

We can start by assuming that of the 2 kw available from the two traveling-wave-tube oscillators, 50% should be available for creating a hot-electron plasma. If we further assume that the electron temperature will be the same as with 3-cm power, about 100 kev, then we can make the following calculation.

The electron scattering time out of a 2:1 mirror is given by

$$\tau(\text{sec}) \cong 10^9 \frac{[T\ (\text{kev})]^{3/2}}{n\ (\text{cm}^{-3})},$$

where we assume electron-electron scattering is the dominant loss process.

The total power required to maintain a volume $\bar{V}$ of this plasma in the mirror is then

$$P(\text{kw}) = \frac{nT_e}{\tau}\bar{V}\,(\text{cm}^3)\,(1.6 \times 10^{-19}\ \text{j/ev})$$

or

$$P \cong \frac{n^2\bar{V}}{10^9 T^{1/2}}\,(1.6 \times 10^{-19})\,.$$

Taking $P = 0.5 \times 2$ kw $= 1$ kw and $T^{1/2} = 10$, then

$$n^2\bar{V} \cong 6 \times 10^{28}\,.$$

The maximum density we could expect would be that associated with the plasma frequency being equal to the applied frequency, or $n \cong 1 \times 10^{13}$. Then $\bar{V} \cong 600\ \text{cm}^3$. If, on the other hand, $n \cong 1 \times 10^{12}$, then $\bar{V} = 60$ liters, which can nearly fill the cavity which will be used. In both cases the density will be sufficient to act as an effective shield against thermal neutrals but not against Franck-Condon neutrals. This will also shed light on the heating mechanism – whether the plasma can absorb power at high densities or whether the plasma will be limited to densities transparent to 8-mm radiation.

ORNL-DWG 64-6248A

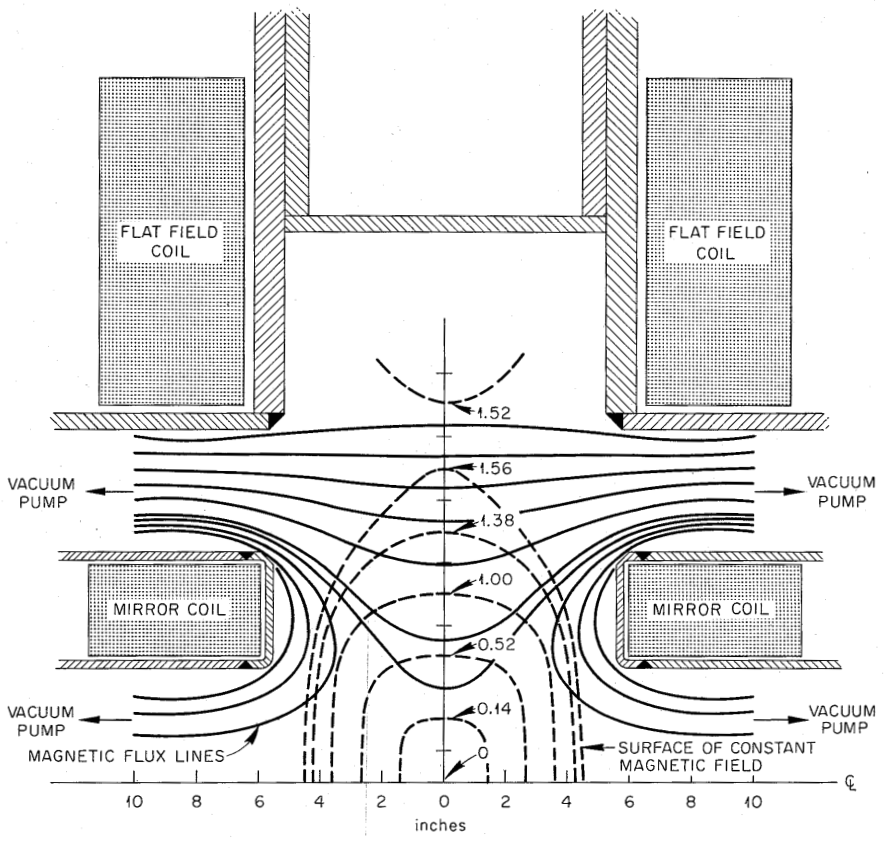

Fig. 3.7. Schematic Diagram of ELMO Facility. The drawing shows half the machine and illustrates the magnetic flux lines, the surfaces of constant magnetic field, the magnetic field coils, and the vacuum tank walls.

4. Plasma Physics

4.1 APPLICATION OF THE BURNOUT PHENOMENA TO ION AND ELECTRON HEATING (EXPERIMENTAL)

Igor Alexeff R. V. Neidigh
W. F. Peed

4.1.1 Introduction

In the last semiannual report,[1] we used a thermodynamic model to describe the method we employ in generating a fully ionized, "burned-out" plasma and presented some experimental data which appeared to verify the model presented. In summary: we found that the power requirement for burnout was approximately correct and varied with pressure as predicted; the escaping ion flux accounted for over 70% of the gas input; the helium discharge was dark, that is, most of the ions were stripped of their electrons; the transition from the non-burned-out, low-resistance mode I discharge to the burned-out plasma of mode II was abrupt as predicted; and the average energy of the ejected ions also agreed with that predicted by the model. In the various experiments the burnout region was the approximately 1-cm^3 10^{-3}-torr region within the anode of the pressure gradient discharge. In contrast, the region of the cathode or cathodes of the pressure gradient discharge is initially at the relatively lower pressure of 10^{-5} torr.

Since the last report we have attempted to exploit this high-pressure region of the discharge by increasing its power density above that required for complete ionization. Ion and electron heating should follow if the increased power density can be obtained, since energy losses due to charge exchange and excitation of gas atoms should be absent. Power into the anode region is via the electron beam. If the beam power is not transferred to the plasma, we haven't accomplished anything. We have taken the successive steps shown in Fig. 4.1. They are intended to permit increased dissipation of the beam power in the plasma and better diagnostics. Volume and magnetic field strength increases were necessary to contain orbits of energetic ions without losing them on the anode cavity walls. Magnetic mirrors were added to give ion and electron containment and a density increase in the midplane by midplane focusing. Additional vacuum pumping was required with the larger volumes to maintain the required pressure gradient. Deuterium gas was used for its diagnostic value.

As shown in the figure, the successively improved devices have been called "Burnout I" through "Burnout V." Burnout V, though still in the shakedown state at this writing, has been operated at 30% of its design power input of 100 kw, and all major components appear to be satisfactory. The data taken have not been significant so far. In this report we are giving only the data from Burnout IV, which has been our best plasma heating device to date.

As indicated in the figure, Burnout IV is the largest of the first four devices. Its working volume, that which is limited by the magnetic field which threads the aperture in the mirror throat, is about 10 cm^3. The size is limited by the gas-handling capacity of an existing vacuum system. A deuterium gas input of $\frac{1}{10}$ cm^3/sec gives the required 10^{-3} torr in the midplane and 10^{-5} in the cathode regions. Burnout IV also uses the maximum magnetic field strength of the facility, 9000 gauss in the midplane and 13,000 in the mirrors. A beam power input of 7 kw (10 kv at 0.7 amp) is applied. We do not presently know the power density of the plasma.

[1] *Thermonuclear Div. Semiann. Progr. Rept. Apr. 30, 1964,* ORNL-3652, Sect. 4.1, p. 46.

ORNL-DWG 64-5139R

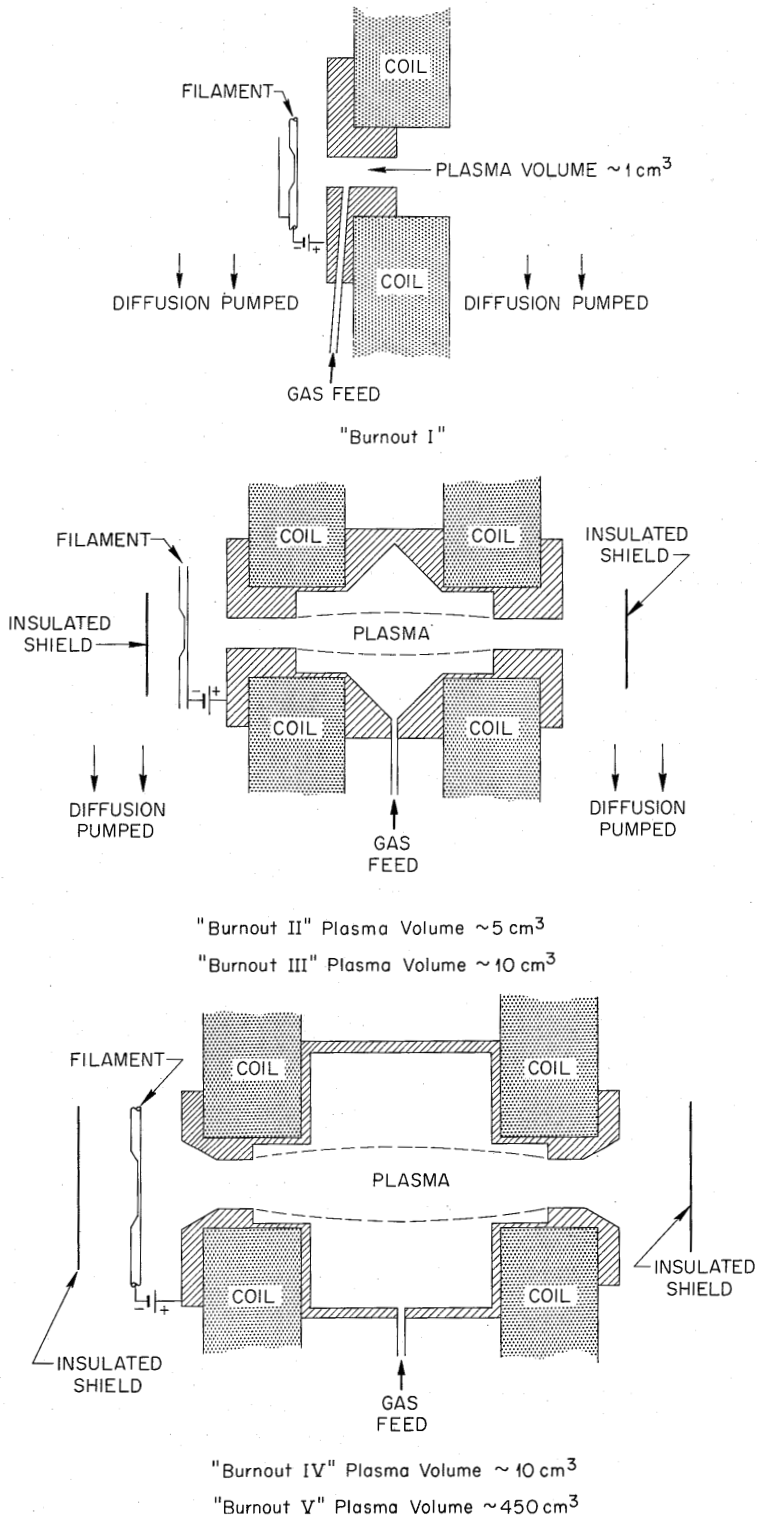

Fig. 4.1. Burnout I Through Burnout V. Burnout III and Burnout IV both have the same size orifice in the mirror throat and therefore the same size working volumes, but Burnout IV has the larger cavity size. The cathode is shielded so that an arc cannot be struck directly to the anode along magnetic field lines.

Numerous experiments have been done to measure this plasma power density, that is, to measure our success at heating electrons and ions. The most pertinent experiments will be described. They fall in the following categories: (1) indications of complete ionization, (2) distribution of power loss in the anode, (3) indications of ion heating, (4) indications of electron heating, (5) plasma density measurements, (6) plasma potential measurements, and (7) neutron emission.

4.1.2 Indications of Complete Ionization

Hydrogen, deuterium, and helium discharges are dark in Burnout IV. That is, spectral light of sufficient intensity to analyze is not emitted from the working volume of the plasma. In discharges with heavier gases the gas appears to be fully ionized but the ions are not stripped.

In all gases which were tried (hydrogen, deuterium, helium, and argon) the input gas is nearly all accounted for as escaping ions. Ions from deuterium and helium discharges were counted by the technique described in Fig. 4.2. We assumed that the symmetry of the device permitted us to measure ion flux through only one mirror. With a 5-kw electron beam we measured an ion flux equal to 60% of the gas input. Even though the transition to mode II was abrupt, indicating burnout, our measurement of the ion flux did not account for all the gas input but continued to increase with beam power up to about 7 kw. With 7 kw, the ion flux equaled the gas input within the 10% accuracy of our measurements.

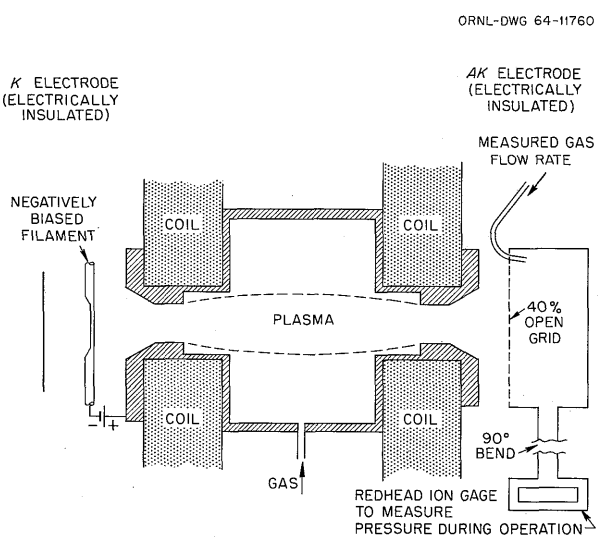

Fig. 4.2. Method of Measuring Plasma Pumping. The insulated AK electrode is made in the form of a plasma catcher with a 40% chance of catching all the plasma. Plasma pumping rate is determined by reproducing, with a measured gas flow rate, the pressure rise in the electrode due to plasma.

4.1.3 Indications of Ion Heating

Even though the ion temperature is not known quantitatively, there is considerable evidence for ion heating. The inner surface of the cavity wall around its intersection with the midplane is extensively sputtered. A glass window in the cavity wall is shown in Fig. 4.3. Note the clean band down the center with deposits on either side. The band appears to be sand-blasted. Analyses of the deposits on either side give about 50% copper (probably some from the sputtered cavity wall) and 50% stainless steel from the coil enclosures, which appear sputtered near the coil throats. The coil throat itself is lined with copper.

Electrostatic and magnetic analyses of ions near the outer cavity wall identify the ions as deuterons with 20 to 25 kev energy. One technique is described in Fig. 4.4. Unfortunately, the MoO_3 detector is not easily calibrated for flux density.

A pinhole image of the orbiting ions may be obtained on the MoO_3 plate. A schematic diagram is shown in Fig. 4.5, and the images using three pinholes are shown in Fig. 4.6. Charge-exchanged deuterons form the images. Note that an asymmetric image of this size requires an orbit diameter equal to or greater than the radius of the cavity. Also note the absence of z-wise spread in the images, indicating that most of the ion energy is perpendicular to the axis.

A velocity selector analyzer, whose sensitivity and aperture can be computed, also looked at the outer plasma (Fig. 4.7). Two peaks were seen. One at 65 to 75 ev indicated a density of about 10^{12} ions/cm^3. A smaller peak at 20 to 25 kev gave about 10^{11} ions/cm^3.

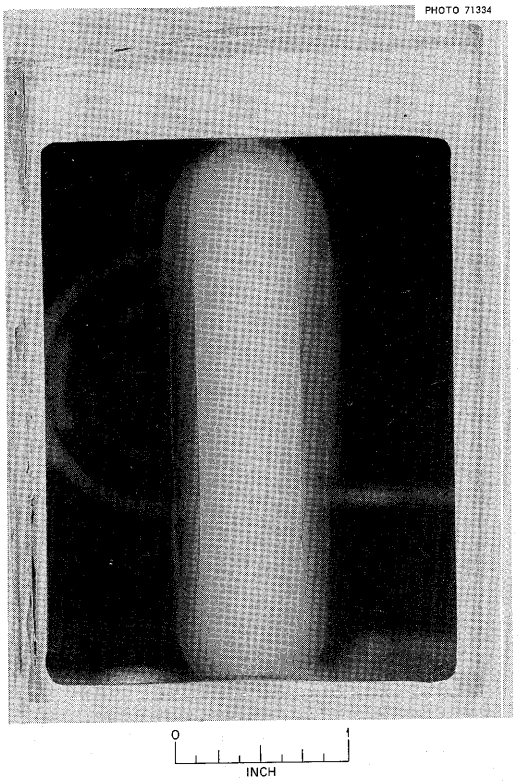

Fig. 4.3. Cavity Window. Note the etched band in the center at the window intersection with the magnetic midplane. The dark region on either side is deposited copper and stainless steel.

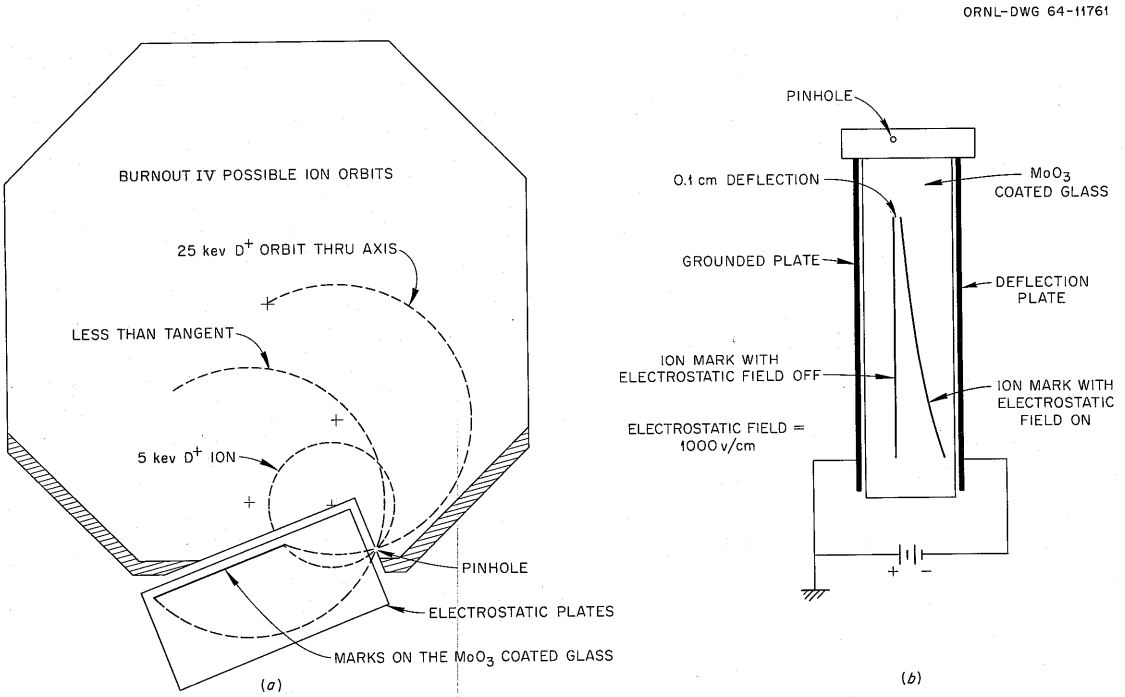

Fig. 4.4. Application of Electrostatic and Magnetic Analyzer to Burnout IV. Part (*a*) is a midplane section; (*b*) shows the marks on the MoO_3 detector. Since the deflected mark shows no *z* spread, only length, it must have been made by monoenergetic ions (25 kev) passing through the pinhole at different angles of incidence but all lying in the midplane.

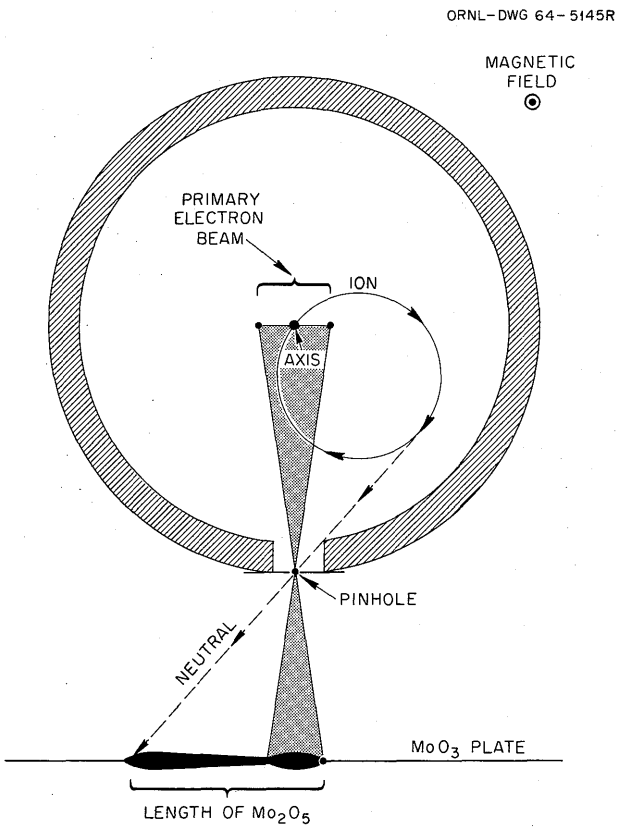

Fig. 4.5. Schematic Diagram Showing Pinhole Image of Ion Orbits. In this instance the image is formed by neutrals. Note that the ion orbits must pass through the axis to give the asymmetric image.

4.1.4 Indications of Electron Heating

There is also electron heating. The electron temperature is not known yet, but x-ray images of the plasma and of the inside cavity walls have been made through 50 kev of absorber. Electronic analysis of the x-ray spectrum is complicated by the abundant 100- to 200-Mc radiation, which is difficult to shield against.

4.1.5 Plasma Density Measurements

Two intense bands of radiation (300 v/m at 1 m) appear. The bands are separated by approximately the ion cyclotron frequency (7 Mc in the midplane). A traveling-wave oscilloscope display is shown in Fig. 4.8. If the 170-Mc signal is associated with the ion plasma frequency, a density of 4×10^{12} ions/cm^3 is indicated. Radiation at the electron plasma frequency has not been looked for, however; 10-kMc signals generated externally are attenuated by the plasma, indicating that the density is probably higher than 10^{12} ions/cm^3.

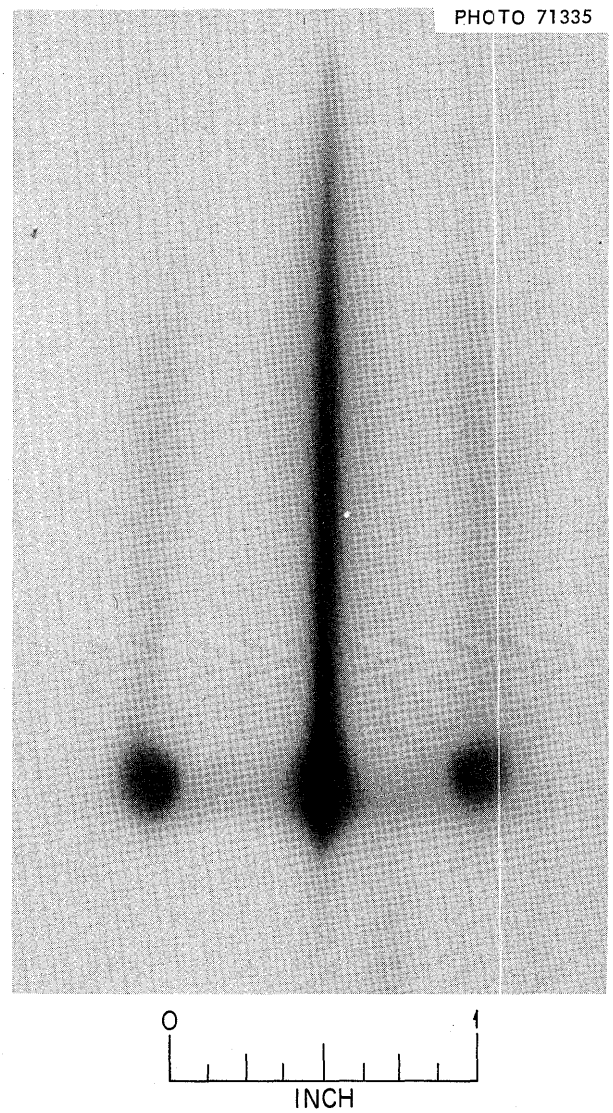

Fig. 4.6. Pinhole Images of Ion Orbits. The pinhole forming the center image was on the midplane. The other two were ½ in. off the midplane.

ORNL-DWG 64-11762

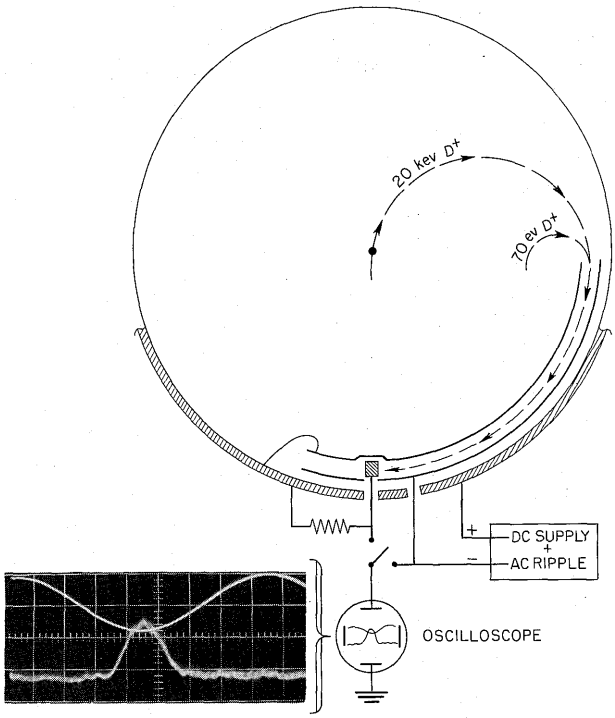

Fig. 4.7. Velocity Selector Schematic Diagram and Oscillogram. The sine curve gives the voltage on the velocity selector. The spread in accepted ion energy is about 10 ev.

PHOTO 65510

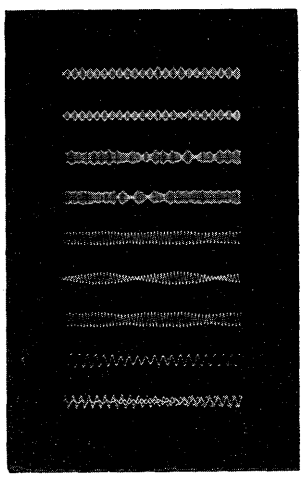

PERIOD	FREQUENCY
3 μsec	~ 7.7 Mc
3 μsec	~ 7.7 Mc
3 μsec	~ 7 Mc
3 μsec	~ 7 Mc
0.3 μsec	~ 166 Mc
0.3 μsec	~ 166 Mc
0.3 μsec	~ 166 Mc
0.12 μsec	~ 166 Mc
0.12 μsec	~ 166 Mc

Fig. 4.8. Radio-Frequency Radiation. Pickup was by an antenna outside the cavity. The oscillogram was made with a traveling-wave oscilloscope. The total period of each trace is indicated. The 7-Mc signal appears to be a beat between two signals near 166 Mc.

4.1.6 Plasma Potential Measurements

We measured the average plasma potential by observing the plasma lost to the end electrodes. Assume that the plasma is fully ionized, that is, only ions escape the cavity through the mirrors, and the escaping ions lose their energy on the end electrodes. The temperature rise and the cooling water flow rate to the end electrodes give the energy loss. Typically, the power lost in this manner is 10% of the input, or 0.7 kw. For an ion flux of 0.7 amp the average plasma potential must then differ from the end-plate potential by 1000 v. But the average end-plate potential is about 15 kv negative as measured by a resistor stack and meter. We therefore conclude that the average plasma potential in the working volume is several kilovolts negative. Probes in the cavity but outside the working volume receive 150- to 200-Mc signals with amplitudes of hundreds of volts, suggesting rather violent plasma agitation.

4.1.7 Neutron Emission

Neutron emission was first observed with a BF_3 counter, and the source strength was estimated to be about 10^5 reactions/sec. Nuclear track plates were used to observe recoil protons from the fast neutrons stopped in the plate. Analyses of the tracks were made by W. A. Woods[2] and indicated: (1) that the BF_3 counter is indeed correct – there are neutrons, and their source strength is about 10^5 reactions/sec; (2) their energy is 2.5 Mev, that is, they come from the D-D reaction; (3) they do not come solely from the cathode, which is incandescent from deuteron bombardment, but appear to arise all along the length of the plasma column, outside the mirrors as well as between the mirrors. We do not at present know whether the neutron source is the plasma, the anode walls, the anticathode end walls, or all three. A distribution of the recoil proton abundance vs energy from an analysis of the nuclear track plates is given in Fig. 4.9.

[2]Summer employee, Ohio Wesleyan University, Delaware, Ohio.

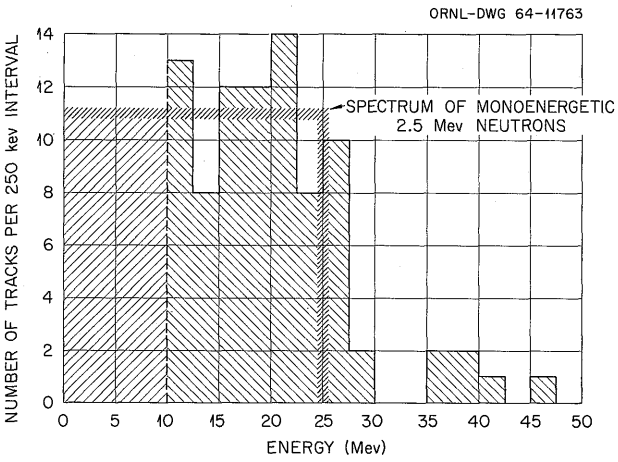

Fig. 4.9. Energy Distribution of Recoil Protons in a Nuclear Track Plate.

4.2 A SIMPLE MOMENTUM PROBE FOR PLASMA STUDIES

Igor Alexeff D. Montgomery[3]
W. D. Jones M. Rankin

The momentum probe, apparently a new device, is simply a bare wire placed in the plasma. If a high current is passed along the wire, the wire is surrounded by a magnetic field that repels charged particles, as shown in Fig. 4.10. The current of charged particles as a function of magnetic field gives information about the *momentum* distribution of the charged particles, and so the information obtained differs from that of the Langmuir probe, which studies the *energy* distribution of the charged particles.

The basic equation which governs the momentum probe is

$$B = \frac{mvc}{er_w \ln (r_c / r_w)} . \qquad (1)$$

Here, B is the magnetic field (gauss) at the surface of the probe required just to prevent the charged particle from reaching the probe, m is the mass of the particle (g), and v is the velocity of the particle (cm/sec). We assume that the particle initially is directed normally toward the wire. The constant c is the speed of light (cm/sec), e is the charge of the particle (esu), r_w is the radius of the wire (cm), and r_c is the effective range of the magnetic field (cm). In vacuum conditions r_c corresponds to that distance from the probe at which the magnetic field drops off faster than the r^{-1} dependence caused by a straight wire. If the probe is a wire loop, r_c is about twice the loop radius. Beyond this distance, the magnetic field begins to drop with the r^{-3} dependence of a dipole. Note how the magnetic field given by Eq. (1) depends on the product of mv, or on the *momentum* of the charged particle.

Our Eq. (1) is inexact, because we have assumed that the charged particles are monoenergetic and are directed normally toward the wire. To be more accurate, one must assume that the charged particles beyond the magnetic field cutoff, r_c, have a Maxwellian distribution and are moving in random directions. One must then solve for the flux of particles reaching the wire as a function of magnetic field. We have been able to solve this problem for an arbitrary magnetic field and for an arbitrary electrostatic potential on the wire. Unfortunately, the solution cannot be obtained in analytic form, but must be found by a digital computer.

The solution for two different magnetic field cutoff distances is shown in Fig. 4.11. In this case, we have assumed that the probe is at the plasma potential. The current density of charged

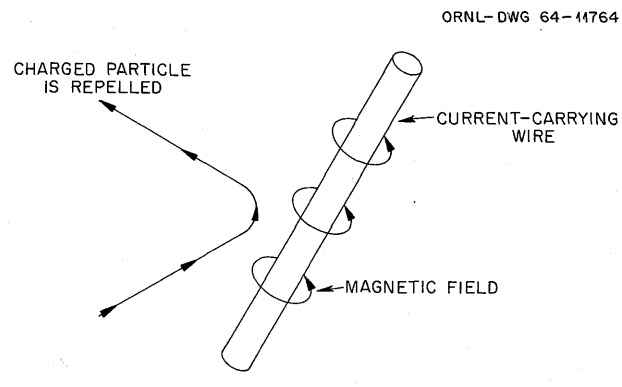

Fig. 4.10. Principle of Momentum Probe. A wire carrying a strong current reflects charged particles.

[3]Consultant from the University of Maryland.

particles in reduced units is plotted as a function of the magnetic field, also in reduced units. The surprising feature of the two reduced curves is that they almost coincide. The curve $r_c/r_w = 1.05$ corresponds to a magnetic shell extending only 5% further than the radius of the wire – in other words, to a case of plane geometry. The curve $r_c/r_w = 100$ corresponds to cylindrical geometry. Thus, the momentum probe essentially has only one free variable, the reduced magnetic field B_r. We also computed six other curves having r_c/r_w between the above limiting values, and all the resultant curves fell between those given in Fig. 4.11.

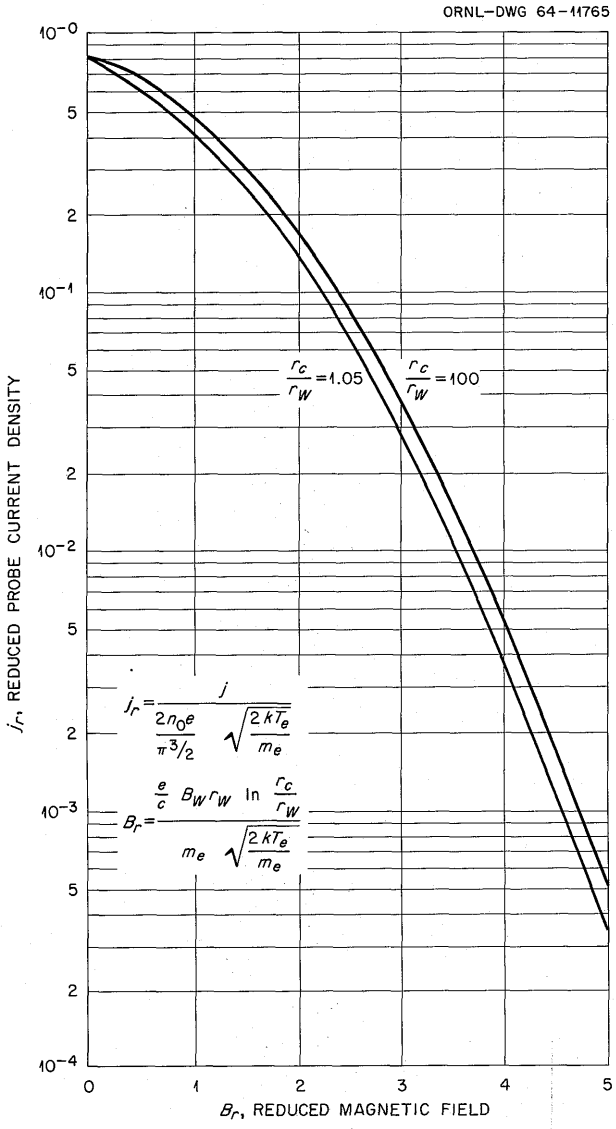

Fig. 4.11. Computed Momentum Probe Response. The variables are as follows: j is electron current density (amp/cm^2), n_0 is electron density (cm^{-3}), e is the electron charge (coulombs), k is Boltzmann's constant (ergs/ev), T_e is electron temperature (ev), m_e is the electron mass (g), c is the speed of light (cm/sec), B_w is the magnetic field at the surface of the wire (gauss), and r_c and r_w are the radii of the magnetic field cutoff, and the surface of the wire, respectively, in centimeters from the center of the wire.

An experimental test of the momentum probe was made using the apparatus shown in Fig. 4.12. Here, a plasma was made using a simple discharge tube. The momentum probe was a simple loop of No. 10 copper wire, fed by an ordinary soldering gun. The larger models of these guns, when matched to the load, are capable of producing peak currents of about 3000 amp. Our small model produced about 500 amp. Heating of the probe wire was not serious as long as the operating period was less than a few seconds. The momentum probe was biased to plasma potential by the battery shown in Fig. 4.12. Both a hot probe and a cold, Langmuir probe (not shown) were used to determine the plasma potential, the electron temperature, and the electron density.

The results of the experimental tests are shown in Fig. 4.13. The upper ac trace in Fig. 4.13*a* corresponds to the magnetic field, and the lower ac trace corresponds to the electron current

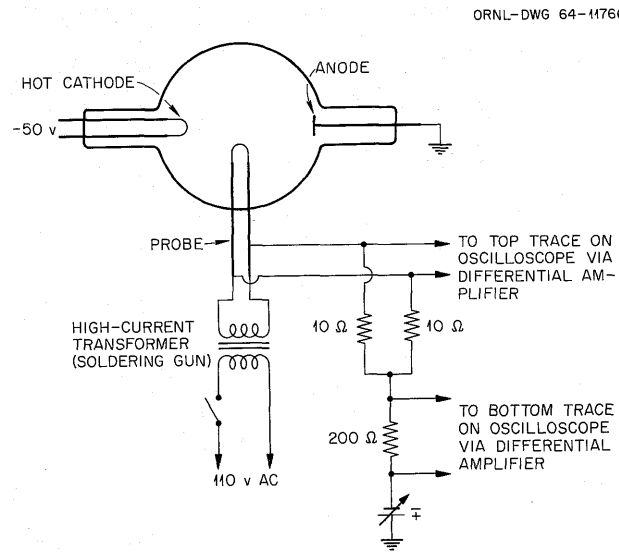

Fig. 4.12. Discharge Tube with Momentum Probe – Schematic of Apparatus.

collected by the momentum probe. At zero magnetic field, the electron current is at a maximum. Note how the electron current drops to zero as the magnetic field increases, regardless of the polarity of the field. In Fig. 4.13*b* the characteristic curve of the momentum probe is represented. Thus qualitatively, the momentum probe appears to work.

PHOTO 65666

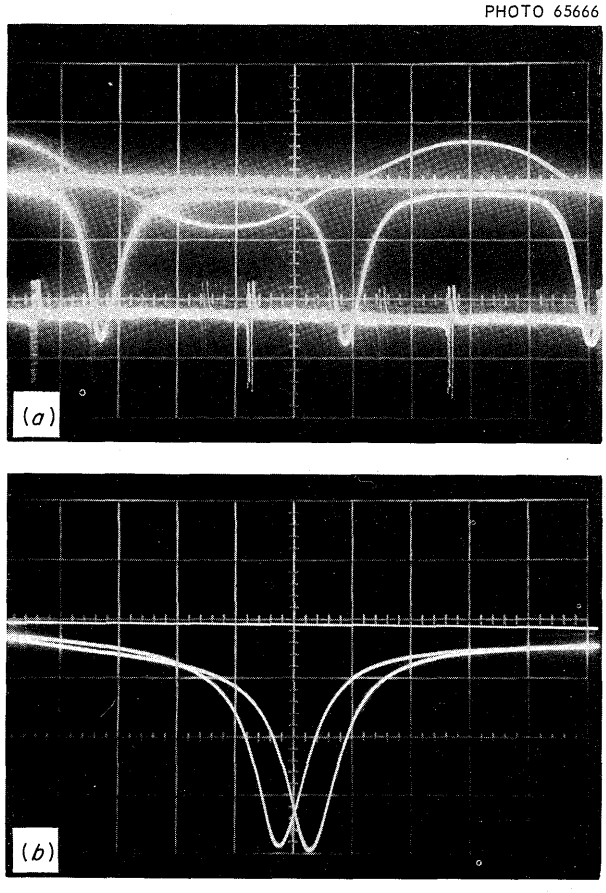

Fig. 4.13. Discharge Tube with Momentum Probe – Experimental Results. *Top:* The upper ac trace represents the magnetic field; the lower ac trace represents the electron current. Note how the electron current trace rises to zero whenever the magnetic field becomes appreciable. (Electron current produces downward deflection.) The upper straight line represents zero electron current and zero magnetic field, and the lower, the steady-state electron current with no magnetic field. *Bottom:* The characteristic curve of the momentum probe is shown. Horizontally, the magnetic field is plotted, increasing in either direction from the center line. Vertically, the electron current is plotted downward from the bright line representing zero.

To use the momentum probe as a quantitative tool for studying plasma electrons, one must take the characteristic curve for the electron gas, shown in Fig. 4.13*b*, and fit to this curve the reduced curves of Fig. 4.11. If one knows r_c, one can determine n_0 and T_e, the electron density (cm^{-3}) and temperature (ev) respectively. However, if we assumed that r_c corresponds to the distance at which the magnetic field departs from an r^{-1} dependence, then we obtained electron temperatures that were too high by a factor of about 200.

To resolve the problem of why the electron temperatures given by the momentum probe were too high, we examined Eq. (1). We observe that we can compute B and v, and we know the values of m, c, e, and r_w. Therefore, the only possible source of error was in using the wrong value for r_c. We next inverted our diagnostic process and, using the values of T_e and n_0 as found by the Langmuir probe, computed r_c.

The results of r_c, as found from a series of experimental runs, are plotted in Fig. 4.14. Data were obtained for all the inert gases. As shown by Fig. 4.14, the experimental values of r_c are much smaller than the magnetic field cutoff – that distance at which the magnetic field of the momentum probe begins to drop off faster than as r^{-1}. Also, the experimental values of r_c are much greater than the mean spacing of the electrons and the mean electron–gas-molecule spacing.

When an experimental value of r_c is compared with the Debye distance, then good agreement is found. As shown in Fig. 4.14, each run is represented by a vertical line segment. At one end of each segment lies the experimental value of r_c; at the other end, the Debye distance. One notes first, that the lengths of the line segments are generally less than 2 on this logarithmic scale and second, that when the Debye distance is large, r_c is large and conversely. Thus, the momentum probe apparently is measuring the *Debye distance.*

That the momentum probe is measuring the Debye distance is tentatively explained as follows: as pointed out by J. L. Tuck, of Los Alamos Scientific Laboratory,[4] the magnetic field of our device cannot reflect ions, since ions have too much momentum. However, in a plasma, charge

[4]Private communication.

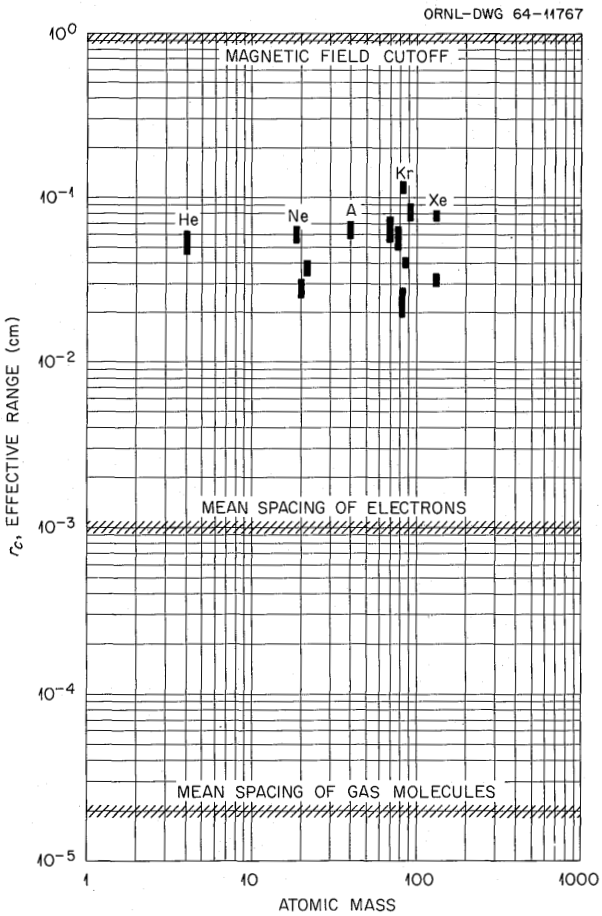

Fig. 4.14. The Experimentally Obtained Values for r_c as Compared with Various Distances in the Apparatus. The length of each vertical line segment corresponds to the discrepancy between the computed value of r_c and the Debye distance in that given run.

neutrality must be maintained; therefore, the ions drag electrons with them across the magnetic field. At approximately one Debye distance from the wire, the restriction that the plasma be electrically neutral breaks down, and the electrons must find their way across this narrow gap without help from the ions.

4.3 A SAMPLING OSCILLOSCOPE AS A COHERENT DETECTOR

Igor Alexeff W. D. Jones

A sampling oscilloscope can easily be used as a coherent detector. With this device, the signal-to-noise ratio of a repeated pulse of arbitrary shape easily can be enhanced by a factor of 100 or more.

The basic principle of a coherent detector is simply the addition of many signals.[5] The desired response must always occur at the same time and have the same phase. Under this restriction, the sum of n desired responses is n times a single desired response. However, the noise follows a different addition law, since the noise is both random in time and in phase. For noise, the sum of n responses is approximately $\sqrt{n}$ times a single response. Thus, by adding n signals containing both the desired response and noise, the signal-to-noise ratio is increased by $\sqrt{n}$. If n is 10^4, a value easy to obtain in practice, then the increase in signal-to-noise ratio is 100.

In our early work, we used a coherent detector made from a Tektronix dual-trace type CA preamplifier. Following the suggestions of A. Garscadden and P. Bletzinger of the Wright-Patterson Air Force Base, we are now using a Tektronix 561A oscilloscope, which has the advantage of being much more free of drift than the earlier device. A diagram of the coherent detector is shown in Fig. 4.15. Our discussion refers to the Tektronix 561A oscilloscope simply because we are familiar with this unit.[6] Presumably, any other oscilloscope having the desired features can also be used.

The coherent detection system operates in the following manner. The desired signal is fed into the upper trace of a dual-trace oscilloscope (a Tektronix 3S76 plug-in unit). In this case, the signal was obtained from a plasma wave arriving at a detector. A triggering signal was obtained from the pulse that produced the wave and was fed to the sampling sweep unit (a Tektronix 3T77 plug-in unit). The sampling sweep unit is equipped with a control for manually scanning the sampling position. Thus, if one has a sweep of 10 μsec duration, he can set the sweep unit to sample the signal at any desired position in time, for example, 3.2 μsec after the arrival of the trigger pulse at the sweep unit. Every time the oscilloscope is triggered, the signal is sampled 3.2 μsec after the trigger pulse.

---

[5] M. P. Klein and G. W. Barton, Jr., *Rev. Sci. Instr.* **34**, 754 (1963).

[6] Tektronix, Inc., P.O. Box 500, Beaverton, Ore.

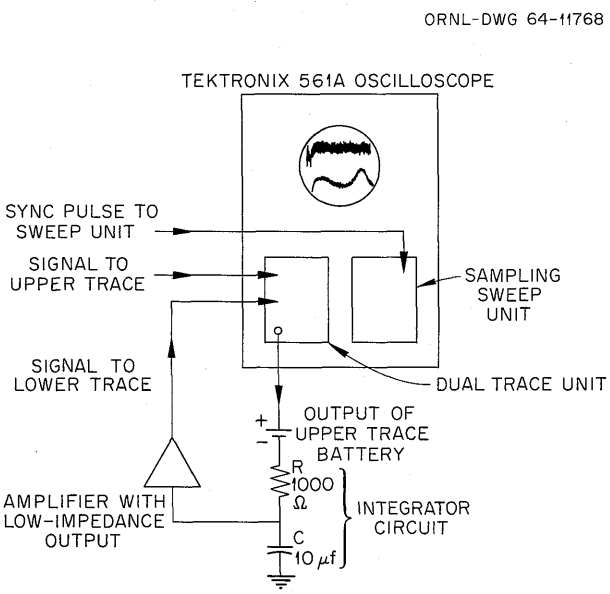

Fig. 4.15. Diagram of Coherent Detector.

Now, the dual-trace sampling unit has an output jack, at which one finds a voltage that corresponds to the voltage of the signal at the moment when the sampling sweep unit obtained a sample. Let one integrate this voltage in time by means of the simple resistor-capacitor network shown in Fig. 4.15. If the resistor-capacitor network has a time constant corresponding to the time in which, for example, 10^4 oscilloscope sweeps occur, then the output voltage of the network is proportional to the average voltage of 10^4 samples.

Incidentally, the dual-trace sampling unit superimposes the sampled signal on a dc potential. The dc potential is removed by the battery shown in Fig. 4.15.

Now, the output voltage of the resistor-capacitor network refers to the average value of the input signal at only one point in time, in our example, 3.2 μsec after the trigger pulse. To obtain the complete noise-free oscilloscope trace, one must plot the output voltage of the resistor-capacitor network as a function of the time between the trigger pulse and the moment at which sampling occurs. This plot of voltage vs time is most conveniently made on the lower trace of the same sampling oscilloscope. Since the output of the resistor-capacitor network is at high impedance (little current available) and the dual-trace sampling unit has a low-impedance input (much current is required to produce a response), a dc amplifier must be used to couple the two components. (Probably, the standard Tektronix P 6032 cathode-follower probe would work well, but the authors used a Tektronix type O unit that was on hand with a Tektronix type 132 power supply.)

The upper trace of the sampling oscilloscope now displays a vertical series of dots, corresponding to the sampled, noisy signal at the sampling position of 3.2 μsec after the trigger pulse. The lower trace displays a fairly steady single dot, proportional to the time average of the upper trace. By manually changing the time at which the sample is being taken, one finds that the spot of the lower trace plots out the desired, coherently detected signal. The upper trace reproduces the original noisy signal. The upper and lower oscilloscope traces are easily photographed with a time exposure. An example is shown in Fig. 4.16. Note the significant improvement in the signal-to-noise ratio.

To manually change the time at which the samples are being taken, one merely turns the appropriate dial on the Tektronix 3T77 sampling sweep unit. The time can also be changed by changing a dc voltage, which is applied to the appropriate pair of input terminals of the sampling sweep unit. One must be careful to change the time at which the sampling occurs slowly enough that the resistor-capacitor network can follow

PHOTO 68009

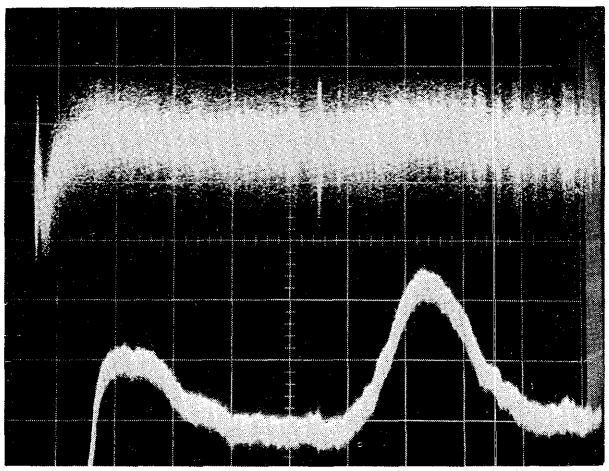

Fig. 4.16. Results of Coherent Detection. Upper trace, direct signal; lower trace, coherently detected signal. The theoretical improvement in signal-to-noise ratio is 33 to 1.

changes in the shape of the coherently detected signal. Thus, if the resistor-capacitor network has a time constant of 0.1 sec, then one should move the spot at which sampling is occurring from one end of the oscilloscope screen to the other in no less time than about 1 min.

Our coherent detector is equipped with a resistor-capacitor network having an integrating time of 0.1 sec. At the slowest sweep rate provided by the Tektronix 3T77 sampling unit (100 μsec/sweep), this integrator averages over 10^3 samples and produces an improvement in the signal-to-noise ratio of about 32. At faster sweep rates, the sampling rate is increased and the signal-to-noise ratio is correspondingly better.

There seems to be no reason why this coherent detector cannot operate up to the maximum frequency limit at which a sampling oscilloscope can operate. This coherent detector has proved to be very easy to construct, drift free, and reliable.

4.4 IONIC-SOUND-WAVE TIME-OF-FLIGHT MEASUREMENTS IN QUIESCENT PLASMAS

Igor Alexeff W. D. Jones

We have continued our time-of-flight measurements of ionic-sound-wave propagation in rare-gas discharges. Due to much quieter plasmas and to improved as well as different ion-wave production and detection techniques, the present results are much more accurate and clear-cut than those reported previously.[7] Also, new information has been acquired. From the present measurements we have been able to evaluate rather accurately the following four properties of the waves and of the plasmas: (1) the velocity of the waves as a function of ionic mass and electron temperature; (2) the value of γ, the adiabatic compression coefficient of the electron gas; (3) the thickness of sheaths on the emitting and detecting ion-wave probes; and (4) the radial drift velocity of the plasma to the walls of the container.

Figure 4.17 shows the apparatus used in our time-of-flight measurements. The measurements were made in a spherical, glass discharge tube about 20 cm in diameter, with background gas pressures ranging from 1 to 20 μ. The plasma in which the waves were propagated was a diffusion-type plasma, being formed from the main discharge produced between the anode and cathode, seen at the right-hand side of the tube. The anode was made of a stainless steel mesh, the mesh spacing being smaller than the Debye distance of the plasma. The diffusion plasma was thus isolated from electrical disturbances in the main discharge, and we found it to be very quiescent.

The ionic sound waves were propagated between the two negatively biased movable probes shown in Fig. 4.17. The waves were generated at the upper probe by a pulser which changed the potential of the probe for a period of a few microseconds. We generally used a negative pulse of approximately 250 v, although smaller negative pulses as well as positive pulses produce similar results.

The arrival of the ion wave at the negatively biased second probe was evidenced by a perturbation of the ion current to this probe. The perturbation was then amplified and displayed on an oscilloscope, the sweep of which had been triggered by the initial driving pulse applied to the

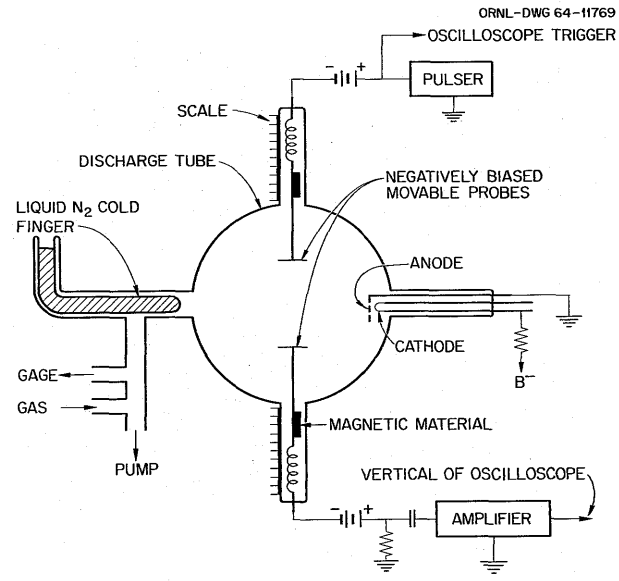

Fig. 4.17. Apparatus Used in Time-of-Flight Studies.

[7] I. Alexeff and W. D. Jones, *Comptes Rendus de la VIe Conference Internationale Sur Les Phenomenes D'Ionization Dans Les Gas*, ed. by P. Hubert and E. Cremieu-Alcan (SERMA, Paris, 8–13 Juillet, 1963), vol. III, p. VI 36; also, Igor Alexeff and W. D. Jones, *Thermonuclear Div. Semiann. Progr. Repts. Apr. 30, 1963*, ORNL-3472, p. 45, and *Oct. 31, 1963*, ORNL-3564, p. 55.

upper probe. The time-of-flight measurements consisted in recording the spacing between the probes and the corresponding time elapsing between the driving pulse and the detected signal on the second probe.

Electron temperatures were measured by means of a swept Langmuir probe,[8] which is not shown in the diagram.

The liquid-nitrogen cold finger was used to improve the purity of the plasma. The ultimate low pressure in the system was better than 1×10^{-6} torr.

Despite the fact that we were working with a quiescent plasma and could therefore detect very weakly transmitted ion-wave signals, generally for propagation distances of over a few centimeters it was not possible to detect the signals by ordinary means. To see the weaker signals, we found it necessary to use coherent noise-rejection techniques.[9]

Figure 4.18 shows the type of perturbation in the ion current which occurs when the propagating ion wave hits the negatively biased second probe. Figure 4.18*a* represents propagation over a path length of a few centimeters and shows detection without noise-rejection techniques; Figure 4.18*b* is for propagation over a larger distance and shows detection both without and with noise rejection. Even though the coherent noise rejector was not adjusted for optimum performance when these data were taken, the capability of the technique for increasing the signal-to-noise ratio for repetitive phenomena is clearly evident.

The ion-current perturbations seen in Fig. 4.18 were produced by using negative-voltage driving pulses on the emitter probe. It was found that when positive-voltage pulses were used, the appearance of the ion current perturbation was inverted relative to that produced by the negative-voltage pulses. This is not surprising, since in one case the leading edge of the wave should produce a compression in the ions, whereas in the other case the leading edge should produce a rarefaction. In fact, this behavior further substantiates the belief that we are observing ionic-sound-wave phenomena.

Figure 4.19 shows plots of some of the time-of-flight measurements. On the vertical scale is plotted the separation of the movable probes; on the horizontal scale is shown a plot of the corresponding wave-propagation time, the propagation time being measured from the beginning of the driving pulse on the first probe until the signal is first detected on the second probe. A line of best fit is drawn through each set of points.

[8]Igor Alexeff and W. D. Jones, *Thermonuclear Div. Semiann. Progr. Repts. Apr. 30, 1963*, ORNL-3472, p. 47, and *Oct. 31, 1963*, ORNL-3564, p. 62.

[9]This report, sect. 4.3.

PHOTO 68010

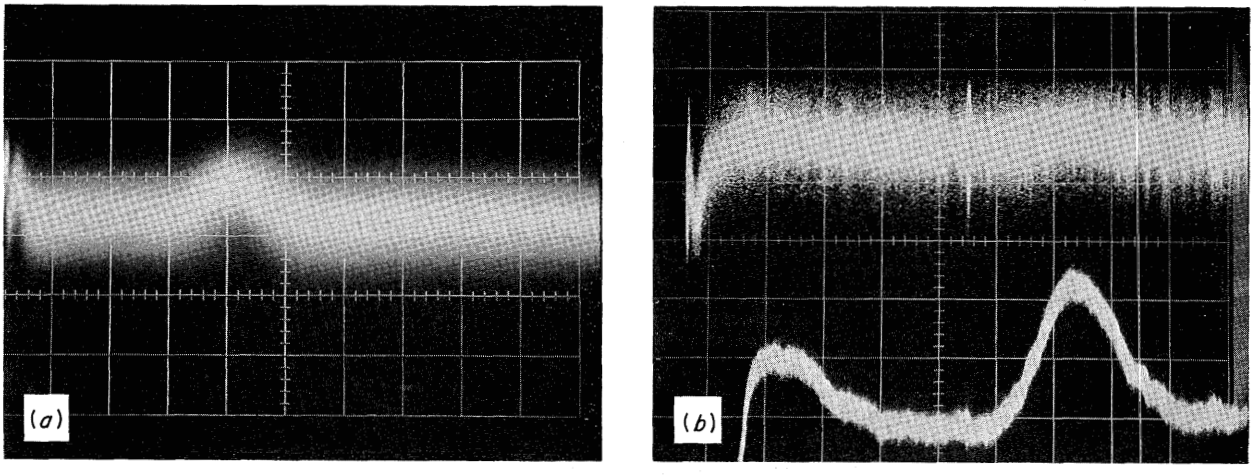

Fig. 4.18. Ionic-Sound-Wave Signal Detection in Argon. Pressure, 6 μ Hg; sweep, 5 μsec/cm. (*a*) Without coherent noise rejection (propagation path length, 5 cm); (*b*) without and with noise rejection (propagation path length, 8 cm).

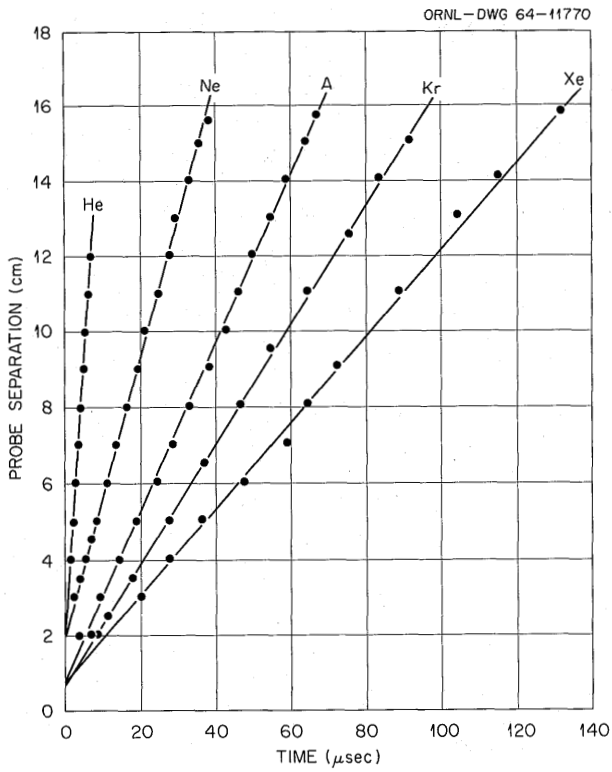

Fig. 4.19. Probe Separation vs Propagation Time.

Two things can be seen immediately from these plots. First, for a given plasma the velocity of the wave, which is given by the slope of the line, is quite constant and independent of probe spacing. Second, extrapolation of the curves gives a finite probe separation at $t = 0$. This would seem to be evidence for the presence of sheaths on the probes. The total thickness of these sheaths is seen to range from about 0.7 to 2 cm.

Under the conditions of these experiments the theoretical velocity of the ionic sound waves is given by the Langmuir-Tonks formula,[10]

$$v = \left(\frac{\gamma k T_e}{m_i} \right)^{1/2} . \qquad (1)$$

Here k is Boltzmann's constant, T_e is the electron temperature, m_i is the ionic mass, and γ is the adiabatic compression coefficient of the electron gas. Theoretically, for our experiments γ should be 1, $5/3$, or 3. Since we know m_i and can measure T_e, we can use our experimental velocities to obtain an estimate of γ for these experiments.

By the use of T_e values obtained from the swept Langmuir probe, we obtain the values of γ shown in Fig. 4.20. Within the accuracy of the data, γ seems to be 1. In other words, at these low pressures we seem to have a collisionless plasma. Since we can determine the wave velocity fairly accurately, the major uncertainty in the correct value of γ arises from the uncertainty in the determination of T_e from the Langmuir probe measurements.

It is interesting to try to give a theoretical explanation of the probe sheaths and to make an estimate of their thickness. From the Langmuir probe curves, we can determine values for both the electron temperature and the density of the plasma. Knowing these quantities, we can calculate the Debye length for the plasma. The Debye length is the distance from a surface in contact with the plasma at which the potential seen by a test particle is down to $1/e$ of the value at the surface. If the potential of the surface is known, then we can calculate the number of Debye lengths required to get the potential down to a given value. In the present experiments the negative dc bias on each of the two probes was approximately 75 v. In addition, there was a negative driving pulse on the emitting probe of approximately 250 v.

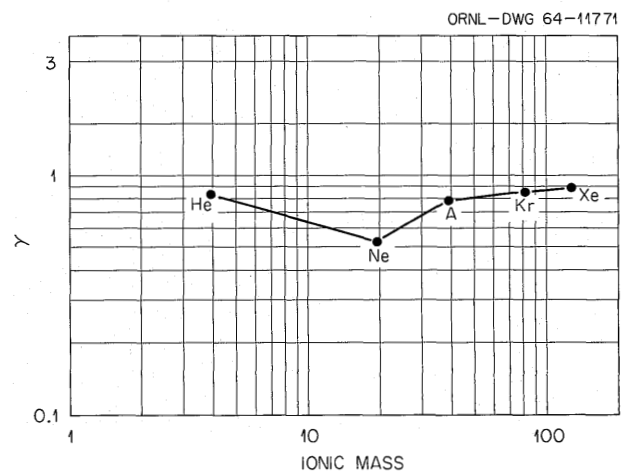

Fig. 4.20. Value of γ vs Ionic Mass.

[10] L. Tonks and I. Langmuir, *Phys. Rev.* **33**, 195 (1929).

Figure 4.21 shows the values of the sheaths observed experimentally – using a least-squares fit to the data points – as well as two sets of sheath sizes estimated theoretically. If we assume that the voltage perturbation reaching out into the plasma must be at least as large as the thermal energy of the electrons, in order to produce or detect an ionic sound wave, then we obtain the sheath sizes given by the lower set of points. If we assume, however, that an ion wave can still be influenced by a voltage perturbation as small as the ion thermal energy – assumed to correspond to room temperature – then the thicker sheaths given by the upper set of theoretical points result. The actual sheath sizes appear to be somewhat greater than these two sets of values.

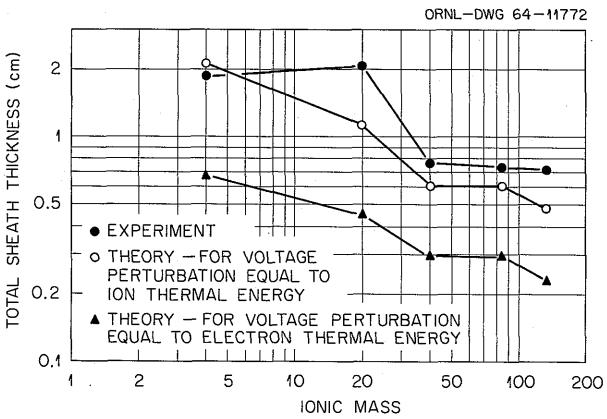

Fig. 4.21. Sheath Thickness vs Ionic Mass.

It was found that, unless the two probes were placed symmetrically with respect to the center of the discharge tube, the propagation times between the probes were not equal upon interchange of the roles of emitter and detector. Figure 4.22 shows such an asymmetry in the propagation times. This was for wave propagation between a probe located at the center of the tube and one located near the tube wall. Figure 4.22*a* represents propagation from the center probe to the wall probe, in the direction of plasma drift, while Fig. 4.22*b* is for propagation in the opposite direction, against the plasma drift. The Doppler shift in the propagation velocity gives the drift velocity of the plasma to the walls. The value obtained, 2.2×10^4 cm/sec, is only about 19% of the ionic-sound-wave velocity but corresponds to the drift velocity, 1.4×10^4 cm/sec, of thermal ions at room temperature.

Figure 4.22 shows detection both without and with noise rejection. The noise rejection circuit used here involved a gated amplifier constructed from a modified Tektronix preamp,[9] and the traces show evidence of the dc drifting which plagued this particular circuit. The sweeping of the gate for the rejection circuit was done manually and had to be slow enough to accommodate the 0.1-sec time constant of the integrating circuit. The center of the three lower traces in Fig. 4.22*b* was swept from right to left and shows evidence of having been swept too rapidly near the detected ion wave signal.

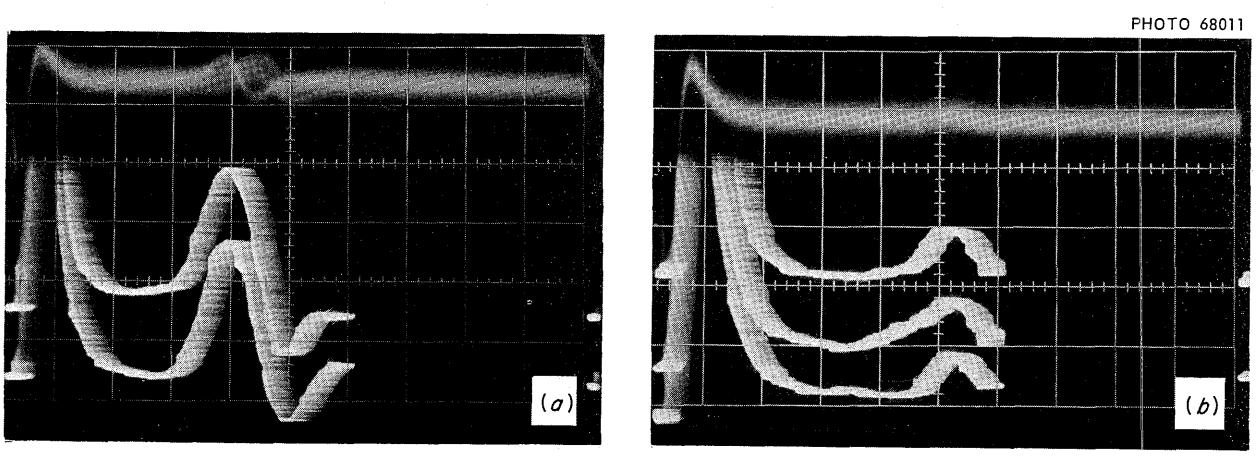

Fig. 4.22. Doppler-Shifted Ion-Wave Propagation in Xenon. Pressure, 3 μ Hg; propagation distance, 9 cm; sweep, 20 μsec/cm. (*a*) Propagation from center probe to wall probe; (*b*) propagation from wall probe to center probe.

4.5 BEAM STABILIZATION IN THE CALUTRON

E. D. Shipley O. C. Yonts
A. M. Veach[11] W. A. Bell[11]
R. N. Goslin[12]

Studies of the effect of boundary condition on beam focus have been continued in the calutron. As suggested in previous reports,[13] a comparison between the flat plate wall and the boundary impedance network (BIN), shown in Figs. 4.23 and 4.24, has been made. Curves of beam imperfection (defined for a given e/m as the ratio of the total beam current to the beam current that enters the collector slit) as a function of spacing with pressure as a parameter were obtained with both types of wall. The family of curves for the flat plate are shown in Fig. 4.25 and for the boundary impedance network in Fig. 4.26.

Some general observations about certain features of these interesting graphs are evident. The graphs show that either boundary wall treatment extends the pressure range where the beam imperfection (BI) value remains in the operable range of ~ 1.2. This extension of the operable pressure holds for a variety of positions of the boundary surface walls with respect to the beam. Another interesting feature of these two three-dimensional graphs of the performance of flat plate and the BIN wall treatment is the intermediate range of pressures around 200 μa ion-gage reading or $\sim 3.4 \times 10^{-4}$ torr, where the BI value departs markedly from the value of ~ 1.2 when the separation is 6 in., and then this value again approaches ~ 1.2 as the separation of boundary surfaces reaches 10 in. Beyond these pressures neither treatment achieves any improvement of beam quality. The low-pressure limit has not yet been determined. If it exists, it must be below 5×10^{-7} torr.

R. L. Hill, H. C. Hoy, H. L. Huff, R. L. Johnson, K. A. Spainhour, R. A. Strehlow, and J. P. Wood have made many creative contributions which have served as a constant source of inspiration throughout the course of these experiments.

[11]Isotopes Division.

[12]Consultant, Oglethorpe University, Atlanta, Ga.

[13]*Thermonuclear Div. Semiann. Progr. Rept. Apr. 30, 1964*, ORNL-3652, sect. 4.5.

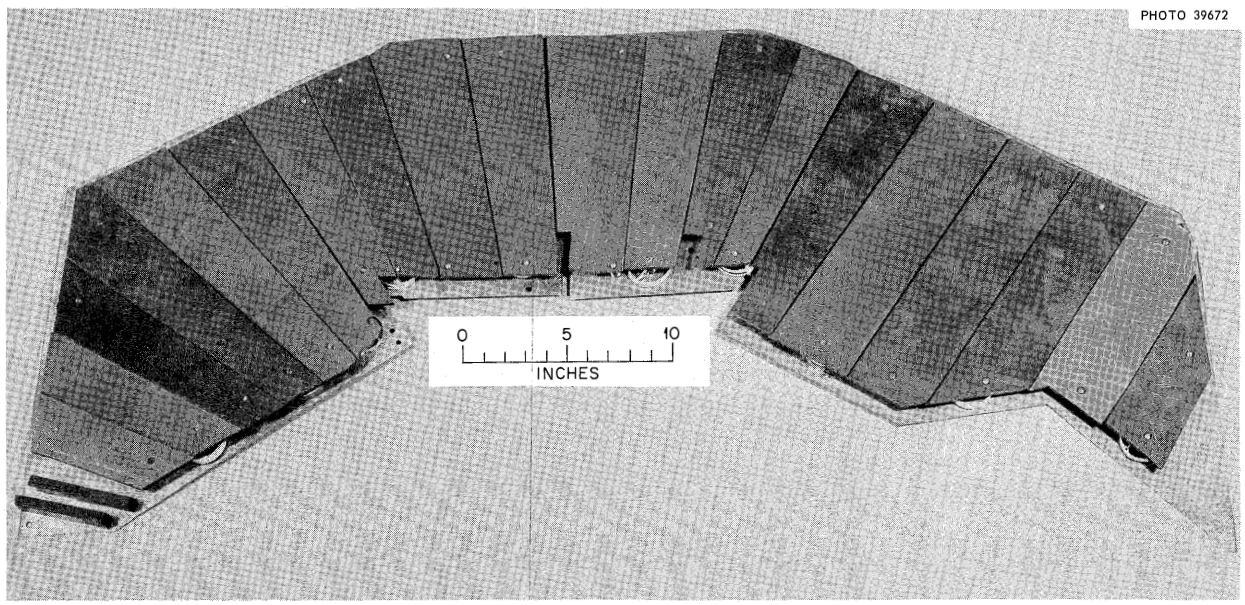

Fig. 4.23. Segmented Plate Boundary Wall Treatment, or BIN.

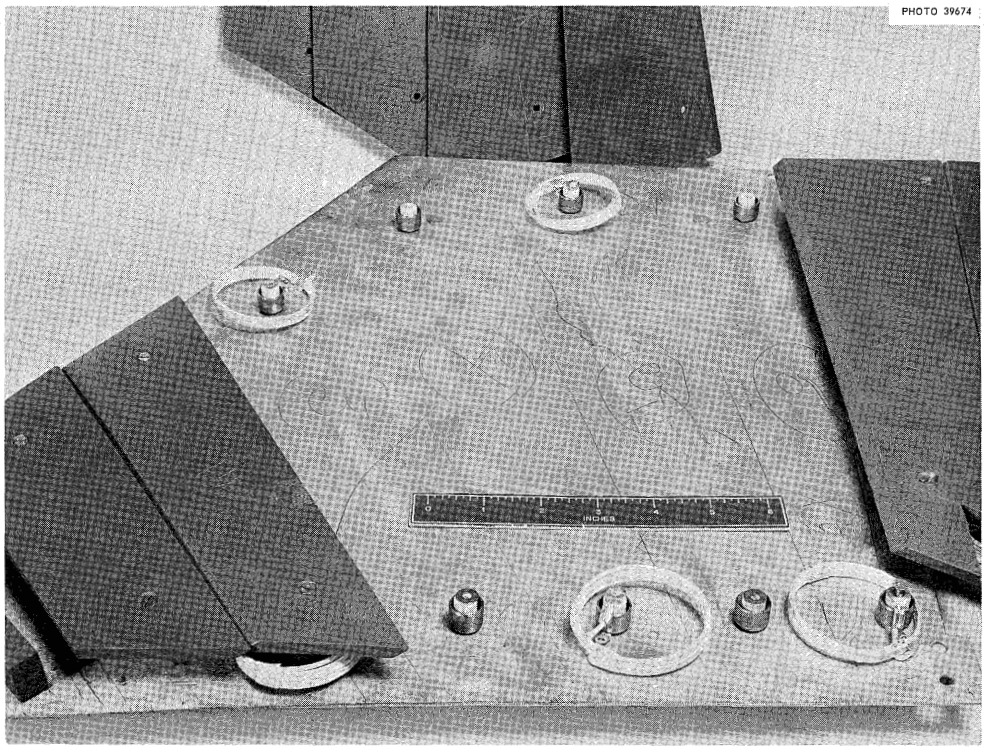

Fig. 4.24. Detailed View of Segments and Coil Position of BIN.

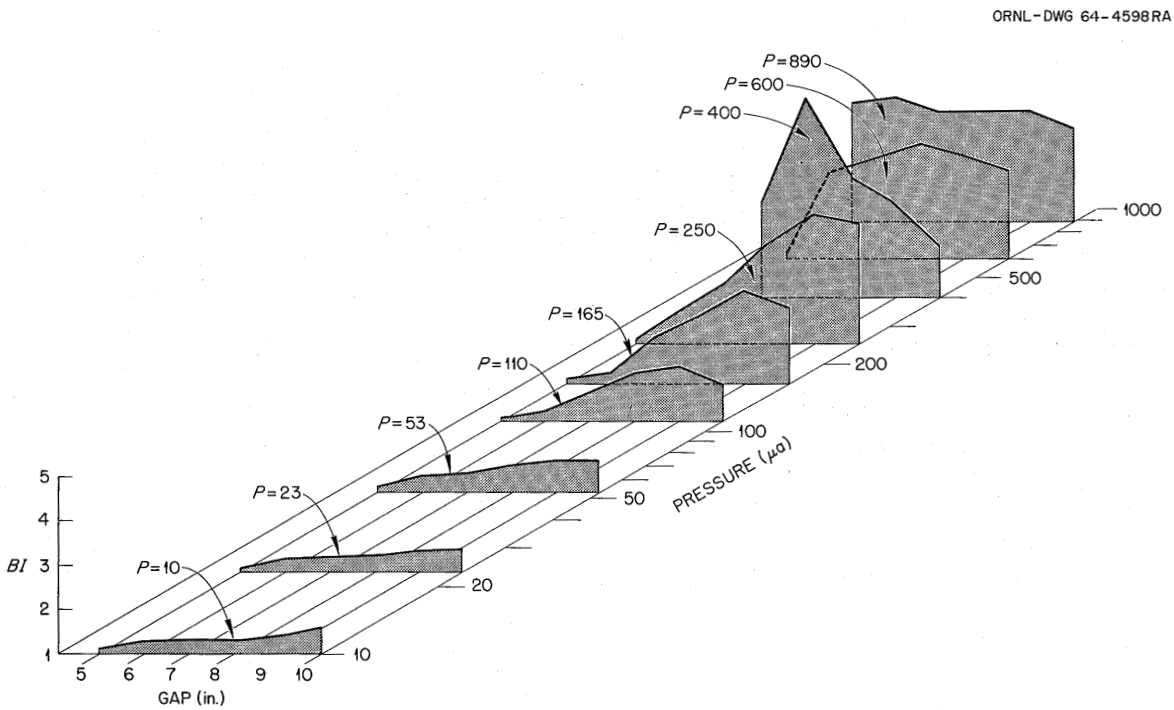

Fig. 4.25. Beam Imperfection as a Function of Position of Flat Plate Surfaces and Environmental Gas Pressure.

ORNL-DWG 64-4599RA

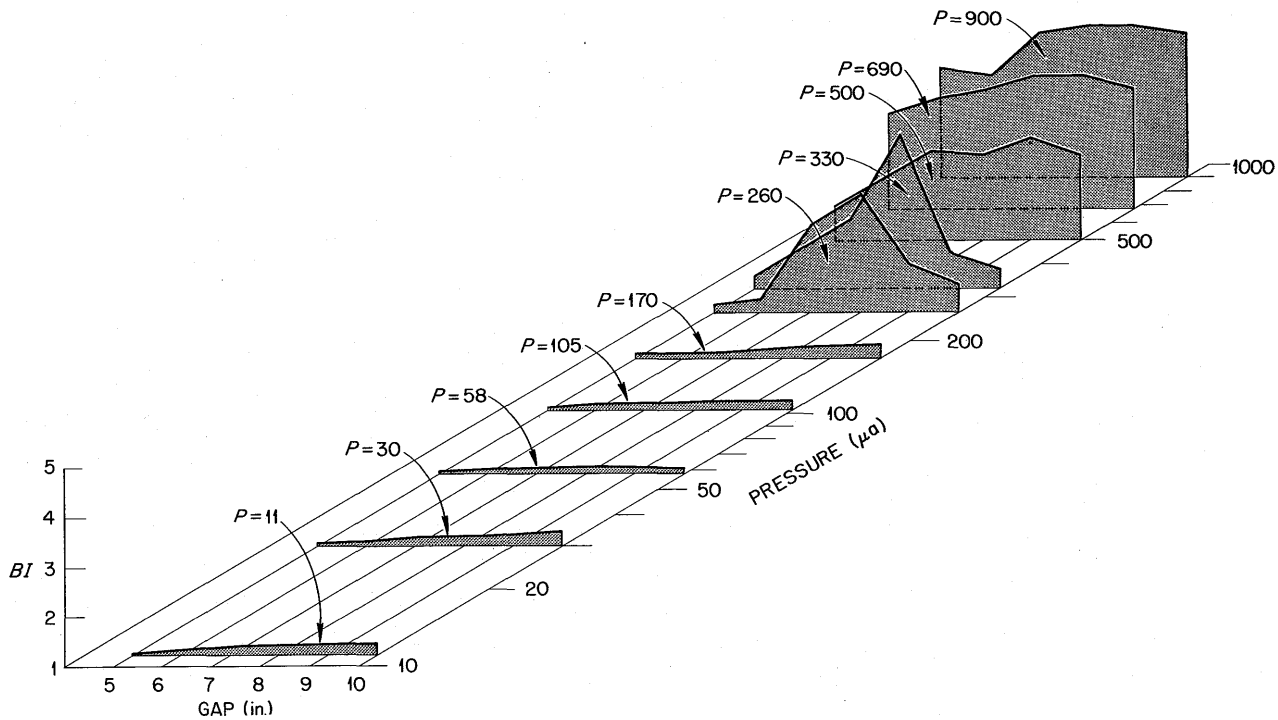

Fig. 4.26. Beam Imperfection as a Function of BIN Surfaces and Environmental Gas Pressure.

4.6 THE BEAM PLASMA FACILITY

J. W. Flowers[14] M. R. Skidmore
V. J. Meece W. L. Stirling

The Beam Plasma Facility has recently been adapted to test a scaled-up version of the reflex discharge experiment of Neidigh.[15] The primary goal of the experiment was to determine the origin of the neutrons observed when operating the discharge with deuterium gas. The mirror ratio of the facility is 2:1, with a maximum axial field at midplane of 10 kilogauss. The separation between mirrors is approximately 67 in.

Three different anode geometries have been tried. The first consisted of a 1-in.-ID copper tube. The inner diameter of the anode end plates was ½ in. The end plates were positioned in the center of the mirrors with the cathode and anticathode about 2 in. from their respective end plates, thus making the separation between cathode and anticathode about 70 in. Gas feed rates between 1 cm^3 in 100 sec and 1 cm^3 in 150 sec gave the required pressure of 10^{-2} to 10^{-3} torr in the anode enclosure. Operation with this anode structure at about 10 kv accelerating potential did not yield any neutrons. However, energetic x rays were produced in abundance.

The second anode geometry tested is shown in Fig. 4.27. The end-plate apertures were increased to ⅝ in. in diameter, and the central anode region was increased to 4 in. in diameter. A gas feed rate of 1 cm^3 in 60 to 80 sec was required to produce the desired pressure in the anode region. A summary of the results obtained can be found in Table 4.1.

The highest neutron counting rate was achieved at a gas feed of 1 cm^3 in 60 sec, the neutrons being monitored in a paraffin-moderated BF_3 detector located between the cathode and anticathode outside the vacuum chamber about 30 in.

[14]Consultant, University of Florida.

[15]This report, sect. 4.1.

from the discharge column. The condition of "burnout" described by Neidigh and Alexeff was not achieved at power inputs up to 25 kw. A Jarrell-Ash Ebert spectrometer, model 82000, was used to measure the relative intensities shown in the figure. The nitrogen obviously originated in the background gas. Only one rf peak was observed on the spectrum analyzer. This peak fell between 9 and 11 Mc for maximum neutron counting rate. Frequencies higher than 22 Mc were not monitored. Six nuclear track plates were positioned along the axis of the

ORNL-DWG 64-11773

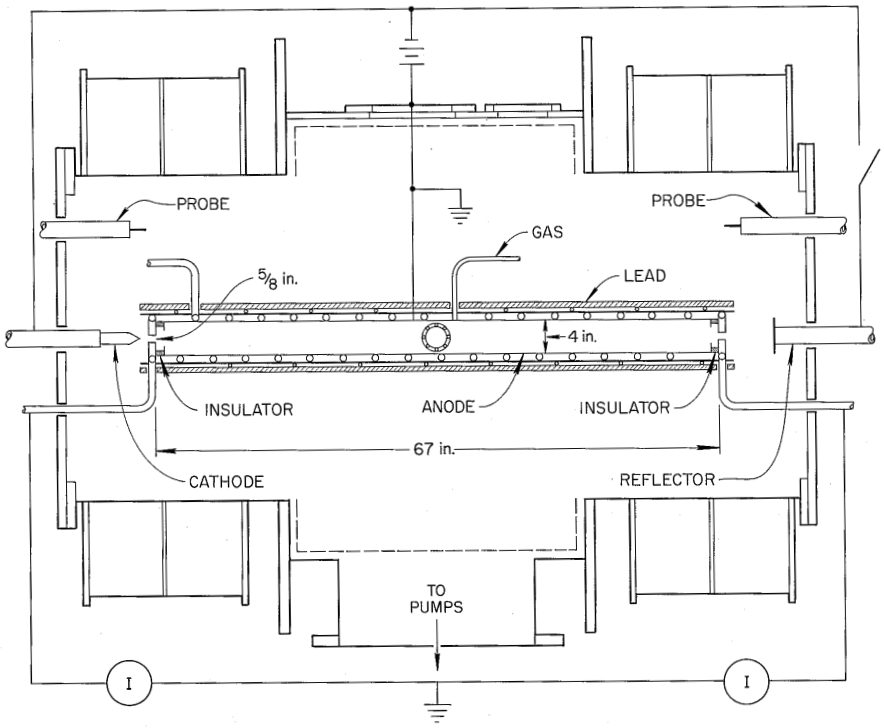

Fig. 4.27. Schematic of Beam Plasma Apparatus with 4-in.-diam Anode.

Table 4.1. Variation of Light Intensity and Neutron Counting Rate with Deuterium Gas Flow

(Magnet Field = 7000 Gauss Midplane; Power Input ≈ 9 kw)

Flow (sec/cm^3)	Relative Intensity H_β = 4861 A	Relative Intensity N_2^+ = 4715 A	Neutron Signal/Background
25	30–40	1.6	(10)
60	16	1.6	13
95	1.6	1.6	3
180	1.6	1.6	1.5
330	1.2	1.2	(6)
450	1	1	1

discharge column and displaced radially from the column about 4 in. After 10 hr exposure, the number of proton recoil tracks was not sufficient to determine the neutron origin unambiguously. Within experimental error, the neutrons were coming uniformly from the entire length of the discharge column.

Two observations led to the third anode geometry tested: (1) neutron counting rate was independent of exact origin of gas feed within the anode (i.e., gas could be fed into either the anode center or the aperture of either end plate), and (2) the observed rf peak could be calculated with no more than 10% error from a very simple model: the period of the oscillation is equal to the transit time of the electrons from cathode to anticathode and back while moving in the potential well of the applied dc potential. Thus, the frequency was dependent on both the applied voltage and the cathode-anticathode spacing. The observed frequency was independent of magnetic field.

For the third anode geometry, the anode end plates were spaced about 30 in. apart and equidistant from the mirrors. Both the cathode and anticathode could be moved axially away from the anode end plates about 20 in. Gas feed was limited to the aperture in the anode end plate nearest the anticathode. The cylindrical enclosure connecting the anode end plates was removed. Operation of the discharge was steady for gas feed rates between 10 and 30 sec/cm^3, even though no neutral pressure differential could now be maintained as before with an anode enclosure. The optical spectrometer no longer could detect any characteristic radiation. However, a thin light bluish column could be seen with the eye between the anode end plates.

Figure 4.28 shows a plot of the neutron counting rate as a function of the ratio of the calculated electron oscillation frequency to the D_2^+ ion cyclotron frequency on axis in the midplane. The data taken with the second anode geometry used are also shown. The applied voltage in kilovolts is shown in parentheses for some of the points. Two of the neutron resonance peaks appear to be present when the electron oscillation frequency is a harmonic of the ion cyclotron frequency (if one assumes that the predominant ion species is atomic, the harmonics are the first and second rather than the second and fourth).

Nuclear track plates were again installed to determine the origin of the neutrons when the

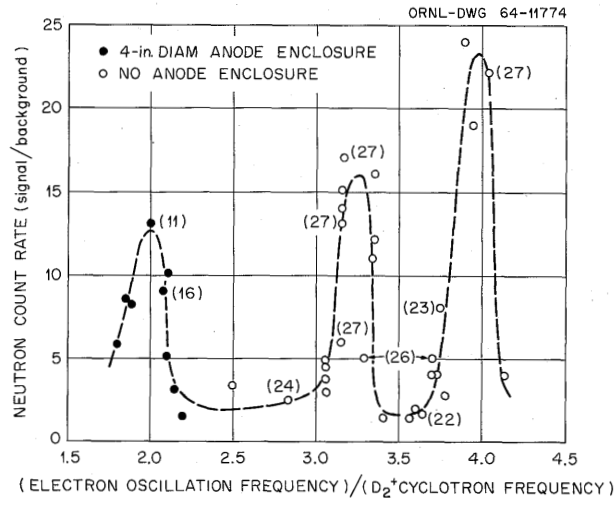

Fig. 4.28. Variation of Neutron Counting Rate with Electron Oscillation Frequency.

system was operating at a ratio of 4, Fig. 4.28. Without question, most of the neutrons originated from the vicinity of the anticathode. A new anode positioner is being installed to aid in experiments designed to confirm the existence of the neutron resonances.

4.7 STABILIZATION OF THE DEUTERIUM ARC

R. A. Gibbons N. H. Lazar

In the last progress report,[16] we described an effort to stabilize the deuterium arc plasma against flute production by applying a quadrupole field in *addition* to the usual mirror field in an attempt to confine the arc in a "minimum *B*" geometry. Unfortunately, because field lines through the cathode missed the anode at significant quadrupole fields, the arc was extinguished, and, as we described, stabilization could not be detected.

We have since succeeded in stabilizing the arc against fluting, however, in another "minimum *B*" geometry with different properties. When the arc is run conventionally, a probe placed at a radius 2.2 cm from the arc center at the axial center of the mirror coil nearest the cathode and biased to

[16] *Thermonuclear Div. Semiann. Progr. Rept. Apr. 30, 1964*, ORNL-3652, pp. 71–73.

ion saturation current is observed to yield a "hashy" trace with fluctuations of more than a factor of 10 above and a factor of 2 below the time-integrated current (Fig. 4.29). As we demonstrated earlier,[17] the time-averaged ion saturation current to a probe radially out from the arc core may be, at least, qualitatively related to the cross-field diffusion rate. Thus variations in the time-integrated current may be related to variations in the anomalous radial loss rate from the arc, which was shown to be dominated by coherent plasma flute motion. This time-integrated current is plotted in Fig. 4.30 as a function of the anode position in the magnetic field. The remarkably sudden fall in the current (through one order of magnitude in about 3 in. of motion) is accompanied by a reduction in the frequency and amplitude of the "spikes" in the time-resolved current trace (Fig. 4.31). Also shown in Fig. 4.30 is the arc voltage as a function of anode position. The constancy of this arc parameter suggests the arc characteristic itself is probably unchanged for the variation of arc length (to the back of the anode) of a factor of about 2.

To be certain that the arc length was not the determining factor for the reduction of fluting, the electrodes were moved so that the short arc was centered axially between the mirror coils. The ion current trace was as "hashy" as that for the conventional length.

We have not yet been able to produce a quantitative explanation for the stabilization but suggest that the positive radial gradient of the single mirror coil is sufficiently strong that fluting is inhibited over the entire arc length despite the remaining negative gradient in the center of the machine. To test this hypothesis, the mirror coil at the anode end was disconnected, producing the field shown dotted in Fig. 4.32. Although the time-integrated current showed only a small change (~10%) since it was already so low, the frequency and amplitude of the few remaining current spikes decreased another order of magnitude.

A quantitative explanation of this plasma behavior still cannot be made because some essential information is still absent. The primary difficulty is the uncertainty as to the cause of the fluting. From optical measurements of impurity radiation, time averaged over many minutes, the surface rotational velocity has been determined as 1.5×10^5 cm/sec. The ion energy in the arc center for the conventional arc length is ~16 ev, observed for these same arc conditions in a central magnetic

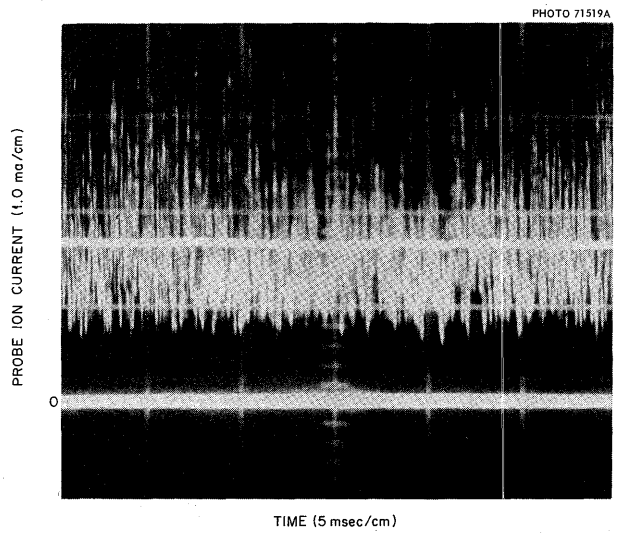

Fig. 4.29. Time-Resolved and Integrated Probe Ion Currents for 120-cm Arc.

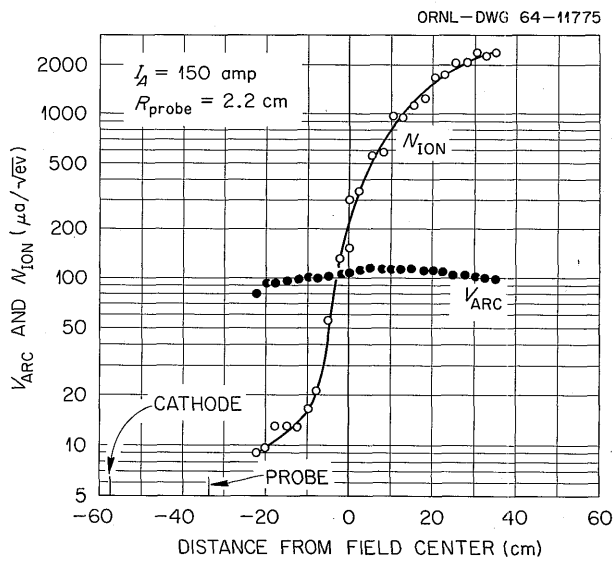

Fig. 4.30. Arc Voltage and Average Plasma Density as a Function of the Anode Position. *Back* of anode 10 in. to right of position shown.

[17] *Thermonuclear Div. Semiann. Progr. Rept. Oct. 31, 1963*, ORNL-3564, pp. 63–66.

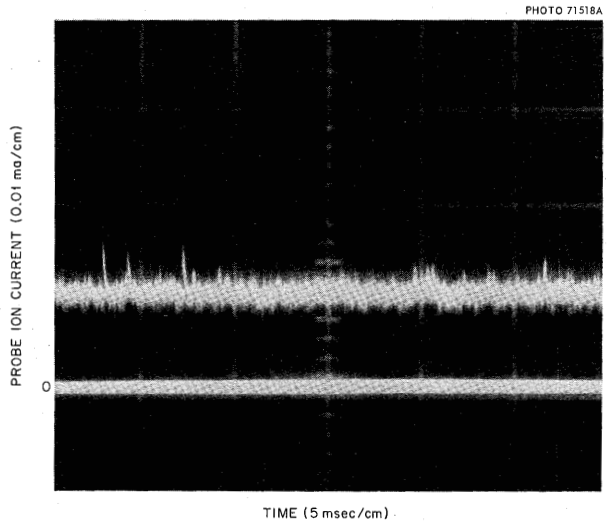

Fig. 4.31. Time-Resolved and Integrated Probe Ion Currents for 60-cm Arc. Compare with Fig. 4.29 (unstabilized arc) noting relative current scales.

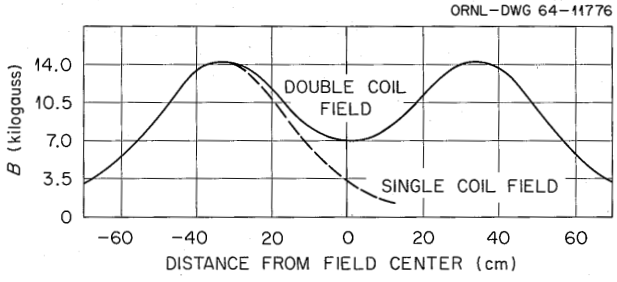

Fig. 4.32. Gas Arc Facility Axial Magnetic Field for Single- and Double-Coil Operation.

field of 7000 gauss. Since the arc density ($\sim 10^{14}$ ions/cm^3) is so high, the usual Rosenbluth, Krall, and Rostoker theory of flute stability with finite ion radius should be applicable.[18] Stability occurs for

$$(ka)^2 > \sqrt{\frac{kv_0^2}{R}} \left(\frac{mc}{eB}\right)$$

or

$$ka > \left(\frac{v_0}{v}\right) \sqrt{\frac{1}{kR}} ,$$

where a is the ion Larmor radius, R is the plasma radius, $\lambda = 2\pi/k$ is the wavelength of the perturbation, v_0 is the drift velocity, and v is the ion thermal velocity. This criterion is satisfied by an order of magnitude for wavelengths comparable to the flute dimensions determined from probe correlations. Thus it is not clear why flutes should occur at all. Further, the observed rotational velocity, v_0, is an order of magnitude greater than the maximum precessional velocity caused by the negative gradient of the central field.

It may, therefore, be somewhat specious to try to estimate the stabilization properties of the average positive gradient of the field for the short arc. A rough dimensional calculation suggesting order-of-magnitude agreement between theory and experiment may be presented as follows:[19] A comparison of the centripetal energy change for interchange of the plasma across flux lines in the positive field gradient with the equivalent variation of the rotational energy can be made which gives for stability

$$\frac{\nabla B}{B} > \frac{1}{R} \left(\frac{v_0}{v}\right)^2 .$$

At the maximum of the positive field gradient, $\nabla B/B \approx 0.001$, $R \sim 1$ cm, and $v_0/v \approx 0.025$.

Despite this apparent order-of-magnitude agreement, a qualitative discussion of the "average" field properties weakens the arguments. If the stability requirements are taken into account all along the arc, the condition for stability[20] is

$$\int_{\text{along arc}} \frac{\partial p}{\partial x} \frac{\nabla B}{B^2} \, dl < 0$$

and, for $\partial p/\partial x < 0$,

$$\int \frac{\nabla B}{B^2} \, dl > 0 .$$

Although the magnitude of $\overline{\nabla p}$ is not known well, we have calculated $\mathcal{J} = \int (\nabla B/B^2) \, dl$ for the arc

[18] M. N. Rosenbluth, N. A. Krall, and N. Rostoker, *Nucl. Fusion: Suppl. 1*, 143 (1962).

[19] T. K. Fowler, this report, sect. 7.6.

[20] H. P. Furth, *Phys. Rev. Letters* 11, 308 (1963).

presuming the integral should be taken from the cathode face to the rear of the cylindrical anode. In this case (mirror field), $\mathcal{J} = -2.7 \times 10^{-7}$. However, the value of the integral taken to a point 2 in. from the rear of the anode is $+1.2 \times 10^{-7}$. One may argue that at the very rear of the anode, the neutral gas pressure is sufficiently high that $\overline{\nabla p}$ may be strongly modified for this region from its negative value along most of the arc, but one would not expect this effect to extend further than a few centimeters in view of the extremely short ionization length. Clearly, this point will be difficult to clarify.

4.8 THE HYDROGEN ARC IN THE LONG SOLENOID: BAFFLE STUDIES

J. E. Francis, Jr. N. H. Lazar
P. R. Bell R. A. Gibbons

4.8.1 Introduction

Studies of the hydrogen arc in the long solenoid have been continued. Most of the measurements have been made on an arc 132 in. long. The cathode is mounted inside a water-cooled copper tube having an inside diameter of $1\frac{1}{2}$ in. This cathode shield is allowed to float electrically. The anode is a water-cooled copper tube having an inside diameter of $1\frac{7}{8}$ in. and a water-cooled tungsten backstop.

4.8.2 Baffle Saturation Current

Four insulated baffles were mounted between the arc electrodes. The baffles were copper washers 3 in. ID and $7\frac{1}{2}$ in. OD. Two baffles separated by 1 in. were placed 10 in. in front of the anode, and two baffles separated by 1 in. were mounted 16 in. from the cathode. The ion saturation currents to these baffles were then measured as a function of the magnetic field. The results are shown in Figs. 4.33 to 4.35. The difference in the curves is caused by varying the shape of the cathode. It is noted that there is a strong reduction of the baffle currents with an increase in magnetic field. The amount of gas feed necessary to maintain a given arc current and voltage is also reduced by increasing the magnetic field.

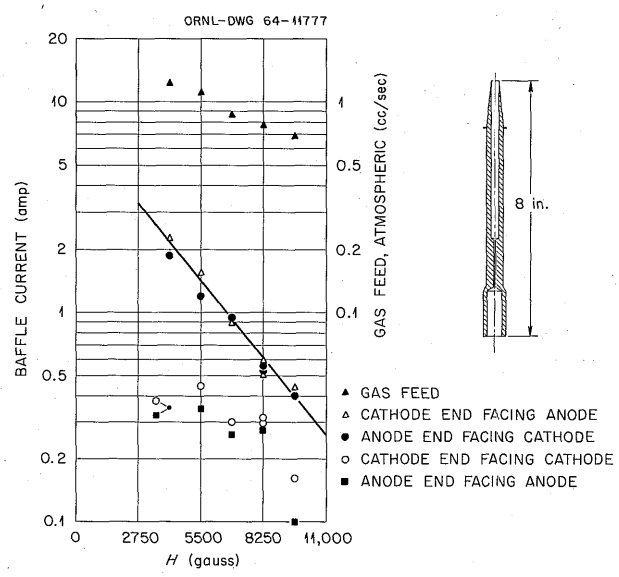

Fig. 4.33. Three-Inch-Inside-Diameter Baffle Saturation Current vs Magnetic Field for an 80-amp, 178-v, 132-in.-long Hydrogen Arc Using a Tapered Cathode.

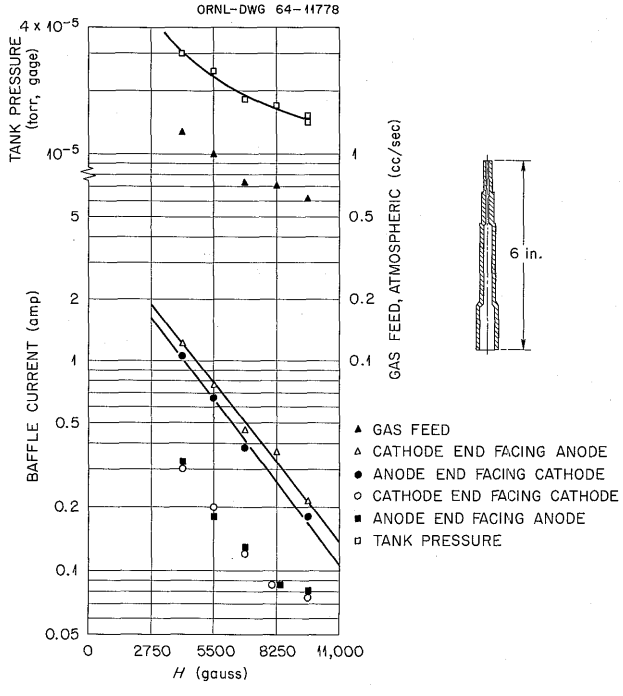

Fig. 4.34. Three-Inch-Inside-Diameter Baffle Saturation Current vs Magnetic Field for a 71-amp, 174-v, 132-in.-long Hydrogen Arc Using a Step Cathode.

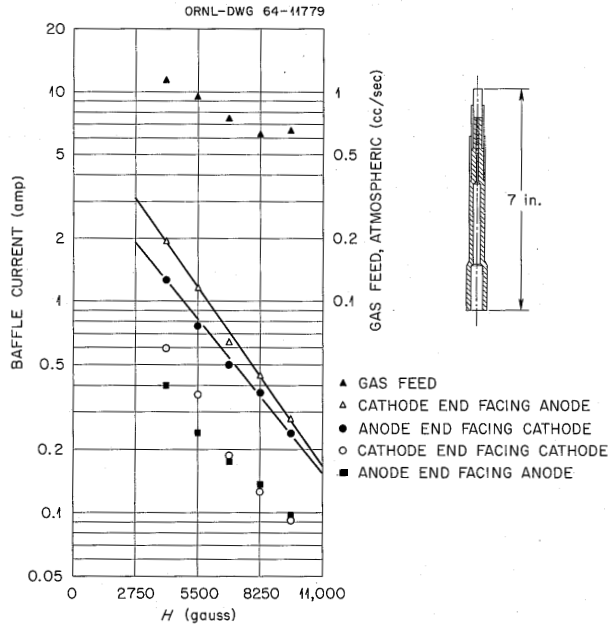

Fig. 4.35. Three-Inch-Inside-Diameter Baffle Saturation Current vs Magnetic Field for an 80-amp, 180-v, 132-in.-long Hydrogen Arc Using a Triple Cathode.

4.8.3 Water-Cooled Probe

An estimate of the density is obtained by inserting a water-cooled copper probe directly into the arc column and measuring the ion saturation current. The probe consists of $\frac{1}{16}$-in.-OD hollow copper tubing which is insulated so that its potential can be varied. Probe characteristics were run as shown in Fig. 4.36. The values of saturation current obtained were plotted as a function of radius, as shown in Figs. 4.37 and 4.38. The arc density σ is obtained from the formula

$$\sigma = \frac{I}{A2ve} ,$$

where I is the arc current in amperes, A is the area of the probe, v is the ion velocity, and e is the charge of an electron. Thus

$$\sigma = \frac{1.6}{(0.32)\, 2 \times 10^{6}\, (16 \times 10^{-20})}$$

$$= \frac{(1.6)(6.2)\, 10^{18}}{0.64 \times 10^{6}} = \sim 1.5 \times 10^{13} \text{ ions/cm}^3 ,$$

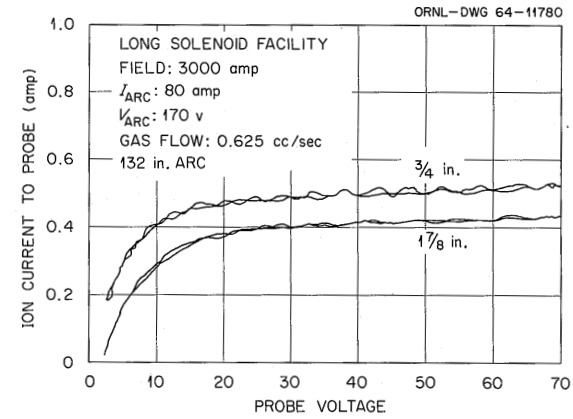

Fig. 4.36. Copper Tube Probe Current vs Probe Voltage at Two Radial Distances from Arc Center.

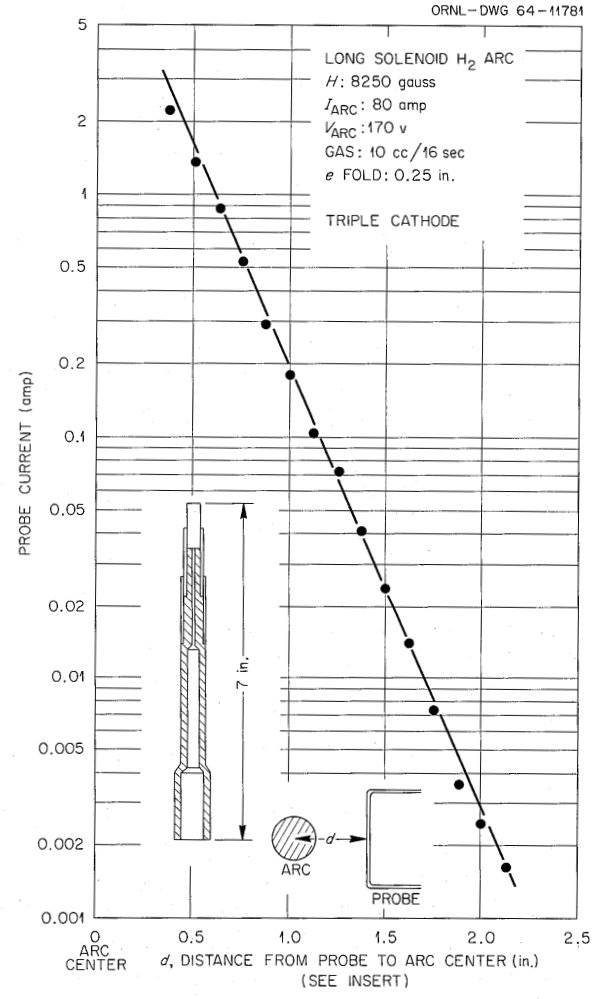

Fig. 4.37. Copper Tube Probe Saturation Current vs Radius for an 80-amp, 170-v, 132-in.-long Hydrogen Arc.

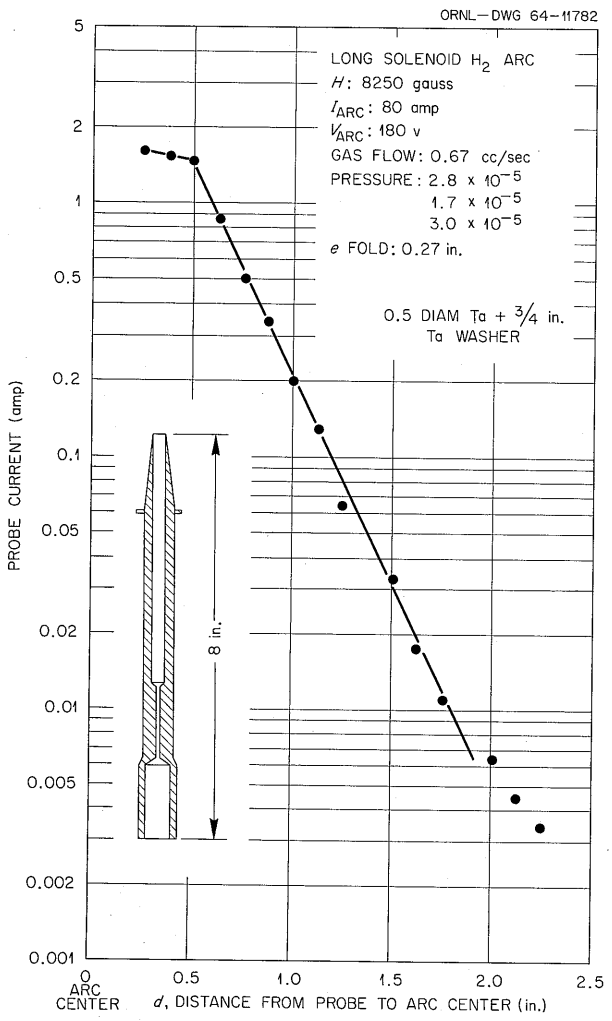

Fig. 4.38. Copper Tube Probe Saturation Current vs Radius for an 80-amp, 180-v, 132-in.-long Hydrogen Arc.

where the ion velocity is assumed to be $\sim 2 \times 10^6$ cm/sec.

4.8.4 Langmuir Probe

A Langmuir probe (0.010 in. in diameter by 0.25 in. long) was used for dc measurements of the ion density as a function of radius in the center of the solenoid as shown in Fig. 4.39. The ion densities were found to be exponentially decreasing functions of radius, with e-folding lengths between $\sim$0.6 and 0.8 cm. The dependence of e-folding length with magnetic field is shown in Table 4.2.

4.8.5 Gridded Probe Measurements

Directional ion and electron currents were measured as a function of radius. Figure 4.40 shows the currents obtained with the probe looking toward either the anode or cathode. They indicate that

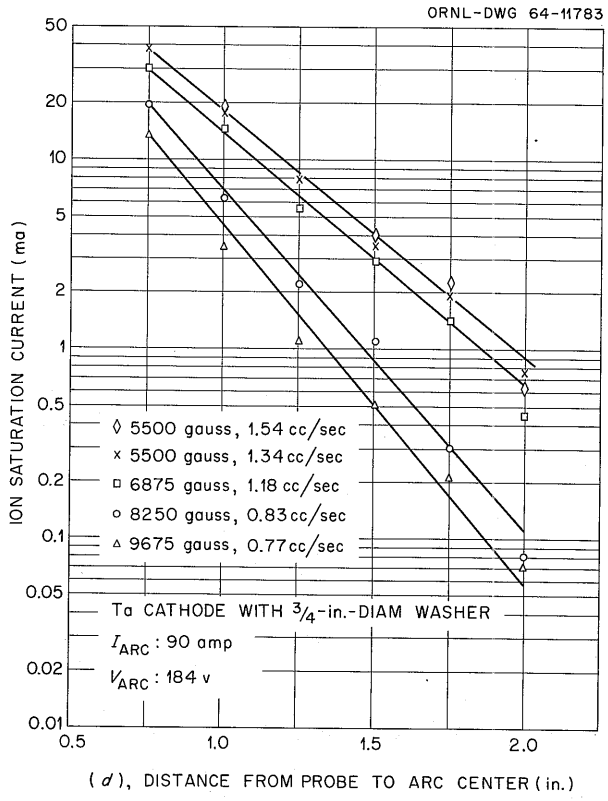

Fig. 4.39. Langmuir Probe Saturation Current vs Radius for a 90-amp, 184-v, 164-in.-long Hydrogen Arc.

Table 4.2. Hydrogen Arc in the Long Solenoid; Langmuir Probe Current Decrease as Function of Radius

Magnetic Field (gauss)	e-Folding Length (cm)
5500	0.83
6875	0.83
8250	0.62
9625	0.59

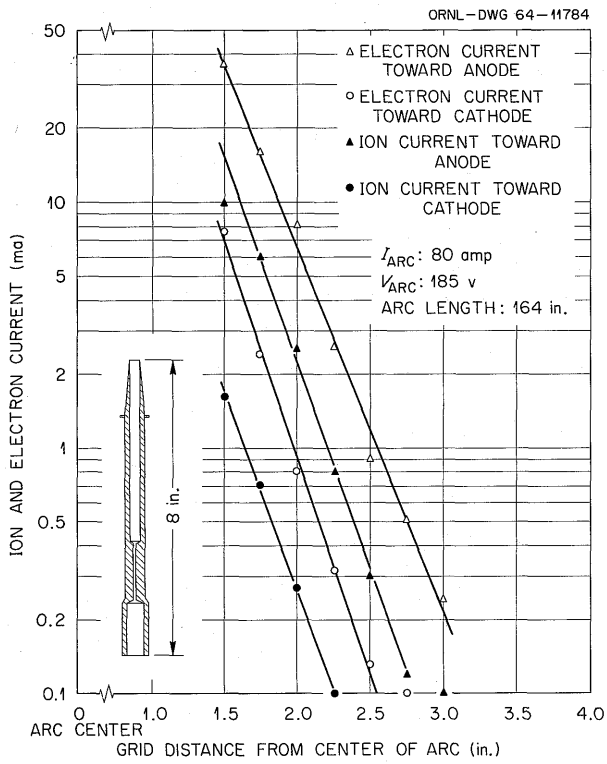

Fig. 4.40. Ion and Electron Current to Gridded Probe vs Radius for an 80-amp, 185-v, 164-in.-long Hydrogen Arc.

there is a preferential motion of the ions toward the cathode. This agrees with measurements of carbon and lithium arcs, where ions formed a deposit only on the anode side of the baffle. Considerable changes in the gridded probe currents at these radii could be obtained by applying potentials to the baffles mentioned above.

4.9 SPECTROSCOPIC STUDIES OF THE HYDROGEN ARC IN THE LONG SOLENOID

J. E. Francis, Jr. J. R. McNally, Jr.
M. R. Skidmore

Transverse observations of the hydrogen arc in the long solenoid have given spectral line broadening of about 0.45 A for the λ4340 A hydrogen line and slant on the parent line (see Fig. 4.41) similar to the spectra of hydrogen arcs in the calutron arc.[21] The broadening can be associated with a temperature of H^+ prior to charge exchange (or recombination), and the slant is evidence of H^+ rotation about the axis of the arc (max $V_\phi \sim 10^6$ cm/sec), also prior to charge exchange (Franck-Condon neutrals of about 2 ev could contribute to the line broadening but not the slant).

Carbon and oxygen impurities with Doppler broadening of 0.4 A and with obvious slant line effects (due to rotation about arc axis) were detected. In an experiment in which the solenoid field was increased by a factor of 2, the overall slant appeared to be roughly the same as for the lower-field case. However, at the higher field the arc appeared more hollow (cylindrical) and with an additional slant in the peripheral region superimposed on the Doppler-broadened line.

[21] J. R. McNally, Jr., and M. R. Skidmore, *J. Opt. Soc. Am.* **47**, 863 (1957).

PHOTO 65843R

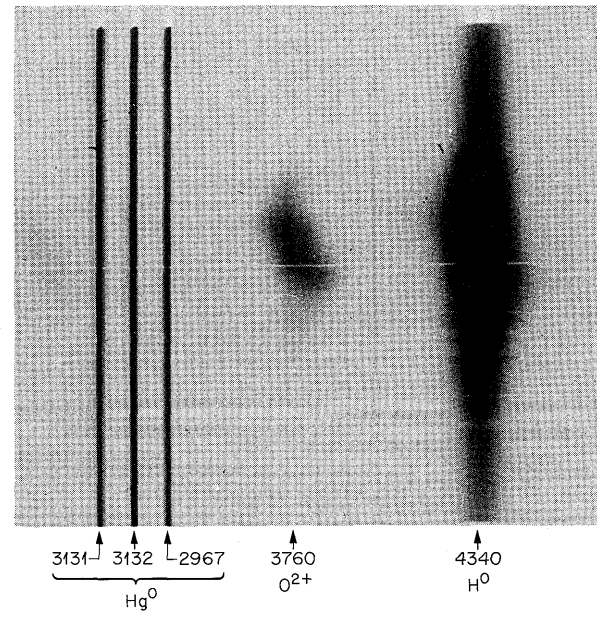

Fig. 4.41. Typical Doppler Effects in Spectra Observed for Hydrogen Arc in Long Solenoid. Note slant due to rotational motion about arc column in spectra of O^{2+} (impurity) and in H^+ (recombination spectrum superimposed on neutral $H\gamma^0$ line). Arc: 14 ft long, 82 amp, 178 v; observation point: 16 in. from cathode; pressure: anode region, 2.5×10^{-5} torr; midtank, 5.2×10^{-6} torr; cathode region, 1.9×10^{-5} torr.

In calutron arc studies an increase of the magnetic field increased the rotational velocity almost linearly, as evidenced by the slant line effect.

Observations made at different solenoid ports along a 14-ft-long hydrogen arc demonstrated no significant change in the Doppler temperature of the hydrogen or the carbon and oxygen impurities. By contrast, the ionic temperature in the energetic carbon arc increased with the square of the distance from the anode to observation point.

In another experiment in which the arc column was about 2 in. in diameter, as determined visually, and relatively diffuse, the spectral line profiles of the arc were quite different compared to the usually small-diameter arc as defined by the cathode diameter. The slant effect on the hydrogen lines was absent or too weak to distinguish, and there was only a very slight slant of the ionic impurity spectrum lines in the main body of the arc; however, in the peripheral region of the arc the ionic impurities did have a typically large slant, indicating an $E \times H$ drift (up to 10^6 cm/sec) of plasma around the arc and hence a strong sheath localized at the surface of the discharge column. A tapered tantalum cathode with a $\frac{3}{4}$-in.-OD washer was used in this experiment. The hydrogen feed was 1.7 cm^3/sec; arc current, 80 amp; arc voltage, 195 v; solenoid current, 3000 amp; and the uncorrected gage pressures were as follows: anode region, 4.5×10^{-5} torr; mid solenoid, 1×10^{-5} torr; and the cathode, 4×10^{-5} torr.

5. Cross-Section Measurements

C. F. Barnett J. A. Ray J. C. Thompson

5.1 FORMATION OF EXCITED H^0 BY ARC DISSOCIATION OF H_2^+

The experimental apparatus and techniques along with preliminary results have been described previously.[1] An ion beam was accelerated to 500 kev by a conventional accelerator and passed through a magnetic analyzer. H_2^+ ions emerging from the analyzer were collimated by a fixed $\frac{1}{16}$-in. aperture. The ions were then passed axially through an arc discharge maintained by an 8000-gauss magnetic field. The H^0 production rate was optimized by making changes in the arc geometry and electrode materials. Initially, the electrode geometry consisted of a tungsten cathode with an outside diameter of $\frac{3}{4}$ in. and an internal bore of $\frac{1}{2}$ in., producing a cylindrical annular arc 10 in. long. The anode consisted of a 3-in.-OD cylindrical carbon block with a center bore of $\frac{3}{16}$ in. through which the beam passed. Provisions were made to admit argon support gas to either the cathode or the anode. For small gas flows (<0.1 std cm^3/min) into the cathode, streamers developed in the arc with subsequent melting of the cathode. To utilize more completely the gas fed into the arc, an insulated shroud was placed around the outside of the cathode and gas was fed into the region between the cathode and the insulated shell. With this geometric configuration, the arc ran more smoothly, and off the end of the tungsten cathode; however, melting of the cathode persisted. Succeeding generations of the cathode geometries saw the replacement of the tungsten with graphite of similar shape; the replacement of cylindrical geometry with a tuning-fork-shaped cathode resulting in two ribbon arcs; and two small solid cylindrical cathodes $\frac{3}{16}$ in. in diameter, spaced $\frac{1}{2}$ in. apart. The only change in the anode was the reduction in size to increase the temperature of the front surface. Standard reactor-grade graphite was replaced by pyrolytic graphite with the c-axis parallel to the arc axis for the anode and perpendicular to the arc axis for the cathode. Typical operating conditions of the arc were 150–300 amp with voltages of 60–90 v for an 8–10 in. arc.

The beam emerged from the anode and passed through a set of electrostatic condenser plates where the H^0, H^+, and H_2^+ components were analyzed. Total neutral yield was determined by measured the H^0 component with a nickel-foil-covered Faraday cup. The foil conversion of 250-kev H^0 to H^+ was measured to be 98% efficient.

The population of the excited states was measured by sampling the H^0 beam with a 0.125-mm aperture, then passing this collimated beam through an electric field ionizer. This ionizer consisted of spherical surfaces 1 mm apart with 0.25-mm apertures providing electric fields up to 5×10^5 v/cm in the direction of the beam. The H^0 ionized by the application of the electric field was then deflected by another set of electrostatic plates and detected by a movable electron multiplier. The ratio of H^+ formed to total neutral yield for a given electric field was then the sum of the population of all principal quantum states n above the threshold electric field necessary to ionize level n.

Typical results are shown in Figs. 5.1 and 5.2. The percent dissociation of H_2^+ as a function of arc current is shown in Fig. 5.1. The dissociation rate usually increased as the arc current increased, although in some geometries the reverse was true. Absolute dissociation rates are meaningless since the percent dissociation could be varied from 10 to 90% by changing the arc geometry or by

[1] *Thermonuclear Div. Semiann. Progr. Rept. Apr. 30, 1964*, ORNL-3652, p. 79.

moving the H_2^+ beam nearer the electron core of the arc. The production of H^0 is shown in Fig. 5.2 as a function of the arc current. Again the shape and magnitude were dependent on the arc geometry; however, one could usually determine an optimum arc current for a given geometric configuration.

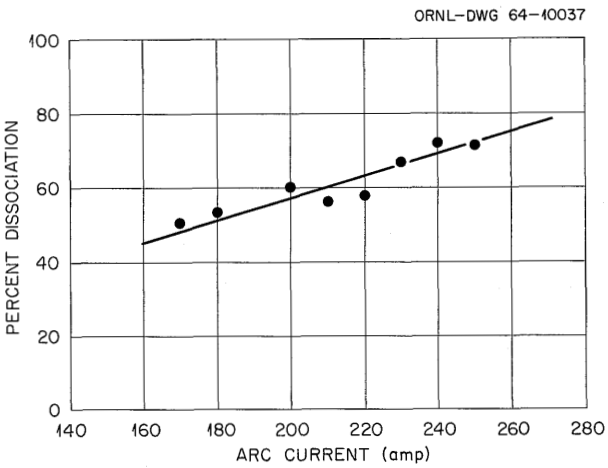

Fig. 5.1. Dissociation of H_2^+ by a Carbon Arc.

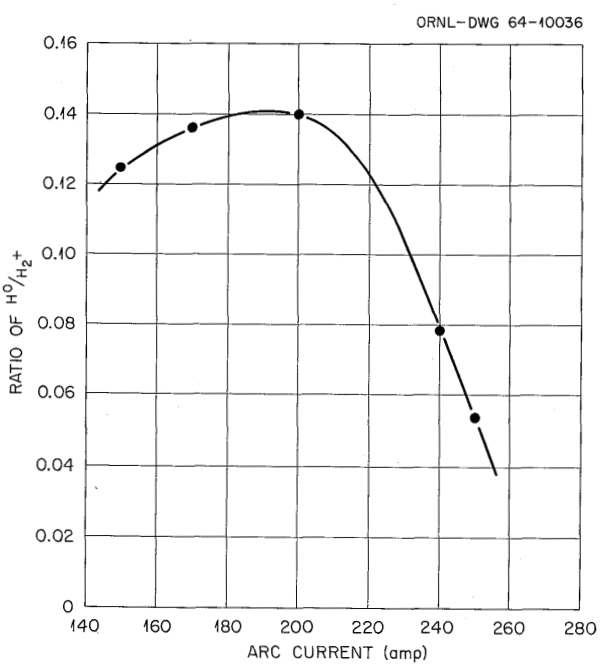

Fig. 5.2. Production of H^0 by the Dissociation of H_2^+ in a Carbon Arc.

The curves of Figs. 5.1 and 5.2 were obtained using pyrolytic graphite electrodes which resulted in a more uniform, steady arc with decreased gas pressure in the region surrounding the arc.

By placing a narrow slit in front of the foil detector and scanning the slit across the dissociated components of the H_2^+ beam, the spatial distribution could be determined and some insight could be gained as to the dissociation reaction kinetics. A summary of the spatial distributions is tabulated in Table 5.1. The width of the undissociated H_2^+ beam emerging from the arc was a factor of 2 greater than the width of the initial H_2^+ beam. This increase resulted from deflections by electric fields present in the arc. These fields were erratic in frequency, with a low-frequency component which one could observe visually if the beam was intercepted by a zinc sulfide surface. The observed deflection of the H_2^+ beam could be accounted for by 200–300 v/cm electric fields in the arc region if the assumption was made that the fields existed over a distance of 10 cm in the direction of beam propagation. Examination of the table also revealed that the H^+ and H^0 components were of different widths, which resulted from the magnetic focusing of the H^+ particles. The tabulated widths of the H^0 and H^+ beams have subtracted from them the original width of the H_2^+ beam. If argon gas was admitted to the center of the anode or the cathode, then the actual width of the H^0 beam arising from dissociation events in the cathode was larger than the width associated with collisions in the anode region; however, if the actual width was translated to angular divergence, then the angular divergence was independent of the region of dissociation. The small increase in divergence when dissociation occurred at the cathode was probably due to the uncertainty of the exact location along the cathode axis where a dissociating collision occurred. The H^0 beam arising from collisions in the arc had the same actual width as the beam formed by admitting argon to the anode, indicating that most of the H^0 produced by arc dissociation occurred in a region near the anode.

In dissociating collisions, one usually assumes that the collision obeys the Franck-Condon principle in that the time of collision is much less than the nuclear vibration time, so that the nuclei remain essentially stationary during the collision. Classically, in a dissociating collision of H_2^+ the individual particles share equally the excessive

Table 5.1. Angular Divergence of the H_2^+, H^0, and H^+ Beams

Particle	Dissociation Mode	Actual Half-Width (in.)	$\Delta\theta$ (milliradians)	$\overline{\Delta\theta}^2$	ΔE (v)
H_2^+	No arc	0.12			
H_2^+	Arc	0.23			
H^0	Gas in anode	0.31[a]	2.4	5.8	2.9
H^0	Gas in cathode	0.37[a]	2.55	6.5	3.2
H^0	Arc	0.31[a]	2.4	5.8	2.9
H^+	Gas in anode	0.13[a]			
H^+	Gas in cathode	0.21[a]			
H^+	Arc	0.26[a]			

[a]H_2^+ width subtracted.

potential energy of the repulsive state. A simple picture results in the H_2^+ breaking up to release two particles with a calculated rms angular spread about the original beam direction of

$$\overline{\Delta\theta}^2 = \frac{\Delta E}{E},$$

where $\overline{\Delta\theta}^2$ is the rms angle between dissociated particles and beam direction, ΔE is the energy acquired by H^+ or H^0 in the collision, and E is the energy of the incident particle. Calculation of this energy change gives an approximate value of 3 v, which may be compared to an average value of 5 v expected from an electronic transition from the ground $^2\Sigma_g$ state of H_2^+ to the first repulsive level $^2\Sigma_u$. The conclusion was drawn that production of H^0 by the arc dissociation of H_2^+ proceeded by an electronic transition to a repulsive level in the same manner as dissociation by gases.

In Fig. 5.3 is shown the fraction of H^0 ionized as a function of the applied electric field across the spherical surfaces for both argon gas and arc production of H^0 from H_2^+ dissociation. The values obtained for the case of argon were consistent from day to day; however, values shown for the carbon arc were the most optimistic results. Fractions up to ten times less than those shown were measured and were a strong function of arc current and geometry. A field strength of 2×10^5 v/cm was sufficient for ionization down to principal quantum number $n = 8$; however, the field-free radiative lifetime to the $n = 8$, $l = 1$ level was of the order of the transit time of the H^0 from the arc

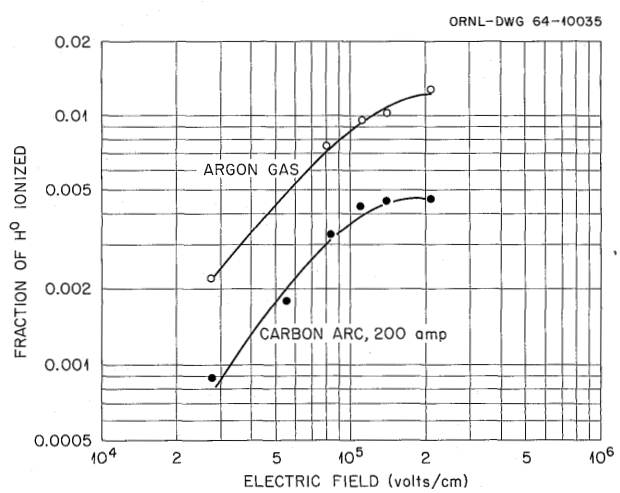

Fig. 5.3. Electric Field Ionization of H^0.

to the electric field. Also, considerations of the Stark lifetimes indicated that all levels with $l = 0$ had their lifetimes greatly reduced; thus we probably measured only the sum of all levels with $n > 8$. Table 5.2 shows a summary of the measurements with arc and gas dissociation. Under optimized conditions the arc produced approximately a factor of 1.5 more H^0 than that produced in a gas cell. The fraction of H^0 in states $n > 8$ was always a factor of 2 or less for arc production than for gas production.

Due to fluctuations in detector reading caused by erratic electric fields in the arc, all of the measurements showed large fluctuations. The estimated probable error in the measurements was 50%. These results did not confirm previously reported results[2] on arc production of H^0 in excited states.

Table 5.2. Comparative Yields of Unexcited and Excited H^0 from Arc and from Argon Gas Cell

Dissociation mode	H^0/H_2^+	$H_0^*/H_0(n > 8)$
Comparative yield		
Arc	0.20	0.0046
Argon gas cell	0.14	0.0127

5.2 PRODUCTION OF HIGHLY EXCITED NEUTRAL ATOMS BY PASSING PROTONS THROUGH ATOMIC HYDROGEN

General theoretical considerations of the electron capture by protons from hydrogen atoms in the 1s state have shown that the electron is captured predominantly in the 1s state of the final atom. This is true for both the high- and low-energy regions for which $hv/e^2 \ll 1$ and $hv/e^2 \gg 1$, where v is the velocity of the incoming proton. If the velocity of the proton is greatly different from the velocity of the bound electron in its initial 1s state, then the maximum overlap of the initial and final wave functions occurs with the formation of a 1s state. When $hv/e^2 = 1$ or the velocity of the proton is equal to the 1s state electron velocity, there is a strong overlap between the initial 1s state wave function and the final highly excited state of the energetic atom formed in the capture collision. Butler and Johnston[3] have shown that at this energy there is a narrow, giant capture resonance for formation of highly excited states. In this treatment use was made of first-order perturbation theory in which there was present a logarithmic divergence at the resonance velocity corresponding to a proton energy of 24.7 kev. Removal of this divergence[4] resulted in a smearing out of the sharp peak, with the cross section for capture into highly excited atoms with principal quantum number n being given by

$$\sigma_n = \frac{256\pi a_0^2}{5n^3p^2\beta^5},$$

where a_0 is the Bohr radius,

$$p = \frac{mv}{h} a_0,$$

m = electron mass,

v = proton velocity, and

$$\beta = \frac{(p^2+1)^2}{4p^2}.$$

The cross section is still predicted to show a maximum at 24.7 kev proton energy, although the sharpness of the resonance has now disappeared, the cross section having a width at half maximum of 20–50 kev for a given n state.

Preliminary measurements have been made to confirm the capture into excited states by the passage of protons through atomic hydrogen. A schematic diagram of the apparatus is shown in Fig. 5.4. Ions were formed in a filament-type source and accelerated to energies of 10–40 kev by a single-stage accelerator. The beam was passed through a magnetic analyzer and the selected beam of protons was incident on a tungsten oven. Molecular hydrogen was fed into the oven, and by maintaining the oven at 2800°C approximately 98% of the H_2 was dissociated to form atomic hydrogen. The oven was constructed

[2] J. S. Luce *et al.*, *Proc Intern. Conf. Ionization Phenomena Gases, 6th, Paris, 1963*, vol. I, p. 83.

[3] S. T. Butler *et al.*, *Phys. Letters* **9**, 141 (1964).

[4] S. T. Butler *et al.*, *Phys. Letters* **10**, 281 (1964).

ORNL-DWG 64-11785

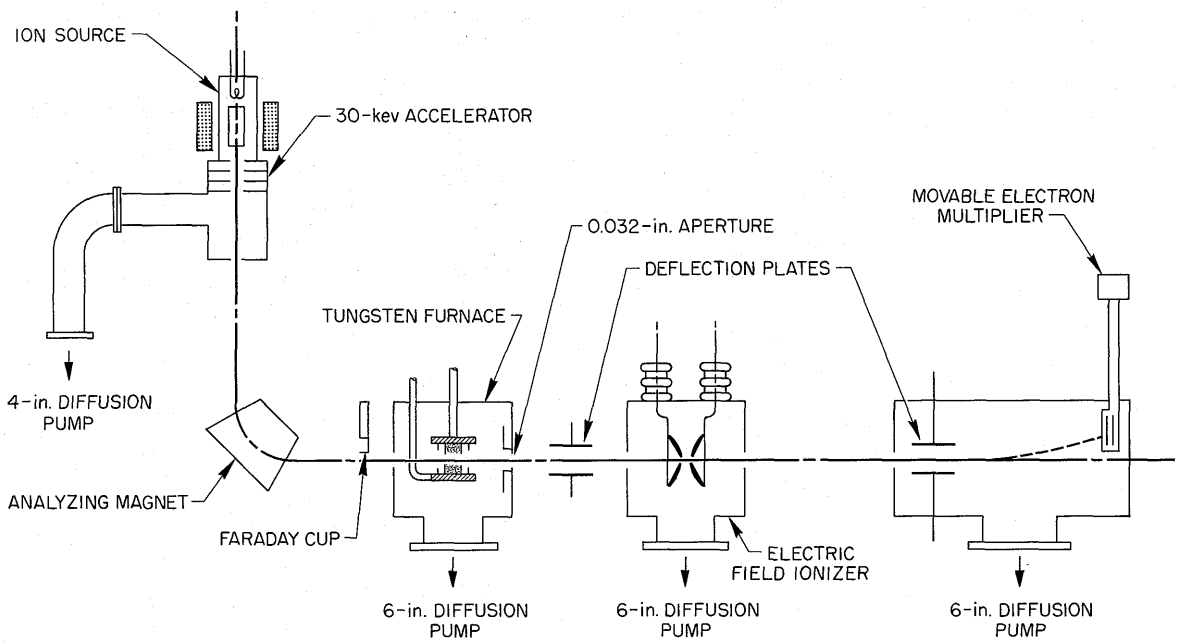

Fig. 5.4. Schematic Diagram of Apparatus Used to Measure Excited State Population in Atomic Hydrogen.

by rolling 0.001-in. tungsten sheets into a cylinder 0.5 in. in diameter. Fine tungsten wire was rolled to form "tungsten wool," which was placed in each end of the tungsten oven. Diffusion of the hydrogen through the wool ensured a dissociation equilibrium between the hydrogen molecules and the walls of the oven.

The energetic beam emerging from the oven was passed through a set of electrostatic deflection plates which removed the protons. The fast H^0 were collimated by a 0.005-in. aperture and then passed through the electric field ionizer, where states with principal quantum number $n = 12$ or greater were ionized. The ionizer consisted of flat Inconel plates separated 0.029 in. with 0.010-in.-diam apertures. Ions formed in the field region were analyzed by another set of electrostatic plates, and both ions and H^0 were detected by an electron multiplier. Ions were formed on various equipotential lines in the field region, thereby gaining or losing energy, which resulted in a spatial distribution of the H^+ beam at the detector position. To ensure uniformity in detecting the ions, a narrow 0.001-in. slit was placed over the opening of the detector which was scanned across the beams. The output of the detectors was amplified and integrated, with the ratio of H^+/H^0 giving directly the ratio of the neutrals in states $n = 12$ or greater to the total neutral beam.

Measurements were taken first with the admission of hydrogen and helium to the room-temperature oven. In Fig. 5.5 is plotted the fraction of H^0 in states $n = 12$ or greater as a function of the proton energy. As is seen, the fraction formed in H_2 was greater than that formed in helium, with both gases producing a monotonically increasing fraction in the energy range 16–34 kev.

The measured fraction of the relative number of excited neutrals to total neutrals does not allow one to compare directly with theory. The electron capture cross section into excited states σ_n^e (following notation of Butler) is proportional to the ratio of excited neutrals to the flux of protons incident on the gas cell or tungsten oven. If we multiply the measured fraction, H^*/H, by the total electron capture cross section into all states, then we have a quantity given by $kH^*/H_{in}^+ \sim \sigma_n^e$. Figure 5.6 is a plot of the results of multiplying the curves of Fig. 5.5 by the known electron capture cross sections in hydrogen and helium. One sees

that the peak of the cross section for H_2 occurs at approximately 25 kev, the same as that predicted for atomic hydrogen. The curve for helium is still increasing over the limited energy range of the data. However, from simple considerations one would expect a maximum at 50–70 kev. Note that

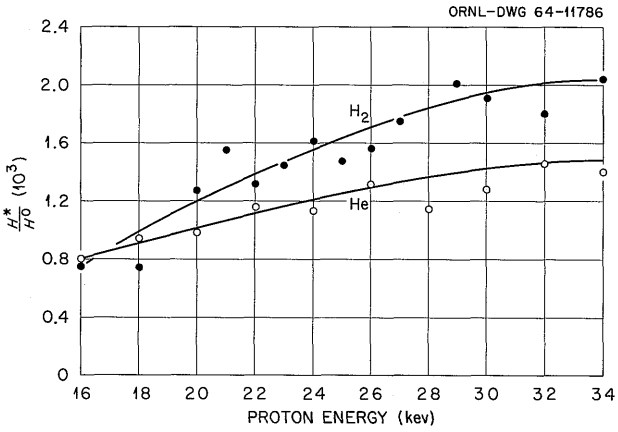

Fig. 5.5. Fraction of H^0 in Principal Quantum Numbers ($\sum_{n=12}^{\infty} H^n$) as a Function of Proton Energy. Electron capture by protons in hydrogen and helium.

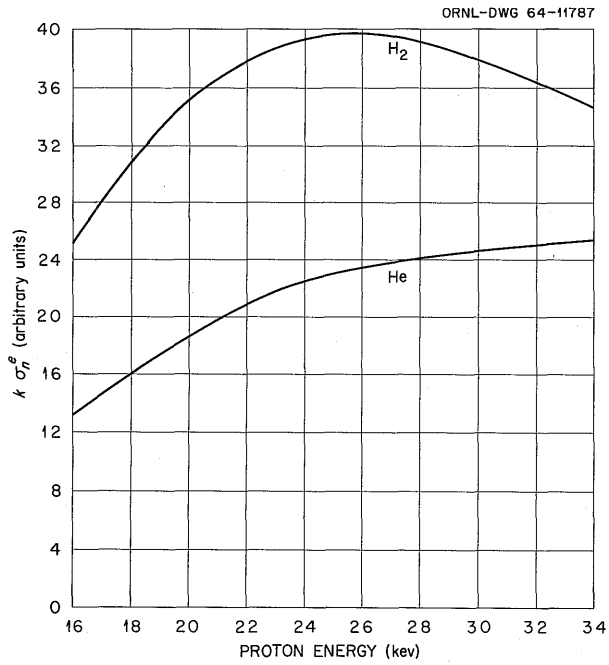

Fig. 5.6. Electron Capture Cross Section into Excited States. Protons passing through hydrogen and helium.

from observing the fraction of atoms in the excited state, the cross section, σ_n^e, is approximately two orders of magnitude less than the total capture cross section, σ_{10}.

Measurement of the electron capture cross section in atomic hydrogen is incomplete due to difficulties encountered with the furnace at elevated temperature. Thermal stresses caused the fragile walls of the furnace to collapse and buckle with repeated temperature cycling. Modifications in design of the support members and current leads are now being made.

5.3 ELECTRIC FIELD IONIZATION OF H_2

If H_2^+ traverses a gas cell at an energy of 30 kev, there is an equal probability that the H_2^+ ion will dissociate into a proton and an H^0 atom, or that the H_2^+ will capture an electron, going either to a repulsive state resulting in two H^0 atoms, or into a stable excited electronic state or ground state of the molecule. The H^0 atoms produced by capture into repulsive levels or dissociation possess an excited-state population different from that produced by electron capture by a proton, so that they yield an excited-state population distribution given by the $1/n^3$ dependence, where n denotes the principal quantum number. To determine the actual distribution resulting from H_2^+ collisions, the experiment was performed.

The apparatus and measurements were as described in the previous section. Scanning the ion beam formed in an electric field of 4.14×10^4 v/cm revealed two separate ion peaks, one corresponding to ions of ½ incident H_2^+ energy (which is that expected from excited H^0), and another at the same energy as the incident H_2^+ beam, which is presumed to be H_2^+ formed by the electric field ionization of H_2^0. The fraction of H^+ and H_2^+ formed depended upon the applied electric field, increasing as the field increased. Transitions involving the well-known levels of H_2 were energetically impossible with modest electric fields of 4×10^4 v/cm. Little is known of the higher levels of H_2; however, some recent work[5] concerning autoionizing levels of H_2 indicates that the

[5] G. R. Cook *et al.*, *J. Opt. Soc. Am.* **54**, 968 (1964).

$^1\Pi_u(3p)$ $v = 6$ or $^1\Pi_u(4p)$ $v = 3$ level of H_2 overlaps the potential energy curve of the ground state ($^2\Sigma_g^+$) of H_2^+. The application of the electric field would then cause transitions between these levels or higher vibrational and rotational levels if the radiative lifetimes of those two $^1\Pi_u$ levels were longer than the transit time of the H_2^0 particle from the gas cell to the field ionizer.

The numbers of H^+ and H_2^+ formed from H^0 and H_2^0, respectively, were approximately equal; however, absolute fractions must await measurements of the relative abundance of H^0 and H_2^0 in the sampled neutral beam.

5.4 PARTICLE DETECTORS

As a continuing program in the evaluation of detectors for neutral and charged beams in atomic collision measurements, we have determined the response of a Bendix electron multiplier.

The Bendix multiplier is a continuous strip anode, $E \times H$ type electron multiplier. Previous evaluation[6] of the multiplier reported the gain to be relatively insensitive to the place of particle impact on the $\frac{3}{4}$- by $\frac{3}{4}$-in. tungsten cathode. However, cross-section measurements made using the Bendix multiplier as a detector were erratic and indicated inconsistent multiplier gain. Using a 0.005-in.-diam beam of protons as a probe, the relative response was measured as a function of position of impact on the cathode surface. In Fig. 5.7 is plotted the multiplier response as a function of distance of the beam from the anode edge. This particular scan was made axially along the center of the cathode using 20-kev protons. There exists a factor of 10 decrease in gain over the first $\frac{1}{2}$ in. of the scan; however, gain changes of the order of 10^5 were measured over the full extent of the cathode, with the areas near the outside edges showing the greatest variations. Also, scanning over the surface revealed small areas of high gain next to areas of moderate gain. Variation of particle energy from 2 to 35 kev, changes in multiplier operating voltages, and testing of three different multipliers all gave essentially the same results. We have concluded that the Bendix multiplier cannot be used as an absolute detector of energetic particles but only as a relative detector when the spatial distribution of ions and atoms is constant throughout a measurement.

The response of silicon barrier detectors has been determined for H^+, H_2^+, and H_3^+ in the energy range of 2.5–35 kev using current measuring techniques. Complete evaluation of these detectors in the low-energy limit awaits further confirming measurements.

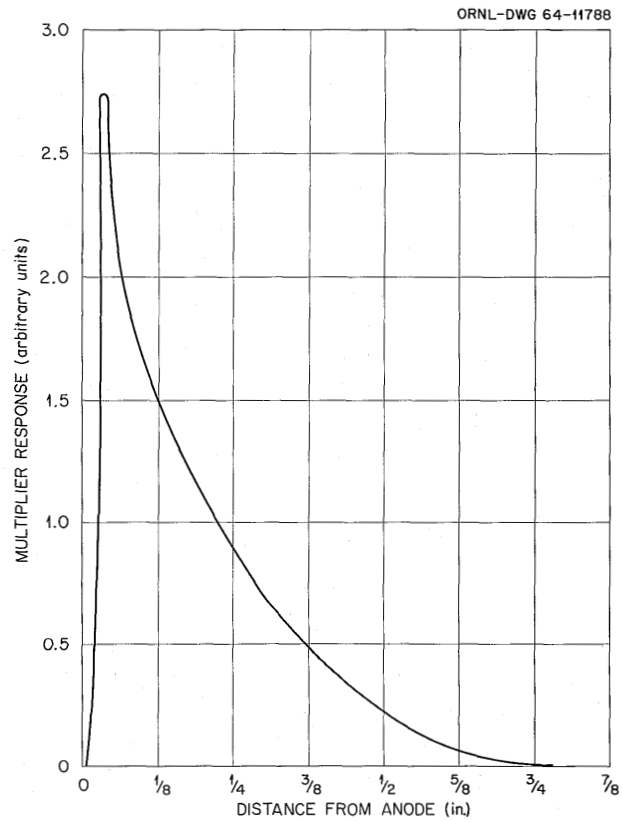

Fig. 5.7. Bendix Electron Multiplier Response as a Function of Cathode Position. 0.005-in.-diam proton beam of 20-kev energy.

[6] G. W. Goodrich *et al.*, *Rev. Sci. Instr.* 32, 846 (1961).

6. Production, Acceleration, and Injection of Ionic and Atomic Beams

6.1 HIGH-CURRENT ION-BEAM PRODUCTION AND INJECTION

R. C. Davis
R. R. Hall
G. G. Kelley
O. B. Morgan
R. F. Stratton
D. C. Weaver[1]

The large change in 600-kev H_2^+ current capabilities with a small variation in the injection duct geometry on the test stand[2] apparently was caused by a large energy modulation of the beam. The 600-kv, 1-amp power supply was found to have deteriorated until it had an 80-kv ripple under load at 600 kv because of a large number of defective rectifiers. With this energy spread the magnetic lens could not focus all of the beam through the injector duct. An exact geometrical duplicate of the DCX-2 injector[2] was limited to ~50 ma of H_2^+ current at 600 kev – the same current limit as found on DCX-2. After repairing the supply, H_2^+ currents of 90 to 100 ma at 600 kev could be obtained with this same duct. No real attempt has been made to maximize the H_2^+ current into DCX-2 since these results were obtained.

The production and acceleration of much larger dc 600-kev hydrogen ion beams is now possible. Total currents of 350 ma at 600 kev have been obtained on the test stand by using a modified duoplasmatron ion source with an expanded plasma extraction region.[3] There was no attempt to extract greater currents from this source, but with a 2-in. plasma surface and a 1-in. spacing, the extracted current capabilities with 150-kv extraction, based on previous tests at 50 to 100 kv, would be >1.5 amp H_2^+. The attainable current in amperes is

$$I = 1.7 \times 10^{-7} \frac{\Phi^{3/2}}{M^{1/2}(Z/r)^2},$$

where Φ is the applied potential difference in volts, M is the ionic mass number, Z is the effective spacing (real spacing plus the radius of the extraction aperture), and r is the radius of the plasma surface. The real problem with the expanded cup sources is to produce a beam with an emittance such that all of a particular ion species (e.g., H_2^+) can be focused through the required injector geometry. The optical problems are difficult because with the DCX-2 injector the beam is on for time periods of from tens of milliseconds to many seconds with intense beams, so that the utilization of grid systems to shape the electric fields is impractical. Using magnetic fields in the vicinity of the extraction surface with this very high gradient accelerator (~2.5 Mv/m) is also very difficult because of PIG discharges if the electrode shapes are not exactly correct. A source with a 1-in. plasma surface has been used to focus 96 ma of H_2^+ through the DCX-2 injector duct geometry on the test stand. This current was obtained from a total beam of 275 ma. No further increase in the analyzed H_2^+ component could be attained when the total beam was increased to 330 ma. A plot of the 600-kev H_2^+ power equivalent in milliamperes obtained through the injection geometry is shown in Fig. 6.1. This information emphasizes a second problem in the production of large 600-kev dc molecular ion beams, which is the decreased relative percentage

[1]On loan from Y-12.

[2]R. C. Davis *et al.*, *Thermonuclear Div. Semiann. Progr. Rept. Apr. 30, 1964*, ORNL-3652, p. 86.

[3]*Ibid.*, p. 85 (Fig. 7.1).

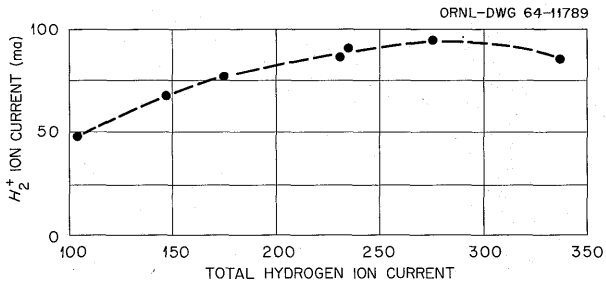

Fig. 6.1. Analyzed H_2^+ Ion Current as a Function of Total Hydrogen Ion Current from Ion Source.

of the molecular component as the total current is increased. Previously, the successful method used to improve this relative production was to scale up the size of the critical regions of the ion source. An attempt to increase the H_2^+ production in this manner with the source used for Fig. 6.1 was not successful. This information is complicated by the fact that the beam emittance was not sufficient with the small ripple remaining on the power supply (25 kv at 600 kv under load) when this work was done to allow for a complete analysis of the beam. (The replacement of all the rectifiers in the power supply took place in several steps over about a three-month period.) For example, the power monitored separately from the H^+, H_2^+, and H_3^+ components of a 200-ma beam with this 1-in. cup source totaled only 150 ma. After the final stage of rectifier replacement (ripple ~2 to 3%) a source with a 2-in. plasma surface was tried, and only 50% of a 260-ma beam was obtained by analysis through the $1\frac{5}{8}$-in. aperture. Using the more conventional ion source with a small plasma surface[4] and with the ripple decreased, all of each component could be focused through the aperture. There has not been time to do a detailed study of this source to determine if one can scale it to increase the H_2^+ production. One discouraging fact about this type of source as compared to the expanded anode sources is that with the maximum practical electric gradients of ~230 kv/cm, used on the test stand with reasonable stability, the total current obtainable with 150-kv extraction is only ~480 ma. A source has been operated with 300-kv extraction, but the stability with even lower potential gradient (200 kv/cm) was not as good.

A series of studies has been made with the 100-kv test stand to evaluate the optimum extraction geometry for a duoplasmatron ion source with a large plasma surface. The work began with a study of the profile of the plasma expanding from the anode aperture as a function of ion source operating parameters. The shape of the energetic electron stream from the ion source was determined by monitoring the floating potential of a very small probe. A typical set of profiles is shown in Fig. 6.2. Using this information as a guide, a series of extraction geometries was designed and tested. These tests were made by observation of a beam in a 14- to 16-in. drift space after extracting at energies of 50 to 100 kev and then neutralizing

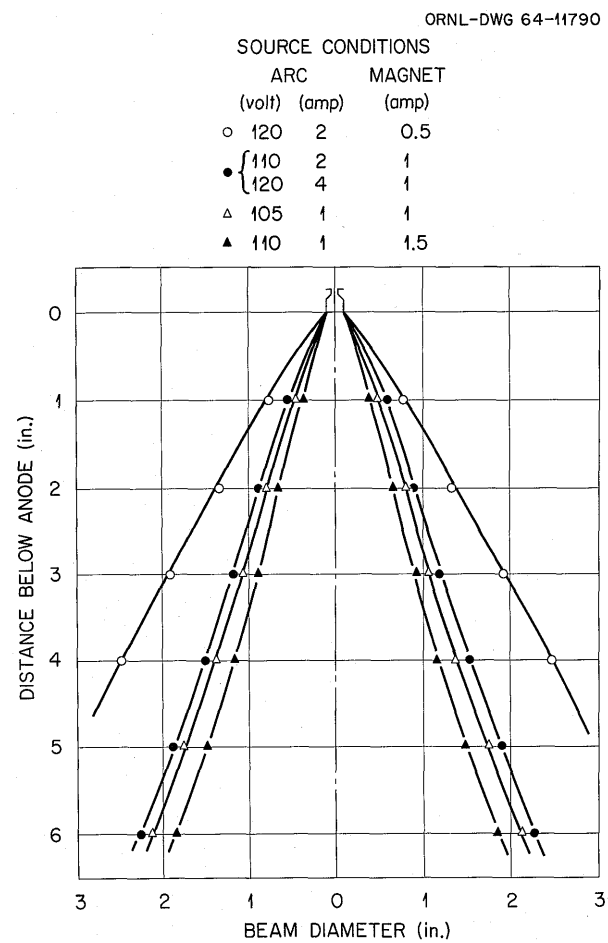

Fig. 6.2. Energetic Electrons from Duoplasmatron Ion Source.

[4]R. C. Davis *et al.*, *Thermonuclear Div. Semiann. Progr. Rept. Oct. 31, 1963*, ORNL-3564, p. 74 (Fig. 7.1).

by a set of accel-decel electrodes. (The important point for effective neutralization is that all surfaces in the region beyond the second electrode must be at the same potential.) In these studies it was found, as reported by other investigators,[5] that the interior of the anode expansion region could be shaped so that the quality of the beam was improved. The beam, which had previously contained a dense central region surrounded by a halo, was then confined to the central dense region. However, one finds that simultaneously the source arc and gas efficiency are reduced dramatically. These observations, combined with further investigation, indicate that the plasma from which the ions in the halo were extracted is now lost to the anode. Since high gas efficiency is critical to an intense high-energy injector and low arc currents are necessary for high molecular ion yields, this approach is not desirable. Some anode geometries (e.g., a 2-in.-diam expansion cylinder 3 in. long beneath the regular anode) without large plasma losses have been found that yield large ion beams (hundreds of milliamperes) that appear to have a small divergence with this type of test. However, when these anodes were incorporated with the 600-kv test stand, where the beam is passed through a $1\frac{5}{8}$-in.-diam aperture 100 in. from the lens, it was apparent, as discussed above, that the beam is not as desirable for this application. Beam emittance measuring equipment is being prepared to do a more detailed study of these beams on the 600-kv test stand.

The 100-kv test stand has also been used to study techniques for improving the DCX-1 600-kv injector. One immediate goal was to increase the H_2^+ beam available for Lorentz-force dissociation.[6,7] The present technique is to inject a 60-kev beam into a water vapor cell and separate by a transverse magnetic field analyzer the 40-kev H_2^+ beam, resulting from the H_3^+ component, for acceleration to 600 kev. An easily incorporated improvement was the inclusion of an accel-decel beam neutralizer at the exit from the electrostatic lens (Fig. 6.3). One previous current limitation had been space-charge forces in the beam at 60 kv reducing the available beam through the $\frac{5}{8}$-in.-diam gas cell to only ~10 ma. Use of an exact geometrical duplicate of this gas cell in the laboratory resulted in the same current limitations. The inclusion of the beam neutralizer has increased the available current through this cell to 30 to 50 ma at 60 kev. Figure 6.4 shows a 60-kv 50-ma neutralized beam. The beam size is ~0.3 to 0.4 in. in diameter and is shown over an ~10-in. drift space. Figure 6.5 shows this same beam when the neutralization is destroyed by biasing the target to remove the electrons. This system will soon be incorporated into the DCX-1

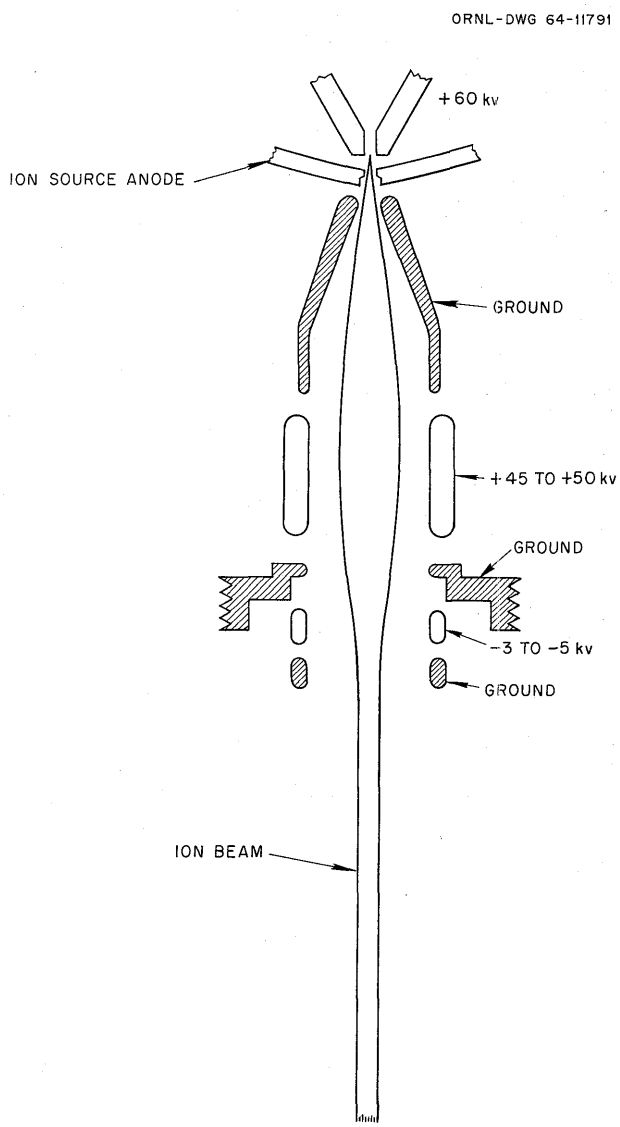

Fig. 6.3. Electrostatic Lens with an Accel-Decel Ion Beam Neutralizer Incorporated in Lower Section.

[5]N. B. Brooks *et al.*, *Rev. Sci. Instr.* **35**, 894 (1964).

[6]J. L. Dunlap *et al.*, *Thermonuclear Div. Semiann. Progr. Rept. Apr. 30, 1963*, ORNL-3472, pp. 6–8.

[7]J. L. Dunlap *et al.*, *Thermonuclear Div. Semiann. Progr. Rept. Oct. 31, 1963*, ORNL-3564, p. 10.

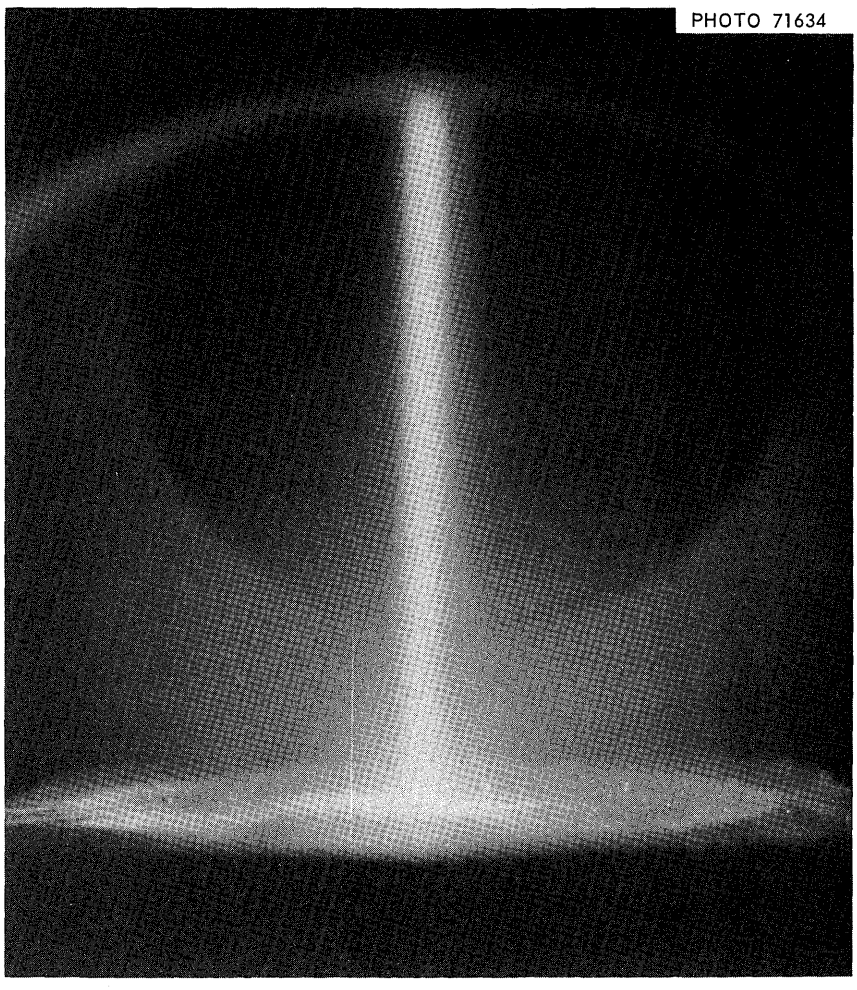

Fig. 6.4. 60-kev, 50-ma Neutralized Hydrogen Ion Beam. Diameter ~0.3 to 0.4 in.

injector. Based on the laboratory results this could increase the available beam for Lorentz dissociation by a factor of 3 to 5.

Studies have recently been started on the 100-kv test stand directed toward the production of large-current (100 ma to 1 amp) low-energy hydrogen ion beams because of the interest in large neutral beams. Initial work has consisted of experiments which could be done rapidly through the modification of existing equipment. A solenoid lens used earlier (1961) on the 100-kv test stand has been reinstalled.[8,9] It had been intended to use this lens to analyze beam currents in excess of 100 ma, but it was found that with the source very close to the lens (necessary at the time because of space-charge forces) the lens magnetic field made the H^+ component predominate. At that time, 100 ma of H^+ at 62 kev was passed through a ½-in. aperture located 12 in. below the lens. The total beam current and the drain on the power supply were 140 ma. The reassembled system uses an accel-decel neutralizer to eliminate space-charge forces above the lens. In initial tests with a large-cup duoplasmatron, ~100 ma of either H^+ or H_2^+

[8]R. C. Davis *et al.*, *Thermonuclear Div. Semiann. Progr. Rept. Jan. 31, 1961*, ORNL-3104, pp. 74–75.

[9]R. C. Davis *et al.*, *Thermonuclear Div. Semiann. Progr. Rept. Oct. 31, 1961*, ORNL-3239, p. 65.

at 40 kev have been passed through a $1\frac{1}{4}$-in. aperture located 12 in. below the lens, the total beam current being 200 ma. By visual observation the beam was actually about $\frac{3}{4}$ in. in diameter. A total current of 200 ma has also been extracted at 20 kev, but with large divergence. It may be possible to use grids at these low energies even for dc beams. With accelerating voltages greater than 40 kv much larger beams will be available. The present limitations are in the calorimeters and targets. These components are being improved.

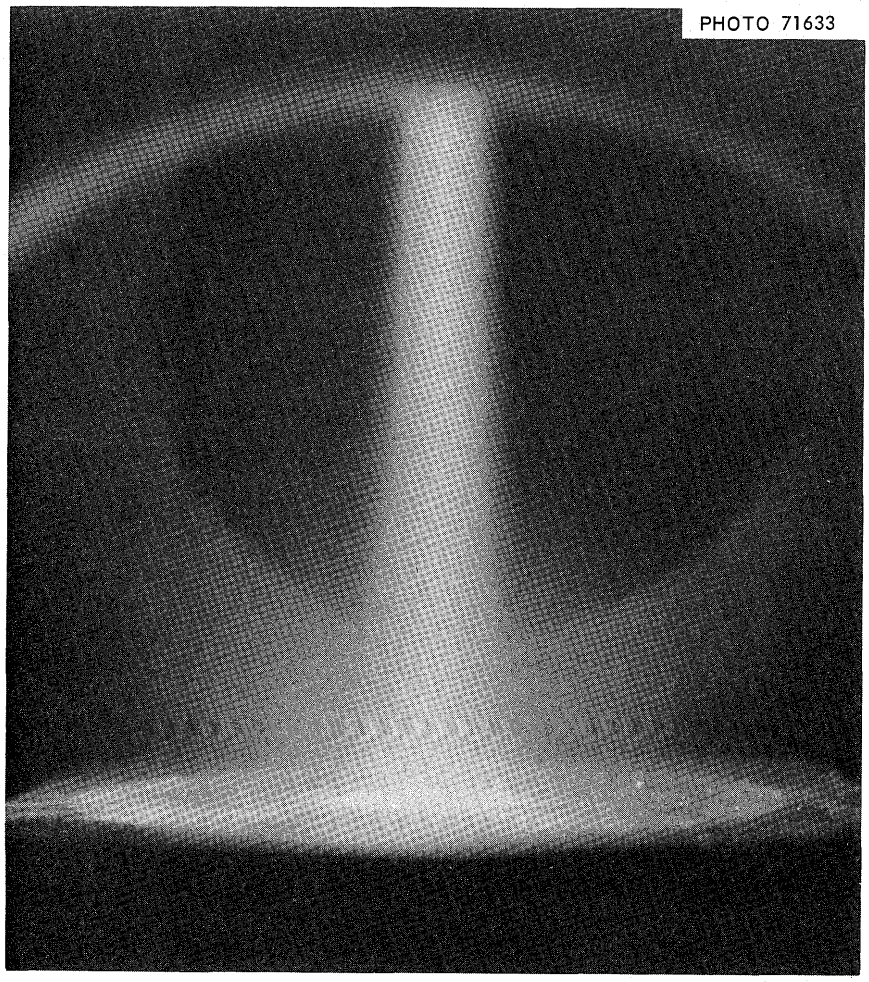

Fig. 6.5. 60-kev, 50-ma Unneutralized Hydrogen Ion Beam with Same Optical System Used in Fig. 6.4.

7. Plasma Theory and Computation

7.1 VELOCITY DIFFUSION BY MICROINSTABILITIES

T. K. Fowler[1]

One manifestation of microinstabilities in DCX's is the spreading, or diffusion, of particles in energy. To calculate this effect, the thermodynamic method of obtaining bounds on microinstability fluctuations, applied previously to estimating spatial diffusion in a torus, has now been applied to velocity diffusion perpendicular to $\vec{B}$. The characteristic time is that required to reverse the particle direction, essentially the slowing-down time. We estimate it in terms of Q defined by

$$Q = \frac{E_\perp^2}{8\pi n T_{\perp i}} , \qquad (1)$$

where $E_\perp$ is the electric field fluctuation amplitude, n is density, and $T_{\perp i}$ is the mean ion energy $\perp \vec{B}$. The reciprocal minimum slowing-down time for an ion, charge e, mass m_i, is $(eE/m_i v_i) \sim Q^{1/2}\,\omega_{pi}$ by (1), where ω_{pi} is the ion plasma frequency. The fraction of all ions which can be slowed down before the full field energy is achieved is Q. Hence, an estimate of the reciprocal average slowing-down time is $Q \cdot Q^{1/2}\,\omega_{pi}$, and the ion velocity diffusion coefficient perpendicular to $\vec{B}$ is

$$D_{vi} \lesssim (2T_{\perp i}/m_i)\, Q^{3/2}\,\omega_{pi} . \qquad (2)$$

The corresponding velocity spread is (for $\frac{1}{2} m_i \times \Delta v^2 < T_{\perp i}$) $\Delta v^2 = D_v \tau$, and the energy spread about an injection energy $T_{\perp i}$ is

$$\Delta E = (2T_{\perp i} m_i D_{vi} \tau)^{1/2} \lesssim 2T_{\perp i} (Q^{3/2} \omega_{pi} \tau)^{1/2} , \qquad (3)$$

where τ is the ion lifetime.

[1]Physics Division.

In applying (3) to DCX-1 and DCX-2 and similar experiments, we estimate Q thermodynamically as described in a forthcoming paper in *The Physics of Fluids*. Essentially, the estimate is the kinetic energy difference between the actual state and a stable (local thermal equilibrium) state toward which instabilities drive the plasma. Our estimate is, for low β,

$$Q = \frac{m_e}{m_i}\left(\frac{a_i}{R}\right)^2 + \frac{2}{3}\frac{\lambda^2}{R^2}\frac{T_e}{T_{\perp i}} + Q_v , \qquad (4)$$

where a_i is the ion gyroradius, R is the plasma radius, and λ, the predominant radial wavelength of the order of a_i, is taken as an unknown parameter. The term Q_v, representing free energy from pressure anisotropy and other non-Maxwellian properties of the velocity distribution, is also not known very well for the very anisotropic injection experiments.

Data on energy spread in DCX-2 fit (3) fairly well with $Q \sim 10^{-4}$, which happens to be the order of magnitude of the first two terms of (4) with $\lambda \sim a_i$ and $R \sim 2 - 3a_i$. For DCX-1, $Q \lesssim 10^{-5}$. At $Q = 10^{-5}$, $E_\perp = Q^{1/2}(T_{\perp i}/e\lambda_{Di}) = 10$ v/cm in DCX-1. Here λ_{Di} is the ion Debye length. New data from the ALICE experiment[2] indicate microinstability losses when $(\Delta E/T_{\perp i})$ would be appreciable according to (3) with $Q \sim 10^{-5}$. At the reduced magnetic field employed in these experiments conditions are about as in DCX-1.

Thus, existing data suggest that $Q_v \lesssim Q \lesssim 10^{-4}$. This is small, despite the fact that in these experiments both velocity anisotropy and the depletion of low-energy ions are acute.

Note the prediction, according to (3), that Q and hence ΔE go up as T_e is increased for sufficiently large T_e. Our approach no doubt omits some

[2]C. C. Damm *et al.*, *Phys. Rev. Letters* **13**, 464 (1964).

effects of stabilization by electron Landau damping. Our result should be interpreted to say that, unless fully successful, stabilization by heating electrons is harmful because more free energy becomes available to drive instabilities.

7.2 EFFECT OF A LOSS CONE ON THE ELECTROSTATIC STABILITY OF A UNIFORMLY MAGNETIZED PLASMA

G. E. Guest R. A. Dory

Rosenbluth and Post[3] have recently suggested that a maser-like amplification of electrostatic waves can take place in many plasmas of practical interest to the controlled fusion program. Such amplification may occur if the distribution of particle velocities, $f_0(v_\perp^2, v_z^2)$, vanishes at $v_\perp^2 = 0$, as is the case, for example, with energetic ions confined in a magnetic mirror configuration (perpendicular is with respect to the magnetic field $\vec{B} = B_0\vec{z}$).

A particularly convenient class of unperturbed distribution functions having this property is the following:

$$f_{0,\,\mathrm{ions}} = \frac{v_\perp^2}{\pi^{3/2}\alpha_{\perp i}^4\alpha_{zi}} \exp\left(-\frac{v_\perp^2}{\alpha_{\perp i}^2} - \frac{v_z^2}{\alpha_{zi}^2}\right).$$

A marginal stability analysis of the type described by Soper *et al.*[4] has been carried out using this ion distribution function together with a Maxwellian electron distribution function in the dispersion relation derived by Harris.[5] Regions of the usual parameter space were delineated in which amplification of electrostatic waves at frequencies near the ion gyrofrequency harmonics does occur. A typical display of such unstable regions is shown in Fig. 7.1. The terminology of this analysis is that used by Soper *et al.*,[4] and is summarized as follows:

$$\gamma = \frac{\omega}{k_z\alpha_{zi}}, \quad \gamma_c = \frac{\omega_{ci}}{k_z\alpha_{zi}}, \quad \gamma_p = \frac{\omega_{pe}}{k_z\alpha_{zi}},$$

$$\lambda = \frac{k_\perp^2\alpha_{\perp i}^2}{2\omega_{ci}^2} = \frac{1}{2}k_\perp^2 a_\perp^2,$$

$$\Theta = T_{ze}/T_{zi}, \qquad T_i = T_{zi}/T_{\perp i}.$$

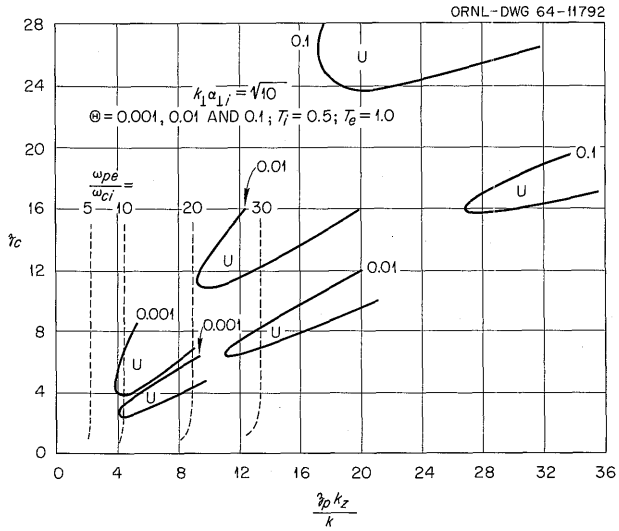

Fig. 7.1. Stability Zone Boundaries (Partial) for Three Electron Temperatures.

The full lines in Fig. 7.1 indicate the relative positions of the stability boundaries for three different electron temperatures. The dashed lines are drawn through points in this plane which satisfy the physical constraint

$$\left(\frac{\omega_{pe}}{\omega_{ci}}\right)^2 \frac{1}{(\gamma_p k_z/k)^2} = 2\lambda T_i + \frac{1}{\gamma_c^2},$$

which is identical to the relation $k^2 = k_\perp^2 + k_z^2$. For a given plasma density and magnetic field strength, only points on this locus are physically accessible. Points on the boundary lines in these diagrams describe propagation of waves having the following properties:

1. $k_\perp a_\perp = \sqrt{2\lambda}$,

2. $k_z a_\perp = \dfrac{1}{\gamma_c\sqrt{T_i}}$;

[3]M. N. Rosenbluth and R. F. Post (to be published).

[4]G. K. Soper and E. G. Harris, *Thermonuclear Div. Semiann. Progr. Rept. Oct. 31, 1963*, ORNL-3564.

[5]E. G. Harris, *J. Nucl. Energy* **C2**, 138 (1961).

3. the angle between $\vec{k}$ and $\vec{B}$ is then given by

$$\tan\theta = \frac{k_\perp}{k_z} = \gamma_c\sqrt{2\lambda T_i} \ .$$

Thus, for example, the waves represented in Fig. 7.1 all have a perpendicular component of wavelength $\lambda_\perp \cong 2a_\perp$. For $\Theta = 0.001$ and $\omega_{pe}/\omega_{ci} = 10$, the parallel components of the wavelengths of the first and second harmonics of the gyrofrequency are around $24a_\perp$ and $12a_\perp$ respectively. Waves near the first gyrofrequency harmonic will grow if their angles of propagation lie between 83 and 86°.

Figure 7.2 illustrates the mapping of boundaries in the γ_c-$\gamma_p k_z/k$ plane into the γ_c-γ plane. If one assumes the growth to be temporal, that is, if $\vec{k}$ is real, he can estimate the growth rates of the unstable waves. For instance, in the $\Theta = 0.001$, $\omega_{pe}/\omega_{ci} = 10$ case cited above, the most rapidly growing wave in the first harmonic region is characterized as follows:

$$\mathrm{Re}(\omega) \cong 0.93\ \omega_{ci} \ ,$$

$$\mathrm{Im}(\omega) \cong 2.5 \times 10^{-3}\ \omega_{ci} \ ,$$

$$\Theta \cong 85° \ .$$

For $\Theta = 0.001$ but $\omega_{pe}/\omega_{ci} \cong 15$, the corresponding numbers are

$$\mathrm{Re}(\omega) \approx 0.95\ \omega_{ci} \ ,$$

$$\mathrm{Im}(\omega) \approx 6 \times 10^{-2}\ \omega_{ci} \ ,$$

$$\Theta \cong 86.4° \ .$$

Figures 7.3 and 7.4 demonstrate the appearance of unstable modes near the higher harmonics of the ion gyrofrequency if one considers successively smaller values of $\lambda_\perp$, the perpendicular wavelength of the disturbance. It is also clear from these figures that proportionately larger values of ω_{pe}/ω_{ci} are required to sustain growing waves in these cases.

It has been found that the unstable zone boundaries lie above a minimum value of γ_c given approximately by the following expression:

$$\gamma_{c,\min} \cong \frac{1}{N}\sqrt{\frac{\Theta}{\delta}\ln\left(\frac{9N\sqrt{\pi}}{T_i\Theta}\sqrt{\frac{\delta}{\Theta}}\right)} \ ,$$

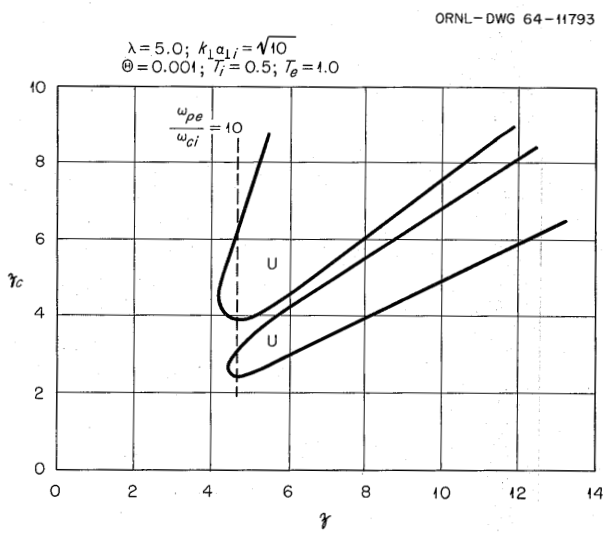

Fig. 7.2. Frequency Bands (Partial) Associated with the Unstable Zone Shown in Fig. 7.1 for $\Theta = 0.001$.

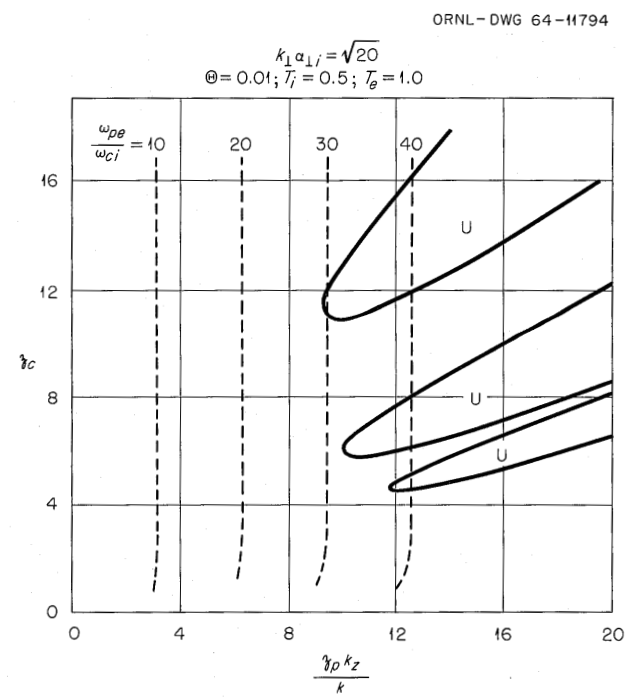

Fig. 7.3. Stability Zone Boundaries (Partial) for Smaller Perpendicular Wavelengths.

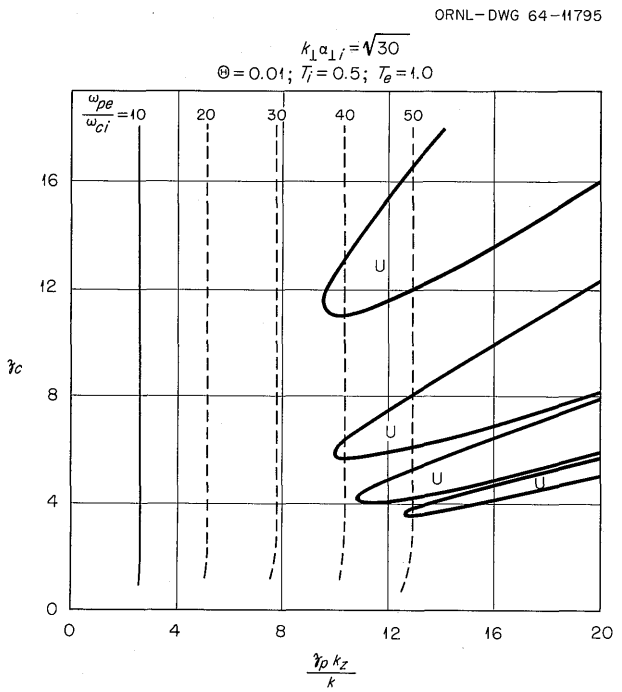

Fig. 7.4. Stability Zone Boundaries (Partial) for Even Smaller Perpendicular Wavelengths, Illustrating the Appearance of Additional Unstable Harmonics.

where N is the harmonic number of the unstable zone in question and δ is the ratio of electron mass to ion mass. Moreover, the unstable zone will only appear if $\lambda \gtrsim N^2$, and in fact, the minimum value of γ_c given above assumes that $\lambda \gtrsim \frac{9}{2}N^2$.

Present efforts are being directed toward more transparent ways of presenting the results of this type of marginal stability dispersion relation analysis.

7.3 ELECTROSTATIC INSTABILITIES IN A PLASMA

Yaakov Shima

The dispersion equation for electrostatic waves in an infinite plasma, situated in a constant magnetic field, has been investigated in a paper to be published.[6]

[6]L. S. Hall and Yaakov Shima, *Note on Electrostatic Instabilities in a Plasma with Anisotropic Velocity Distribution*, ORNL-TM-919. (To be published in *Physical Review Letters*.)

It was found that a system described by a bi-Maxwellian distribution function f_0,

$$f_0(v_{\parallel}, v_{\perp}) \sim \exp\left(-\frac{mv_{\parallel}^2}{2kT_{\parallel}} - \frac{mv_{\perp}^2}{2kT_{\perp}}\right),$$

is stable if $T_{\parallel}/T_{\perp} > \frac{1}{2}$, where $T_{\parallel}$ and $T_{\perp}$ are, respectively, the temperatures parallel and perpendicular to the magnetic field.

The same result is true when the distribution function is Maxwellian in the perpendicular direction and Lorentzian in the parallel direction,

$$f_0(v_{\parallel}, v_{\perp}) \sim \left(1 + \frac{mv_{\parallel}^2}{2kT_{\parallel}}\right)^{-1} \exp\left(-\frac{mv_{\perp}^2}{2kT_{\perp}}\right).$$

7.4 DCX-2 DECAY CURVES

C. O. Beasley, Jr. Mozelle Rankin

A numerical computation which is thought to represent, mathematically, all dominant processes which occur in DCX-2 upon beam turnoff has been attempted. The processes included in the program are loss of particles through charge-exchange collisions with background neutral gas atoms, scattering losses out the mirrors by collisions with electrons in the lithium arc and as computed by the Fokker-Planck code,[7] ion cooling by collisions with the electrons in the arc, and ion-energy diffusion through ion-ion collisions. The rate of the latter process can be increased to account for some nonclassical enhanced diffusion process.

The input data for the program consist of an integral (over the volume of the machine) neutral-particle detector signal (neutral current) as seen in the machine before beam turnoff. The signal is converted to a particle distribution $n(E)$ by using a given charge-exchange cross section. An analytic fit to the latest data by Barnett[8] for nitrogen is

[7]Mozelle Rankin and T. K. Fowler, *Thermonuclear Div. Semiann. Progr. Rept. Apr. 30, 1963*, ORNL-3472, p. 82.

[8]C. F. Barnett, W. B. Gauster, and J. A. Ray, *Atomic and Molecular Cross Sections of Interest in Controlled Thermonuclear Research*, ORNL-3113.

used to obtain the cross section. The form of this fit is

$$\sigma_{cx} = \frac{8.64 \times 10^{-10}}{\sqrt{E}(E^3 + 6.46 \times 10^5)} .$$

Nitrogen is thought to account for most charge-exchange loss.

The code then integrates the distribution $n(E)$ in small time steps; new distributions are printed out when requested. Also printed out are the average particle density in the machine, $n = \int dE\ n(E)$, and more important, the neutral particle current which would be observed at a given time from a given distribution $n(E)$. Thus one may obtain a decay curve for the neutral particle current as observed from the plasma.

The parameters used are:

background density $n_0 = 10^{10}/\text{cm}^3$,

arc density $n_e = 10^{13}/\text{cm}^3$,

electron temperature $T_e = 30$ ev ,

particle density normalized at $t = 0$ to $10^{11}/\text{cm}^3$.

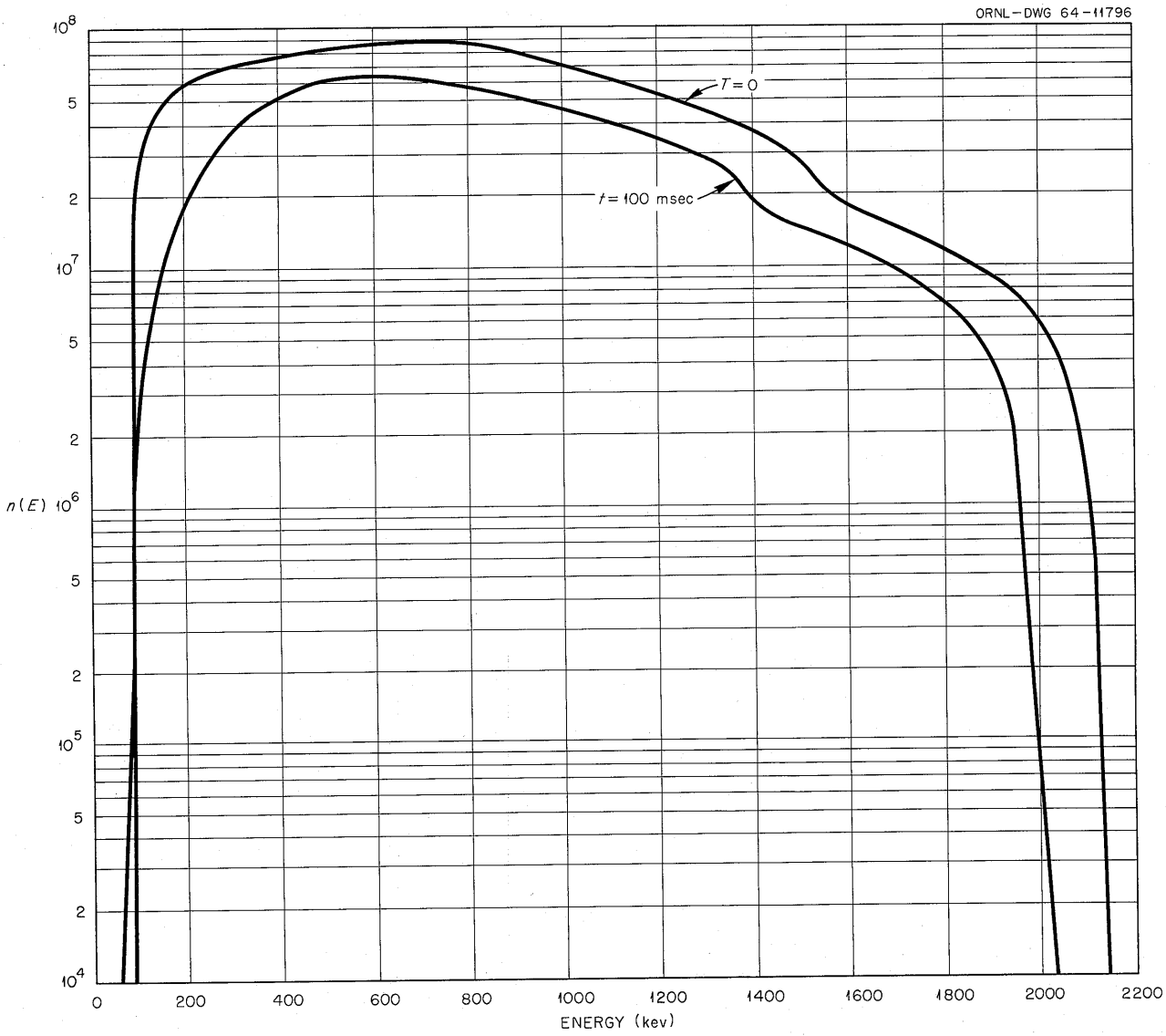

Fig. 7.5. Energy Distributions in DCX-2 at $t = 0$ (Before Beam Turnoff) and 100 msec After Beam Turnoff.

The arc electrons are averaged over the entire volume of the plasma, since all particles are thought to sample the arc through their precession. For these parameters, one should expect an ion-ion diffusion time of around 100 sec, so this process should be completely negligible. This process was assumed to entail only classical diffusion for the case considered. Ion cooling occurs at the rate of 3 kev/msec. Charge-exchange time for 300-kev particles is about 100 msec.

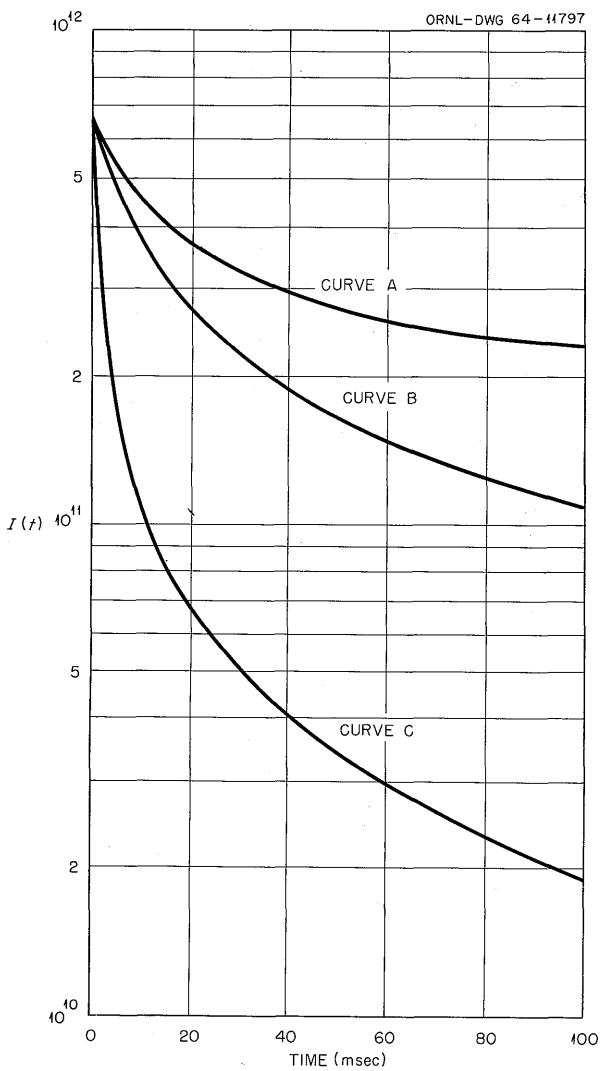

Fig. 7.6. Neutral Particle Current Decay. Curve A: calculation includes cooling, diffusion, mirror losses; $n_0 = 10^{10}$. Curve B: loss through charge exchange only; $n_0 = 10^{10}$. Curve C: loss through charge exchange only; $n_0 = 10^{11}$.

Figure 7.5 shows the initial distribution $n(E)$ and the distribution as it would appear at 100 msec. A loss occurs at high energy, and the rate of drop of the distribution is consistent with the cooling rate. High loss rate at low energies is caused by the large charge-exchange cross section.

In Fig. 7.6, curve A is a plot of neutral particle current as a function of time. For comparison purposes, a plot of the same quantity considering charge exchange to be the only loss mechanism is shown by curve B. (This calculation involves no integration and is much faster than the entire code.) The initial decay, that is, the slope at $t = 0$, should reflect loss by charge exchange alone, since any diffusion requires a finite time to cause a change of shape of $n(E)$ which would change this slope. This is true even considering enhanced diffusion. Also, charge exchange of course dominates over mirror losses. The role of the background density is also seen in Fig. 7.6 by noting the different decay for $n_0 = 10^{11}/\text{cm}^3$.

7.5 COLLISIONAL AND ANOMALOUS DIFFUSION

E. G. Harris[9] O. C. Eldridge[9]

This is a preliminary account of work in progress.

We calculate the diffusion coefficient in the following manner: We solve the equations of motion for a charged test particle in a constant magnetic field and a fluctuating electric field. The electric field is taken to be a superposition of longitudinal plane waves. Thus

$$\vec{E}(\vec{x},t) = -\nabla\phi$$

$$= \sum_{\lambda=-\infty}^{+\infty} \int \frac{d^3k}{(2\pi)^3} \vec{E}^{\lambda}(\vec{k})\, e^{i(\vec{k}\cdot\vec{x} - \Omega_k^{\lambda} t)} \quad . \qquad (1)$$

We have in mind waves due to an instability such as a cyclotron instability. In general there will be many frequencies, Ω_k^{λ} for each wave vector $\vec{k}$, so we distinguish between these by the superscript λ. We make the approximation that $\vec{E}(\vec{x},t)$ can be evaluated at the position of the particle on its

[9]Consultants, University of Tennessee.

unperturbed path. We assume that the different waves are uncorrelated so that

$$\left\langle E_l^{\lambda}(\vec{k})\, E_m^{\mu}(\vec{k}\,')\right\rangle = (2\pi)^3\, P^{\lambda}(\vec{k})\, \frac{k_l k_m}{k^2}\, \delta_{\lambda\mu}\, \delta(\vec{k}+\vec{k}\,') \ , \quad (2)$$

where the angular bracket indicates an ensemble average. We call the quantity $P^{\lambda}(\vec{k})$ the energy spectrum. It is related to the energy density in the electric field by

$$\left\langle \frac{E^2(\vec{k},t)}{8\pi}\right\rangle = \frac{1}{8\pi}\sum_{\lambda}\int \frac{d^3k}{(2\pi)^3}\, P^{\lambda}(\vec{k}) \ . \quad (3)$$

We find that for large times (times much longer than the period of a typical wave), the mean-square departure of the test particle perpendicular to the magnetic field from its unperturbed path is proportional to time. That is,

$$D_{\perp} = \lim_{t\to\infty} \frac{\left\langle (\Delta x_{\perp})^2\right\rangle}{t} = \text{constant} \ . \quad (4)$$

We interpret $D_{\perp}$ as the diffusion coefficient for diffusion across the magnetic field. For a particle of velocity $\vec{V} = (\vec{V}_{\perp}, V_z)$, charge e, mass m, and cyclotron frequency ω_c it is

$$D_{\perp} = \frac{e^2}{m^2}\frac{2\pi}{\omega_c^2}\sum_{\lambda=-\infty}^{+\infty}\sum_{n=-\infty}^{+\infty}\int \frac{d^3k}{(2\pi)^3}\, P^{\lambda}(\vec{k})\, \frac{k_{\perp}^2}{k^2}$$
$$\times\left[J_n^2\left(\frac{k_{\perp}V_{\perp}}{\omega_c}\right) + \frac{1}{2}J_{n-1}^2\left(\frac{k_{\perp}V_{\perp}}{\omega_c}\right) + \frac{1}{2}J_{n+1}^2\left(\frac{k_{\perp}V_{\perp}}{\omega_c}\right)\right]$$
$$\times\, \delta(k_z V_z - \Omega_k^{\lambda} + n\omega_c) \ . \quad (5)$$

The diffusion coefficients in velocity space have also been calculated. They are

$$\frac{\left\langle (\Delta v_z)^2\right\rangle}{t} = 2\pi\frac{e^2}{m^2}\sum_{\lambda=-\infty}^{+\infty}\sum_{n=-\infty}^{+\infty}\int\frac{d^3k}{(2\pi)^3}P^{\lambda}(\vec{k})\frac{k_z^2}{k^2}$$
$$\times J_n^2\left(\frac{k_{\perp}V_{\perp}}{\omega_c}\right)\delta(k_z V_z - \Omega_k^{\lambda} + n\omega_c) \quad (6)$$

and

$$\frac{\left\langle (\Delta V_{\perp})^2\right\rangle}{t} = 2\pi\frac{e^2}{m^2}\sum_{\lambda=-\infty}^{+\infty}\sum_{n=-\infty}^{+\infty}\int\frac{d^3k}{(2\pi)^3}P^{\lambda}(\vec{k})\frac{k_{\perp}^2}{k^2}$$
$$\times\left[\frac{1}{2}J_{n+1}^2\left(\frac{k_{\perp}V_{\perp}}{\omega_c}\right) + \frac{1}{2}J_{n-1}^2\left(\frac{k_{\perp}V_{\perp}}{\omega_c}\right)\right]$$
$$\times\, \delta(k_z V_z - \Omega_k^{\lambda} + n\omega_c) \ . \quad (7)$$

In the above equations J_n is the Bessel function of order n.

The spirit of this calculation is the same as that of Drummond and Rosenbluth,[10] but it differs from their calculation in that we have not made a simplifying assumption which was made in their paper. They assumed that the motion across the field was given by the drift velocity cE/B. We do not make this assumption. Our result should be more accurate if the typical frequencies are near the cyclotron frequency and typical wavelengths are near the Larmor radius.

Before the calculation can be completed, $P^{\lambda}(\vec{k})$ must be found. In the paper by Drummond and Rosenbluth[10] it was found from a quasi-linear calculation assuming a particular instability.

For collisional diffusion the energy spectrum may be calculated by calculating the fields due to uncorrelated dressed test particles (sometimes called dressticles). The result is

$$P^{\lambda}(\vec{k}) = (4\pi e_{\alpha})^2 \frac{J_n^2(k_{\perp}v_{\alpha\perp}/\omega_{c\alpha})}{k^2\,|\,\epsilon(\vec{k}, k_z v_{z\alpha} + n\omega_{c\alpha})\,|^2} \ . \quad (8)$$

In Eq. (8), λ stands for both n, the harmonic number, and α, which denotes the particle. The summation over λ becomes a summation over n, an integration over the velocity distribution of the particles of species s, and a sum over species. The quantity $\epsilon(\vec{k},\omega)$ is the plasma dielectric

[10] W. E. Drummond and M. N. Rosenbluth, *Phys. Fluids* **5**, 1507 (1962).

constant. Substituting into Eq. (5) gives the collisional diffusion coefficient:

$$D_\perp = \frac{e^2}{m^2}\frac{2\pi}{\omega_c^2}\sum_s \sum_{n'=-\infty}^{+\infty} \sum_{n=-\infty}^{+\infty} \int d^3v\, f_s(\vec{v}) \int \frac{d^3k}{(2\pi)^3}$$

$$\times \left[J_n^2\left(\frac{k_\perp V_\perp}{\omega_c}\right) + \frac{1}{2} J_{n-1}^2\left(\frac{k_\perp V_\perp}{\omega_c}\right) + \frac{1}{2} J_{n+1}^2\left(\frac{k_\perp V_\perp}{\omega_c}\right)\right] \delta[k_z(V_z - v_z)$$

$$+ n\omega_c - n'\omega_{cs}] \frac{k_\perp^2}{k^2} \frac{(4\pi e_s)^2 J_{n'}^2(k_\perp v_\perp/\omega_{cs})}{|\epsilon(\vec{k}, k_z v_z + n'\omega_{cs})|^2} . \quad (9)$$

The dielectric constant which enters Eq. (9) is

$$\epsilon(\vec{k},\omega) = 1 - \sum_s \sum_{n=-\infty}^{+\infty} \frac{\omega_{ps}^2}{k^2} \int d^3v \frac{J_n^2(k_\perp v_\perp/\omega_c)}{(\omega + k_z v_z + n\omega_{cs})}$$

$$\times \left(\frac{n\omega_{cs}}{v_\perp}\frac{\partial f_s}{\partial v_\perp} + k_z \frac{\partial f_s}{\partial v_z}\right) . \quad (10)$$

It should be noted that Eq. (9) is actually divergent. The integration over k_z gives a factor

$$\frac{1}{|V_z - v_z|} ,$$

which blows up in the integration over v_z unless $f_s(\vec{v})$ vanishes for $v_z = V_z$. Physically, the origin of the divergence is the following: The particles which have the same velocity parallel to the field as the test particle act on it for an infinitely long time and produce an infinite drift. The fault lies in our assumption that the field could be calculated at the unperturbed position of the test particle. Actually, when the test particle has drifted a distance about equal to an interparticle distance, the configuration of particles in its neighborhood will change and the direction of its drift will change. Some sort of cutoff must be invoked to take this into account.

The same sort of divergence occurs in Eqs. (5), (6), and (7), where the integration over k_z gives a factor $|V_z - \partial\Omega_k^\lambda/\partial k_z|^{-1}$, which may diverge if the velocity of the test particle equals the group velocity of one of the waves in the plasma. This was not explicitly noted in the paper by Drummond and Rosenbluth,[10] where this factor was set equal to $|V_z|^{-1}$.

7.6 EFFECT OF PLASMA POTENTIAL ON MINIMUM-B STABILITY

T. K. Fowler

The early proofs that magnetic wells (minimum-B) inhibit interchange instabilities applied only to charge-neutral plasmas at low pressure. Recently, Hastie and Taylor[11] have shown that stability persists to high plasma pressure. We have now found that stability persists also despite the sizable plasma potential expected to develop because of the difference in ion and electron loss rates with mirror confinement. The potential ϕ has two destabilizing influences: interchange moves a net charge outward from the charge center and thereby reduces the potential energy, and it moves a net charge toward weaker fields and thereby reduces $\vec{E} \times \vec{B}$ drift energy. However, since we find that $\nabla\phi$ and ∇B are parallel, in a magnetic well these energy decreases are always compensated by an increase in magnetic potential, μB. We estimate $e\phi \sim T_e$ and $|\nabla \ln \phi|^{-1} \sim R$, the plasma radius. Then the changes in electric potential energy and drift energy are smaller than the change in magnetic potential by factors $(\lambda_{De}/R)^2(B/\Delta B)$ and $(a_i/R)^2(B/\Delta B)$, respectively, where λ_{De} is the Debye length, a_i the ion gyroradius, and ΔB the magnetic well depth. Thus, previous stability criteria neglecting the electric energies remain valid and stability is assured if the plasma pressure is maximum at the magnetic minimum.[12] Equilibria having this property can be exhibited. Recent experiments by Gibbons and Lazar,[13] in which flutes in arcs are suppressed by very shallow magnetic wells, give qualitative support to our results.

---

[11] R. J. Hastie and J. B. Taylor, *Phys. Letters* **9**, 241 (1964); *Phys. Rev. Letters* **13**, 123 (1964).

[12] J. B. Taylor, *Phys. Fluids* **7**, 767 (1964); H. P. Furth, *Phys. Rev. Letters* **11**, 308 (1963).

[13] R. A. Gibbons and N. H. Lazar, this report, sect. 4.7.

8. Magnetics and Superconductivity

8.1 DCX-2 BEAM INJECTION DUCT

P. R. Bell R. L. Brown J. S. Culver

Previous reports[1] have described the beam injection duct (snout) and its function in DCX-2. This report will follow up with some additional engineering details. All remarks will be confined to the latest model snout.

Hiperco (a high-permeability material composed of 70% iron and 30% cobalt) not only shields the injection duct magnetically, but also provides a structural support for the correcting coils. Abnormal magnetic forces will result if trouble occurs in the surrounding coils or in the main field coils. The Hiperco was machined on an automatic coded milling machine (see Figs. 8.1 and 8.2). This intricate machining was performed to match the shape of the transverse corrector coil, which is formed to fit the lands in the Hiperco, as shown in Fig. 8.3.

The transverse corrector coil (Fig. 8.4) almost exactly counteracts the magnetic distortion created by the Hiperco. Turns of varying length compensate for the varying field strength entering transverse to the axis of the injection duct.[2] Water path lengths were adjusted to be approximately the same in each of the four water currents. For most turns the conductors have been reduced to one-half size at the end of the Hiperco because of the very limited amount of space available and the need for getting around the hole forming the injection duct.

The helical corrector coil consists of three major parts (Fig. 8.5). The upper part is separated from the lower parts to make room for the mechanical support. The middle part terminates into a bus that connects to the lower part, which consists of four smaller segments connected electrically and hydraulically in parallel. From Fig. 8.5 it can be seen that the ampere turns per inch vary along the length of the coil because of the varying magnetic field that the coil must produce.[3] The field to be canceled is shown in Fig. 8.6 along

[1] *Thermonuclear Proj. Semiann. Progr. Rept. July 31, 1960,* ORNL-3011; *Thermonuclear Div. Semiann. Progr. Rept. Jan. 31, 1961,* ORNL-3104; *Thermonuclear Div. Semiann. Progr. Rept. Oct. 31, 1961,* ORNL-3239; *Thermonuclear Div. Semiann. Progr. Rept. Apr. 30, 1962,* ORNL-3315; P. R. Bell *et al., Engineering Features of DCX-2,* ORNL-3325 (July 12, 1963).

[2] L. J. Bledsoe, *Calculations for Redesign of Snout Transverse Field Shielding Coil,* DCX-2 Technical Memorandum No. 101 (Dec. 17, 1962).

[3] L. J. Bledsoe, C. E. Parker, and P. A. Thompson, *Snout Region Field Calculations,* DCX-2 Technical Memorandum No. 100 (Nov. 1, 1962).

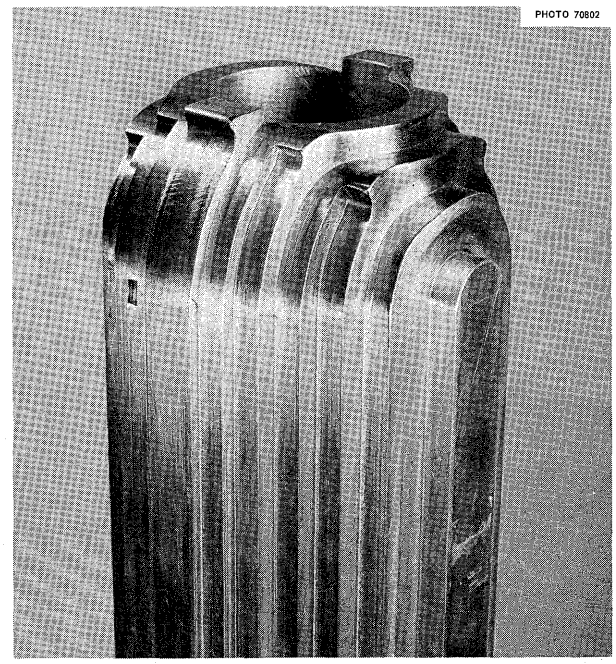

Fig. 8.1. End View of Hiperco.

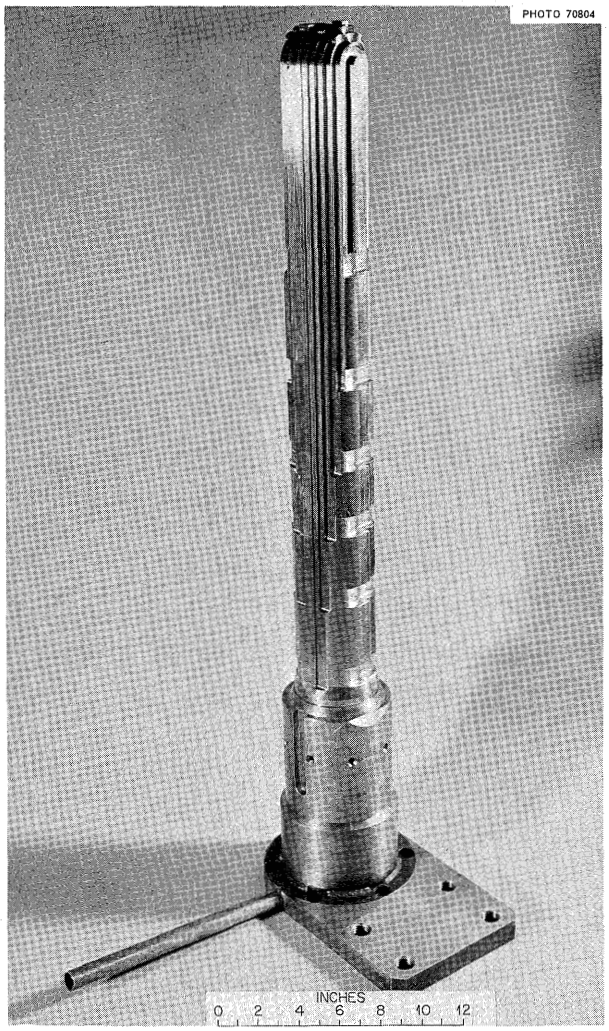

Fig. 8.2. Hiperco.

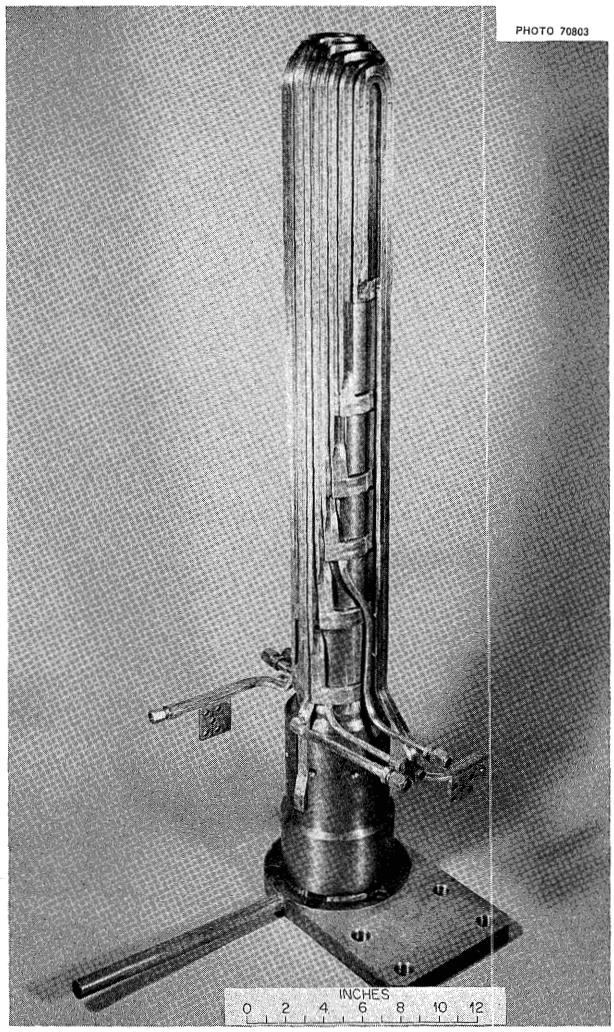

Fig. 8.3. Hiperco and Transverse Corrector Coil.

with the actual measured field of the coil without the presence of the Hiperco. Fine adjustments were made by shifting individual turns up or down the axis until the best fit was obtained. The coil was potted in glass-cloth-reinforced epoxy to hold turn positions and provide structural strength. The dip observed between the upper and middle sections is due to the gap in the coil required for the mechanical support. Fortunately the field strength at this position is not high enough to saturate the Hiperco, and no transverse field penetration occurs. By adding a mirror image of the field at the end of the coil to the measured field, an approximation can be obtained of the field shape with the presence of the Hiperco, which exactly matches the desired field.

A view of both coils mounted on the Hiperco is shown in Fig. 8.7. The completely assembled snout is shown in Figs. 8.8 and 8.9. Magnetic measurements of the completed snout after installation in DCX-2 are shown in Figs. 8.10 and 8.11.[4] Good shielding of the beam from the 12-kilogauss external field is obtained, and no evidence of disturbance of the main plasma by residual external field has been noted.

[4] O. B. Morgan and R. C. Davis, DCX-2 Data Supplement (June 5, 1964).

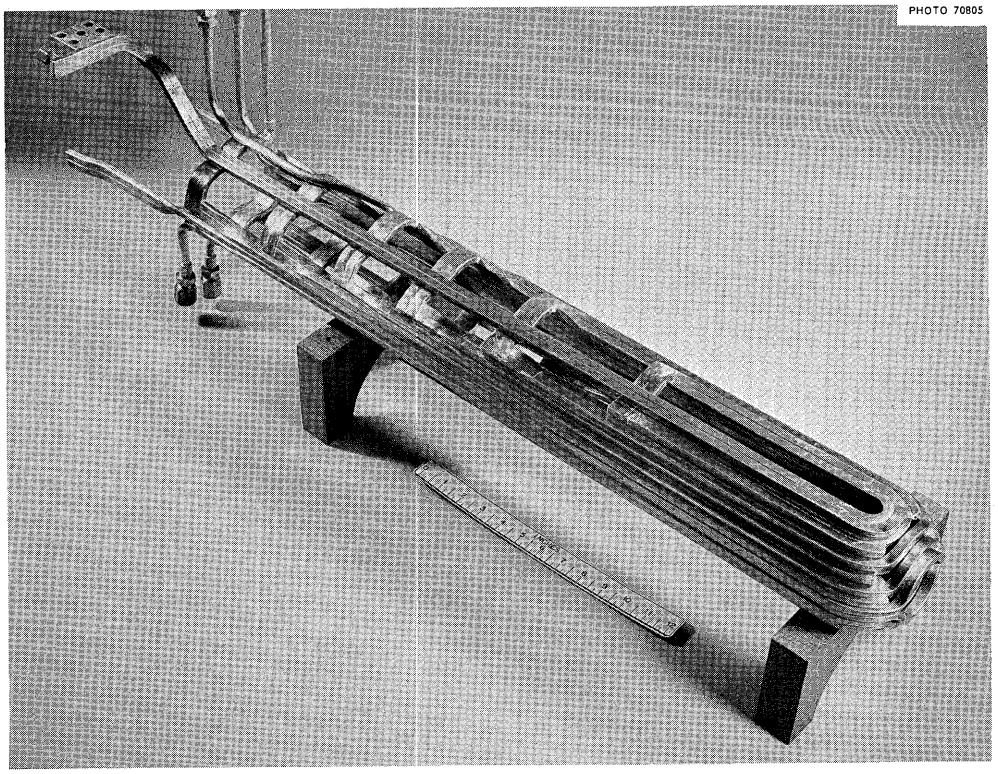

Fig. 8.4. Transverse Corrector Coil.

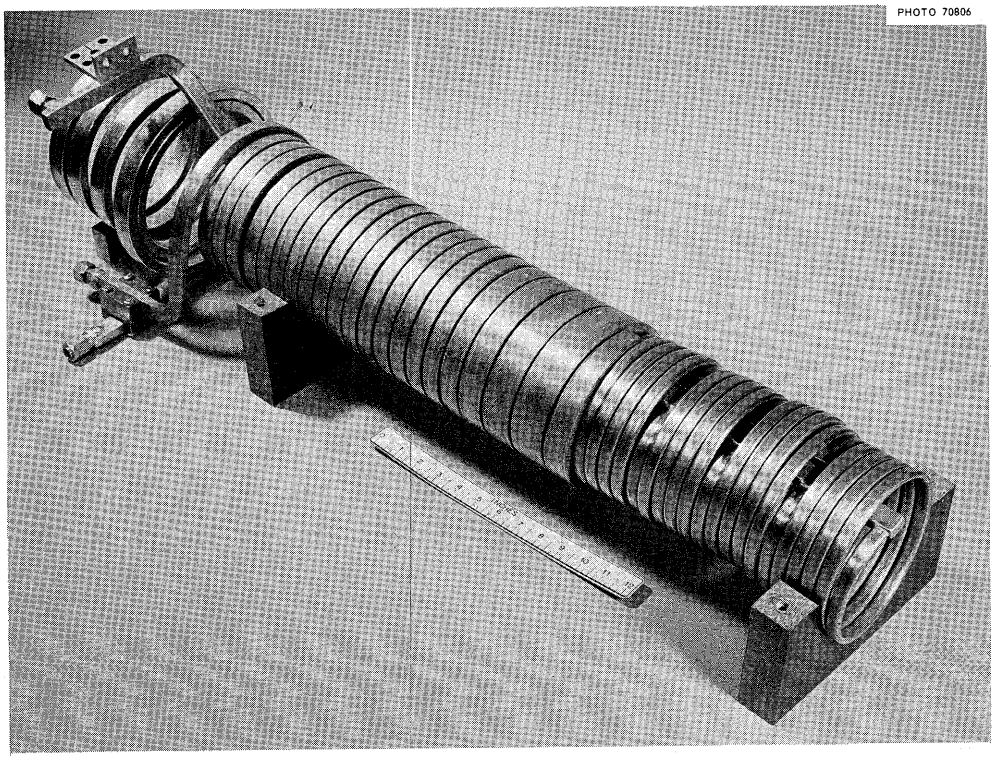

Fig. 8.5. Helical Corrector Coil.

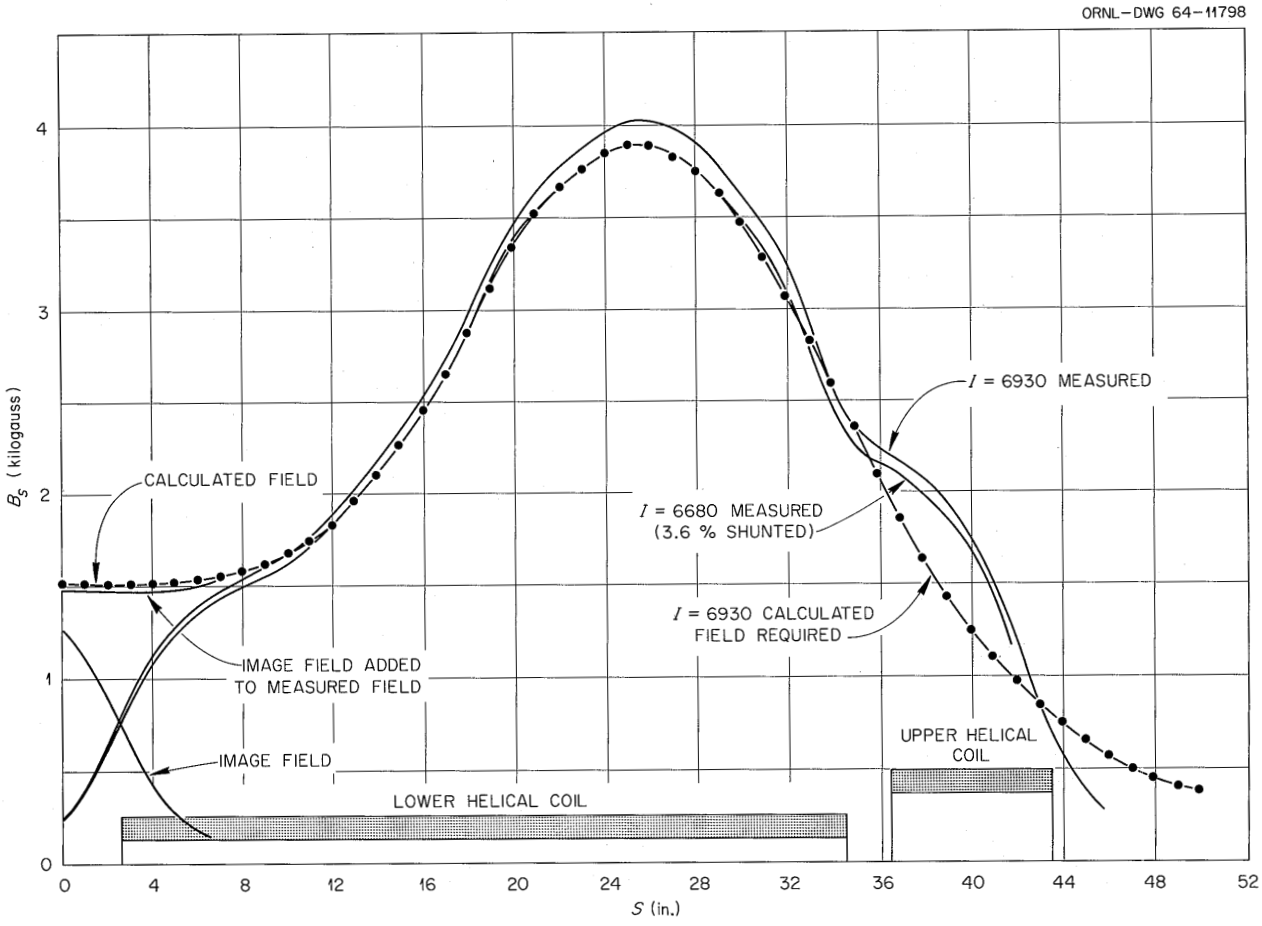

Fig. 8.6. DCX-2 Snout – Helical Coils B_s vs S.

Pertinent specification data are shown in Table 8.1.

8.2 DESIGN OF A HIGH-HOMOGENEITY, POWER-OPTIMIZED SOLENOID

J. N. Luton, Jr. C. E. Parker

A method of minimizing the power in a conventional coil while simultaneously optimizing the field homogeneity was described in the preceding report.[5] Lagrange's method of undetermined multipliers was used to find the current density distribution which, under the auxiliary condition that the field shape be of a certain "order," gives the highest central field strength for a given power. The numerical work to solve for the current density i was coded for a digital computer.

The above method and resulting code have now been applied to the design of solenoids of sixth and of eighth order. It was assumed that such a water-cooled copper coil should consume 7 Mw and produce about 60 kilogauss over a cylinder 13 in. in diameter by 13 in. long.

The coil weight was first fixed by cost considerations at approximately 7000 lb. This corresponds to a volume factor $v = 2\pi(\alpha^2 - 1)\beta \approx 100$. The field homogeneity optimization procedure was performed with various β values and

[5] W. F. Gauster and M. W. Garrett, *Thermonuclear Div. Semiann. Progr. Rept. Apr. 30, 1964*, ORNL-3652, pp. 105–12.

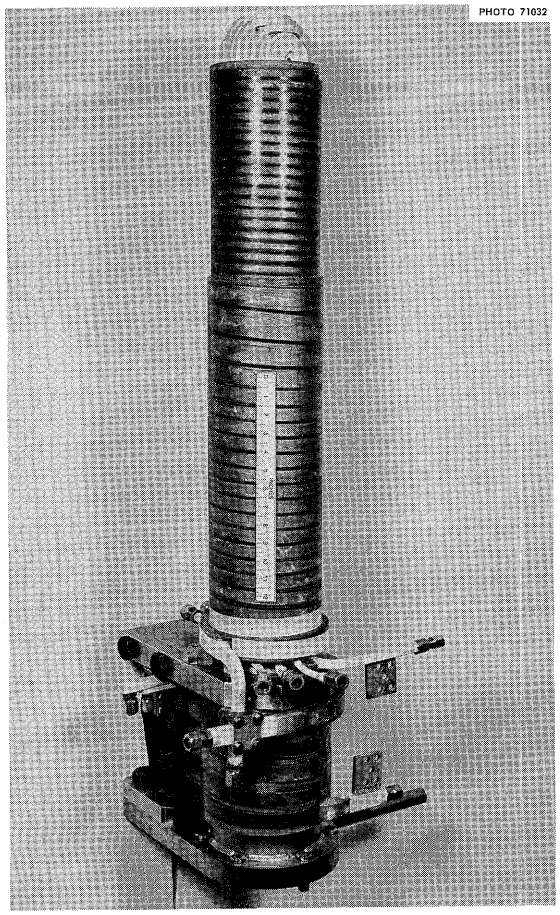

Fig. 8.7. Coils Assembled on Hiperco.

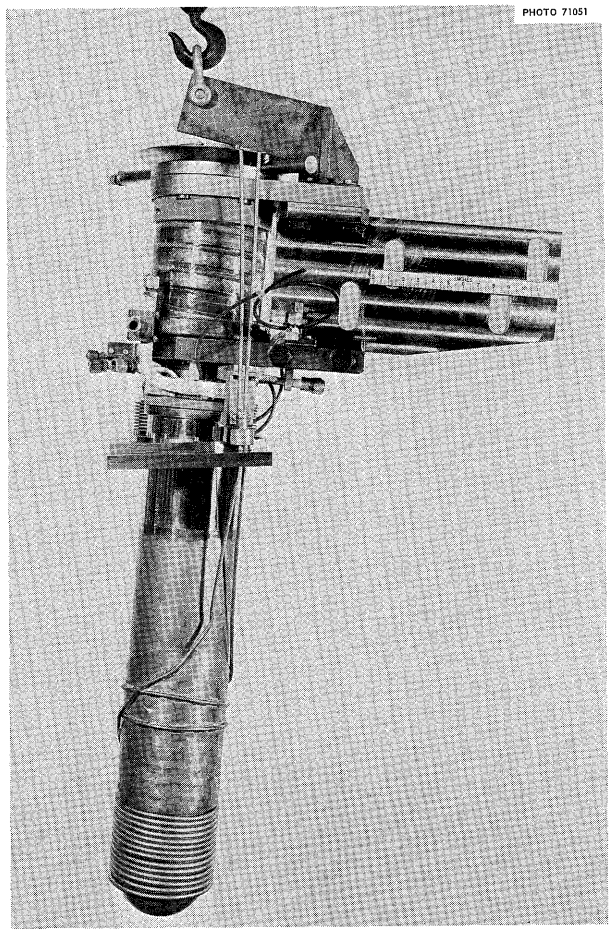

Fig. 8.8. Completely Assembled Snout. View looking north.

Table 8.1. Snout Coil Specifications

Transverse Coil	Helical Coil
$I = 6930$ amp	$I_{tot} = 6930$ amp (0.036 I_{tot} goes through parallel shunt)
$V = 24$ v	$V = 9.6$ v
$P = 166$ kw	$P = 67$ kw
$N = 14$ turns	$N_1 = 26$ turns at $I = 6680$ amp
$Q = 29$ gpm water	$N_2 = 20$ turns at $I = 1336$ amp
$\Delta p = 180$ psi pressure drop	$Q = 8.9$ gpm
$\Delta t = 35^\circ$C maximum ambient water temperature	$\Delta p = 180$ psi pressure drop
	$\Delta t = 30^\circ$C ambient water temperature

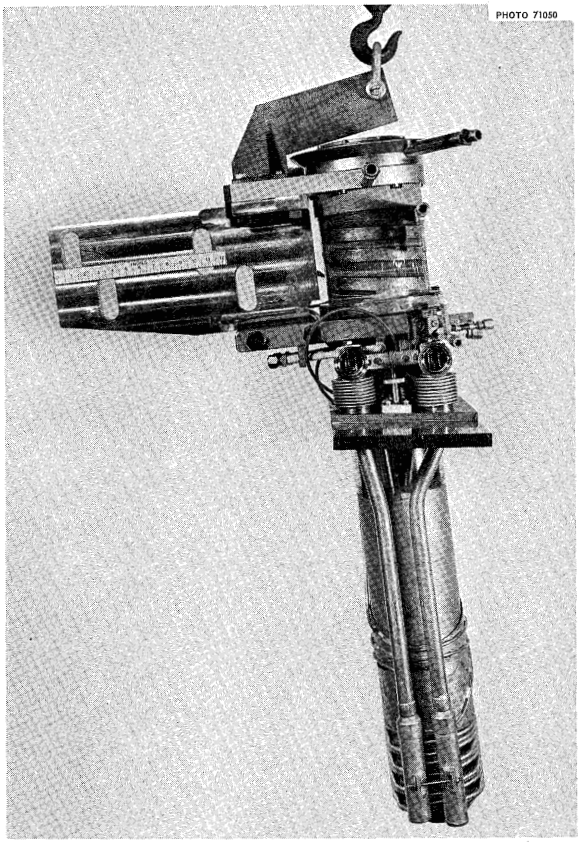

Fig. 8.9. Completely Assembled Snout. View looking south.

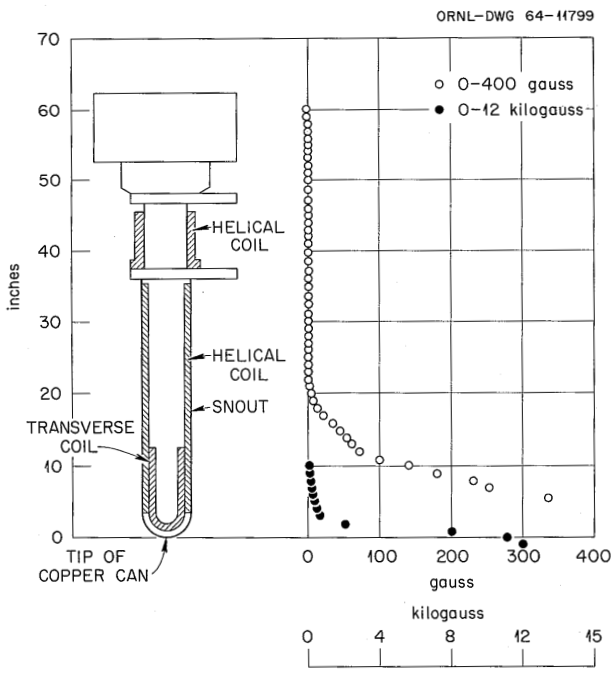

Fig. 8.10. Transverse Magnetic Field in New Snout.

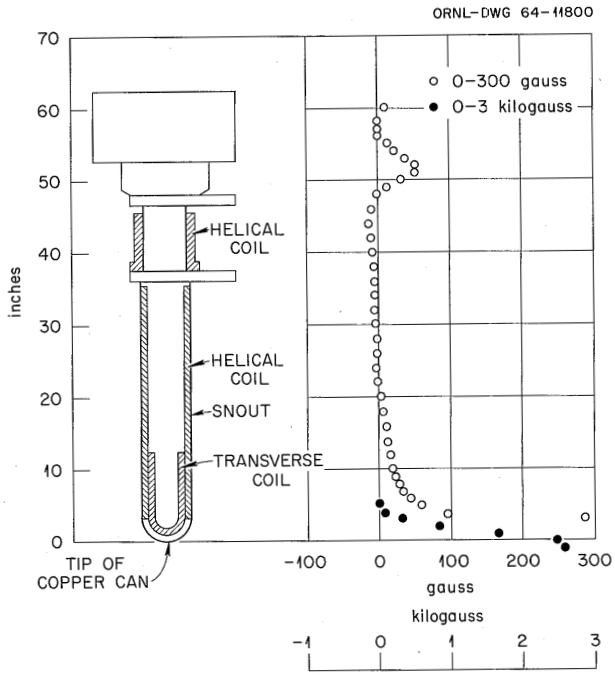

Fig. 8.11. Axial Magnetic Field in New Snout.

showed that a flat optimum for the Fabry factor G occurred at $\beta \approx 3.0$. For this optimization procedure it was initially assumed that the coil is divided into 60 "pancakes"[6] of equal axial thickness and uniform current density. The resulting axial current density distributions for sixth- and eighth-order solenoids are represented in Figs. 8.12 and 8.13. Figures 8.14–8.16 apply to coils of sixth and eighth order and show curves of constant magnitude of the flux density B, these being the intersections of the B = constant axisymmetrical surfaces with the z-r plane. Figure 8.14 indicates the 1% error contours, that is, inside the volume limited by the surfaces $B = 1.01$ and $B = 0.99$, the flux density deviates less than 1% from the B value at the coil center. Figure 8.15 shows corresponding curves for 0.1% maximum deviation, and finally Fig. 8.16 for 0.01% deviation. In each case the eighth-order coil offers appreciably more volume within a given set of contours.

[6] J. N. Luton, Jr., *Thermonuclear Div. Semiann. Progr. Rept. Oct. 31, 1963*, ORNL-3564, pp. 121–25.

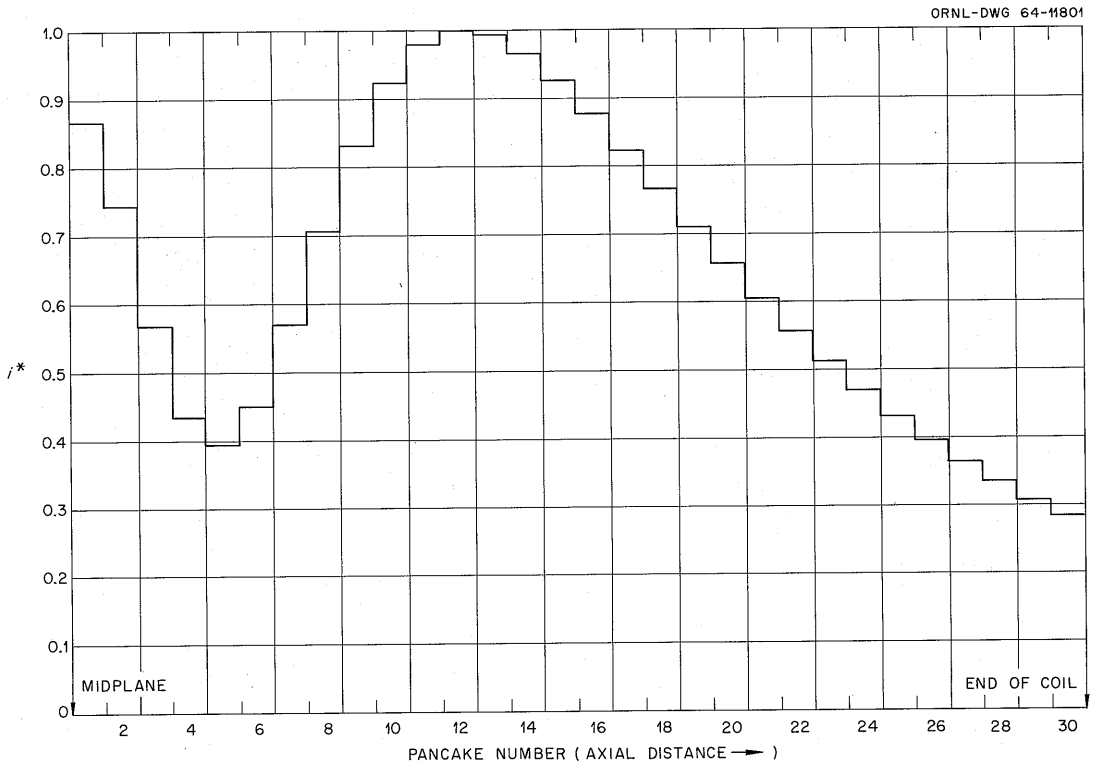

Fig. 8.12. Current Density Distribution for Ideal Sixth-Order Solenoid with 60 Pancakes.

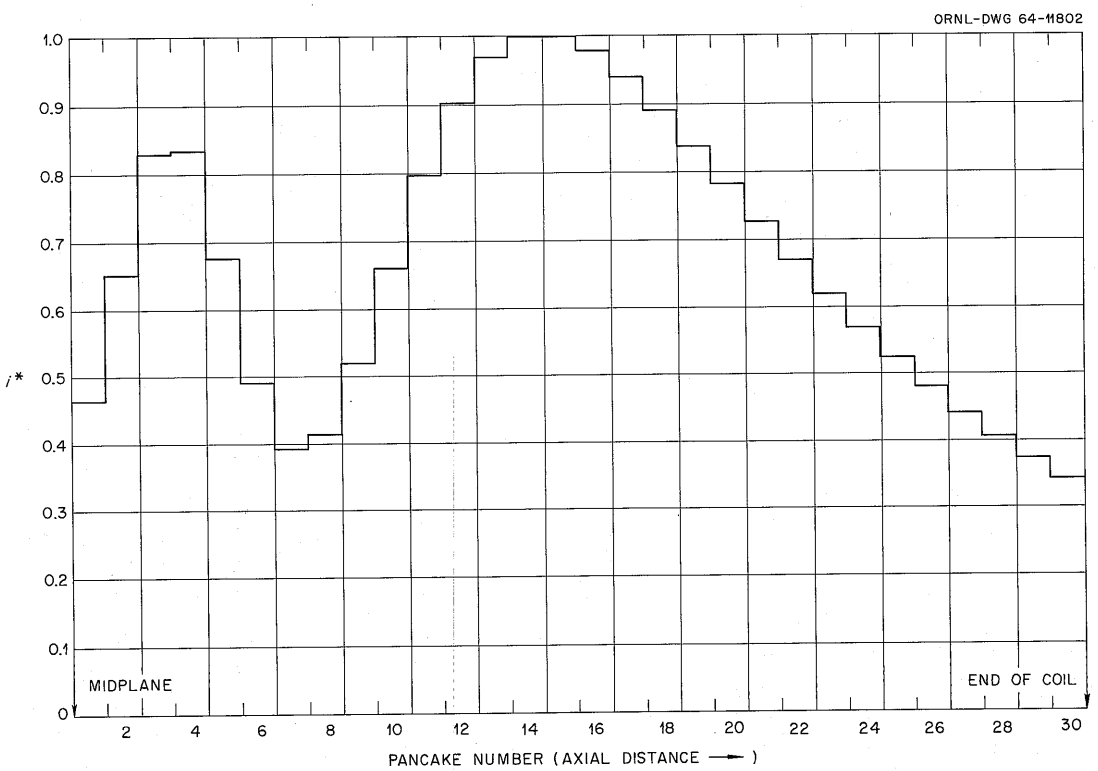

Fig. 8.13. Current Density Distribution for Ideal Eighth-Order Solenoid with 60 Pancakes.

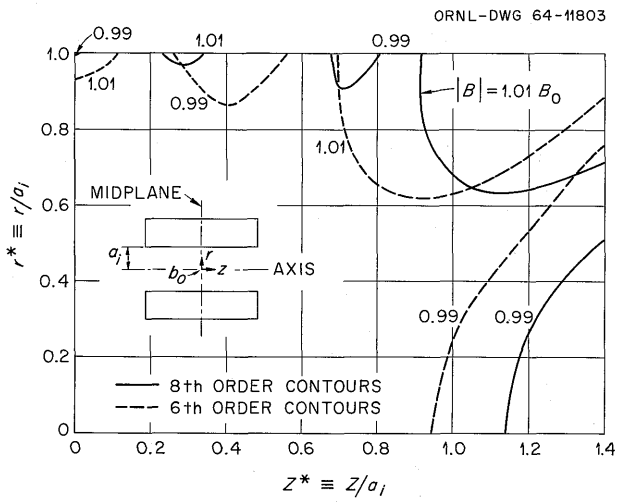

Fig. 8.14. Constant-B Contours (1% Errors) for Ideal Sixth- and Eighth-Order Solenoids.

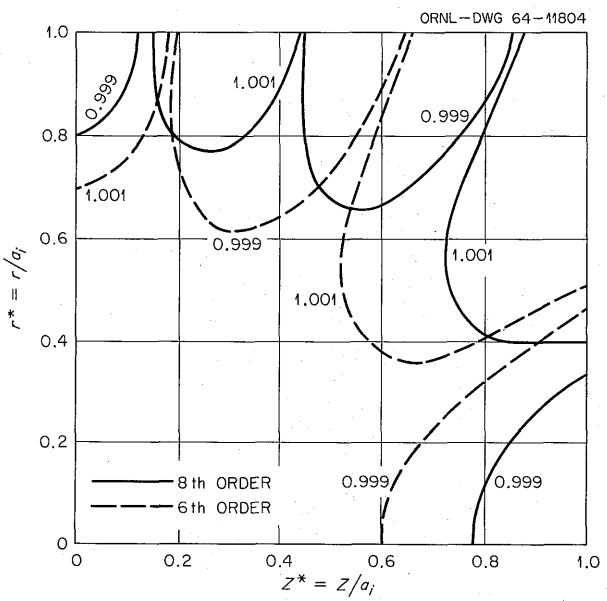

Fig. 8.15. Constant-B Contours (0.1% Errors) for Ideal Sixth- and Eighth-Order Solenoids.

Based on the locations of the peaks of the i^* vs z curves, an actual width of conductor was next chosen for each of the two solenoids. In order to be compatible with the cross-sectional areas demanded by the current and voltage capacities of the power supply, the actual width selected was larger than the width used in the 60-pancake coil. The coils were then reoptimized, using the actual widths of pancakes. The resulting current densities are shown in Tables 8.2 and 8.3 in column "Desired i^*."

Since large tubular conductors of nonstandard size cannot be purchased in quantities of less than 2000 lb, it is not feasible to purchase a separate conductor size for each of the desired i^* values specified in Table 8.2 or 8.3. However, many "effective" conductor sizes can be obtained by winding together conductors of a fixed axial width but with different radial heights. Since coils of large diameter require several parallel water paths for sufficient cooling, the above "mixing" can easily be done. In this way many different current densities can be achieved with only a few different conductor sizes. Thus, if m is the number of water paths and n the number of conductor sizes, then the number N of different average current densities which can be provided is just the number of combinations of n different things taken m at a time with repetitions of items being permitted, that is,

$$N = C_m^{n+m-1} = \frac{(n+m-1)!}{m![(n+m-1)-m]!} . \qquad (1)$$

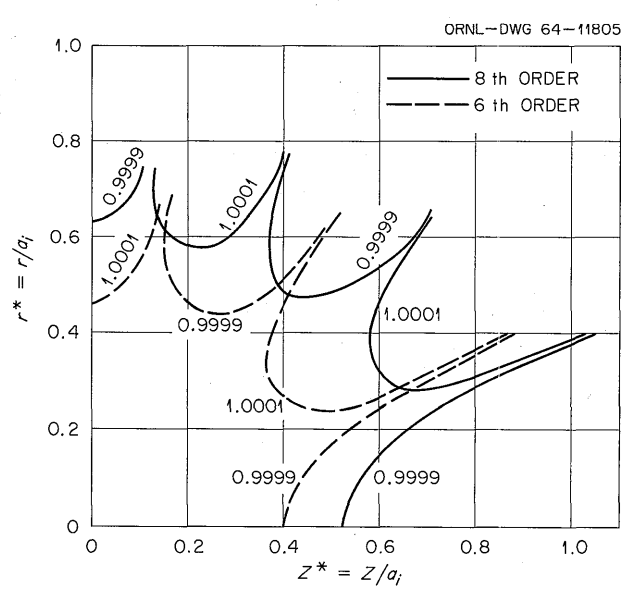

Fig. 8.16. Constant-B Contours (0.01% Errors) for Ideal Sixth- and Eighth-Order Solenoids.

In our case, with seven water paths, three conductor sizes give a sufficiently large number of current density possibilities ($N = 36$). The eighth-order solenoid thus made use of three conductors. However, for the sixth-order solenoid the ratio of i_{max} to i_{min} was larger, and to avoid consuming an excessive amount of power by having conductors (in series) with greatly differing cross-sectional areas in the same pancake, four conductor sizes were used.

In some instances, it is desirable to adjust the current density in axial steps of one conductor width instead of steps of one two-layer pancake. This may be done by the splicing, at the crossover, of conductors of differing radial thickness, still using the scheme of "mixing" conductors described above. However, it might be accomplished more advantageously by mixing conductors

Table 8.2. Normalized Current Densities for a Sixth-Order Solenoid with Conductor Width of 0.712 in.

$i^* \equiv i/i_{max}$

Pancake No.	Layer No.	Desired i^*	Actual i^*
1	1′	0.890	0.903
	1[a]		
2	2	0.649	0.657
	3		
3	4	0.403	0.418
	5		
4	6	0.543	0.543
	7		
5	8	0.821	0.819
	9		
6	10	0.984	1.0
	11		
7	12	1.0	1.0
	13		
8	14	0.925	0.966
	15		
9	16	0.813	0.788
	17		
10	18	0.695	0.717
	19		
11	20	0.585	0.595
	21		
12	22	0.490	0.490
	23		
13	24	0.409	0.401
	25		
14	26	0.342	0.353
	27		
15	28	0.287	0.294
	29		

[a]The coil is symmetrical about its midplane, which lies between layers 1 and 1′.

Table 8.3. Normalized Current Densities for an Eighth-Order Solenoid with Conductor Width of 1.02 in.

$i^* \equiv i/i_{max}$

Pancake No.	Layer No.	Desired i^*	Actual i^*
1	1′	0.511	0.519
	1[a]		
2	2	0.833	0.814
	3		
3	4	0.488	0.496
	5		
	6		
4	7	0.715	0.715
	8	0.899	0.870
	9	0.999	1.0
5	10	1.0	1.0
	11		
6	12	0.870	0.898
	13		
7	14	0.698	0.715
	15		
8	16	0.543	0.544
	17		
9	18	0.418	0.409
	19		
10	20	0.323	0.307
	21		

[a]The coil is symmetrical about its midplane, which lies between layers 1 and 1′.

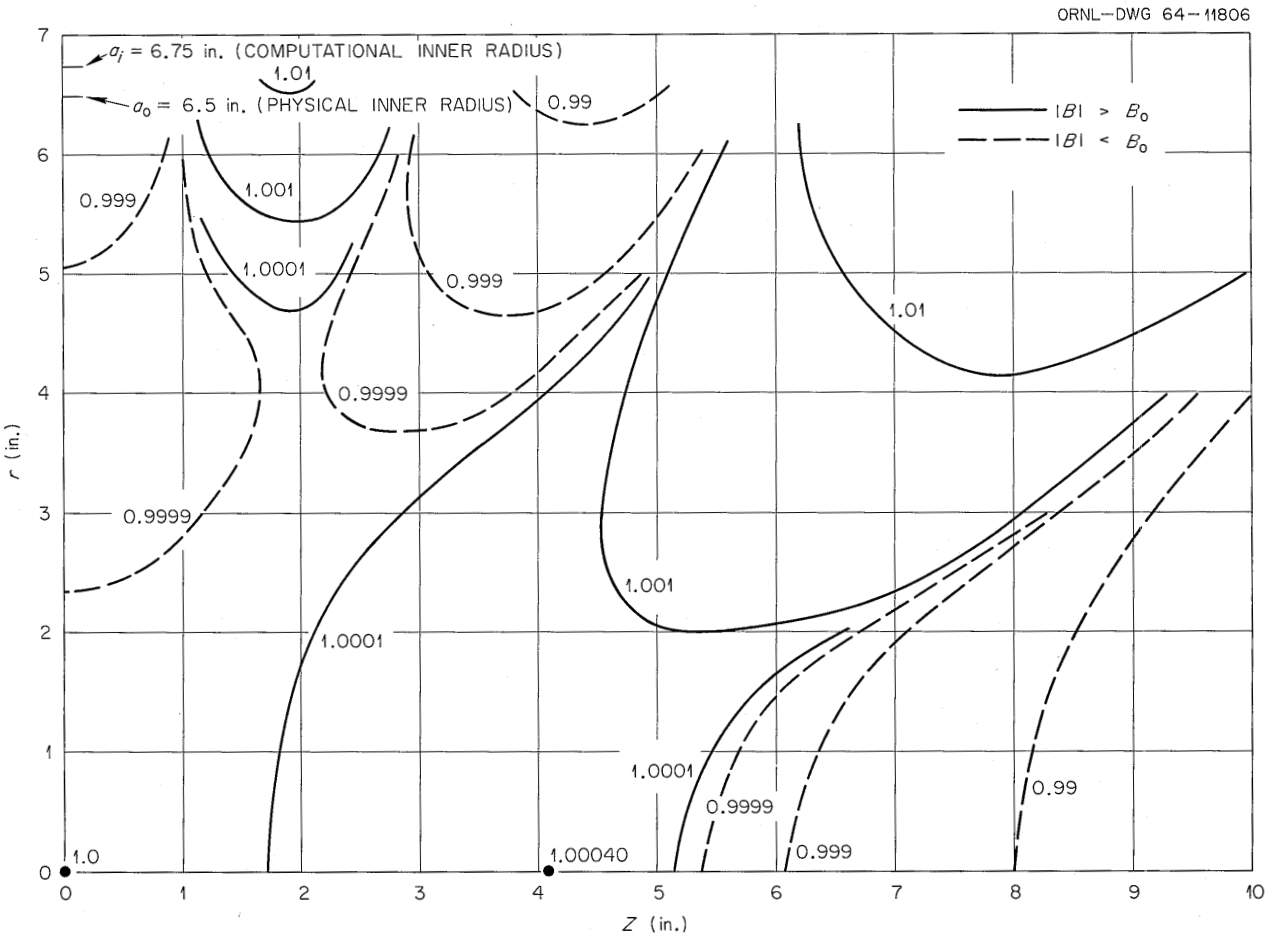

Fig. 8.17. Constant-B Contours for the Actual Eighth-Order Solenoid.

in the type of three-layer pancake previously described.[6] In such a pancake, each water path appears in exactly two layers – the middle layer and one or the other of the outer layers. The average current density of each of the outer layers can therefore be independently controlled, and the current density of the middle layer is the average of the current densities of the two outer layers, weighted by the number of water paths in the respective outer layers. Thus, if one outer layer has a current density i_1 different from that of the other outer layer, i_3, then the current density of the middle layer is

$$i_2 = \frac{m_1 i_1 + m_3 i_3}{m_1 + m_3} , \qquad (2)$$

and so can be varied between the limits i_1 and i_3 by the proper choice of m_1 and m_3, the number of water paths in the respective outer layers. Two three-layer pancakes were used to achieve the eighth-order solenoid of Table 8.3, one as described above and one with constant current density.

Some field computations were made with conductors displaced axially from their expected positions, similar to one case of conductor dislocation calculations previously made for DCX-2.[7] Since the field homogeneity showed no more sensitivity against conductor displacement for the eighth than for the sixth order, an eighth-order coil was selected. The field contours for the eighth-order "actual case" of Table 8.3 are shown in Fig. 8.17. The contours of the actual case are quite comparable to those of the ideal case, except for

[7] G. R. North, *Thermonuclear Div. Semiann. Progr. Rept. Oct. 31, 1961,* ORNL-3239, pp. 82–84.

the 0.01% contours, which enclose much less volume. Further calculations show, however, that the 0.01% error contours of the actual case can closely approach those obtained with the "desired" current densities if current shunts of up to 500 amp are provided across the pancakes.

8.3 TWO COMPUTER PROGRAMS FOR FIELDS OF IDEALIZED MAGNETIC RINGS AND CYLINDERS

M. W. Garrett[8]

8.3.1 Introduction

It may be useful to modify the field of an axially symmetric current system by including small amounts of magnetizable matter. For example, U. Christensen has succeeded in reducing the axial field ripple of a long solenoid with a series of gaps by a factor of 8 by adding a set of ferromagnetic rings.[9] The empirical adjustment of such a system can be greatly aided by pilot calculations.

Two general utility magnetic field packages for current systems that have been described previously[10,11] have now been modified to accept rings or cylinders of magnetic charge or magnetic dipole moment, alone or in combination with a set of current-carrying coils. They compute the field components B_z and B_ρ, the vector potential A, and flux function ρA, for the complete system, and the results of the two programs agree to seven significant figures.

The nonlinearity and hysteresis of actual ferromagnetic matter complicate the calculations and introduce an experimentally undesirable dependence on current. Such effects may be mitigated by a suitable choice of material and of geometry, or diluted by laminating with nonmagnetic inserts. There remains the demagnetizing field due to polarization, whose effect may be estimated by computing an effective permeability μ_e, dependent on the geometry. Nevertheless, a full solution would require a relaxation method that would compute the polarization vector of each element from the combined fields of the currents and all the magnetized matter, revising the estimates of the latter field in successive iterations.

The codes reported here do not attempt an iterative solution. They assume only that the polarization vector is a known constant for each circular element. A thin magnetized ring is treated as a circle whose linear density of magnetic dipole moment is λ'. The moment vector makes an angle β with the axis. In the simplest case, it is reasonable to assume that

$$\lambda' = \mu_e B \, dS, \tag{1}$$

where μ_e is the effective permeability and dS is the area of cross section. The polarization vector is assumed to be parallel to the local field B. Since both codes use the gauss as a magnetic unit, it is convenient to adopt Gaussian units for all equations.

The dipole ring (λ', β), of radius a, is normally the appropriate magnetostatic element. When $\beta = 0$, it is also easy to calculate the fields of uniformly magnetized cylinders, though because of nonuniform demagnetization the ideal cylindrical case has limited validity, and an actual physical cylinder must normally be divided into ring elements. An ideal axially polarized cylindrical sheet is equivalent to two rings with opposite magnetic charges $\pm Q = 2\pi\lambda a$, where the linear charge density $\lambda = \lambda'$, and the rings coincide with the ends of the sheet. It is convenient in any case to develop the theory from the scalar potential $V(Q)$ of a ring of charge, and both codes accept such elements routinely.

The well-known equivalence of a current and a magnetic shell may be used to replace a thick magnetized cylinder by a pair of opposed current sheets coinciding with its inner and outer cylindrical boundaries. Such ideal solenoid elements are accepted by both programs in their original form.

---

[8] Consultant, Swarthmore College.

[9] *Project Matterhorn Ann. Progr. Rept. Dec. 31, 1963, MATT-Q-21*, p. 371.

[10] M. W. Garrett, *Computer Programs Using Zonal Harmonics for Magnetic Properties of Current Systems*, ORNL-3318 (Nov. 19, 1962); C. E. Parker, *Thermonuclear Div. Semiann. Progr. Rept. Oct. 31, 1962*, ORNL-3392, p. 66.

[11] M. W. Garrett, *J. Appl. Phys.* 34, 2567–73 (1963). This paper discusses the mathematical content of the second set of programs, which combine the use of elliptic integrals with Gaussian numerical quadrature, adding only a brief summary of the scope of the 7090 programs. A full report similar to ref. 10 has now been completed, which includes details of the newly added magnetostatic section. This report, ORNL-3575, is in publication.

8.3.2 The Zonal Harmonic Method

The "central" magnetic field of any axially symmetric magnetic system is defined as the region within a source-free sphere of convergence, whose center is an arbitrary axial point. The "remote" field is an infinite source-free region with an inner spherical boundary that encloses the system. These fields may be derived from the central and remote scalar potentials V_C and V_R, which can be expanded in ascending and descending zonal harmonic series respectively:

$$V_C = \sum_{n=0}^{\infty} q_n r^n P_n(\cos\theta) , \qquad (2)$$

$$V_R = \sum_{n=0}^{\infty} p_n r^{-(n+1)} P_n(\cos\theta) , \qquad (3)$$

where r, θ are spherical field coordinates and q_n and p_n are constant coefficients.[12] The constant p_n is an ideal multipole moment of order n, while q_n is proportional to the nth axial derivative $\partial^n V_C/\partial z^n$, evaluated at the origin.

Within the limits of convergence, the principal properties of axially symmetric systems of currents and/or magnetic matter can all be calculated from a set of equations that are derived from (2) and (3). These field equations include series for field components, vector potentials, flux, forces, torques, and mutual inductances. It is the peculiar strength of the zonal harmonic method that the complete set of field equations depends on the source geometry only through the magnitudes of the "source constants" q_n and p_n, which are computed once for all for each system. Moreover, a source constant such as q_n for a complete system is just the scalar sum $\sum_K q_{nk}$ over all its component "source rings." Each isolated filament of current, charge, or dipole moment counts as one source ring, each uniform cylindrical sheet as two, and each thick coil or thick magnetized cylinder as four. The "sources" that replace the actual physical sheets or cylinders occur in matched pairs with opposite algebraic signs.

It is possible to modify the complete zonal harmonic package to permit the optional use of magnetostatic elements, merely by adding to the source section the calculation of constants for charge and dipole rings. No change is required in the field subroutines. Expressions for the source constants of charge rings may be derived by expanding the potential V_k contributed by the kth ring Q_k along the axis in a Taylor's series, and comparing the coefficients with those of Eqs. (2) and (3):

$$q_n(Q_k) = Q_k r_k^{-(n+1)} P_n(\cos\alpha_k) , \qquad (4)$$

$$p_n(Q_k) = Q_k r_k^n P_n(\cos\alpha_k) , \qquad (5)$$

where r_k, α_k are spherical source coordinates. Equation (5) is not currently coded in the source subroutine of the programs.

It is convenient to drop the subscript k, except in the case of r_k, which must be distinguished from the field radius r, and to write the source equations for dipole rings in terms of the linear density λ', as in Eq. (1). If the moment vector of a dipole ring makes an angle β with the axis, evidently since q_n is scalar,

$$q_n(\lambda', \beta) = q_n(\lambda', 0)\cos\beta + q_n(\lambda', \pi/2)\sin\beta . \qquad (6)$$

The values of q_n for angles 0 and $\pi/2$ may be found by differentiating (4) with respect to the cylindrical coordinates z_k and a_k respectively. Details are omitted.

8.3.3 The Elliptic Integral Method

This method makes no distinction between central and remote fields, and there is no limitation on convergence; but the field and source coordinates are not separable. Each field magnitude, at each field point, must be summed over all the component source rings of a system.

Let z, a be cylindrical coordinates of a single source ring measured from an origin at the center of a coaxial field ring of radius ρ. Then

$$r_1 \equiv [(a+\rho)^2 + z^2]^{1/2}$$

is the maximum distance from the field point to any source point, while the modulus k is defined as $2(\rho a)^{1/2}/r_1$. If the source is a charge ring with

[12] The notation of ref. 10 differs from that used here by assimilating certain normalizing factors into q_n and p_n.

total magnetic charge Q, then the scalar potential at any point of the field ring is[13]

$$V(Q) = \frac{2Q}{\pi r_1} K , \qquad (7)$$

where K is the complete elliptic integral of the first kind, to modulus k.

To find the axial field of a charge ring, or the scalar potential of an axially polarized dipole ring, differentiate Eq. (7) with respect to z:

$$B_z(Q) \left[= \frac{Q}{2\pi\lambda' a} V(\lambda', 0) \right] = \frac{-2Q_z}{\pi r_1^3 (1 - k^2)} E . \qquad (8)$$

Here the equation in brackets, which uses the same notation as (6), depends on the recognition that a small axial displacement of a charge is equivalent to the creation of an axial dipole; E is the complete elliptic integral of the second kind, to modulus k.

In an analogous manner, the radial field of a charge ring and the vector potential of an axially polarized dipole ring can be found by differentiating with respect to ρ:[14]

$$B_\rho(Q) \left[= \frac{Q}{2\pi\lambda' a} A(\lambda', 0) \right]$$

$$= \frac{2Q}{\pi r_1} \left[\frac{k}{2\rho} - \frac{E}{k(1 - k^2)} \right] \frac{\partial k}{\partial \rho} . \qquad (9)$$

To derive $V(\lambda', \pi/2)$, the scalar potential of a dipole ring polarized in its own plane, differentiate (7) with respect to a. The result is just the right side of (9) with a in place of ρ. By differentiating this expression in turn, the fields $B_z(\lambda', \pi/2)$ and $B_\rho(\lambda', \pi/2)$ may be found. Details are omitted. Finally, a relation similar to (6) may be used to calculate the field $B(\lambda', \beta)$.

The expressions for the fields of magnetic dipole rings have an interesting application to pure current systems. They may be used to estimate the effects of simple winding errors, since the field increments that arise from uniform radial expansion or from axial displacement of a circular current filament are identical with the fields $B(\lambda', 0)$ and $B(\lambda', \pi/2)$ respectively.

8.4 MAGNETIC FIELD CODES DEVELOPED IN ORNL THERMONUCLEAR DIVISION

C. E. Parker Mozelle Rankin

Increasingly severe demands are constantly made on the calculation of the performance of complex magnetic systems and on the tracing of particle orbits in such systems. Several laboratories have spent much time on these problems, and we have received inquiries from time to time about magnetic field codes available here. In the hope that it may avoid some duplication of effort, a brief summary of such codes is offered below.

These first four codes are in FORTRAN; all magnetic field quantities are calculated for cylindrical coordinates.

8.4.1 Program STORE

For a given system of axially symmetric coils, this code calculates the magnetic field and its first and second derivatives. The method used is the summation of contributions of arbitrarily placed circular loops by means of elliptic integral evaluation;[15] hence, it is not suitable for calculation inside the coils. The grid at which the field is calculated is arbitrary, and the output is printed and/or stored on magnetic tape. With stored output this code is used as an auxiliary to program MADCAP.

8.4.2 Program MADCAP[16]

This code calculates the orbit of a single particle (of any charge-to-mass ratio) in a given magnetic field. (An electric field may also be added.) The integration method is Nystrom's modification of the Runge-Kutta scheme, in which the magnetic

[13] Ernst Weber, *Electromagnetic Fields*, p. 125, Wiley, New York, 1950.

[14] For further discussion of significant differential relations, see ref. 11, p. 2569.

[15] M. Rankin, *Thermonuclear Proj. Semiann. Rept. Jan. 31, 1959*, ORNL-2693, p. 111.

[16] M. Rankin and D. A. Griffin, *Thermonuclear Div. Semiann. Progr. Rept. Oct. 31, 1962*, ORNL-3392, p. 62.

field is called for only three times per integration step. When needed, the magnetic field is obtained from a Taylor series expansion through the second derivatives from quantities stored on tape by program STORE. Any other desired magnetic components (such as from Ioffe bars) may be calculated and superimposed on the stored field. With the Calcomp-508 plotter, this code also gives an r, θ plot and an r, z plot of the motion.

8.4.3 Programs IOFFIN and TERPJO

1. Program IOFFIN calculates the field due to four Ioffe filaments of infinite extent.
2. Program TERPJO sums the contributions of many arbitrarily placed current-carrying straight conductor segments. With it, fields arising from Ioffe bars of complicated shape and the effects of end connections may be calculated.[17]

8.4.4 Programs FINDRZ and FINDRT[18]

These are codes written for use with the Calcomp-508 plotter. They may use any calculated magnetic field, including a superimposition of a Ioffe field with a stored mirror field.

1. For a fixed value of θ, FINDRZ gives a graph of constant-B curves in the r, z plane.
2. For a fixed value of Z, FINDRT gives a graph of constant-B curves in the r, θ plane.

Codes 8.4.5 and 8.4.6 contain one FAP routine each, code 8.4.7 has two FAP routines, and code 8.4.9 contains one FAP routine. The remaining routines are in FORTRAN.

8.4.5 Zonal Harmonic Package

The main program with two subroutines computes zonal harmonic coefficients through the 33d order for any axially symmetric system of currents[19] and/or rings of magnetostatic charge or dipole moment. To extend the range of convergence, up to 24 origins may be assigned at arbitrary axial points. The coefficients may be used for system design or, through options provided in additional subroutines, for the following calculations: cylindrical components of the magnetic field, vector potential and flux function, force and mutual inductance between components of the system, and mapping of lines of constant axial field, in particular, the constant-error contours of a uniform field.

8.4.6. Elliptic Integral–Gaussian Quadrature Package

This parallels the preceding package, with the addition of a more general routine to trace lines which are loci of constant magnitude for the flux function, vector potential, total scalar field magnitude, or either cylindrical field component.[11] It calculates fields and traces lines, both inside and outside the winding volume, and it can compute force and mutual inductance even between coils in contact, also self-inductance of solenoids or thick cylindrical coils. Axial and azimuthal integrations proceed analytically through the use of elliptic integrals of all three kinds, while the integration in radial depth is performed by Gaussian numerical quadrature.

8.4.7 Double Gaussian Integration Code

This code evaluates the axial and radial field components of an axially symmetric system using two Gaussian numerical integrations (azimuthal and radial).

8.4.8 Infinitely Long Nonzero-Cross-Section Ioffe Bars

This code evaluates the field in polar coordinates for infinitely long nonzero-cross-section Ioffe bars using loop replacement. Any number of pairs can be specified.

---

[17] W. F. Gauster, *Thermonuclear Div. Semiann. Progr. Rept. Apr. 30, 1964*, ORNL-3652, p. 118.

[18] Mozelle Rankin and D. A. Griffin, *Thermonuclear Div. Semiann. Progr. Rept. Apr. 30, 1964*, ORNL-3652, p. 113.

[19] M. W. Garrett, *J. Appl. Phys.* 22, 1091–1107 (1951). This paper discusses the theory. For additional details of theory with a full description of the working codes, see ref. 10.

8.4.9 Power and Homogeneity Optimization

This code provides a simultaneous optimization of power and field homogeneity.[5] The lowest-order zonal harmonic coefficients are annulled while producing a given field with minimum power. This code is compatible with No. 8.4.5 above, with which it shares several subroutines. Fields and error contours of the optimized system can be computed directly without reentry of data.

8.4.10 Semi-Infinite Current Sheets

This is a table which was calculated by A. C. Downing and Nancy B. Alexander.[20] An axial integration was performed analytically, but the azimuthal integration was done by a Gaussian numerical integration. Later on a second Gaussian numerical integration in radial depth was added to make the code outlined in No. 8.4.7.

Codes 8.4.1 and 8.4.3 were written by Mozelle Rankin; codes 8.4.2 and 8.4.4 were written by Mozelle Rankin and D. A. Griffin.

Code 8.4.7 was written by A. C. Downing and Nancy Betz of the Mathematics Division.

Additional information about codes 8.4.5–8.4.10 can be obtained from C. E. Parker.

8.5 A NEW VIBRATING-COIL MAGNETOMETER

W. F. Gauster J. H. Todd[21]
H. A. Ullmaier

8.5.1 Introduction

In a previous report,[22] a ballistic method for measuring the magnetic moment of superconducting samples has been described. Several other possibilities of performing such measurements have been discussed there. The best method is the use of a fixed sample with a demagnetization factor $n \sim 1$, and a short pickup coil which surrounds the homogeneous middle zone of the sample. The pickup coil must be moved sufficiently far away so that the field in the final coil position is not distorted. If possible, a second coil (compensation coil) should be employed. Of course, with such an arrangement no continuous measurements can be made. Furthermore, the signal-to-noise ratio is not very high.

8.5.2 Principle of a New Vibrating-Coil Magnetometer

Vibrating-sample[23] and vibrating-coil[24] magnetometers have been built which allow continuous measurements with relatively high sensitivity. However, the flux measurements are not performed in the homogeneous zones of samples with $n \sim 1$. The first author has suggested a new type of vibrating-coil magnetometer which does measure the flux in the homogeneous zone. This is achieved by providing a long vibrating coil (Fig. 8.18), which is coaxial with the sample S and whose lower end oscillates with a small amplitude around the middle of the sample. The coil length l must be sufficiently large so that at the upper end of the coil the field is not distorted by the sample. It is, however, not necessary that the external field be homogeneous along the entire length of the coil. A sinusoidal vibration of the coil is assumed:

$$x = a \sin \omega t \ . \tag{1}$$

The total number of turns of the homogeneous coil winding is N; the coil cross section is A_c. Then the induced coil voltage without a sample inside the oscillating coil becomes

$$e_0 = -\mu_0 \frac{N}{l} \frac{dx}{dt} (H_1 - H_2) A_c \ , \tag{2}$$

$$\mu_0 = 4\pi 10^{-7} \text{ henry/m (mks system)} \ .$$

[20] Nancy B. Alexander and A. C. Downing, *Tables for a Semi-Infinite Circular Current Sheet*, ORNL-2828 (Sept. 29, 1959).

[21] Instrumentation and Controls Division.

[22] *Thermonuclear Div. Semiann. Progr. Rept. Oct. 31, 1963*, ORNL-3564, pp. 116–18.

[23] S. Foner, *Rev. Sci. Instr.* **30**, 548 (1959); J. W. Heaton and A. C. Rose-Innes, *J. Sci. Instr.* **40**, 369 (1963).

[24] D. O. Smith, *Rev. Sci. Instr.* **27**, 261 (1956); H. Plotkin, *Quart. Rep. MIT Res. Lab., Electronics* (Oct. 15, 1951), p. 28.

ORNL-DWG 64-11807

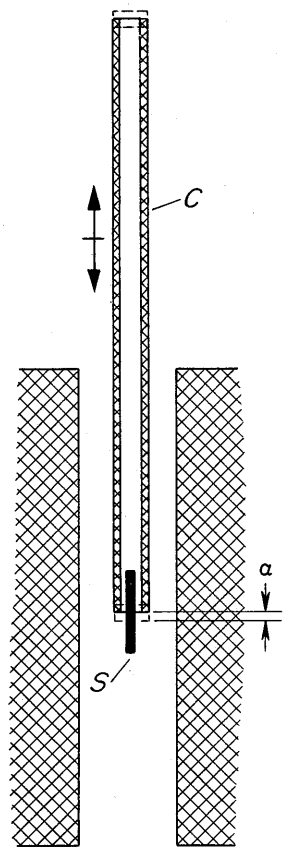

Fig. 8.18. Principal Arrangement of the Vibrating-Coil Magnetometer.

With a sample cross section A_s, the voltage is

$$e = -\frac{N}{l}\frac{dx}{dt}\{H_1[\mu_0(A_c - A_s) + \mu A_s] - H_2\mu_0 A_c\} . \quad (3)$$

Therefore,

$$e_0 - e = \frac{N}{l}\frac{dx}{dt}(\mu - \mu_0) H_1 A_s . \quad (4)$$

The difference of the voltage amplitudes E_0 and E is

$$E_0 - E = -\frac{N}{l} a\omega(\mu - \mu_0)H_1 A_s . \quad (5)$$

In the mks system

$$B = \mu_0 H + nM . \quad (6)$$

For $n \sim 1$

$$M = B_1 - \mu_0 H_1 = H_1(\mu - \mu_0) . \quad (7)$$

From Eq. (5) follows

$$-M = \frac{(E_0 - E)l}{a\omega A_s N} = k(E_0 - E) . \quad (8)$$

8.5.3 Block Diagram of the Electric Circuits

Figure 8.19 shows the block diagram of the coil-driving and of the signal-processing systems. The first consists of two loudspeaker assemblies (1) and (2), one used as the driving and the other as a feedback element. A signal generator (3) provides a 22.9-cycle driving signal (resonance with 60 cycles must be avoided). The differential amplifier (4) ensures an almost constant amplitude (about 1 mm large).

The signal (several millivolts) produced in the oscillating coil (5) [inside the external magnet coil (11)] is amplified in an ac amplifier (6) and rectified in an ac-dc converter (7). The resulting dc signal corresponds to the quantity E in Eq. (8). The voltage amplitude E_0 (as used in the same equation) is proportional to the undisturbed field

ORNL-DWG 64-11808

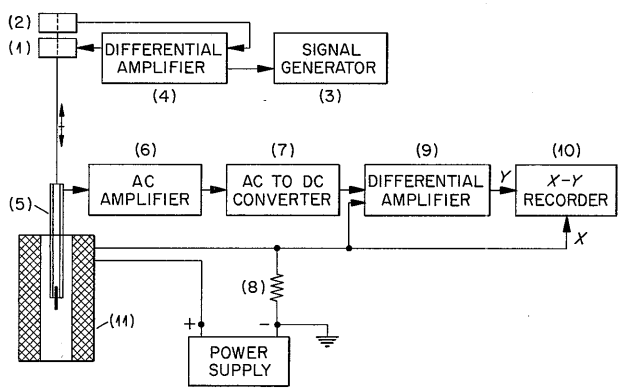

Fig. 8.19. Block Diagram of the Electric Circuits of the Vibrating-Coil Magnetometer.

H_1 and therefore proportional to the current in the external magnet coil (11). The signal-processing system considers the voltage E in the following way. The voltage across the shunt (8) is fed to the differential amplifier (9), which amplifies the voltage $(E_0 - E)$. This is already the desired signal, which is proportional to the magnetic moment M of the superconducting sample. An x-y recorder (10) is used, as shown in Fig. 8.19.

8.5.4 Present State of Development

A model of this new vibrating-coil magnetometer has been built, and initial tests yielded encouraging results. The following points need further careful consideration:

1. to ensure the necessary minimum coil length by measuring a safe distance at which the field disturbance due to the sample can be neglected,
2. to check the constancy of dx/dt, that is, especially that of the amplitude a,
3. to investigate the exact rectifier characteristic of the ac-dc converter,
4. to consider, if necessary, residual fields of the external magnet coil (11), which is a superconducting coil (Magnion coil, ID = 1 in., B_{max} = 50 kilogauss).

It is hoped that it will be possible to develop the new vibrating-coil magnetometer to a measurement instrument of very high accuracy. It is also intended to make magnetic moment measurements using the fields produced by conventional, water-cooled solenoids with an inside diameter of $6\frac{1}{2}$ in. available in the magnet laboratory of the Thermonuclear Division. In this case, a modified magnetometer model with vibrating compensation coil could be used. The principle of this arrangement is similar to that of the previously described ballistic measurements.[22] The advantage would be a simplification of the signal-processing circuit and herewith a greater accuracy. Finally, it would not be necessary to consider remanent fields, as might be required when a superconducting external coil is used.

9. Vacuum Systems, Techniques, and Materials Studies

D. M. Richardson[1] R. A. Strehlow[1]

9.1 INTRODUCTION

Methane and other low-molecular-weight carbon-containing molecules have been found to be among the dominant species in many ultrahigh vacuum systems, including some of those used for plasma research.[2,3] Earlier work has shown that the adsorption characteristics of these compounds (methane, ethane, and carbon dioxide) account for the observed behavior for the temperature range to about 110°K.[4] The presence of methane particularly has been shown to lead to large pressure fluctuations in systems which have extensive areas cooled with liquid nitrogen. The origin of these gases, especially in controlled fusion research devices, has been variously attributed to ion gage reactions, hydrogen ion bombardment of surfaces containing carbon, oil reaction with freshly deposited metal films, and inadequate compression ratios for methane by the mechanical or diffusion pumps of the apparatus. Demonstration that electron bombardment of oil-contaminated surfaces would yield a wide variety of neutral species added an additional possible source, but also established a better basis for

[1]Reactor Chemistry Division.

[2]E. R. Wells and Herman Postma, *Trans. Natl. Vacuum Symp.* **9**, 266 (1962).

[3]D. Lichtman and A. Hebling, *Trans. Natl. Vacuum Symp.* **7**, 194 (1960).

[4]D. M. Richardson and R. A. Strehlow, *Trans. Natl. Vacuum Symp.* **10**, 97 (1963).

ORNL-DWG 64-11809

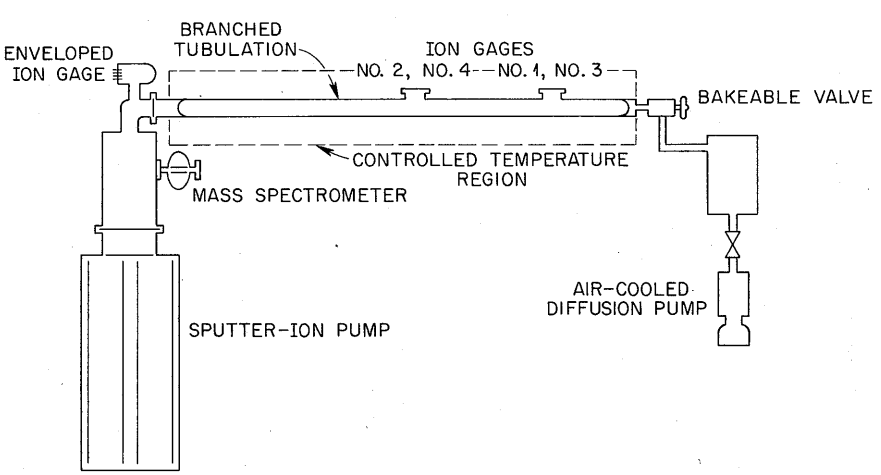

Fig. 9.1. Surface Creep Study Apparatus. Side view of pumps and tubulation.

the use of nude ionization gages to diagnose the local presence of oil.[5]

During the last reporting period, a facility was designed and constructed to study gas evolution from freshly sputtered titanium surfaces, oil transport, and ion gage reactions which result in particular residual gas compositions.

This facility, shown in Fig. 9.1, includes a 280-liter/sec sputter-ion diode pump, a mass spectrometer analyzer for residual gas (with sensitivity of 5×10^{-10} torr for a signal-noise ratio of unity, and resolution adequate to distinguish some peaks near mass 40), and a specially designed tubulation of 2-in.-diam copper tubing 2.3 m long with four nude ion gages and equipment to permit maintenance of tubulation temperatures from 15 to 350°C. The tubulation described below is attached on one end to a dome above the sputter-ion pump and on the other end to a 1-in. bakeable valve and a small diffusion-pumped vacuum system.

9.2 GAS EVOLUTION FROM SPUTTER-ION PUMPS

Sputter-ion pumps are characterized by a relatively large surface of freshly sputtered titanium plate (about 3000 cm^2 for the pump used in this apparatus) serving as a cathode, and about an equal area of titanium deposited on the anode. Experimental distinction between gas evolution from the two types of titanium surface could not be made in the tests conducted and reported here. A 3-kv potential produces an ionizing discharge between the two plates of titanium in a magnetic field established by permanent-magnet assemblies. The ions so produced bombard the titanium and result in ion burial and sputtering with consequent getter pumping.

During pump operation most of the evolving gases are pumped. In our tests, after the pump was turned off, however, evolution of these reaction products resulted in a pressure increase of about 5×10^{-5} torr/hr. Mass spectra and the intensities of various mass peaks were monitored and recorded as a function of time after turnoff. The spectra were obtained with no ion gage operating. (The pumping speed for methane, of a tubulated ion gage with thoria filament, was measured and found to be 0.29 liter/sec; carbon monoxide and carbon dioxide were two of the products.) Several operating parameters prior to turnoff were considered and studied. These included pump temperature, time of operation, applied pump voltage, water pressure, argon and hydrogen pumping demands placed on the pump, and off-time between successive measurements. Although sputter-ion pumps are known to have an argon "memory" persisting for many months, no study of the effect of water vapor partial pressure on the residual gas composition has been found in the literature.

Many of the parameters studied had a reproducible effect on the initial rise rates (for the first 2 or 3 min after turnoff) of hydrogen, carbon monoxide, methane, and argon. Only the water partial pressure, however, substantially affected subsequent rise rates and the total quantities of gases evolved from the pump at room temperature. Figure 9.2 shows the effect of water partial pressure on the pressure of the dominant gases other than argon as a function of time after pump turnoff. The terminal methane production rate measured was always 1.2 to 3×10^{-7} torr liter sec^{-1} and was constant for periods to 1.5 hr. Hydrogen and carbon monoxide evolution rates after turnoff were approximately proportional to the water partial pressure over two orders of magnitude variation in the water pressure. Initial rise rates for hydrogen for the water pressure range of 1 to 6×10^{-8} torr were also found to increase, but proportionality was not observed. At water partial pressures less than 10^{-8} torr, carbon monoxide was not determinable due to the very small height of the mass 12 peak and to the relatively large amount of ethane in the system. Ethylene was not observed, and higher-molecular-weight hydrocarbons could not be detected in the present study.

The very low hydrogen evolution rate found in the absence of water, when contrasted with the continued dominance of methane and ethane in the mass spectra, indicates that the measured enhancement of hydrogen pumping speed by titanium films at liquid-nitrogen temperatures may be substantially due to retention of synthesized hydrocarbons by titanium at low temperatures.

[5] *Thermonuclear Div. Semiann. Progr. Rept. Apr. 30, 1964*, ORNL-3652, p. 138.

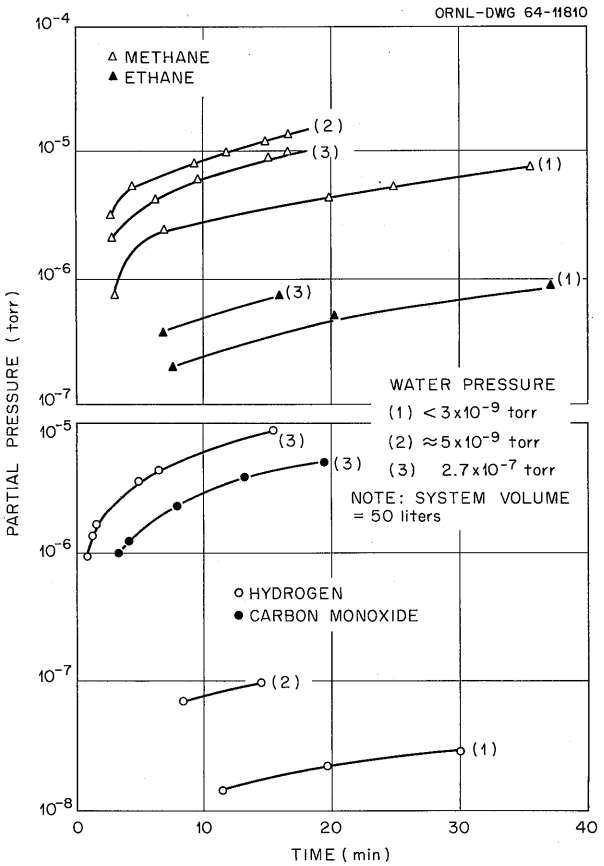

Fig. 9.2. Partial Pressures of CH_4, C_2H_6, CO, and H_2 After Ion Pump Turnoff.

9.3 MASS TRANSPORT OF OIL IN VACUUM SYSTEMS

The tubulation of 2-in.-diam copper shown in Fig. 9.3 with the ion gages numbered for identification was specially designed to allow a study to be made of oil transport and, specifically, to try to distinguish between surface diffusion and vapor transport. The apparatus was designed to allow a distinction to be made between the oil transport time from gage 1 to gage 2, connected by 60 cm of uninterrupted tubing, and the time between gages 3 and 4 in a parallel branch circuit connected by 60 cm of 2-in. tubing interrupted by a $\frac{1}{16}$-in. circumferential gap. Surrounding the section of tubing with the gap was a 40-cm section of 3-in.-diam tubing, thus giving a surface diffusion (creep) path 142 cm long for this branch of the circuit. The ratio of the two path lengths was 2.3. A time delay for gage 4 relative to gage 3 equal to 2.3 times the delay of gage 2 relative to gage 1 was expected for a surface-diffusion transport process. No difference in delay times would be expected for a vapor transport process. The inlet was connected by a bakeable valve to an oil-diffusion-pumped system which served in our experiments as an oil source to the uncontaminated tubulation and ion pump.

After baking the tubulation to remove residual traces of oil and reaching a pressure as read by the gages in the low, 10^{-7} torr, pressure range at a thermostated temperature of 50°C, the bakeable valve was opened to permit oil transport to begin. The pressure readings of gages 1 and 3 (both 60 cm from the valve) began to increase steadily after about $2\frac{1}{2}$ to 3 hr, ultimately reading more than 1×10^{-6} torr. An increase in the pressure reading of gage 2 began about 6 to 10 hr later. Gage 4 did not indicate any increase in pressure until 16 hr had elapsed after the beginning of the pressure reading rise of gage 3. (An emission current of 100 μa was used to avoid a limitation of pressure reading by the arrival rate of oil on the grids of the gages.) Surface diffusion, therefore, appeared to be the dominant transport mechanism.

The two factors which were found to introduce uncertainty in the measurement of observed time delay for gage 2 (the 60-cm path) were (1) a lack of zero stability for the control of gage 2 (leading to the 4-hr uncertainty in the delay time reported above) and (2) an increased sensitivity to temperature variations for all the gages as they became contaminated. The gases synthesized by each gage did have an effect on the readings of the other gages, but this was readily diagnosable by turning off the gages individually and measuring the pressure drop of the remaining gages.

The temperature of the tubulation was maintained to within 1.5° by circulating heated water through external tubing, but, even with this control, pressure readings fluctuated by almost 10%. Measurements of the pressure readings at the close of the experiment as a function of a programmed temperature rise from 50 to 60°C (at a rise rate of near 0.2°C/min) were made for two temperature cycles, one at 100 μa and one at 2 ma gage emission currents. The slopes of the Arrhenius plots of these data corresponded to

ORNL-DWG 64-11811

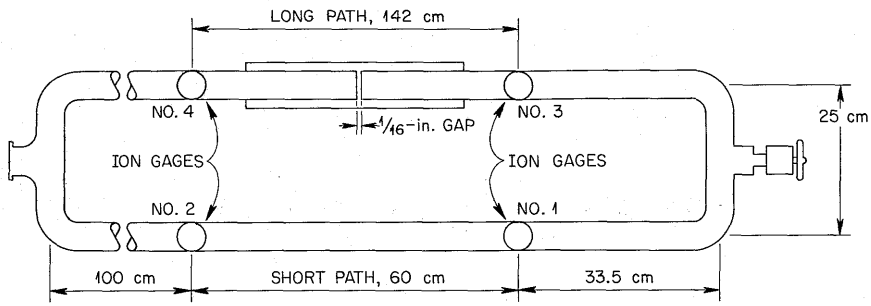

Fig. 9.3. Surface Creep Study Apparatus. Top view of tubulation detail.

13.8 and 14.1 kcal/mole. The estimated heat of activation for the oil was about 14 kcal/mole for surface diffusion and 23 to 36 kcal/mole for vapor transport.[6]

An earlier experiment was conducted before the diffusion-pumped system was cleaned, and when it presumably was more heavily contaminated with oil, which led to an almost immediate rise of pressure reading for gages 1 and 3 and a time delay of 3.5 hr for gage 2 (short surface path) and 7.6 hr for gage 4 (long path). The estimated uncertainty for these times was ±1 hr. A delay-time ratio of between 1.5 and 3.0 was found in these experiments. This ratio compares favorably with the predicted value of 2.3.

[6] *Thermonuclear Div. Semiann. Progr. Rept. Apr. 30, 1964,* ORNL-3652, p. 140 (identifying the excess surface energy, 0.6 ΔH_v, as the heat of activation for surface diffusion and the heat of vaporization as the heat of activation for a vapor transport process).

9.4 HYDROGEN PRODUCTION BY NUDE ION GAGES IN THE PRESENCE OF OIL

With the sputter-ion pump not operating and with oil in the apparatus, the mass spectrometer hydrogen peak height was measured as a function of ion gage emission current. Gas produced was removed by the diffusion-pumped system through the 1-in. valve with an air conductance of about 10 liters/sec. At a tubulation temperature of 50°C it was found that the hydrogen partial pressure varied linearly with emission and that operation of the tungsten filament contributed about the same amount of hydrogen (presumably by thermal cracking) as each 2 ma of electron bombardment current. At emissions greater than about 3 ma, the hydrogen production rate decreased with time, presumably as limited by the arrival rate of oil to the ion gage grid.

10. Fusion Chain Reactions

J. R. McNally, Jr.

Consider the bombardment of stripped ^{6}Li by charged particles of 3 Mev or more in a magnetic system capable of retaining the nuclear reaction products. The bombarding particles we shall take to be protons in the example to be developed, although similar systems can also be constructed starting with d, T, ^{3}He, or ^{4}He. Our primary reaction is then

$$^6\mathrm{Li}(p,{}^3\mathrm{He})\alpha,\ Q = +4.02\ \mathrm{Mev}\ ,$$

but, inasmuch as the ^{3}He is retained in the system, it can also react with surplus ^{6}Li, leading to

$$^6\mathrm{Li}({}^3\mathrm{He},p)2\alpha,\ Q = +16.9\ \mathrm{Mev}\ ,$$ [1]

and thus the high-energy proton is regenerated. The alphas, half of which have an energy of about 8 Mev, can then induce further reactions, notably the slightly endothermic reaction

$$^6\mathrm{Li}(\alpha,p)^9\mathrm{Be},\ Q = -2.13\ \mathrm{Mev}\ ,$$

so that a further proton is generated, making the multiplication constant exceed unity. In an equilibrium situation, with all charged reaction products retained, a complex of nuclear reactions follows, most of which are exothermic and some of which regenerate further protons. (If losses should reduce the proton multiplication factor slightly below unity, injection could be continued to an extent required to keep the fire burning.) The secondary reactions are principally as follows:

$$^6\mathrm{Li}(x,x')d + \alpha - 1.5\ \mathrm{Mev}$$

followed by

$$^6\mathrm{Li}(d,p)^7\mathrm{Li} + 5.0\ \mathrm{Mev}$$

or

$$^6\mathrm{Li}(d,t)p + \alpha + 2.6\ \mathrm{Mev}\ ,$$

and they would be supplemented by tertiary reactions:

$^6\mathrm{Li}(t,p)^8\mathrm{Li}$	$Q = +0.8$ Mev
$^6\mathrm{Li}(t,n)2\alpha$	$Q = +16.1$ Mev
$^6\mathrm{Li}(t,d)^7\mathrm{Li}$	$Q = +1.00$ Mev
$^6\mathrm{Li}(d,\alpha)\alpha$	$Q = +22.4$ Mev
$^6\mathrm{Li}(p,d)^5\mathrm{Li} \rightarrow p + \alpha$	$Q = -3.2 + 1.8$ Mev
$^6\mathrm{Li}(d,{}^3\mathrm{He})^5\mathrm{He} \rightarrow n + \alpha$	$Q = +0.8 + 1.0$ Mev
$^6\mathrm{Li}(d,n)^7\mathrm{Be}$	$Q = +3.4$ Mev
$d({}^3\mathrm{He},p)\alpha$	$Q = +18.4$ Mev
$d(t,n)\alpha$	$Q = +17.6$ Mev
$d(d,p)t$	$Q = +4.0$ Mev
$d(d,n)^3\mathrm{He}$	$Q = +3.3$ Mev
$^3\mathrm{He}(t,\alpha)d$	$Q = +14.3$ Mev
$^3\mathrm{He}({}^3\mathrm{He},p)^5\mathrm{Li} \rightarrow p + \alpha$	$Q = +11.1 + 1.8$ Mev

These considerations, based upon particle conservation alone, would seem to suggest the possibility of igniting a charged-particle fusion chain reaction *in the plasma*. It is to be noted that neutrons play a minor role.

A literature survey has been made of the pertinent nuclear reaction rate parameters, σv, and some of the results are given in Fig. 10.1. The reaction $^6\mathrm{Li}({}^3\mathrm{He},p)2\alpha$ has a total σv of about $2.5 + 10^{-16}$ cm^3/sec for 3- to 5-Mev ^{3}He ions,

[1] The reaction can go through either of the unstable intermediates ^{8}Be or ^{5}Li without affecting the argument and without appreciably changing the Q value.

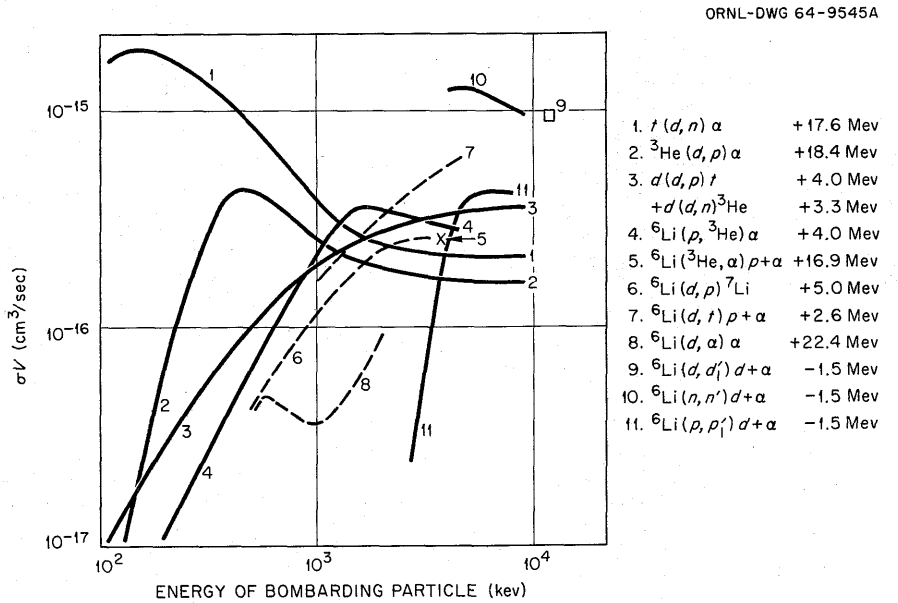

Fig. 10.1. Reaction Rate Parameter, σv, vs Energy of Projectile Particle (Data Only Approximate in Numerous Cases).

and the figure shows that this value is comparable with the σv values for the conventional fusion reactions.

As an example, the case of bombardment of ^{6}Li by 1-Mev protons has been examined. Taking into account the various branchings and reactions produced by secondary particles, guessing at unmeasured branching ratios, neglecting energy degradation, and assuming no losses, one finds that on the average one such proton striking ^{6}Li will produce after three generations 1.35 reactive protons, 3.04 ^{4}He of less than 2.5 Mev, 0.74 ^{4}He above 2.5 Mev (and therefore reactive), 0.80 reactive deuteron, 0.20 reactive triton, 0.1 neutron, 0.28 ^{7}Be, 0.25 ^{7}Li, and 0.08 ^{9}Be. The total energy release initiated by the 1-Mev proton in three generations is 16.0 Mev. The average multiplication factor for new reactive chain centers produced per generation is about 1.5 for this admittedly naive example.

The advantages of very-high-energy injection (several Mev) pointed out in an earlier report[2] hold for a system of this kind. Disadvantages are: (1) the rate of cooling of the hot ions by slow electrons is probably fatal unless reduced by supplementary electron heating,[3] and (2) a fusion plasma created at Mev energies will necessarily be comparatively dilute at customary magnetic field strengths because of β limitation.

The conventional $d(t,n)\alpha$ fusion reaction, of course, uses ^{6}Li as primordial fuel. Fusion chain reactions such as the above would burn the ^{6}Li directly in the reactor vessel, obviating the conventional ^{6}Li blanket and external chemical plant required for tritium regeneration.

A similar but shorter chain has been suggested by R. F. Post (*Nuclear Fusion*, 1962 Supplement, Part 1, p. 119) in the form of a "breeding" cycle for ^{3}He. This and other speculations in the literature miss the element of *multiplicative* breeding in the plasma that appears in the more generalized complex of reactions described above.

[2]*Thermonuclear Div. Semiann. Progr. Rept. Apr. 30, 1963*, ORNL-3472, sect. 10

[3]Although it should be noted that, because of relative velocities, the ions will lose energy only upon a class of electrons of very low energy, and the rate of ion energy loss will really be determined by the rate at which this low-energy pocket is refilled from the main electron population.

11. Design and Engineering: Service Report

J. F. Potts, Jr.

Design activities for this reporting period are summarized as follows:

Jobs on hand 5-1-64 on which work had not started	11
New jobs received	185
Total jobs	196
Jobs completed	171
Jobs in progress	18
Backlog of jobs 10-31-64	7
Total drawings completed for period (does not include drawings for use in reports, slides, etc.)	270

Shop fabrication for this reporting period is summarized as follows:

Machine Shops

Completed jobs requiring 16 man-hours or less	60
Completed jobs requiring 17 to 1200 man-hours	291
Completed jobs requiring over 1200 man-hours	1
Completed jobs of miscellaneous character in plating, carpenter, electrical, glass, lead, etc., shops)	80
Average manpower per week (machine shop)	19.9
Average manpower per week (miscellaneous)	2

Electromagnet Fabrication

Completed jobs	7
Number of jobs in progress	1
Completed jobs by outside contractors	1
Average manpower (per week)	2

Publications, ORNL Reports, and Papers

PUBLICATIONS

Author(s)	Title of Article	Journal
Igor Alexeff and R. V. Neidigh	Observation of Burnout in a Steady-State Plasma	*Phys. Rev. Letters* **13**, 179 (1964)
C. F. Barnett and J. A. Ray	The Dissociation Cross Section of H_2^+ in Hydrogen Gas	Pp. 743–50 in *Atomic Collision Processes, Proceedings of the Third International Conference on the Physics of Electronic and Atomic Collisions, North-Holland*, Amsterdam, 1964.
S. Cuperman	Impurity Radiation from Non-Maxwellian Spherical Plasmas	*Phys. Fluids* **7**, 803 (1964)
T. K. Fowler[1]	Bounds on Plasma Instability Growth Rates	*Phys. Fluids* **7**, 249 (1964)
C. C. Harris and H. Rohrer[2]	The Assay and Dosimetry of Mercury-197	*J. Nucl. Med.* **5**, 317–18 (1964)
T. K. Fowler[1] and M. Rankin	Ambipolar Scattering Losses from Magnetic Mirrors	*J. Nucl. Energy, Pt. C* **6**, 513–14 (1964)
C. C. Harris	Certain Fundamental Physical Considerations in Scanning	Chap. I, pp. 1–15, in *Scintillation Scanning in Clinical Medicine*, ed. by J. L. Quinn III, Saunders, Philadelphia, 1964
C. C. Harris, J. C. Jordan, M. M. Satterfield, J. K. Goodrich,[3] H. L. Stone,[3] and Rebecca Hill[3]	A Collimator for Scanning with Low-Energy Photons	*J. Nucl. Med.* **5**, 653–56 (1964)
W. F. Gauster and D. C. Freeman, Jr.[4]	Superconducting Magnet Coils for Thermonuclear Research	*Nucl. Fusion* **4**, 185 (1964)

[1]Physics Division.
[2]Consultant from Emory University, Atlanta, Ga.
[3]University of Mississippi Medical Center.
[4]Linde Company.

ORNL REPORTS

Author(s)	Title	Number	Date
C. F. Barnett, J. A. Ray, and J. C. Thompson	Atomic and Molecular Collision Cross Sections of Interest in Controlled Thermonuclear Research	ORNL-3113, Revised	August 1964
A. H. Snell	Thermonuclear Division Semiannual Progress Report for Period Ending April 30, 1964	ORNL-3652	July 1964
Y. Shima and L. S. Hall[1]	Note on Electrostatic Instabilities in a Plasma with Anisotropic Velocity Distribution	ORNL-TM-119	September 1964
G. K. Soper	Studies of the Ion-Cyclotron Resonance Instability (thesis)	ORNL-3696	October 1964

[1]Lawrence Radiation Laboratory, Livermore, Calif.

PAPERS PRESENTED AT SCIENTIFIC AND TECHNICAL MEETINGS

Plasma Physics Theory Meeting, Gatlinburg, Tenn., May 7–8, 1964

G. K. Soper[1] and Y. Shima, "The Effect of Finite Ion and Electron Temperatures on the Ion-Cyclotron Resonance Instability."

American Physical Society, Denver, Colo., June 25–27, 1964

O. C. Yonts, A. M. Veach,[2] E. D. Shipley, W. A. Bell,[2] and R. N. Goslin,[3] "Ion Beam Stabilization. I."

A. M. Veach,[2] O. C. Yonts, E. D. Shipley, W. A. Bell,[2] and R. N. Goslin,[3] "Ion Beam Stabilization. II."

International Symposium on Diffusion of Plasma Across a Magnetic Field, Feldafing Starnberger See, Germany, June 29–July 3, 1964

N. H. Lazar, C. W. Blue, R. A. Gibbons, and O. D. Matlock, "Studies in the Halo of the Deuterium Arc and a PIG-Type Discharge."

T. K. Fowler,[4] "Bounds on Diffusion by Microinstabilities."

Third Symposium on Engineering Problems in Thermonuclear Research, Munich, Germany, June 22–24, 1964

W. F. Gauster, "Recent Progress in Magnetic Field Technique," an invited and summarizing paper for the Magnetics Session of the Conference.

[1]ORINS Graduate Student.

[2]Isotopes Division.

[3]Consultant, Oglethorpe University, Oglethorpe, Ga.

[4]Physics Division.

1964 Linear Accelerator Conference, Midwestern Universities Research Association, Stoughton, Wis., July 22–23, 1964

G. G. Kelley and O. B. Morgan, "Ion Source and Column Performance at ORNL."

United Nations Conference on the Peaceful Uses of Atomic Energy, 3rd, Geneva, Switzerland, Aug. 31–Sept. 9, 1964

A. H. Snell, "Controlled Fusion Research at ORNL," part of joint USA paper presented by H. Roderick, Controlled Thermonuclear Research, Division of Research, U.S. Atomic Energy Commission, Washington, D.C.

Colloquium on Interaction Between Electromagnetic Waves and Plasma, Institut National des Sciences et Techniques Nucleaires, Saclay, France, Sept. 10–12, 1964

A. C. England, W. B. Ard, M. C. Becker,[5] R. A. Dandl,[5] H. O. Eason, and G. M. Haas, "Experiments on a Large Volume Electron-Cyclotron Heated Plasma."

World Power Conference, Lausanne, Switzerland, Sept. 13–17, 1964

W. F. Gauster, D. C. Freeman, Jr.,[6] and H. M. Long,[6] "Applications of Superconductivity to the Improvement of Electrical Energy Economics."

Culham Study Group on Plasma Waves, Culham Laboratory, UK Atomic Energy Authority, Sept. 21–25, 1964

Igor Alexeff and W. D. Jones, "Study of Ionic Sound Wave Pulses Using Electronic Noise Rejection."

Third National Meeting, Society of Applied Spectroscopy, Cleveland, Ohio, Sept. 28–Oct. 2, 1964

J. R. McNally, Jr., "On an Unusual Dynamic Equilibrium in Magnetically Confined Arc-Plasmas."

General Meeting of the German Physical Society, Dusseldorf, Germany, Oct. 5–9, 1964

W. F. Gauster, an invited paper, "High Field Superconductors and the Development of Superconducting Magnets."

Southeastern Chapter, Society of Nuclear Medicine, Atlanta, Ga., Oct. 22–24, 1964

C. C. Harris, D. A. Ross, M. M. Satterfield, and J. K. Goodrich,[7] "A Collimator for Scanning with Low-Energy Photons."

D. A. Ross, "High Pressure on Low-Energy Emitters."

---

[5]Instrumentation and Controls Division.

[6]Linde Company.

[7]University of Mississippi Medical Center.

ORNL-3760
UC-20 – Controlled Thermonuclear Processes
TID-4500 (37th ed.)

INTERNAL DISTRIBUTION

1. I. Alexeff
2. W. B. Ard
3. C. F. Barnett
4. C. O. Beasley
5. M. C. Becker
6–11. P. R. Bell
12. D. S. Billington
13. E. P. Blizard
14. C. W. Blue
15. G. E. Boyd
16. R. L. Brown
17. G. W. Charles
18. E. H. Christy, Jr.
19. D. L. Coffey
20. F. L. Culler
21. J. S. Culver
22. R. A. Dandl
23. R. C. Davis
24. S. M. DeCamp
25. R. A. Dory
26. J. L. Dunlap
27. H. O. Eason, Jr.
28. R. S. Edwards
29. A. C. England
30. J. C. Ezell
31. D. E. Ferguson
32. J. L. Fowler
33. T. K. Fowler
34. J. E. Francis, Jr.
35. J. H. Frye, Jr.
36. W. F. Gauster
37. R. A. Gibbons
38. J. H. Gillette
39. P. M. Griffin
40. W. R. Grimes
41. G. E. Guest
42. E. Guth
43. G. M. Haas
44. W. Halchin
45. C. C. Harris
46. G. R. Haste
47. R. E. Hill
48. A. S. Householder
49. H. C. Hoy
50. R. P. Jernigan, Jr.
51. W. D. Jones
52. G. G. Kelley
53. M. T. Kelley
54. R. L. Knight
55. J. A. Lane
56. C. E. Larson
57. N. H. Lazar
58. G. F. Leichsenring
59. W. J. Leonard
60. J. Lewin
61. R. S. Livingston
62. J. N. Luton, Jr.
63. J. F. Lyon
64. H. G. MacPherson
65. J. R. McNally, Jr.
66. O. D. Matlock
67. K. Z. Morgan
68. O. B. Morgan
69. R. V. Neidigh
70. M. L. Nelson
71. J. Neufeld
72. C. E. Parker
73–74. R. B. Parker
75. W. F. Peed
76. H. Postma
77. J. F. Potts
78. M. Rankin
79. J. A. Ray
80. L. H. Reber
81. R. G. Reinhardt
82. D. M. Richardson
83. D. A. Ross
84. P. W. Rueff
85. W. K. Russell
86. H. E. Seagren
87. Y. Shima
88. E. D. Shipley
89. M. R. Skidmore
90. M. J. Skinner
91–111. A. H. Snell
112. W. L. Stirling
113. R. F. Stratton, Jr.
114. R. A. Strehlow
115. E. H. Taylor
116. H. A. Ullmaier
117. H. L. Watts
118. A. M. Weinberg

119. E. R. Wells
120. T. A. Welton
121. G. C. Williams
122. W. L. Wright
123. A. J. Wyrick
124. O. C. Yonts
125. Gale Young
126. Owen Eldridge (consultant)
127. J. W. Flowers (consultant)
128. D. C. Freeman, Jr. (consultant)
129. M. W. Garrett (consultant)
130. H. Grad (consultant)
131. E. G. Harris (consultant)
132. W. Heckrotte (consultant)
133. R. Hefferlin (consultant)
134. G. W. Hoffman (consultant)
135. V. W. Hughes (consultant)
136. E. W. McDaniel (consultant)
137. D. R. Montgomery (consultant)
138. C. E. Nielsen (consultant)
139. W. B. Pardo (consultant)
140. J. M. Reynolds (consultant)
141. H. S. Robertson (consultant)
142. H. G. Rorschach (consultant)
143. D. J. Rose (consultant)
144. L. P. Smith (consultant)
145. P. M. Stier (consultant)
146. J. D. Tillman (consultant)
147–167. Thermonuclear Division Library
168. Reactor Division Library
169. Biology Division Library
170–172. Central Research Library
173. Laboratory Shift Supervisor
174–249. Laboratory Records Department
250. Laboratory Records, ORNL RC
251–252. ORNL – Y-12 Technical Library Document Reference Section

EXTERNAL DISTRIBUTION

253. S. C. Brown, Massachusetts Institute of Technology
254. O. Buneman, Stanford Electronics Laboratories
255. M. B. Gottlieb, Princeton University
256. F. W. Crawford, Stanford Electronics Laboratories
257. J. L. Tuck, Los Alamos Scientific Laboratory
258. D. W. Kerst, University of Wisconsin
259. A. C. Kolb, Naval Research Laboratory
260. Morton A. Levine, Air Force Cambridge Research Laboratories
261. J. A. Phillips, Los Alamos Scientific Laboratory
262. R. F. Post, University of California, Lawrence Radiation Laboratory
263. A. Simon, General Atomic, San Diego, California
264. L. Spitzer, Princeton University
265. E. Teller, University of California, Lawrence Radiation Laboratory
266. C. M. Van Atta, University of California, Lawrence Radiation Laboratory
267–268. Research and Development Division, AEC, ORO (1 copy each to H. M. Roth and R. B. Martin)
269–272. Controlled Thermonuclear Research Branch, AEC, Washington (A. E. Ruark)
273. L. D. Smullin, Massachusetts Institute of Technology
274–284. USAEC, Division of Research, Controlled Thermonuclear Research Program (Stephen O. Dean)
285–900. Given distribution as shown in TID-4500 (37th ed.) under Controlled Thermonuclear Processes category (75 copies – CFSTI)